Fischer-Tropsch synthesis inside a nanoreactor

By

Tumelo N. Phaahlamohlaka

Thesis submitted to the Faculty of Science, University of the Witwatersrand, Johannesburg, in fulfilment of requirements for the Degree of Doctor of Philosophy.

Declaration

UNIVERSITY OF THE
WITWATERSRAND,
JOHANNESBURG

I **Tumelo Nathaniel Phaahlamohlaka**, hereby declare that the work on which this thesis is based is my original work that has not been and will never be submitted to any other institution of higher learning other than the University of the Witwatersrand where the work was carried out. Furthermore, I declare that every detail of this thesis taken from other people's work has been recognized and cited accordingly.

Signature: ***Date:*** 10/7/2017

Abstract

Coal, biomass and natural gas are traditional energy carriers whose conversion via the Fischer-Tropsch process can be used to generate multiple hydrocarbon products such as fuels and fine chemicals. At the center of the Fischer-Tropsch process is the catalyst used for converting the syngas to hydrocarbons. Generally these catalysts using Co or Fe active sites are supported on high surface area inert materials such as silica and alumina. Our procedure in this thesis was to study some of the fundamental processes that affect Fischer-Tropsch catalysts (i.e. catalyst reduction, Ru as a reduction promoter and deactivation) using a so-called nanoreactor. This was done by loading metallic nanoparticles on either side of the nanoreactor surface. In this work hollow carbon sphere nanoreactors were mainly used as the catalyst support of choice to evaluate the processes mentioned above. First the effect of the hollow carbon sphere porosity on Fischer-Tropsch synthesis was evaluated using encapsulated Ru nanoparticles. Limited mass transfer limitations were observed on the mesoporous nanoreactor, thus suggesting the encapsulated nanoparticles were as accessible to reactants as the Ru nanoparticles loaded on the outside of the hollow spheres.

Using mesoporous hollow carbon spheres the effect of hydrogen spillover on Co Fischer-Tropsch nanoparticles using a Ru promoter was evaluated by controlling the nanoparticle intimacy [of Ru and Co] by exploiting the hollow carbon sphere morphology. Primary hydrogen spillover was found to be more favorable in enhancing the Co nanoparticles extent of reduction and Fischer-Tropsch activity. However, secondary hydrogen spillover from the Ru nanoparticles to Co nanoparticles on the carbon shell was responsible for a complete reduction of the cobalt oxide when compared to an unpromoted Co Fischer-Tropsch catalyst on the hollow carbon spheres. It was also shown that the secondary hydrogen spillover led to the formation of highly hydrogenated products during Fischer-Tropsch synthesis.

In terms of catalyst stability, the nanoparticles, by virtue of being embedded inside the carbon nanoreactor shell, showed good stability against sintering and re-oxidation by added water during process conditions. Furthermore a simple design of a highly sinter resistant catalyst is presented by making a compact nanoreactor on a titania supported Co Fischer-Tropsch catalyst.

This study illustrates the benefit of rationally designing and characterizing materials for a comprehensive understanding of important catalytic reaction processes; in this case our focus was on the reduction behavior and stability of Fischer-Tropsch catalysts.

Dedication

To the Lion and Lioness in my life: mommy and daddy, Esther and Mautu Phaahlamohlaka

"Commit to the LORD whatever you do, and your plans will succeed" Proverbs 16:3

Acknowledgements

My supervisor **Professor Neil Coville**, I will forever be grateful for your kindness and patience. You are a top class scientist and supervisor. Your suggestions were always well thought out and inspirational as proven by the success this thesis.

I acknowledge my co-supervisor, **Professor Linda Jewell**, you have been amazing to me and your meticulous reading and scientific insights of my manuscripts helped refine the thesis's contents.

To all the members of **CATOMMAT group,** for all the professional and scientific experiences I gained from each and every one of you.

It would be presumptuous to not specifically mention my fellow sojourners who were always there to give me both scientific and extramural support at any point in my postgraduate studies at Wits. **Dr. Lerato Hlekelele, Dr. David Kumi, Mr. Ofentse Makgae, Dr. Wilson Mogodi, Dr. Farai Dziike, Dr. George Bepete, Dr. William Dlamini, Dr. Themba Tshabalala, Mr. Arthur Moya, Mr. Shahil Ramallal and Dr. Pierre Kalenga, Dr. Bridget Mutuma, Ms Gugulethu Nkala, Ms Boitumelo Matsoso,** each one of you contributed in no small part to the successful completion of this PhD degree and for that I am very thankful.

I thank **Basil Chassoulous** and **Tshepo Moshoene** for all their technical help in setting up my catalyst reactors and furnaces.

Khutso Mokami, meeting and befriending you in the second year of my varsity life was a life changer our shared passion and definite optimism helped carry us through the toughest times. Thank you for your support still and soon we will all make it ☺!

I would like to express my sincere gratitude to my very influential high school science teacher, **Mr. Sepeke Tshukudu**; it was him who introduced me to a university level chemistry book (Zumdahl general chemistry ^{4th} Ed) that invigorated my love for the chemical sciences.

I thank the following centres that were also instrumental to the completion of this thesis: (1). **XRD central**, for all the powder X-ray measurements and help with the Rietveld refinement method.

(2). **Microscopy and Microanalysis Unit,** for making the microscopes accessible and all the training that was given to me by the imminently competent staff at the Unit.

I thank my **Family** for their support in all that I do; my love for you is immeasurable. To my **Father and Mother**, I have no doubt that your glorious interceding on my behalf before our Sovereign God kept me strong and level headed during the lows and highs of my PhD studies, my accomplishments, if any will always be yours too.

I am grateful to the research group (**Center for Catalysis Research**) of **Prof. Michael Claeys** at the University of Cape Town for their help with in situ magnetometer measurements of my catalysts and data interpretation.

I wish to recognize the **National Research Foundation (NRF)** of South Africa, **University of the Witwatersrand** and the **DST-NRF Center of excellence in catalysis** for funding my studies.

School of Chemistry and Molecular Sciences Institute, from the head of school, safety officer to the entire academic and support staff at the Humphrey Raikes building. You were mostly gracious to me and cultivated for me a wonderful working climate.

Publications, Presentations and Awards

Publications

1. **Tumelo N. Phaahlamohlaka**, David O. Kumi, Mbongiseni W. Dlamini, Linda L. Jewell, and Neil J. Coville. "Ruthenium nanoparticles encapsulated inside porous hollow carbon spheres: A novel catalyst for Fischer–Tropsch synthesis." Catalysis Today 275 (2016): 76–83

2. **Tumelo N. Phaahlamohlaka**, David O. Kumi, Mbongiseni W. Dlamini, Roy Forbes, Linda L. Jewell, David G. Billing, Neil J. Coville "Effects of Co and Ru intimacy in Fischer-Tropsch catalysts using hollow carbon sphere supports: assessment of the hydrogen spillover processes." ACS Catalysis 2016 7, (2017): 1568–1578

3. **Tumelo N. Phaahlamohlaka**, Linda L. Jewell, and Neil J. Coville. "Hollow carbon spheres as ideal supports for hydrogen spillover studies using ruthenium and cobalt nanoparticles." European Microscopy Congress 2016: Proceedings. Wiley-VCH Verlag GmbH & Co. KGaA.

4. Mbongiseni W. Dlamini, David O. Kumi, **Tumelo N. Phaahlamohlaka**, Anton S. Lyadov, David G. Billing, Linda L. Jewell, and Neil J. Coville. "Carbon Spheres Prepared by Hydrothermal Synthesis—A Support for Bimetallic Iron Cobalt Fischer–Tropsch Catalysts." ChemCatChem 7, no. 18 (2015): 3000-3011.

5. **Tumelo N. Phaahlamohlaka**, Linda L. Jewell and Neil J. Coville. "Fischer-Tropsch synthesis in a carbon nanoreactor: spillover effect observed on Co@MHCS@Ru.**" Manuscript to be submitted.**

6. **Tumelo N. Phaahlamohlaka**, Linda L. Jewell, Michael C. Clays and Neil J. Coville. "Effect of Water on the Stability of Co Fischer-Tropsch Nanoparticles inside Hollow Carbon Spheres: An In Situ Magnetometer Study." **Manuscript to be submitted.**

7. **Tumelo N. Phaahlamohlaka**, Linda L. Jewell, Michael Clays and Neil J. Coville. **"**A sinter resistant cobalt Fischer-Tropsch catalyst supported on Titania; with Ru as an electronic promoter and mesoporous silica as the structural promoter." **Manuscript to be submitted.**

Presentations

1. DST-NRF Centre of Excellence in Catalysis (c*change) Workshops. 2014-2016, (Pretoria, Hermanus and Drakensberg, South Africa, **Oral Presentations**.

2. Catalysis Society of South Africa annual Conference, Pretoria, South Africa, November 2014, **Poster Presentation**. Paper Title: *TPR/O and Chemisorption studies on Co/Ru particles inside hollow carbon* spheres.

3. Microscopy Society of Southern Africa annual conference, Pretoria, South Africa, December 2015, **Poster Presentation**. Paper Title: *Ruthenium nanoparticles inside porous hollow spheres as a catalyst for Fischer-Tropsch Synthesis.*

4. Second International Syngas Convention, Cape Town, South Africa, March 2015, **Oral Presentation**. Paper Title: R*uthenium nanoparticles encapsulated inside porous hollow spheres: A novel catalyst for Fischer-Tropsch synthesis reaction.*

5. Catalysis Society of South Africa annual Conference, Hermanus, South Africa, November 2015, **Poster presentation**, Paper Title: *Preparation of RuCo on hollow carbon spheres for Fischer-Tropsch synthesis and H_2 spillover studies.*

6. 7th Wits Cross-Faculty Graduate Symposium, University of the Witwatersrand, Johannesburg, South Africa, March 2016, **Poster presentation**. Paper Title: *Developing a stable catalyst for production of liquid fuels by a Fischer-Tropsch process.*

7. South African Nanotechnology Innovation, NanoAfrica 2016, Johannesburg, South Africa, April 2016, **Oral Presentation**. Paper Title: *Cobalt nanoparticles inside hollow carbon spheres: A nanoreactor endowed with high catalytic activity.*

8. The 16th European Microscopy Congress, Lyon, France, September 2016, **Poster Presentation**. Paper Title: *Hollow carbon spheres as ideal supports for hydrogen spillover studies using ruthenium and cobalt nanoparticles.*

9. South African Nanotechnology Innovation, Young Scientists Nano Symposium, Mintek, Johannesburg, November 2016, South Africa, November 2016, **Oral Presentation**. Paper Title: *Demonstrating hydrogen spillover through a rational design of Ru promoted Co Fischer-Tropsch catalyst on hollow carbon nanoreactors.*

10. Catalysis for Fuels Faraday Discussion, Cape Town, South Africa, January 2017, **Poster and flash Presentation**. Paper Title: *Demonstrating hydrogen spillover through a rational design of Ru promoted Co Fischer-Tropsch catalyst on hollow carbon nanoreactors.*

Awards

1. **Honorable Mention Poster presentation**: Catalysis Society of South Africa Annual Conference, November 2014, Pretoria, South Africa
2. **Mary Veenstra Prize for the Best Materials Science Poster presentation:** Microscopy Society of Southern Africa Annual Conference, December 2015, Pretoria, South Africa
3. **National Research Foundation Innovation PhD Scholarship:** 2014-2017, University of the Witwatersrand
4. **Postgraduate PhD Merit award:** 2014-2016, University of the Witwatersrand
5. **Young Scientist Travel Grant:** European Microscopy Congress 2016, Lyon, France
6. **Student grant (2016):** Microscopy Society of Southern Africa (MSSA) Trust
7. **SACI Postgraduate Award of the South African Chemical Institute**: 2017, University of the Witwatersrand, School of Chemistry nominee

Contents

List of Figures

List of Tables

List of Abbreviations

Abbreviation	Description
ASF	Anderson Schulz Flory
BET	Branauer Emmett Teller
MHCS	Mesoporous Hollow Carbon Spheres
CVD	Chemical Vapor Deposition
CNTs	Carbon Nanotubes
CVD	Chemical Vapor Deposition
FID	Flame Ionization Detector
FTIR	Fourier Transform Infrared Spectroscopy
FTS	Fischer-Tropsch Synthesis
GC	Gas Chromatography
GHSV	Gas Hourly Space Velocity
HDP	Homogenous Deposition Precipitation
PXRD	Powder X-Ray Diffraction
TCD	Thermal Conductivity Detector
TEM	Transmission Electron Microscopy
TGA	Thermo-Gravimetric Analysis
TPR	Temperature Programmed Reduction
WGS	Water Gas Shift
α	Alpha Value
PSSs	Polystyrene Spheres
RF	Resorcinol Formaldehyde
STEM	Scanning Transmission Electron Microscopy
SEM	Scanning Electron Microscopy
HCS	Hollow Carbon Spheres
W/F	weight to mol flow rate

Chapter 1

Introductory chapter

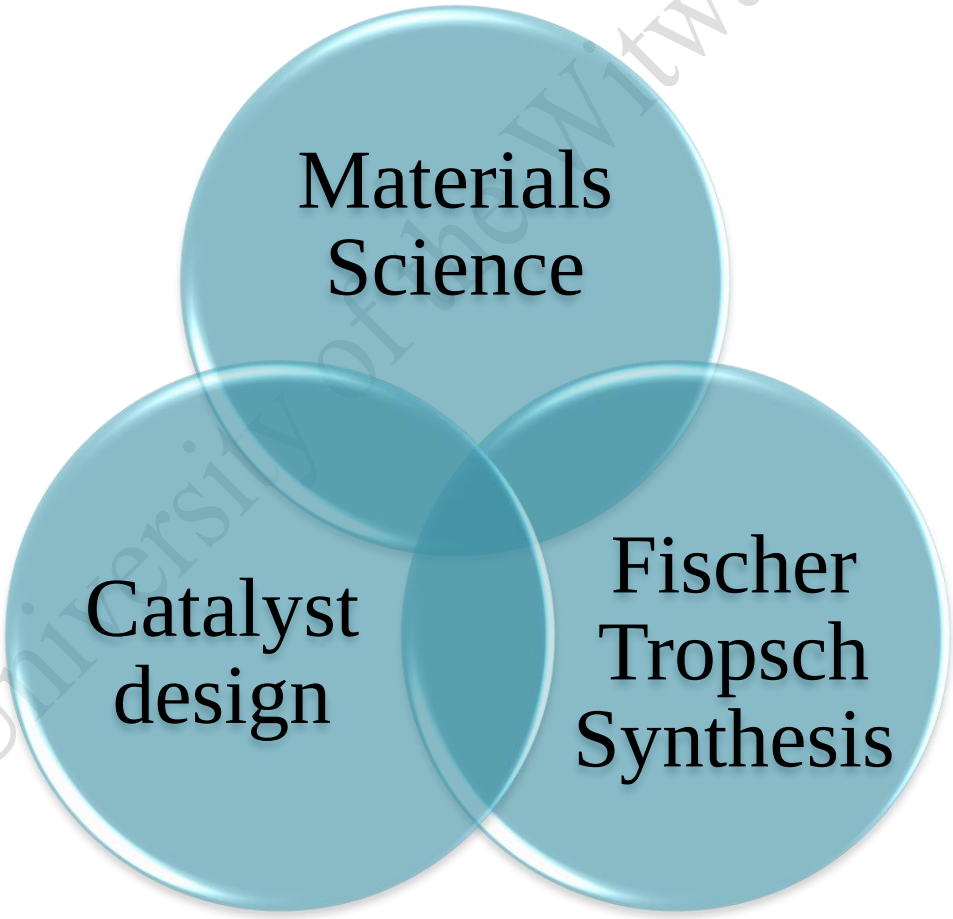

1.1. Synthetic oil production and Fischer-Tropsch catalysts

With the increasing global energy demands **[1]**, it is imperative that existing technologies for energy generation be optimized to enhance their efficiency with little environmental damage, whilst new advanced technologies are being developed. Fischer-Tropsch products offer an alternative to crude oil products, the Fischer-Tropsch fuels also burn in a cleaner way than typical crude oil fuels because of their high purity and good quality **[2]**.

Since the discovery of the Fischer-Tropsch reaction, a quest to make catalysts with better activity and selectivity has always been interlinked with the industrial development of the Fischer-Tropsch process. This is evidenced by the different Fischer-Tropsch commercial set-up by different companies, whose catalyst systems are quite diversified **[3, 4]**. In the first half of the 20^{th} century Germany through Ruhrchemie was the leader in the industrialization of the Fischer-Tropsch process using Co catalysts **[3, 5]**. In South Africa, Sasol has used different catalysts systems for a profitable use of Fischer-Tropsch synthesis, using both Co and Fe catalysts ranging from low to high temperature Fischer-Tropsch synthesis depending on the source of syngas used and the desired end products **[3, 6]**. Further developments in catalysts research by Sasol and Shell has resulted in the commissioning of Fischer-Tropsch plants based on Co supported on oxidic supports at places such as Qatar, Malaysia and Nigeria, whereby natural gas is used as the syngas source. Several companies especially in China are also exploring and developing catalysts materials for commercialization of the Fischer-Tropsch process.

Table 1.1: Global Fischer-Tropsch plants and their catalyst systems **[3, 6]**.

Company	Country	Technology	Catalyst main components	Year
Sasol	South Africa	Sasol I	Precipitated Fe	1955
Sasol	South Africa	Sasol II	Fused Fe	1980
Sasol	South Africa	Sasol III	Fused Fe	1982
PetroSA	South Africa	Sasol 2 and 3	Fused Fe	1993
Shell	Malaysia	SMDS[a]	Co/ SiO_2	1993
Sasol/Qatar petroleum	Qatar	SPD[b]	Co/Al_2O_3	2006
Shell/Qatar petroleum	Qatar	SMDS	Co/ SiO_2	2012
Sasol/Chevron and Nigerian Petroleum Company	Nigeria	SPD	Co/Al_2O_3	2014

[a]SMDS = Shell middle distillate synthesis process
[b]SPD = Sasol slurry phase distillate process

1.2. Project background and details

Catalytic processes play an important role in the chemical industry for the production of many products that are vital for the sustenance of our civilization and our way of life **[7-9]**.

The economic benefits of these catalytic processes have been realized using both homogenous and heterogeneous catalysts **[8, 9]**. In heterogeneous catalysis the Fischer-Tropsch synthesis (FTS) stands out as a premier catalytic reaction that has not only been economically beneficial. It is due to the intensive study of this process that the field of heterogeneous catalysis has significantly advanced **[10-12]**.

The rich history of FTS can be traced back to the 1920s when Han Fischer and Franz Tropsch observed the hydrogenation of carbon monoxide to liquid hydrocarbons at high pressures **[10]**. Since then significant advances of this technology have been made in terms commercialization and development of new optimized catalysts and reactors. The FTS process is an XTL (i.e. X = coal natural; gas or biomass) technology thus has an inherent ability to be modified to produce a variety of high value products such as a cleaner fuel

(that is environmentally friendly than crude oil fuel) and a multiplicity of essential daily life chemicals **[13-15]**.

With the latest discoveries of more coal and natural gas reserves of which it is predicated they will last for the next 100 years (coal) and 30 years (natural gas), and the abundant biomass whose technology for converting to syngas (i.e. hydrogen and carbon monoxide) has improved over the years and its forecast to even get better [**[16-18]**. As a result of these determining factors, there has been an increased interest in the modification and development of new Fischer-Tropsch catalysts with better activity, selectivity and stability. The development of new Fischer-Tropsch catalysts inadvertently interlinks with materials chemistry that deals with a rational design and synthesis of advanced functional materials **[11, 13-15]**.

The development of these catalysts is generally aimed at understanding and improving the fundamental processes that affect the performance of the metal sites used in Fischer-Tropsch synthesis. These includes a myriad of processes that have been and are being studied in detail such as structure sensitivity, catalyst activation and deactivation, sintering, and selectivity control etc. **[12, 14, 15, 19]**.

Of particular interest is the reducibility of the catalysts and the role that the reduction promoters (using Pt, Ru, Re, Au, etc.) play in the activation catalyst of catalytic active sites. Several studies have suggested that promotion on these Fischer-Tropsch synthesis catalysts (mainly Co and Fe) by reduction promoters can be attributed to their ability to spillover hydrogen atoms from their surfaces to the Co or Fe metal or metallic oxides (even the catalyst support) **[20]**. In the literature there have been several attempts to evaluate the effect of spillover mechanisms (primary and secondary) in Fischer-Tropsch catalysts in relation to the promoter and promoted metal intimacy. Interesting results were observed for promoters such as gold and platinum **[21]**, and spillover the processes were observed using the platinum promoter metals while on a gold promoter it was not necessarily evident **[21]**. In this previous and other study the hydrogen transporting layer might have been long and not necessarily well suited for hydrogen atom transportation **[22-24]**. This therefore pointed to a need for further development of model catalysts that are suited for delineation of both primary and secondary spillover processes, for evaluation of their effects on Co Fischer-Tropsch catalytic activity and selectivity. Mesoporous hollow carbon spheres (MHCS, nanoreactors) provide good model catalysts supports for making catalytic nanoreactors in which the promoter and promoted metal's intimacy can be successfully manipulated in the nanoscale (using the hollow sphere carbon shell) to study the effect of both the secondary and primary hydrogen spillover processes. Working with Ru (as a promoter) and Co (as the promoted FTS active metal) porous nanoreactors with metal nanoparticles could be prepared in good yield. The method for synthesizing the hollow carbon spheres was adapted to encapsulate either Co or Ru, with the carbon shell serving as a physical barrier between the Co and Ru metal for secondary hydrogen spillover studies.

Thus the project focused on the synthesis and characterization of encapsulated metal nanoparticles in hollow carbon spheres and related materials for Fischer-Tropsch evaluation. Although the literature is replete with methods for preparing metal nanoparticles encapsulated inside hollow carbon spheres **[25]**, these methods involved the encapsulation of noble and platinum group metals, therefore to the best of our knowledge there has been no reports on the efficient encapsulation Co or Fe nanoparticles inside hollow carbon spheres. In this project a method was devised using a pseudo-soft template method to encapsulate Co nanoparticles.

Stability of Co Fischer-Tropsch catalysts against sintering and re-oxidation under reaction conditions is also an important aspect to be considered in catalyst development **[19]**. Thus these novel Co nanoreactors' stability (when compared to Co loaded outside the MHCS) was also evaluated using in situ techniques under simulated Fischer-Tropsch conditions (i.e. co-feeding water in the presence of syngas). As catalysts prepared using the hollow carbon sphere nanoreactors (or carbon nanomaterials, although good for fundamental catalysts studies) have hardly been used in large scale Fischer-Tropsch synthesis, a compact nanoreactor using titania as the support was designed to make a sinter resistant Fischer-Tropsch catalyst by coating the Co nanoparticles supported on titania with a thin layer of porous silica shell.

Because a major part of this project involved materials synthesis of the catalysts, numerous characterization techniques were employed. Electron microscopy and powder X-ray diffraction techniques proved to be essential in understanding the catalysts structure and physico-chemical properties, as has been the case in materials science studies involving a synthesis of carbon materials and related ones.

1.3. Aim and objectives

A development of new materials for understanding and improving catalysts is one of the ongoing challenges in materials science. Therefore the key aim of this study was to perform ***Fischer-Tropsch catalytic reaction inside nanoreactors*** with controlled morphologies and porosities, with a goal of exploiting these functional materials to understand fundamental factors that affect FTS catalysts as it relates to reduction, oxidation and sintering. With this in mind the objectives of this thesis are as follows:

- ***i.*** *Developing a synthesis method for encapsulating Ru nanoparticles inside highly porous hollow carbon spheres using a modified Stöber method.*
- ***ii.*** *Providing a novel and optimum non Stöber general synthetic technique for decorating cobalt nanoparticles (or any non-noble and non-platinum group metal) inside porous hollow carbon spheres.*
- ***iii.*** *Preparation of novel Co Fischer-Tropsch catalysts using Ru promoter whereby the Co and Ru intimacy is controlled by exploiting the hollow carbon spheres morphology.*
- ***iv.*** *Understanding effect of Ru promoter on Co nanoparticles reduction and Fischer-Tropsch synthesis, in light of the metals relative location on the support, and evaluating the predominant hydrogen spillover mechanism and its effect in Fischer-Tropsch Synthesis.*
- ***v.*** *Study and evaluate the sinter and re-oxidation resistant capabilities of the prepared catalytic nanoreactors*

1.4. Thesis outline

References for the entire thesis are listed at the end of the manuscript; this was done because some of the references are repeated in different individual chapters.

Chapter 1 *details background and justification for the study and the thesis's main objectives.*

Chapter 2 and 3 *covers Fischer-Tropsch synthesis literature and the recent advances in the synthesis of hollow carbon spheres their pore structure and applications in heterogeneous catalysis.*

Chapter 4 *gives details of the characterizations techniques used in this thesis and some of the experimental procedures.*

Chapter 5 *presents the synthesis of Ru nanoparticles inside hollow carbon spheres with different porosities and their behavior under Fischer-Tropsch synthesis. This chapter has been published as; Tumelo N. Phaahlamohlaka et al.* ***Catalysis Today 275 (2016): 76–83****.*

Chapter 6 *studies the use of mesoporous hollow carbon spheres to separate the effects of both the primary and secondary hydrogen spillover in Co Fischer-Tropsch synthesis. This chapter has been published as; Tumelo N. Phaahlamohlaka et al.* ***ACS Catalysis 2016, 7, (2017): 1568–1578****.*

Chapter 7 *presents a facile synthesis of Co nanoparticles inside hollow carbon spheres for further hydrogen spillover studies using Co and Ru nanoparticles.*

Chapter 8 *looks on the stability of the encapsulated Co nanoparticles under high water contents using an in situ magnetometer.*

Chapter 9 *studies the stability of Co against sintering on a compact Fisher-Tropsch nanoreactor using oxidic supports and a porous silica shell.*

Chapter 10 *gives overall conclusions and recommendations for future studies on the use of carbon nanoreactors to study important Fischer-Tropsch processes.*

Chapter 2

Contemporary issues in Fischer-Tropsch Synthesis

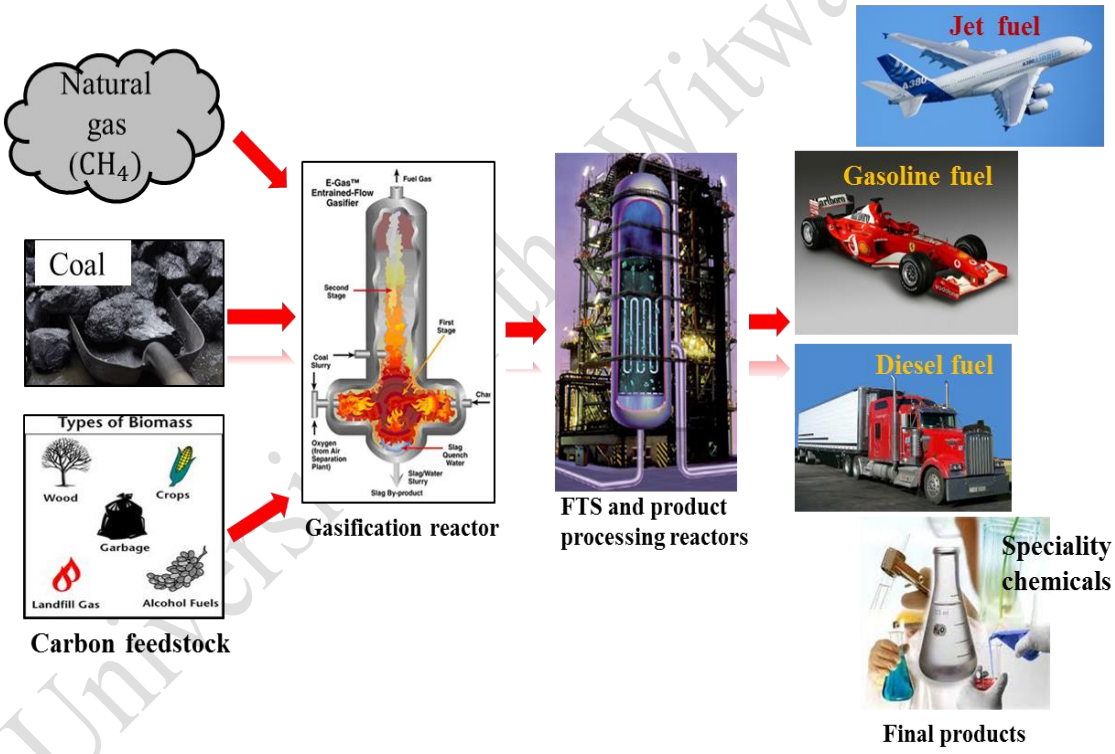

Figure 2.1: Generalized process scheme for Fischer-Tropsch Synthesis technology, from raw materials to final products adapted from **[15]**.

2.1. General introduction

Fischer-Tropsch synthesis is a valuable catalytic process that is used to produce liquid fuels and chemicals from synthesis. Over the past 80 years this process has yielded significant economic benefits for some countries and multinational companies. It has also benefited and advanced the science of heterogeneous catalysis because of the reaction complexity, and fundamental discoveries in the catalytic process of Fischer-Tropsch synthesis have had far reaching effects on the understanding of other catalytic process **[10, 11, 26-28]**. It is defined as a surface-catalyzed polymerization process that uses CHx monomers formed by hydrogenation of adsorbed CO to produce hydrocarbon products with varying chain length and functionality. The synthesis gas, which is a mixture of the carbon monoxide and hydrogen, can be obtained from natural resources like coal, natural gas and biomass (Figure 2.1). With the world's confirmed reserves of natural gas and coal far surpassing that of crude oil it is not surprising that the Fischer Tropsch process is still a valued process as a future energy resource or alternative **[29, 30]**.

The Fischer-Tropsch process produces hydrocarbons and water as the main products. The main hydrocarbons formed are linear alkanes and alpha olefins. Several oxygenates such as aldehydes and alcohols are also produced during the synthesis process together with some branched hydrocarbons.

Typical operational conditions in terms of pressure and temperature range from 5-60 bar and 200-350 ℃ respectively. The reaction is also an exothermic process producing large amounts of heat **[10, 31]**. Although the process is defined as a polymerization process it is not a traditional polymerization reaction because, (1) the monomers are formed in-situ (2) primary products can [and do] undergo secondary reactions (3) and rates of surface reactions depend on the formation of C_1-C_4 units **[53]**. The Fischer-Tropsch kinetic models are closely related to the mechanistic details of the chemical reaction. Because of the complexity of the reaction mechanism, FT reaction kinetics have also become very complex **[31]**. The FT reaction can be simplified as:

$$\mathbf{CO + \left(1 + \frac{m}{2n}\right)H_2 \rightarrow \frac{1}{n} C_nH_n + H_2O} \quad \Delta H_{R,240\,℃} = -153.7\ \text{kJ/mol}$$

Where, n and m are the average carbon and hydrogen numbers of the hydrocarbon products respectively.

The main reactions involved in FTS can be summarized as;

(1) Paraffin formation:

$$\boldsymbol{nCO + (2n + 1)H_2 \rightarrow C_nH_{2n+2} + nH_2O}$$

(2) Olefin formation:

$$\boldsymbol{nCO + 2nH_2 \leftrightarrow C_nH_{2n} + nH_2O}$$

(3) Water-gas shift (WGS) reaction:

$$CO + H_2O \leftrightarrow CO_2 + H_2$$

(4) Boudouard reaction:

$$2CO \rightarrow C + CO_2$$

Cobalt, iron and ruthenium are the main metals that can catalyze the Fischer-Tropsch process on a commercial scale. However, ruthenium is expensive thus most Fischer-Tropsch studies for possible commercialization are performed on iron and cobalt catalysts**.** Iron catalyst can be operated at low hydrogen to carbon monoxide ratios because of the water gas shift reaction that lowers the amount of CO in the reaction vessel and increases the hydrogen content. Co is generally the preferred catalyst for hydrogen rich feed because it catalyzes the synthesis of predominantly wax enriched hydrocarbons. In many studies these catalysts are dispersed on supports such as silica, alumina, titania and several carbon materials using several catalyst preparation methods (e.g. deposition-precipitation, incipient wetness impregnation and loading of pre synthesized nanoparticles).

2.2. Product Distribution

2.2.1. Anderson-Schulz-Flory distribution

The Fischer-Tropsch synthesis product distribution shows a strong regularity, since the mechanism of the process resembles a polymerization reaction of monomer species (*CH_2 , *CO) for chain growth **[32, 33]**. Chain propagation and termination probabilities are relatively constant and are independent of the chain length. However, catalyst properties can play a vital role in the product distribution **[33, 34]**. A relation for describing the molar product distribution of the Fischer-Tropsch synthesis was derived by Friedel and Anderson **[35]** and a similar relationship was developed by Flory **[36]**. This relation is now known as the Anderson-Schulz-Flory (ASF) distribution **[31]**.

It is written as: $m_n = (1 + \alpha) \times \alpha^{n-1}$ which can be expressed in terms of a weight distribution: $W_n = n(1 + \alpha)^2 \times \alpha^{n-1}$

where m_n is the mol fraction of hydrocarbon with carbon number n, W_n is the weight fraction of hydrocarbon with carbon number n. The chain growth probability (α) can be physically interpreted as the ratio of the rate of chain propagation to the sum of rate of chain propagation and termination rates for each carbon number.

i.e. $\alpha = \frac{\sum_{i=n+1}^{\infty} m_i}{\sum_{i=n}^{\infty} m_i} = \frac{r_{prop}}{r_{prop} + r_{term}}$

The value of α is usually almost constant for all carbon numbers, thus the FT product spectrum can be described to some extent by a single α value.

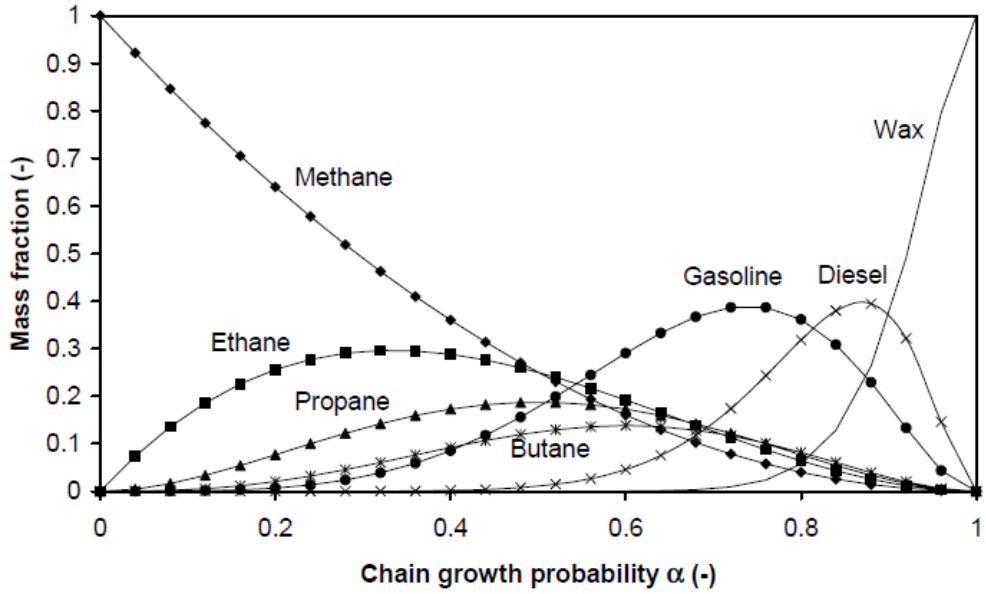

Figure 2. 2: ASF model for FT product selectivities.

The inherent nature of polymerization processes implies that product yields can be predicted as shown in the Figure 2.2 above with yields to different products dictated by the value of α. The most preferred value is for the commercial FT reaction ≥ 0.8 to provide enough hydrocarbons in the fuel range (C_6-C_{18}) and wax that can also be hydrocracked into middle distillate products **[37]**.

2.2.2. Non-Anderson-Schulz-Flory distributions

It has been realized that the ASF model for the Fischer-Tropsch synthesis product distributions provides only a broad generalization. Many product distributions in the literature have been found not to follow the ASF distribution model to the product distribution produced. Typically high methane and low ethane/ethene selectivities are always observed **[31].**

Different explanations for this phenomenon have been put forward for the observed anomalies and include.

: Analytical difficulties due to experimental artefacts **[38]**.

: Different active sites responsible for different chain growth probabilities **[39, 40]**.

: Different termination mechanisms **[41]**

Further, it has been suggested that secondary reactions such as re-adsorption reactions of olefin products can lead to deviation from the ASF model. This is an accepted to proposal to explain deviations from the ASF distribution **[31],** but it has not gone forward without being challenged **[42]**.

The olefin re-adsorption hypothesis has been used successfully to model the kinetics for hydrocarbon distributions by many authors **[43, 44].** This model also explains the exponential decrease in the olefin paraffin ratio with increasing carbon number. The secondary reactions that lead to the deviation of the product spectrum for the ASF model and low olefin paraffin ratio are generally believed to be dependent on the olefin chain length. Three different proposals have been outlined in an effort to explain chain length dependent processes.

(1) Diffusion limitations with increasing olefin carbon number **[45, 46]**.
(2) Increasing physisorption strength with olefin carbon number **[47]**.
(3) Product solubility in wax **[48]**.

The suggested process conditions that affect Fischer-Tropsch product selectivity have been summarized as shown in Table 2.1 as reported by Schulz **[49]**.

Table 2:1: Process conditions that affect FT selectivities;

Parameter[a]	α	O/P ratio	Carbon deposition	CH_4 selectivity
Temperature ↑	↓	↓	↑	↑
Pressure ↑	↑	-	-	↓
H_2/CO ratio ↑	↓	↓	↓	↑
Conversion ↑	-	↓	↑	↑
Space velocity ↑	-	↑	-	↓

[a]↑:Increase, ↓: Decrease and -: No clear relation.

2.3. Possible Fischer-Tropsch mechanisms

The Fischer-Tropsch reaction has been classed as a polymerization reaction because of the wide range of linear products with different chain lengths that result from the process. In this reaction carbon monoxide and hydrogen are converted into high molecular weight hydrocarbons with multiple carbon atoms from a single carbon atom source **[28, 32].** However, the complexity of the Fischer-Tropsch process mechanism arises because the resulting polymerization products are distributed over a wide range from hydrocarbon with one carbon (i.e. methane) to large molecular hydrocarbons well above carbon number fifty (i.e. waxes). To compound this problem other minor products with distinct functionalities deviating from normal hydrocarbons (paraffins) are also formed during the Fischer-Tropsch synthesis. These include olefins, oxygenated hydrocarbons and branched

hydrocarbons amongst other products. It should be noted that all these products are formed concurrently with the main Fischer-Tropsch products at similar reaction conditions **[28, 31]**. Although all these Fischer-Tropsch product classes still form via a polymerization-like mechanism, this means certain reaction steps have to occur to yield different products. For chain polymerization reactions these steps include, (1) adsorption of reactants (2) chain initiation (3) chain growth or propagation (4) and the termination step **[50]**. Studies on Fischer-Tropsch mechanisms are still ongoing and many studies using model catalysts in surface science, theoretical or density functional theory and microkinetic studies are involved in an effort to elucidate the most probable Fischer-Tropsch mechanism **[27]**.

It is for this reason that at the moment there exist no single all-encompassing Fischer-Tropsch mechanism that can individually explain the observed Fischer-Tropsch product spectrum in its entirety. Over the years a number of mechanisms have been postulated to explain formation of the different classes of Fischer-Tropsch products and also to develop experimentally sound kinetics of the reaction **[32, 40, 51].** Burtron Davis **[32, 52]** has detailed some of the most credible reaction mechanisms that have been hypothesized in the literature. Surveying the literature shows that three major mechanisms can be listed as follows:

1. Carbide (carbene) mechanism
2. Oxygenate (enol) mechanism
3. CO insertion mechanism

The **Carbene mechanism** also known as the carbide mechanism is the earliest of the postulated Fischer-Tropsch mechanisms **[32]**. C_1 units are formed on the catalyst surface after dissociation of chemisorbed CO. The resulting metal carbide is then furthermore hydrogenated to CH_x species by the hydrogen atoms that are also formed by dissociatively adsorbing on the catalyst surface. In this mechanism CH_3 units are the assumed chain initiators and CH_2 units on the catalyst surface are the polymerization species. The CH_2 units are therefore inserted between the metal-carbide bonds of CH_3 or alkyl species for chain propagation process. The resulting surface species can terminate to form Fischer-Tropsch products, such a step can occur via several routes:

(1) Addition of a hydrogen atom to form normal alkanes.
(2) Removal of a β-hydrogen from the adsorbed growing chain to form an α-olefin.

Several studies have confirmed the carbide mechanism. For example, Iglesia and co-workers used experimental and theoretical analysis (DFT calculations) to provide evidence for this mechanism on Fe based catalysts in which the CO molecule on the surface is completely activated to form a metal-carbide without the help of hydrogen atoms and most of the resulting oxygen atoms are then removed by forming carbon dioxide **[53].** Surface

science studies by Weststrate et al. on a Co(0001) surface suggest the CO bond scission occurs on the surface defects, thus confirming the first step of the carbide mechanism **[54].** The chain propagation step via CH_2 has been experimentally verified by Brady et al., whereby CH_2 (produced from CH_2N_2) monomers were co-fed into a Fischer-Tropsch reactor with the syngas. Upon addition of the monomers the alpha value was reported to have increased from 0.24 to 0.51, hence hinting to an increased chain propagation kinetics relative to the termination step **[55].** In a study by Nijs and Jacobs it was concluded that the carbide route was only responsible for the formation of methane product **[56].** However, at present the carbide mechanism, because of the requirement for direct CO dissociation, is no longer considered to be major mechanism under normal Fischer-Tropsch process. The high energy barrier for dissociating CO without the assistance of hydrogen is seen as a step that makes the mechanism unfavourable **[51, 57].**

The **enol mechanism** was formulated about 25-30 years after the discovery of the Fischer-Tropsch reaction **[32, 58]**. In this mechanism adsorbed CO molecules are hydrogenated to oxmethylene groups (CHOH), which are the chain initiation units. Chain propagation then proceeds via condensation of the oxymethylene units followed by the removal of water. Chain termination can then occur to form an aldehyde by alkylhydroxycarbene desorption or by β-elimination of water to form olefins. The olefins can also be re-adsorbed and hydrogenated to form alkanes.

The hydrogen assisted dissociation of CO as envisaged in the enol mechanisms has been well documented. King and co-workers showed, using DFT calculations on a Co(0001) surface, that it is easier to form a CHOH monomer on the surface than to directly CO dissociate CO to form a metal carbide **[57]**. Monomer formation on Fe and Co surfaces was experimentally and theoretically evaluated by Ojeda et al. **[53]**; in this study the hydrogen assisted cleavage of CO was postulated to be the main initiation step to form CHOH units, which was then followed by the chain propagation steps.

The third mechanism called the **CO insertion** mechanism emphasizes on the chain propagation step. In this mechanism the growth of the hydrocarbon chains occurs by an insertion of adsorbed CO monomers on an already formed metal-alkyl bond. The mechanism also explains the synthesis of oxygenate (aldehydes and alcohols) and normal hydrocarbon yields, based on the resultant termination steps.

Evidence for this mechanism has been widely reported in literature. Theoretical work by Zhuo et al. **[59]** showed that chain growth propagation by CO on a Co(0001) surface was energetically favourable compared to the propagation step that required CO hydrogenation. Hence, the CO insertion turnover frequency was found to be about two times faster than the hydrogen assisted growth and four times faster than the direct CO activation mechanism. Experimental work by Schweicher and co-workers **[60]** using chemical transient kinetics to change gas compositions during the FT process under atmospheric pressure provided

evidence for the CO insertion mechanism. In their work it was observed that the chain growth probability (α) decreased when the CO partial pressure was lowered and showed an increase when the CO partial pressure increased. This was not the case for atomic surface C (i.e., CH_x monomers) coverages. Xiang et al. **[61]** were able to selectively synthesize long chain alcohols from syngas on a specially designed CoCuMn catalyst. It was suggested that the most applicable mechanism for the Fischer-Tropsch synthesis in their case was the CO insertion mechanism as it is also energetically feasible and can also explain the observed catalyst selectivity.

2.4. Fischer-Tropsch catalyst deactivation

Fischer-Tropsch catalysts gradually lose activity under reaction conditions. The loss is dependent on multiple factors that occur on the catalyst surface and within the bulk structure. The reduction of a catalyst lifetime from ideal periods can be especially cumbersome in industrial applications because a regular change in a catalyst performance can potentially reduce the process's profitability over time **[19, 62].** Numerous studies have attempted to understand the mysteries of the catalyst deactivation phenomena in Fischer-Tropsch Synthesis in an effort to define the prominent mechanisms or processes that are responsible for the loss of activity. The graphic below shows the possible deactivation mechanisms that can occur Co Fischer-Tropsch catalysts (Figure 2.3) **[63]**.

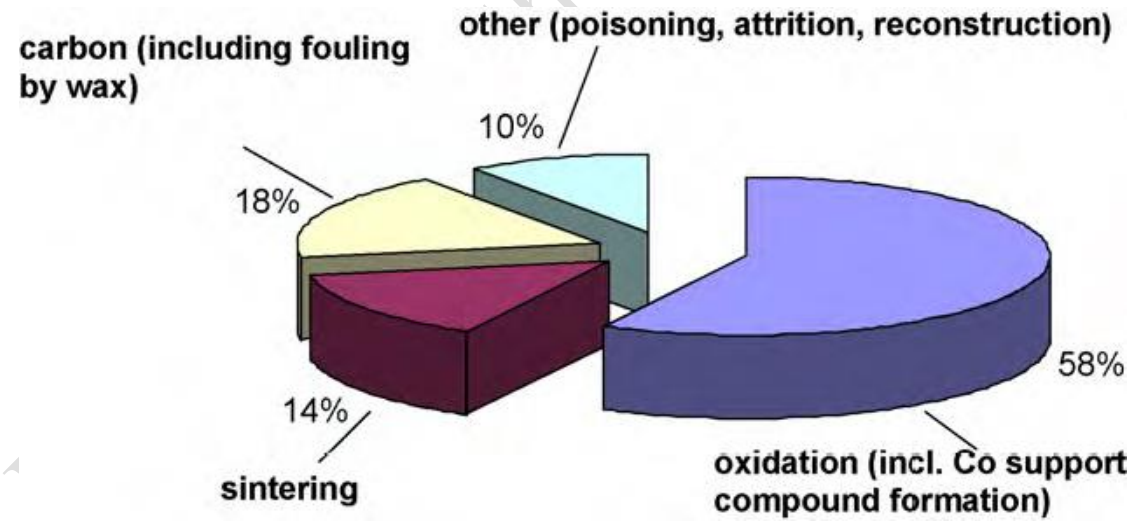

Figure 2. 3: Emphasis on Co FTS deactivation processes as assessed by Saib et al. **[63]**.

Sintering of the active phase is one of the main deactivation processes on Fischer-Tropsch catalysts. This occurs by thermal modification of the active nanoparticles which changes the nanoparticles morphology and sizes resulting in the loss of active sites **[64]** . Work by Eschemann and de Jong, reported on the deactivation of a Co/TiO_2 catalyst prepared by incipient wetness impregnation and deposition precipitation, with different Co loadings (8% and 16 wt/wt%). By evaluating the Co nanoparticle size distribution before and after Fischer-Tropsch synthesis (220 ℃ and 20 bar), the loss of activity was correlated with the Co nanoparticle growth. This effect was especially prominent at high CO conversion. At high CO conversion the activity of the catalysts called IWIS16S (made by incipient wetness impregnation, initial Co size = 8.3 nm and χ_{CO} = 70.4%) and DPA16 (made by deposition precipitation, initial size = 8.0 nm and χ_{CO}= 61.4%) dropped. The final/initial cobalt time yield ratio was measured to be below 0.8, and a corresponding average particle sizes of the spent catalysts after 200 h time on stream was of 9.4 nm for IWI16S and 10.1 nm for DPA16. Although activity loss could be correlated with nanoparticle sintering the authors cautioned that the deactivation could be occurring through sintering in tandem with other processes as illustrated in Figure 2.3. Increased crystallite size (from 3-9 nm to 20-50 nm) after 100 h (at 340 ℃, 20 bar, H_2/CO = 1) was also observed to be a source of catalytic deactivation on an Fe Fischer-Tropsch catalysts supported on carbon nanofibers **[65]**. At high CO conversions the water partial pressure is also expected to play an influential role on the nanoparticle sintering in Fischer-Tropsch synthesis **[66, 67]**

Poisoning of Fischer-Tropsch catalysts is prompted by the adsorption of molecules containing heteroatoms such as sulphur, chlorine and nitrogen. The strong adsorption of these impurities is not easily reversible hence leading to a reduction in the catalyst number of active sites and consequently the Fischer-Tropsch activity **[19, 68]**. Borg et al. studied the effect of impurities (H_2S, $(CH_3)_2S$, Cl and NH_3) on Fischer-Tropsch catalysts (Co/Al_2O_3, promoted with Re) by mimicking synthesis gas derived from biomass. The study showed that chlorine did not lower Co activity, while sulphur induced significant deactivation. This was dependent on steric hindrance around the sulphur atom and nitrogen in low quantities did not affect catalysts activity and selectivity **[68]**.

Catalyst deactivation by **surface reconstruction** in Fischer-Tropsch Synthesis is caused by the interaction of the nanoparticles with adsorbates that change the active site configuration –this is because of the invasive nature of the adsorbates (i.e. O, CO, C. etc) **[19]**. Deactivation (which occurs indirectly) by this process has been studied using model planar surfaces. STM work by Wilson et al. **[69]** showed that a Co(0001) surface undergoes severe reconstruction (by an etch-regrowth mechanism, forming triangular Co nano-islands) after exposure to syngas at 250 ℃ and 4 bar. Similar observations on the formation of triangular islands [on Co(0001)] upon introduction of carbon monoxide were made by Banerjee et al., by means of density functional theory calculations **[70]**

Carbon deposition on Fischer-Tropsch catalyst as a result of carbon monoxide dissociation to form stable metal-C species during the reaction also reduces catalyst activity. It has been suggested that the formation of a cobalt carbide phase or the formation of small graphene domains (i.e. polymeric carbon) are responsible for the loss of activity **[71, 72].** Karaca et al. **[71]**, showed through the use of in situ PXRD that the formation of cobalt carbide (on a $CoPt/Al_2O_3$ catalyst) under Fischer-Tropsch conditions (20 bar H_2/CO =2 and 220 ℃) was responsible for the loss of activity after the catalyst had spent a long period in the reaction chamber. A comprehensive study of the carbon deposition by Moodley et al. **[62]** determined that this carbon was deposited on both the support and the active sites and was hydrogen resistant. The carbon deposition was influenced by both reaction temperature and gas composition. **Fouling** of catalytic sites also can also occur due to the formation of wax and other hydrocarbon products that potentially reduce gaseous reactants diffusion. Hence deactivation by this process is by physical surface coverage and not necessarily due to chemisorption of carbonaceous species **[19, 63]**

Deactivation by **attrition** is mostly observed on unsupported catalysts; attrition is the breaking of the particles either via abrasion or fragmentation and is more prominent in slurry and fluidized bed reactors **[73, 74]**. O'Brien and co-workers **[74]** studied the attrition of Fe catalysts promoted by K and Cu under Fischer-Tropsch conditions in a slurry reactor. Deactivation by attrition was more prominent on the unsupported Fe particles as they disintegrated from 30-50 μm to 1-3 μm (as studied using TEM) after 24 hours under reaction conditions. The work furthermore indicated the necessity of using a binder in the form of silica to prevent catalysts deactivation by attrition when compared to the use of alumina or magnesia as binders.

Oxidation of active sites in Fischer-Tropsch reactions is a plausible deactivation mechanism that has been investigated with great interest. It has been suggested that water being the main product of the FT process, is also responsible for the re-oxidation of the catalytic sites **[75, 76]**. Thermodynamic studies by Van Steen et al. **[76]** shed light on the size dependency of nanoparticle oxidation by water (Figure 2.4). In this study it was shown that Co nanoparticles with sizes below 4 nm were more susceptible to oxidation to Co(II)O even at low water to hydrogen partial pressure ratios. The re-oxidation process of Co nanoparticles was further studied by an in situ magnetometer under Fischer-Tropsch synthesis conditions; two catalysts with different Co crystallite sizes (4.5 and 9. 5 nm) were employed. At low conversion the Co catalysts did not show any loss of magnetization hence indicating that no re-oxidation of the nanoparticles had occurred. However, at high CO conversion - simulated by co-feeding water - the Co crystals with crystallite size of 4.5 nm significantly lost the magnetization and corresponding Fischer-Tropsch activity when compared to the Co catalysts with a size of 9.5 nm. The implication was that deactivation by re-oxidation is only significant on small Co crystallites in Fischer-Tropsch synthesis **[77]**.

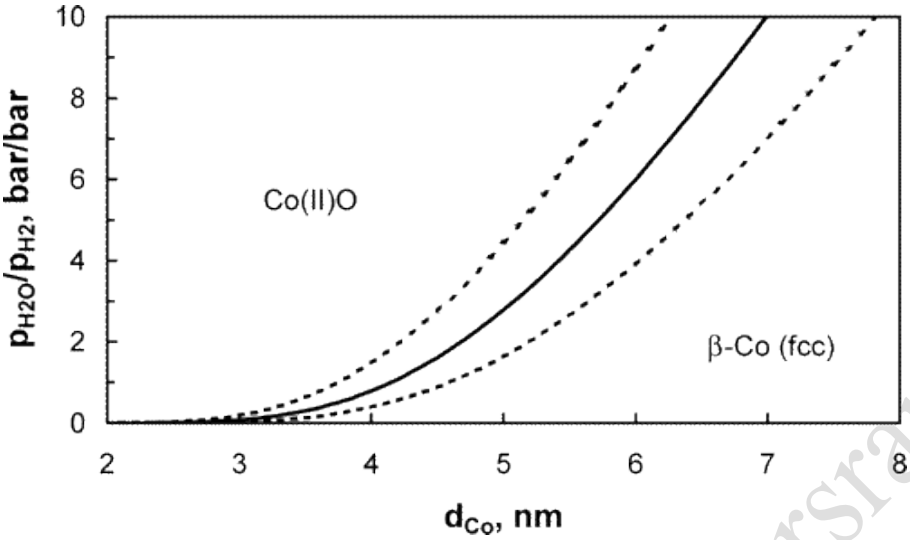

Figure 2. 4: Size dependent stability region of Co and CoO under different water hydrogen partial pressures **[76]**.

Similar work on Co nanoparticles using pre-synthesized monodisperse Co_3O_4 nanoparticles with supported on Stöber silica spheres showed that small Co nanoparticles (3.2 nm) oxidized easily in comparison to Co crystallite with larger crystallites (5.3 nm) under simulated Fischer-Tropsch condition (i.e. 99% CO conversion) **[78]**. Although water has also been shown to play a role in other deactivation mechanisms on Fischer-Tropsch catalysts (sintering and restructuring), its effect on oxidation of Co catalysts, regardless of particle size can never be discounted even though the effects are more pronounced at high CO conversions and on small crystallite sizes.

2.5. Influence of particle size on the Fischer-Tropsch reaction

Active metal nanoparticles have been shown to be structure sensitive in Fischer-Tropsch synthesis. Thus active sites on different sized nanoparticle under Fischer-Tropsch conditions give different activities in terms of turnover frequencies as well as different selectivities. The different surface atomic configurations, called ensembles, due to the different particles sizes are responsible for this phenomena **[79-82]**. Numerous studies on the structure sensitivity of Co nanoparticles in FTS have been reported. In a study by Wang et al. **[83]**, the authors claimed no intrinsic Co particle size effect in Fischer-Tropsch reaction for Co particles between 1 to 11 nm on model catalysts prepared under ultrahigh vacuum on a silica support. The low turnover frequency by the Co crystallites with size in the range of 1-3 nm was attributed to Co re-oxidation by water. However, Bezemer et al. **[79]** evaluated the influence of Co crystallite sizes (range 2.6-27 nm) in the Fischer-Tropsch reaction on carbon nanofiber supports. In this study the reaction was performed at two pressure and temperature regimes of 1 bar/220℃ and 35 bar/210 ℃. It was observed

that the TOF was dependent on Co nanoparticle sizes below 6 nm and 8 nm. High methane selectivity and lower degree of reduction was also associated with small Co nanocrystals under FTS conditions. A comprehensive study by Fischer et al. **[82]** using cobalt oxide nanoparticles prepared by the reverse micelle method with different crystallite sizes (Co sizes; 3.7, 4.7, 6.0, 8.2 and 9.3 nm) and supported on alumina was performed to evaluate the structure sensitivity of Co catalysts in FTS. In this scenario it was determined that the catalyst chain growth probability and the FTS product olefinicity were not affected by Co crystallite size. However, selectivity towards branched hydrocarbons and methane increased with decreasing Co crystallite size, while the catalyst turnover frequency increased with particle size without plateauing in the Co sizes ranges that were studied.

An X-ray absorption spectroscopy study by Tuxen et al. **[84]** revealed that the dissociation of carbon monoxide on Co crystallites is dependent of their sizes. In this study Co nanoparticles of different sizes were prepared by a colloidal method (with average sizes of 4, 10 and 15 nm) and supported on gold foil. An in situ XAS cell was used to test the catalysts for dissociative CO adsorption and revealed CoO_x phases for nanoparticles with sizes of 10 and 15 nm (as seen from the O-K edge and Co-L edge) upon exposure of CO on the metallic nanoparticles. The CoO_x phases on these catalysts signified dissociative adsorption of the CO to C and O on the nanoparticle surfaces. This suggested that small nanoparticles adsorbed more CO molecularly, leading to their low FTS turnover frequency. The CO cleavage step has been suggested to be one of the rate determining steps in the FTS mechanism. A similar study was performed by Herranz and co-workers **[75]** in which Co nanoparticles with a size range between 3 and 25 nm were tested in a syngas environment ($3CO/10H_2/20Ar$). The data showed that both the dissociation of hydrogen and CO on the nanoparticles was structure sensitive as the catalyst turnover frequency increased, with Co average size stabilizing at sizes above 10 nm.

Den Brejeen **[85]** and co-workers used steady state isotopic transient kinetic analysis (SSITKA) techniques to study the effect of Co crystallite size (range of 2.6-16 nm) in Fischer-Tropsch synthesis on carbon nanofiber supports. The results were consistent with data reported by others in the literature **[79, 82, 86]**. To rationalize the observed data using SSITKA based on the CO, OH_x and CH_x coverages, it was proposed that low CO surface coverage and high residence times of CH_x intermediates were responsible for the low TOF on the Co smaller nanoparticles (< 6 nm). Furthermore irreversible bonding of CO on these small nanoparticles was associated with an increased localization of the Co atom valence electrons, resulting in the lower turnover frequency.

Other Fischer-Tropsch active metals such as Ru and Fe have also been shown to be structure sensitive in Fischer-Tropsch synthesis **[87-90].** Quek et al. **[88],** Figure 2.5 used unsupported Ru nanoparticles in the range of 1-5 nm to study the effect of their sizes on Fischer-Tropsch synthesis in an aqueous environment at low temperature (i.e. 150 ℃). In this study the Ru nanoparticle sizes were prepared by varying the reduction method, the

synthesis temperature and the Ru precursor. The nanoparticles had a high degree of reduction (> 80%). It was observed that the crystallite turnover frequency increased with particle size and levelled off between 2.3 and 3.7 nm. This was followed by an increase when the Ru sizes were above 4 nm. The C_{4+} hydrocarbons and oxygenates showed an increase when the Ru particle size was between 2.3 and 5.2 nm, with Ru nanoparticles with an average particles size of 1.2 nm displaying a high methane selectivity, when compared to the methane selectivity of Ru nanoparticles with sizes between 2.3 and 5.2 nm. The work by Gonzalez-Carballo and co-workers **[91],** suggested two reaction regimes in which the Ru crystallite size influence existed during Fischer-Tropsch synthesis. At steady state the turnover frequency increased with crystallite size reaching a maximum at a Ru size of approximately 10 nm. However, when the TOF was measured at the start of the reaction the turnover frequency was observed to increase with Ru nanoparticle size up to 71 nm. The authors attributed this to the rearrangement of Ru surface sites with time on stream during Fischer-Tropsch synthesis. This suggested the existence of CO dissociation sites, step edges on Ru nanoparticles with sizes > 10 nm, which deactivated over time under reaction condition.

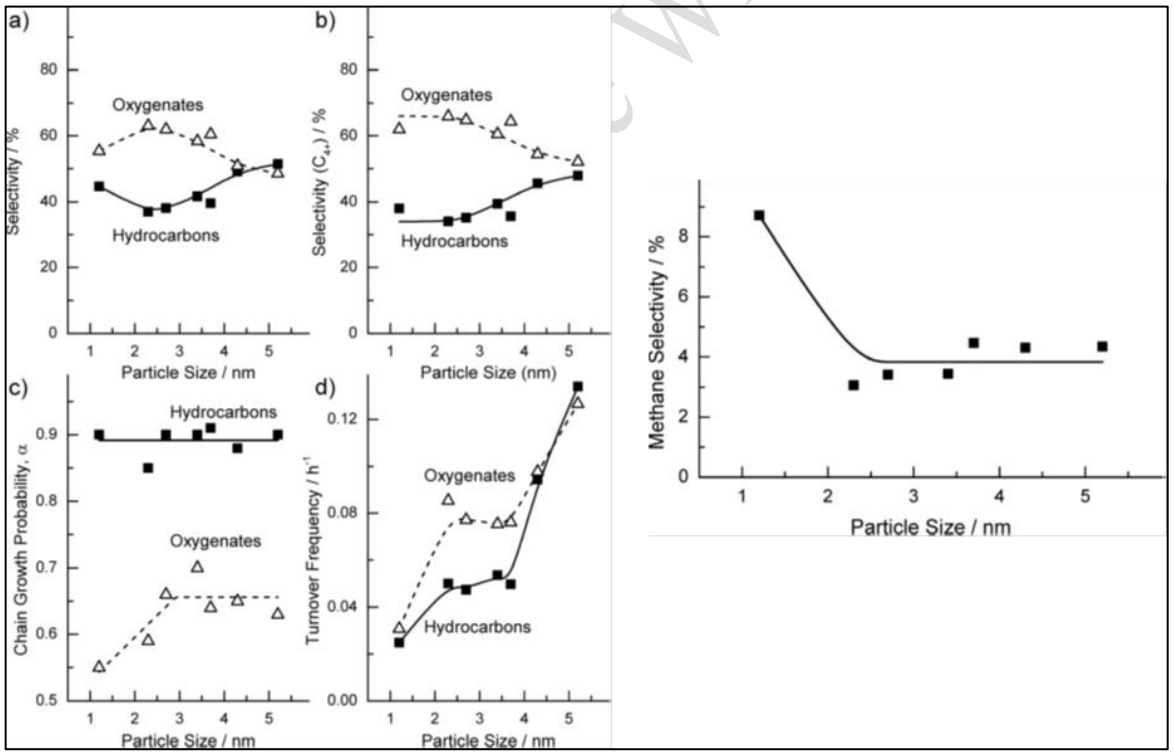

Figure 2. 5: Effect of Ru nanoparticle size on the Fischer-Tropsch reaction selectivity **[88]**.

Park et al. **[90]** studied the influence of Fe nanoparticle size in Fischer-Tropsch synthesis and obtained similar results as observed on Co and Ru catalysts. The iron oxide (Fe_2O_3) nanoparticles with different crystallite sizes (2.0, 1.5, 6.1, 9.0 and 12.0 nm) were prepared by a solvothermal method using different synthesis temperatures to vary their sizes. It was shown that the particle size greatly influenced the iron oxide interaction with the support and the catalyst reduction or carburization. The Fischer-Tropsch turnover frequency increased with Fe particle size from 2.4 nm to 6.1 nm, remaining almost constant up to 11.5 nm. Also the methane and C2-C4 selectivity increased with Fe crystallite size, due to the smaller Fe nanoparticles ability to preferentially dissociatively adsorb hydrogen rather than carbon monoxide. The water gas shift reaction (i.e. conversion of CO to CO_2) was found to relate to the catalyst activity, as it followed the same trend as CO conversion rate.

From the data in the literature it is thus seen that the effective size that gives high intrinsic activity (i.e. TOF) on Co Fischer-Tropsch Synthesis catalysts has been established. This has been neatly summarized by Van de Loosdrecht et al. and Van Helden et al. **[27, 80]**- A size between 6-8 nm has been shown to optimal in FT reactions (Figure 2.6).

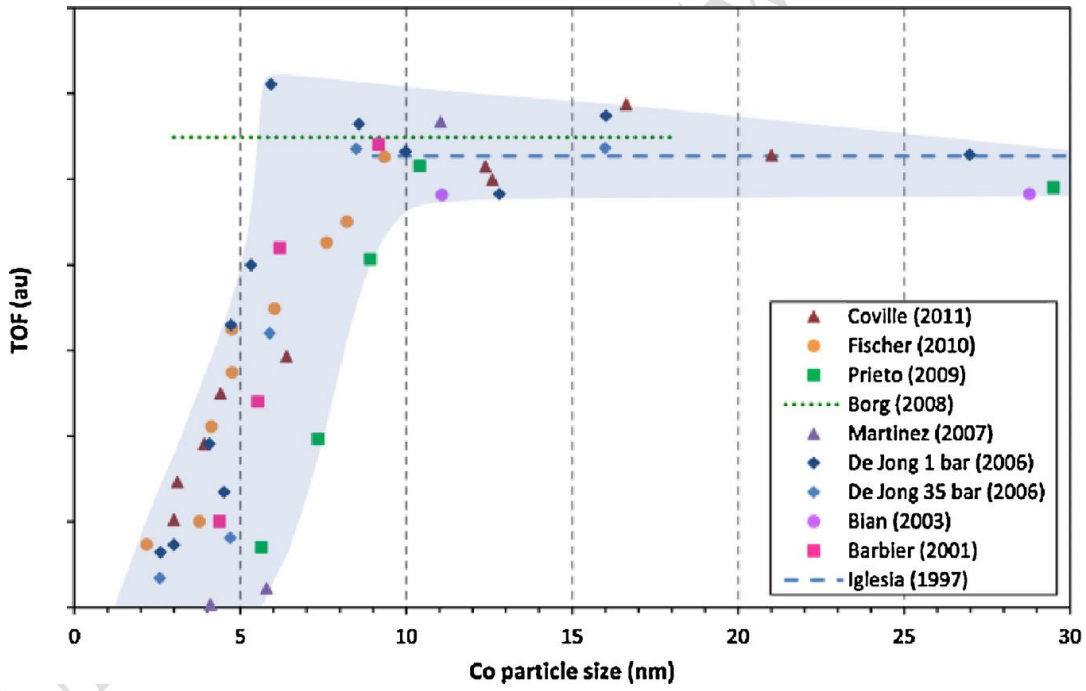

Figure 2. 6: A summary of several studies showing a particle size dependency of turnover frequency in Co Fischer-Tropsch Synthesis **[27, 80]**.

Several studies **[79, 82]** have associated the structure sensitivity of Co nanoparticles in Fischer-Tropsch Synthesis with the presence of ensembles of defect sites that are more catalytically active. These are the so called B_5 ensembles as articulated by Van Hardeveld Hartog **[81]** they used a hard packing statistical model to calculating surface atoms in a nanoparticle, and the efficient sites were shown to be size dependent and to possibly play

an important role in CO adsorption and dissociation in Fischer-Tropsch catalysts. Recently a theoretical work by Van Helden et al. **[80]** was conducted to determine whether the ensemble site composition was dependent on the Co (fcc) crystallite size. The designed model was able to 1) generate realistic and thermodynamically favorable Co nanoparticles of different sizes, and 2) define and count different surface sites (B_3, B_4, …B_n sites, where n is the number of atoms in the ensemble).

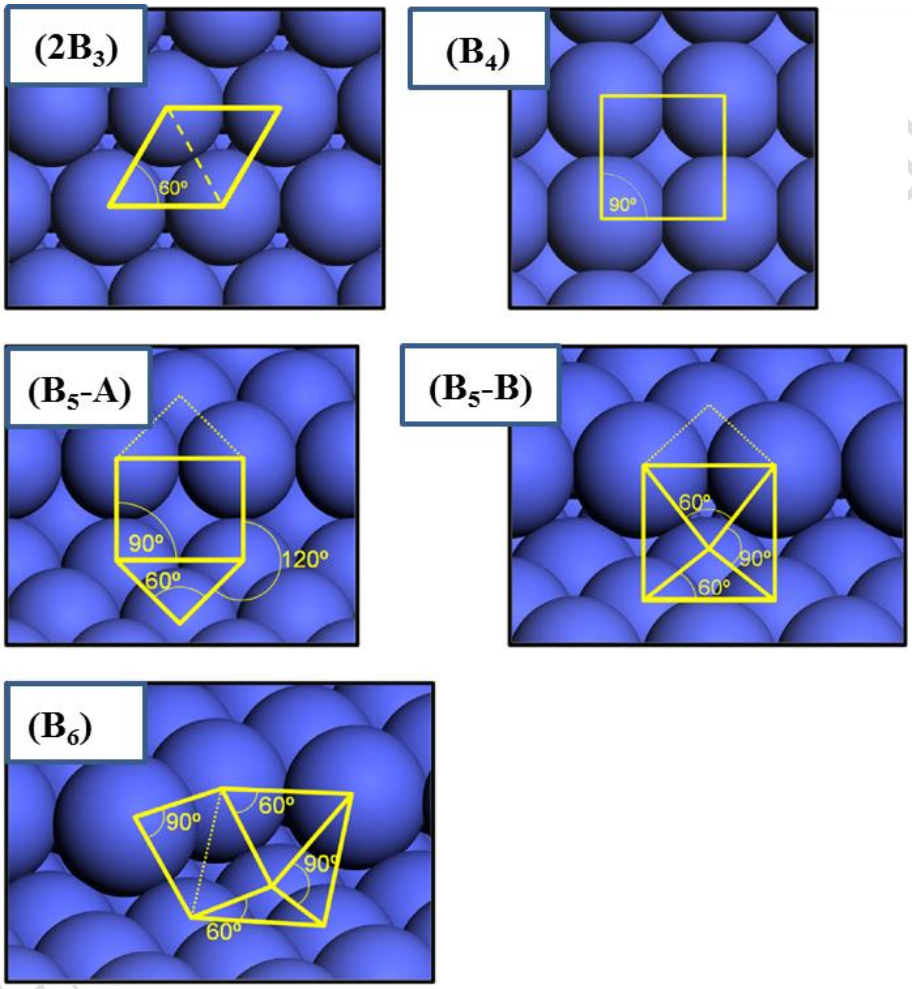

Figure 2. 7: Surface sites on Co nanoparticles as defined by Van Helden and co-workers model **[80]**.

With these model the surface sites of several nanoparticles with sizes in the range of 0.7 to 11 nm were identified and counted; below 1 nm it was found that the $2B_3$ sites were dominant, while above 1 nm there was an increase in the B_4 sites, before reaching a stable value was found just below 2 nm. The B_5/B_6 sites were seen to increase with a further increase in Co crystallite size. However, the B_5-A and B_6 site concentration levelled off at sizes above 4 nm, whereas the B_5-B ensembles gradually increased up to 8 nm. Because the $2B_3$ and B_4 ensembles have a higher energy barrier for CO dissociation that the B_5 and B_6

ensembles it was suggested that the TOF frequency variation in Fischer-Tropsch synthesis with particle size might have a direct correlation the surface site dependency on the Co nanoparticle size (Figure 2.7).

The origin of this structure sensitivity has also been attributed to the propensity of the small Co nanoparticles to undergo oxidation by water under Fischer-Tropsch synthesis conditions **[66, 76, 85]** as well as electronic effects that affect the CO and H_2 dissociation rates **[85]**.

2.6. Fischer-Tropsch Catalysts supports

The effects that have been described above (deactivation, mechanisms and structure sensitivity) in Fischer-Tropsch studies and that relate to different active sites have been studied on different catalytic supports. The function of a catalyst support is to help disperse catalyst nanoparticles and hence circumvent severe nanoparticle agglomeration. Furthermore, an ideal Fischer-Tropsch catalyst support should also have and maintain good mechanical strength under reaction conditions and have a high surface area together with sufficient porosity to reduce mass transfer limitations **[15, 92-94].**

The supports have also been shown to have different impacts on the behavior of Fischer-Tropsch nanoparticles owing to variable support-metal interactions that are dependent on their chemical composition **[95]**. For instance, Jacobs and colleagues studied the effects of catalysts supports on a Co Fischer-Tropsch catalyst loaded using incipient wetness impregnation on different supports (Al_2O_3, SiO_2, TiO_2 and ZrO_2). This study showed that Co catalysts reduction decreased following the trend $SiO_2 > TiO_2 > Al_2O_3$. The variable degree of reduction was attributed to the different degree of metal support interactions induced on the Co nanoparticles **[92]**. Storsæter et al. studied cobalt nanoparticles supported on SiO_2, Al_2O_3 and TiO_2, it was observed that the Co crystallite and reducibility were dependent on the support pore size up to a given value. The support dependence was also be attributed to the metal-support interactions influenced by the support pore size **[93]**. An issue with oxidic catalyst supports is their metal support interactions with the Fischer-Tropsch metal to form an inactive (and irreducible) metal oxide such Co_2AlO_4 **[96]**, $CoTiO_4$ **[97]** or Fe_2SiO_4 **[98].** To circumvent this problem catalysts have been modified with promoters to allow the reduction of the active metal to occur at lower temperatures **[99]**.

In several cases the use of inert catalysts supports such as carbon materials has been sufficient to overcome these strong metal support interactions. The advantage of using carbon as a support related to the reduced metal support interactions in Fischer-Tropsch catalysts. This permits a more significant number of the exposed active nanoparticles surface atoms to take part in the catalytic reaction **[11, 100, 101]**.

2.6.1. Use of carbon as support in Fischer-Tropsch synthesis

The carbon atom is able to form many stable carbon materials using a combination of both sp^3 and sp^2 hybridized orbitals. Because of the versatility of the carbon atom that arises from the stability carbon using the two hybridizations states, several allotropic forms of carbon exist. They have desirable properties that can be exploited in materials chemistry. It is the combination of the sp^3 and sp^2 carbons in different amounts that gives the resulting carbon materials their shapes, physical properties and electronic properties (Figure 2.8) **[86, 100, 102, 103]**. This has led to their widespread use in many heterogeneous catalytic reactions. The early reports on the use of carbon materials as supports in Fischer-Tropsch synthesis can be traced back to the 1980-1990s, with the studies mostly focused on the use of activated carbon, glassy carbon and carbon black **[100]**.

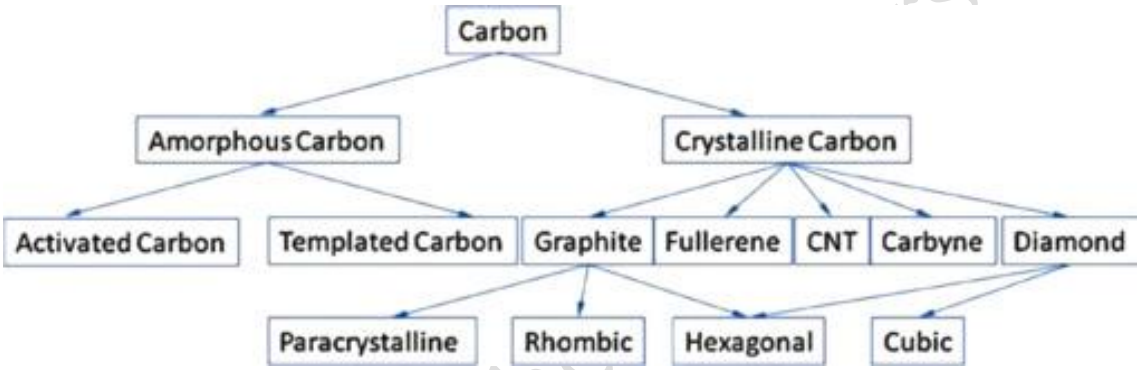

Figure 2. 8: Carbon material polymorphs **[101]**.

Carbon materials as catalyst supports despite some drawbacks (i.e. low density and cost of production) have several advantages that make them desirable for application in Fischer-Tropsch catalytic evaluation both for fundamental studies and possible industrial applications.

These are **[100, 101, 104-107]**:

1. *Limited strength of metal support interactions that allow an increased degree of reduction of catalyst active sites.*
2. *Modifiable pore structure and surface area*
3. *Resistance towards both acid and basic environments.*
4. *Controllable surface polarity by functionalization methods and doping with heteroatoms such as nitrogen, boron, sulphur or phosphorus.*
5. *Stability at high temperatures, with easy recovery of the active metal after catalytic reaction.*

Detailed reviews on the use of carbon materials in Fischer-Tropsch Synthesis can be found in these references **[100, 101]**. Amongst the carbon materials that have gained traction for application in Fischer-Tropsch synthesis are carbon nanomaterials such as nanotubes,

nanofibers, spheres and graphene. These carbon materials have been prepared by a variety of methods using gas and liquid phase carbon precursors employing synthetic techniques such as the chemical vapor deposition and high pressure solvothermal synthesis **[108, 109]**.

Several studies have shown that the modification of these carbon materials do have substantial impacts on supported Fischer-Tropsch metallic sites. These are the carbon material morphology, doping and functionalization, location of active sites on the support and the pore structure **[86, 100, 110, 111]**.

These carbon materials provide good model supports for understanding several processes affecting catalytic systems. In the work by Bezemer and Den Brejeen as well as the group of De Jong **[79, 85]**, carbon nanofibers prepared using Ni catalysts were used as supports for Co nanoparticles to study the effect of Co nanoparticles on the process. Carbons have a low metal support interaction so a comprehensive study on the size effect was made possible yielding results that have had far reaching effects on the design of FTS catalysts for industrial applications. In another work by Xiong and co-workers **[86]**, it was revealed that carbon nanotubes and carbon spheres generally have the same effect (due to similar surface properties) on the Co nanoparticles as it was shown that on both these supports the catalytic turnover frequency followed the same trend with regards to the influence of Co crystallite size.

Further to the modification of the metal support by varying the support interactions, it has been suggested that the carbon support lattice can be doped using nitrogen to increase the active nanoparticles interaction. This would prevent sintering significantly affecting the metal support interactions observed in oxidic supports that lower the catalyst degree of reduction **[112-114]**.

Yang and co-workers **[113]** studied the effect of nitrogen doping of ordered mesoporous carbon (OMC) on cobalt Fischer-Tropsch catalysts. The ability of the CoO nanoparticles to auto-reduce on the carbon support was found to increase with the nitrogen content to a certain level, possibly due to the increased defects on the carbon supports. Thus the conversion of CoO to Co using CO occurred at lower temperatures in relation to the CoO supported on the unpromoted carbon support. Furthermore, nitrogen doping allowed for a more uniform distribution of the Co nanoparticles when compared to the undoped carbon support. The Co Fischer-Tropsch activity was found to be dependent on the metal support interaction and Co particle sizes, both of which were influenced by the amount of nitrogen in the carbon support. From the study the authors concluded that pyridinic nitrogen served as the anchoring sites for Co nanoparticles, increasing the metallic dispersion and support interaction. With regards to carbon surface modification for use in Fischer-Tropsch, several other methods have been employed generally employing wet oxidizing agents (i.e. HNO_3, H_2SO_4, $KMnO_4$, H_2O_2, etc.) **[106, 115, 116].** Motchelaho et al. **[106]**, modified surface of carbon nanotubes using nitric acid with different concentrations, for application as a

support in Fischer-Tropsch synthesis. Use 55% HNO_3 acid to modify the CNTs surface resulted in a support with a rougher texture that had an increased negative charge due to a greater number of oxygen functionalities when compared to CNTs functionalized using 30% HNO_3 and functionalized CNTs. The resulting oxygen functionalities allowed better dispersion of Fe nanoparticles hence yielding a catalyst with a high Fischer-Tropsch activity and low methane selectivity. Schulte et al. found that the N atoms served as better anchoring sites for Fe nanoparticles than O atoms of functionalized carbon nanotubes **[105].** The effect of the location of Fischer-Tropsch nanoparticles on these carbon nanomaterials was demonstrated by Chen et al. using carbon nanotubes with inner diameters in the range of 4-8 nm. Iron oxide (Fe_2O_3) nanoparticles (2-10 nm) were confined inside the CNTs by capillary forces using iron nitrate solution **[111].** An in situ XRD analysis under both hydrogen and carbon monoxide showed that iron oxide nanoparticles inside the CNTs channels reduced at lower temperatures. The encapsulated Fe nanoparticles easily formed iron carbide resulting in higher Fischer-Tropsch activity and C_{5+} selectivity than the catalysts where the Fe nanoparticles were placed on the CNTs outer surface. These confinement effects have been attributed to the pyramidalization angle on the carbon bonds that change with the carbon material morphology, and the misalignment of the π orbitals. Hence the nanoparticles inside and outside the carbon nanotubes have a different interaction with the π electron density as it shifts from the concave to the convex surface **[110]**. Nanoparticle confinement also limits the nanoparticles ability to sinter during reduction and Fischer-Tropsch synthesis (*i.e.* d_{range} *after FT recation was 4-14 nm for Fe-in-CNT and 8-22 nm for Fe-out-CNT*), and this can increase the lifetime of the catalysts. The pore structure of carbon nanomaterials in Fischer-Tropsch synthesis has been evaluated by Xie et al. using CNTs **[117]**. CNTs with average pore sizes of 5, 11 and 17 nm had Co_3O_4 nanoparticles filled inside the channels (10Co-in-CNT(5), 10Co-in-CNT(11), 10Co-in-CNT(17)). The CNTs with pore size of 5 nm had high BET surface area and the supported cobalt oxide nanoparticles displayed a smaller average particle size (4.2 nm). The crystallite sizes increased with pore size. The catalytic activity and stability increased with decreased support pore size, as the Co nanoparticles supported on CNTs with pore size of 17 nm had a faster deactivation rate. In this study the catalyst selectivity was not significantly affected by the support pore structures as the catalyst methane and C_{5+} selectivity were in the range of 9-10% and 79-83% respectively.

2.7. Fischer-Tropsch synthesis promoters

Several elements [Mn, Pt, Ru, and K etc.] have been investigated to study their abilities as catalytic promoters in Co or Fe based Fischer-Tropsch synthesis **[92, 118-120]**. These promoters have diverse effects on the Fischer-Tropsch catalysts which can be both beneficial but some can also poison a catalyst surface **[19].** The promoter effects can however be influenced by other variables such as the catalyst preparation methods and the Fischer-Tropsch reaction conditions been employed. It is commonly agreed that promoters are used for the following reasons **[121, 122]**.

(1) To assist the reduction of the metal oxide species and to reduce metal support interactions.

(2) To increase the number of accessible metal active sites for the catalytic process.

(3) To stabilize catalysts against deactivation and

(4) To enhance catalyst selectivity.

Promoters have been generally divided into two groups; structural and electronic promoters (Figure 2.9). Structural promoters affect the formation of and stability of the active phase while electronic promoters directly affect the active phase and electronic structure which changes the chemisorption capabilities **[123]**.

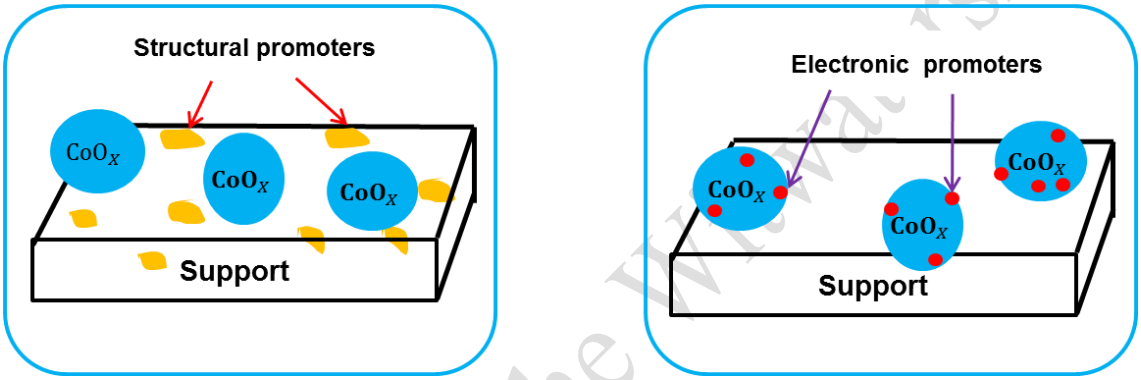

Figure 2. 9: Two classes, structural and electronic promoters.

Noble metals such as **ruthenium** (which can act as a Fischer-Tropsch metal) are in essence both electronic and structural promoters in **cobalt** based Fischer-Tropsch synthesis **[124]**. It has been observed that the ruthenium helps to enhance the catalytic activity of the cobalt catalyst. This has been explained by suggesting that the ruthenium acts as a facilitator to enhance a lower temperature reduction of the cobalt oxide species and to keep the cobalt surface clean. This helps keep the number of exposed cobalt atoms high during the Fischer-Tropsch synthesis, and thus avoid high temperature activation of the Co nanoparticles, thus avoiding possible sintering by thermal degradation **[121, 125]**. Overall the ruthenium promoter serves to decrease the reduction temperature of the cobalt oxide species during the activation process leading to higher active site dispersion. Schulz et al. observed, using in-situ XANES that addition of ruthenium to Co/SiO_2 led to an easy reduction of the cobalt oxide (37.5% Co) while the unpromoted Co/SiO_2 did not reduce to Co during the in situ reduction steps at 450 ℃ **[126]**. Park et al. employed a ruthenium promoter as an electronic promoter by preparing Co-Ru nanoparticles using oleic acid as a capping agent. The nanoparticles were loaded on γ-Al_2O_3. The catalyst showed high C_{5+} selectivity (> 80 %) and lower olefin to paraffin ratio because of the enhanced olefin re-adsorption induced by the ruthenium promoter **[121]**. The proposed acceptor sites are the active Fischer-Tropsch

sites such as cobalt or iron **[121, 127].** Rodrigues et al. reported that addition of a ruthenium promoter to a Co/SBA-15 catalyst for Fischer-Tropsch synthesis increased the C_{5+} selectivity to 80% because of the synergistic effect by the ruthenium promoter resulting from the easy reducibility of the Co active phase **[122]**. An in situ X-ray absorption study by Hong et al. **[128],** suggested that the Ru promoter ions get entrapped inside the cobalt oxide phase (i.e. Ru atoms replace some Co atoms in the oxide lattice, as the ions have equal atomic sizes, between 61 and 68 pm). These Ru atoms were then observed to promote the reduction of the cobalt oxide phases to form a Co-Ru bimetallic catalytic phase, and the promoter effects [on Co_3O_4 reduction] were independent of the Ru loading. The preparation procedure for these catalysts also proved vital for retaining ample amounts of Ru on the Co, as it was observed that some of the Ru was lost by gasification during catalyst preparation, during drying and during the calcination step. Fischer-Tropsch evaluation revealed higher activity for the promoted catalyst, with the catalyst prepared by impregnation using an organic additive (sorbitol, CoRu-sorb/SiO_2) giving a higher activity than the one prepared without an additive (CoRu/SiO_2).

In Fischer Tropsch synthesis hydrogen spillover is generally inferred to explain the promoter effects of noble metals such as platinum, rhenium and ruthenium in Fischer-Tropsch synthesis.

2.8. Hydrogen spillover mechanism and its effects in heterogeneous catalysis

The hydrogen spillover process was first reported in 1964 for a Pt/WO_3 material as evidenced by the reduction of WO_3 to a blue WO_{3-x} material (x= number of oxygen atoms lost **[23, 129]**. This spillover process has great implications in heterogeneous catalysis and for hydrogen storage in the hydrogen economy for application in fuel cells.

Hydrogen spillover is defined as the transportation of hydrogen atoms formed by decomposition of a hydrogen molecule on an initial surface (called the initiator) onto a subsequent surface (i.e. acceptor) that does not under the same conditions (mostly pressure and temperature) dissociate hydrogen molecules to their corresponding active sites **[23, 130]**. The spillover of hydrogen atoms is completely feasible when the initiator and acceptor are in direct contact. However, a second possible spillover mechanism in which the components are separated by a carrier is also possible. This leads to the existence of two mechanisms called primary and secondary spillover respectively (Figure 2.10). The kinetics of the spillover process is dependent on the materials on which the processes take place.

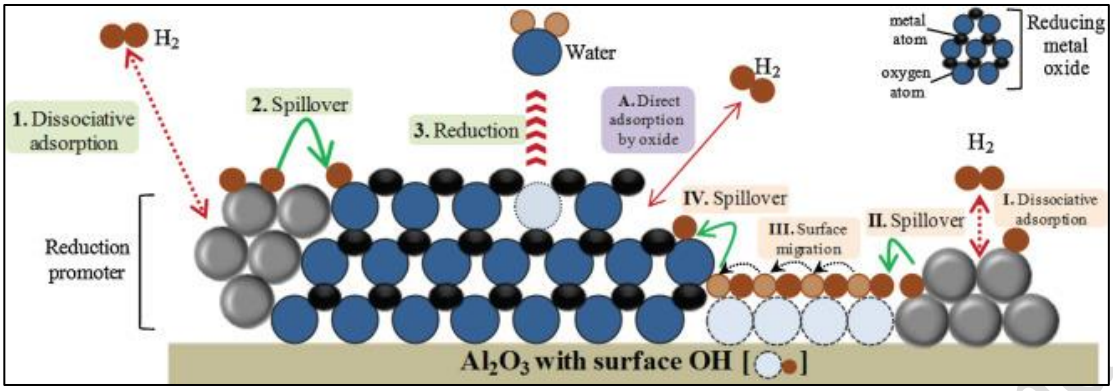

Figure 2. 10: Schematic showing the two hydrogen spillover processes in a promoted heterogonous catalysts system **[131]**.

Conner Jr and Falconer pointed out that the diffusion of the spilled over species over a surface is dependent on the electronic interactions of the surface and the active species. Invariably the transfer will then require a formation of a weak but sufficiently strong bond (either through Van der Waals interactions or localized bonding). These interactions are also thought to be affected by the manner in which the active species interact with the initiator and acceptor components at the interface **[130]**.

Molecular orbital energy studies on the spillover of hydrogen atoms to non-reducible supports such as SiO_2 and Al_2O_3 suggest a higher energy barrier for the process to occur favourably **[132].** In an extensive review of hydrogen spillover, Prins argued that the H-D exchange studies did not necessarily provide sufficient proof of hydrogen spillover. The transport of hydrogen on the support was not energetically favoured, partly because irreducible supports were used, and the support-hydrogen atom bond energy was found to be generally less than the H_2 molecule dissociation energy of 218 $kJ.mol^{-1}$ that is required to keep the hydrogen atoms from combining again after dissociation **[23]**.

However, hydrogen spillover has been observed on many materials and the most accepted or proposed hydrogen spillover is the **Bucket-Brigade mechanism** which is similar to the Grotthuss mechanism (Figure 2.11) **[133]**. The mechanism suggests a transfer of hydrogen atoms by the successive formation of oxygen-hydrogen-oxygen networks on a surface with hydroxyl-like terminations **[21, 130, 133, 134]**.

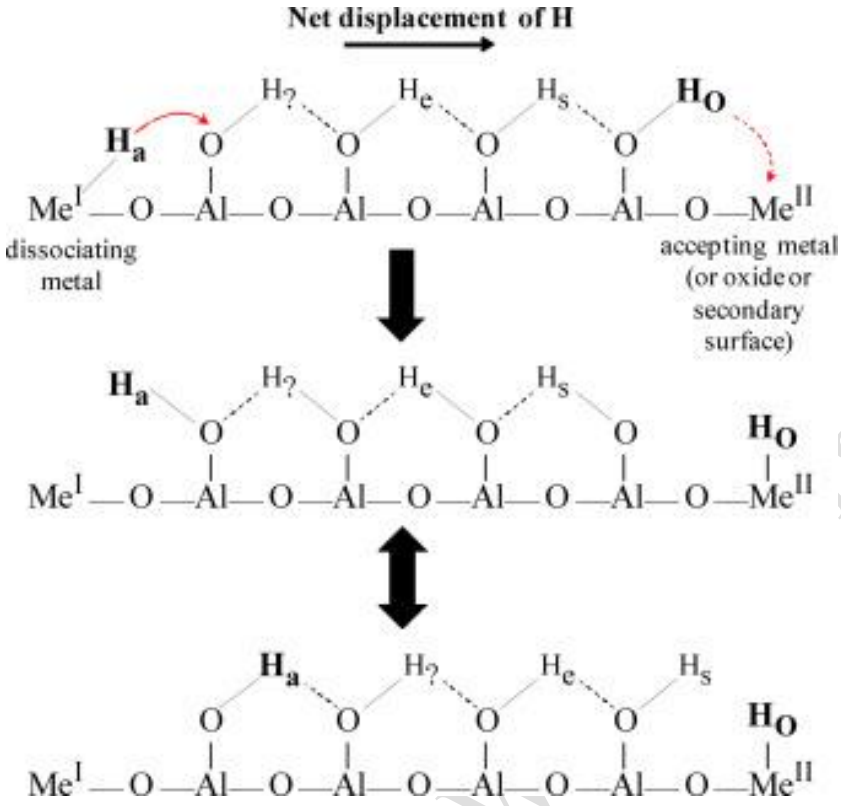

Figure 2. 11: Bucket-brigade surface migration in hydrogen spillover. Movement of hydrogen is only possible by the hydrogen bond forming-breaking exchange from Me^{I} to Me^{II} **[131]**.

After witnessing the effect of hydrogen spillover on the hydrogenation of benzene on the surface of an aluminosilicate (NaA, pore size between 0.3-0.4 nm) that had 1 nm Pt nanoparticles encapsulated inside the dense zeolite framework, Im and colleagues then used density functional theory calculations to show that the surface hydroxyls (i.e. sites generated by Bronsted acid sites) on the aluminosilicate surface play a crucial role in the process of hydrogen spillover as shown in the Figure below.

In this mechanism defect sites are generated by a movement of protons from the framework interior, followed by the "defect" movement in the framework. Here adding a H radical is added to a defect site and this result in the formation of a three centered O-H-O bond (i.e. Bronsted acid). Migration of this O-H-O, by a polaron conduction mechanism eventually allows the cationic defective site to be reached. Any contact with an electron gives hydrogen radical that is then involved in the reaction (it's the spilt-over hydrogen). The mechanism then suggests that spillover on to the non-reducible aluminosilicate becomes feasible because of the O-H and O-H-O connectivity exchange with low energy barrier (Figure 2.12) **[135]**.

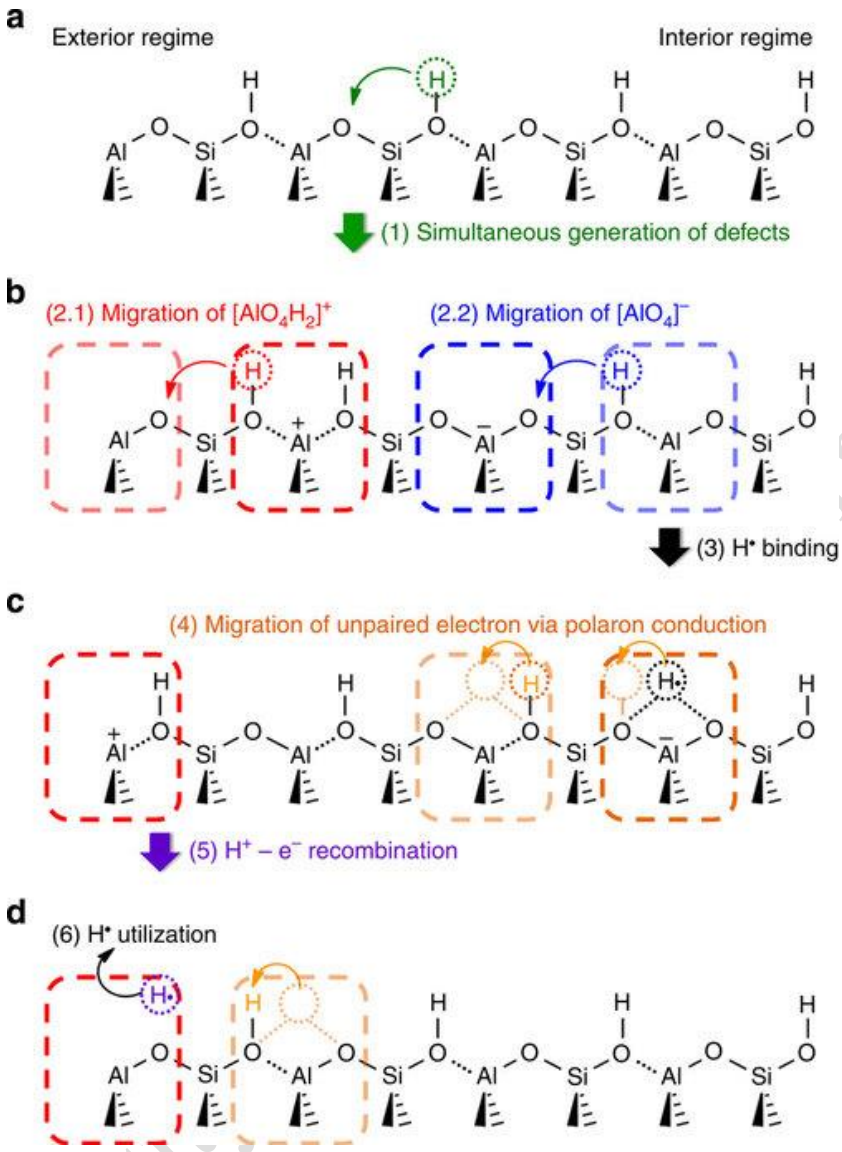

Figure 2. 12: Hydrogen spillover mechanism as proposed by Im and Co-workers **[135]**.

Beaumont et al. studied the reaction kinetics of hydrogen spillover by increasing the Pt and Co spacing in the hydrogenation of carbon dioxide. In this work pre-synthesized Co (10 nm) and Pt (12 nm) colloidal nanoparticles were supported on mesoporous silica (MFC-17), to make Co/MCF-17, CoPt/MCF-17 and Pt/MFC-17. A mechanical mixture of the Co/MFC-17 and Pt/MFC-17 gave similar hydrogenation turnover frequency as found for the CoPt/MFC-17 catalyst, which was prepared by mixing the colloidal solution of the Co and Pt nanoparticles. The high methane TOF of these two catalysts was attributed to the promoter effects of the Pt nanoparticles by hydrogen spillover on to the silica support. The hydrogenation kinetics of this systems were evaluated by calculating the activation energies from Arrhenius plots (at 60 bar, T_{range} = 200-300 ℃). A lower activation energy

was obtained for the catalysts prepared from a mechanical mixture (Co/MCF-17 + Pt/MCF-17), suggesting diffusion limited movement of hydrogen active species from the Pt to Co nanoparticles (migration distance of about 400-500 nm) through the support material **[136].**

In another work the mobility of hydrogen on both reducible (TiO_2) and non-reducible (Al_2O_3) surface was studied and verified using in situ X-ray absorption spectroscopy (XAS) by Karim et al. **[24]**. In this work nanolithography was used to make model systems on a titania or alumina films where the platinum and iron oxide nanoparticles (30 and 60 nm respectively) were separated by a distance from 0 to 45 nm. Exposing these model catalyst system to hydrogen gas at 70 ℃, resulted in the substantial reduction of the iron oxide nanoparticles on the titania support (up to 17 % degree of reduction). However, the reduction process on the alumina film was dependent of the separation distance between the platinum and iron oxide nanoparticles. The work of Karim and colleagues enforces the necessity of reducibility of the hydrogen transporting layer to allow hydrogen spillover over long distances.

In **heterogeneous catalytic reactions** it has been shown that hydrogen spillover does assist in the reduction of molecules as has been observed for CO_2 **[136, 137]**, benzene conversion To cyclohexane **[135]**, and styrene to ethylbenzene **[138]**. For example Beaumont et al. evaluated the role of Pt in the hydrogenation of carbon dioxide on Co catalysts by in situ NEXAFS. The study used catalysts were Co, Co-Pt bimetallic and Co + Pt nanoparticles supported on MFC-17 silica support. High values of methane production were observed on the Co+Pt/MFC-17 catalyst. Since all the catalysts were optimally reduced at 450 ℃, the high turnover frequency of this catalyst was attributed to the Pt nanoparticle ability to dissociate significant amounts of hydrogen that transferred to the nearby Co nanoparticles with chemisorbed CO_2 resulting in high hydrogenation rates **[137].** In Fischer-Tropsch synthesis Nabaho and colleagues studied hydrogen spillover over a milled alumina support using a Co catalyst with Pt and Au promoters. Hybrid catalysts of Pt/Al_2O_3 and Co/Al_2O_3 were used as a model catalyst in which the Co and Pt nanoparticles could be separated. TPR studies of the catalysts showed that the bimetallic CoPt catalyst and the hybrid catalyst (i.e. Pt/Al_2O_3 and Co/Al_2O_3) reduced at low temperatures when compared to the TPR profile of the unpromoted catalysts. The Pt promoter affected the transformation of CoO to Co by lowering the reduction temperature. Fischer-Tropsch activity of the hybrid catalysts (hybrid $Co\text{-}Pt/Al_2O_3$) was greater than that of Co/Al_2O_3. These also corresponded to the hybrid catalysts highly hydrogenated hydrocarbons for the Pt promoted catalysts due to hydrogen spillover leading to a hydrogen rich environment increasing hydrogenation rates on the unsaturated hydrocarbon**[131].** An analogous study using Au as the promoter yielded insignificant spillover effects because of the inability of Au to dissociate hydrogen as easily as Pt metal **[139]**.

Chapter 3

Nanoreactors with Hollow Morphologies and Their Pore Structures: Synthesis and Applications in Catalysis

Hollow spheres

3.1. Background

The increasing interest and continued growth of nanotechnology and nanoscience as an umbrella field incorporating many scientific fields (chemistry, physics, material science, etc.) has yielded many great innovations. This includes, among many others, the development of new generation techniques like scanning tunneling microscopy (STM) and atomic force microscopy (AFM) **[140, 141]** ,the fabrication of carbon nanomaterial only solar cells **[142]** and the current intensive research focused on electronic properties of single/few layer graphene that promises to revolutionize the future of the electronics industry **[143]**. However, even though great attention has focused on these major "newsmakers" in the nanotechnology world there have been other major offshoot developments with, just as much scientific relevance as the ones mentioned above. This involves the development of carbon nanotubes and nanofibers as fillers in the composite industry **[144, 145]**, in waste water purification **[146]** and in catalysis as catalyst supports. The discovery and the application of quantum dots as energy harvesting entities for solar cells have also not gone unnoticed **[147]**.

Over the last two decades the use of nanoreactors to make pharmaceuticals for drug delivery **[148]** and in catalysis to prevent nanoparticle agglomeration **[149]** has led to the development of new materials to make these nanoreactors (Figure 3.1). These hollow nanoreactors have also found increasing applications in other areas of study such as in lithium-ion batteries, as sensors and as antibacterial agents **[150].**

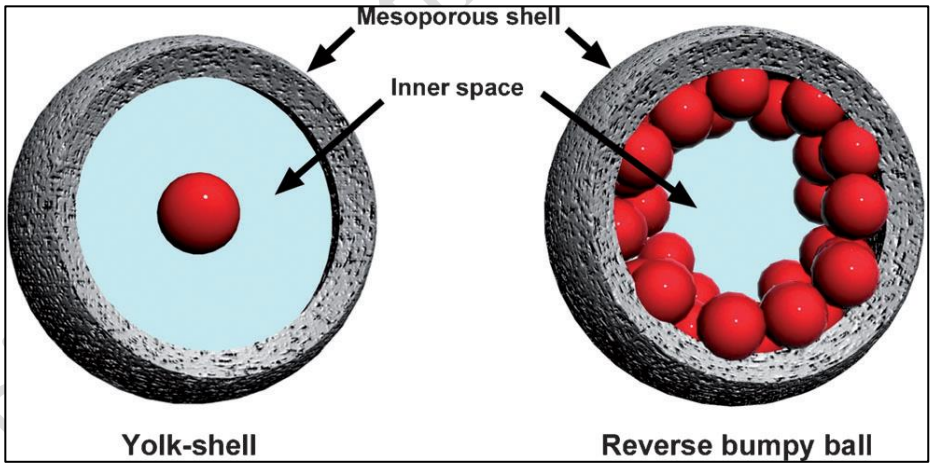

Figure 3. 1: Typical nanoreactors that have been prepared.

In essence this concept of nanoreactors is part of an ongoing pursuit by the nanotechnology community to mimic the bio-compartmentalization as observed in living cells whereby diffusional and mass transport effects help in maximizing the efficiency (activity and selectivity) of the chemical processes in the cell **[151]**. A key component of any nanoreactor is the control of porosity as the porosity controls the movements of chemical

species in and out of the nanoreactor compartment. The nanoreactors frequently reported in the literature involve hollow spheres made of different materials such as titania, silica and graphitized carbon **[150].** Figure 3.2 derived from data in SciFinder shows the growth in the number of publications using the word "nanoreactor" thus emphasizing the increasing interest in the synthesis and application of these novel materials over the past 14 years in various fields of studies.

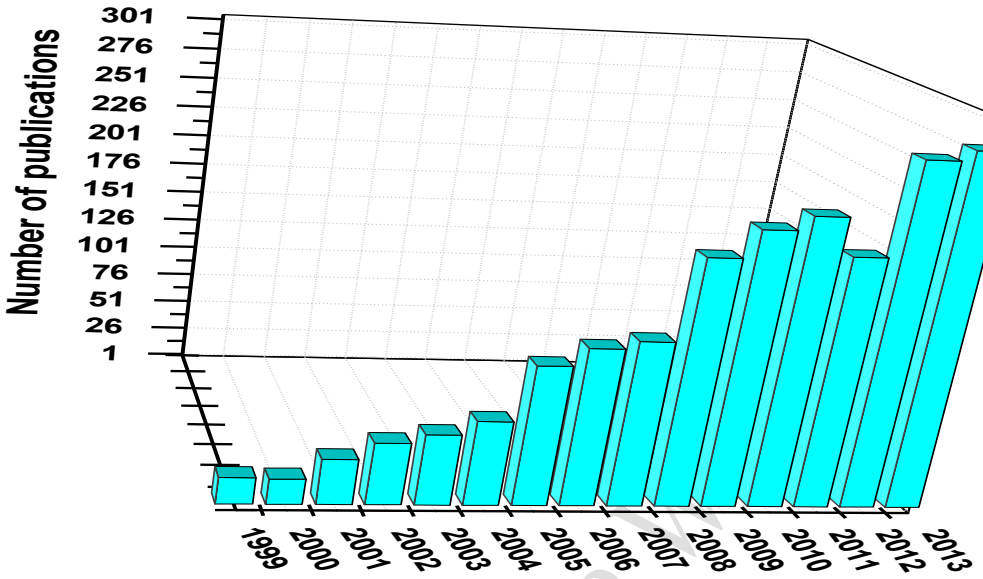

Figure 3.2: Growth in the number of publications dealing with nanoreactors (data obtained using SciFinder, February 2014)

3.2. Synthesis of nanoreactors

In the discussion to follow the term nanoreactors will refer to hollow spheres with different porosities (i.e. nonporous, micropores and mesopororesl), in particular hollow carbon spheres.

The hollow spheres have been synthesized using a variety of different techniques; this typically starts with the use of templates as the structure directing agents. The templating method generally involves at least three steps: (1) preparation of the template (2) direct synthesis of the desired material on the template surface and (3) template removal**.** Templates can be soft and hard colloidal templates and can even be non-colloidal templates. The hard physical templating method has proven to be the most valuable and reproducible way of making hollow nanostructures such as titania, silica and carbon spheres while the hard chemical templating method has also been applied for making hollow silica spheres**.** In hard physical templating the template does not form part of the resulting structure as it can be totally removed by etching or by some other decomposition

method. However, in the hard chemical templating method the initial template material is transformed into the final product **[152].**

3.2.1. Hollow silica spheres

Hollow silica spheres were the earliest of the reported hollow nanostructures. Because silica is abundant and environmentally friendly, coupled with the hollow silica spheres' outstanding properties (excellent mechanical and thermal stabilities) **[148, 153, 154].** Great research innovations in the synthesis and modification of these materials have been advanced. The synthesis is achieved by the template methods and it is to be noted that both the hard and soft templating methods have been used with great success **[152]**. The hard physical template method has been applied by Caruso et al. and many other authors using a layer-by- layer approach to make hollow silica spheres on a positively charged polymer template by an assembly of the negatively charged silica particles **[155]**. A sol-gel method has been the most employed method of the direct synthesis methods because they allow a synthesis of monodisperse hollow structures **[152, 156, 157]** Chen et al. used the sol gel method to make monodisperse hollow silica spheres by using monodisperse polystyrene (PS) spheres as a template and TEOS as the silica source **[158].** In this synthesis procedure the TEOS (with a cationic monomer) was hydrolyzed using ammonia solution to deposit the silica particles onto the PS template. The concentration of the ammonia solution and TEOS affected the kinetics of the synthesis process and consequently determined the shape and shell thickness of the hollow silica structures **[158]**. This kind of sol-gel method has also been applied using different templates from that of PS **[152].** Carbon spheres have been used as templates for making rattle type hollow mesoporous silica spheres with Pd nanoparticles inside **[159, 160]**. A method was reported by Chen et al. whereby silica was deposited on to a Pd/C composite using a modified a sol-gel method to form Pd/C@mSiO2 followed by thermal heating (in nitrogen) at 400 ℃ and carbon removal by oxidation at the same temperature to give a Pd@mSiO_2 **[160]**. Although a great number of the synthesis techniques are centered on the hard physical templating method, hollow silica spheres with mesopores have also been made by the hard chemical templating method **[148, 161] .** Zheng et al. performed a surface protected etching process on silica spheres to form york/shell SiO_2@void@SiO_2 particles. This was achieved by forming silica (SiO_2@SiO_2) particles with the inner core and outer shell coated with a PVP polymer (M_w = 50000). Selective etching using NaOH results in the removal of the unprotected SiO_2 and the resultant composite material that formed was a SiO_2@void@SiO_2 **[162]**. The hard chemical template method is generally based on the use of structural difference of the silica species. In this procedure solid silica spheres (from TEOS) are coated with a mesoporous silica shell made from a different silica source (i.e. from TEOS and C18TMS), and during the etching process the inner core is first dissolved leaving a hollow mesoporous silica sphere **[161]**.

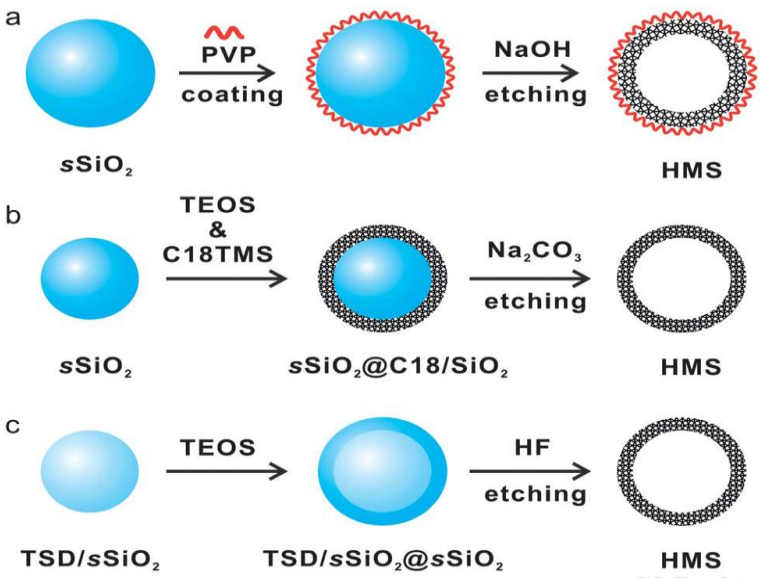

Figure 3. 3: Scheme showing some of the etching strategies employed in the hard chemical templating method **[148].**

Other template methods such as soft templating methods for making hollow silica spheres have also been reported. These include methods such the one step reverse-phase micro-emulsion **[152, 163]**, and surfactant assisted templating procedures **[148]**. However, it is difficult to obtain narrow particle size distributions and to obtain a narrow pore size distribution using this approach **[148]**.

3.2.2. Hollow Titania Spheres

Titanium oxide is known as one of the best semiconducting materials for applications in photocatalysis and energy storage **[164-166].** This is partly due to its wide energy band gap **[167]** and the fact that it is nontoxic and a chemically resistant material. Coupled with these properties the hollow morphology of a titania sphere makes it material of great interest, hence the increasing effort to find novel ways of making hollow mesoporous titania **[168]**. The synthesis of these titania spheres involve the aggregation of small titania clusters reacting on a template or any other structure directing agent **[165, 169]**. In the synthesis of the hollow titania nanostructures a hard template method is the most viable route as it allows control of the resulting material morphology. Wang et al. fabricated hollow titania structures (for testing in lithium ion batteries) of different shapes (peanuts, pseudocubes, capsules and ellipsoids) using a hydrothermal method using TiF_4 as the titania precursor. In that study α-Fe_2O_3 of different shapes were used as templates **[169]**. Different titanium precursors (titanium t-butoxide, titanium fluoride, titanium oxysulphate, etc.) can also be employed to synthesize the hollow titania spheres using different methods such as the conventional sol-gel method or even the solvothermal methods **[150, 164, 165]**. The porosity of these materials is important to control if they are to be applied in various fields

such as catalysis and drug delivery systems. The templates used during the synthesis process are usually functionalized with porogens (i.e, surfactants) to allow a formation of mesopores on the titania shell **[150]**. This was observed in the two methods employed by Joo et al. in which spherical silica templates functionalized with hydroxypropyl cellulose resulted in the synthesis of mesoporous hollow titania spheres **[164]**. The work of Wang et al. employed unfunctionalized Fe_2O_3 to uniformly form hollow titania structures with a low surface area (i.e. having a small number of mesopores) **[169]**.

3.2.3. Hollow carbon spheres

Carbon nanomaterials have been unquestionably at the forefront in the advancement of the nanotechnology initiative. One of the these carbons that have been studied are the hollow mesoporous carbon spheres partly because of the versatility and robustness of the carbon material (its graphitic nature, tunable porosity, etc.) that allows the hollow spheres to be applied and studied in many areas of material science **[170, 171]**. The synthesis procedures to make hollow carbon spheres can be grouped according to the hard and soft template methods (templates include silica, metal or metal compounds and polymer latex spheres) **[172, 173]**. This arises since a direct formation of the spherical hollow nanostructures is not favoured thermodynamically **[152].** Since in most cases the template surface and the carbon source are not usually compatible, functionalization of the templates or any other modification of the surface with electrostatic groups or functional groups helps to make the template surface compatible with the carbon source **[173]**. These modifications can also help in fine-tuning the resulting porosity of the hollow carbon spheres. For example Chen et al. managed to synthesize mesoporous hollow carbon spheres (MHCSs) by a chemical vapour deposition (CVD) method using solid silica spheres modified with a mesoporous silica shell ($sSiO_2@mSiO_2$, using C18TMS as a surfactant). The MHCSs fabricated at 800 ℃ with shell thickness of 90 nm had a high surface area of 948 $m^2.g^{-1}$ and a pore volume of 0.3824 $cm^3.g^{-1}$ due to the use of the mesoporous template **[174]**. Nanocasting methods have also been used to make hollow carbon spheres with a thin shell thickness (4 nm), as reported by Liu et al. They reported a synthesis using method dopamine as the carbon source by simply immersing the spherical silica templates in the dopamine aqueous solution followed by carbonization and the removal of the silica template **[175]**. Hollow carbon spheres can be produced hard template method using different methods such as the CVD method **[176]** the solvothermal method followed by carbonization at high temperatures **[177, 178]** and even direct carbonization in nitrogen of the carbon source without any solvothermal treatment **[175]**. Soft template methods for making hollow carbon spheres are gaining momentum because of the reduction of the number of steps involved in the synthesis process in comparison to the hard template method. However, control of the particle size distribution is a challenge using this method **[173]**. The shell thickness of hollow carbon sphere has also be tailored by varying the template mesoporous shell thickness or the concentration of the carbon source **[174, 179, 180].** Chen et al. used

the C18TMS/silica ratio to tune the shell thickness of hollow spheres from 25-90 nm while keeping all other reaction conditions the same **[174]**. Many carbon sources ranging from gaseous ones like acetylene and ethylene **[174]**, to polymers such as PVA and phenolic resins **[181]** have been employed in the synthesis of hollow carbon spheres; in essence any carbon source that can interact and is compatible with the template and can easily undergo carbonization may be used as a carbon source. Given the porous nature of the hollow carbon spheres, removal of the template is easy, either by chemical dissolution as in the case of silica spheres **[175]** or thermal removal of polymer latex templates **[178]**.

3.3. Application of hollow spheres (nanoreactors) in catalysis

Mesoporous hollow spheres offer a great advantage in material science, as noted above. Catalysis is one of the growing fields of study in which the mesoporous hollow spheres have been studied and their hollow morphology exploited **[149]**. The porous structure of the hollow spheres can provide efficient mass transport pathways through the nanostructure's interior voids. This yields yolk/shell composites wherein the active sites (i.e., metal nanoparticles) are encapsulated inside the hollow spherical nanostructure (e.g. silica, carbon etc.) **[149, 182]**. The hollow morphology is also useful when studying the catalytic activity of different nanoparticles because the particles can be tested inside the inert shells with a possibility of limited metal support interaction and any other deactivation mechanism that can arise through particle sintering **[183, 184]**. Controlled synthesis of the metal nanoparticle yolk or rattle type carbon composites for application in catalysis are usually achieved by the core-shell-shell method. In this metal nanoparticles are coated inside (or loaded outside) a template that serves as a sacrificial layer to be used for encapsulating the metal nanoparticles. This is then covered by a porous carbon shell to form metal core@void@MHCS after template (MHCS = mesoporous hollow carbon spheres) **[149, 185]**.

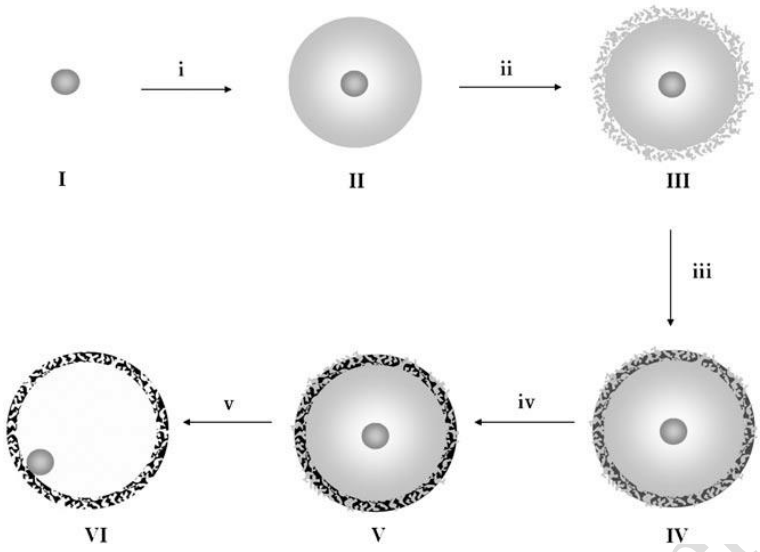

Figure 3. 4: General core-shell-shell route for making metal@hollow mesoporous carbon composites **[185].**

Several studies have shown the potency of these systems in catalysis. Liu et al. prepared an Au@mesoporous-C catalyst using a one-step core-shell-shell method for the reduction of ortho-nitrophenol. The encapsulated gold nanoparticles displayed high catalytic activity with greater than 99% conversion observed within ten minutes of the reaction progress. The catalysts also showed good recyclability without any loss of any activity (after 5 cycles) hence showing that the carbon shell served as a protective capsule that prevented any deactivation of the active catalytic sites **[185]**. Galeano et al. used the hollow mesoporous carbon spheres in an effort to document the effect of particle size for a catalytic CO oxidation reaction in air, it was observed that the catalytic composite Au@C (particle size ~ 7 nm) had high activity for CO conversion in comparison with encapsulated Au NPs of particle size ~ 14 nm **[186]**. Particle size studies with these nanostructures are advantageous because the support effects can be eliminated because due to the use of graphitic hollow carbon spheres. Many other metal nanoparticles such as rhodium, platinum etc. have also been encapsulated within mesoporous carbon shells for catalytic applications and showed significant performance. They showed little sign of diffusion limitations because the porosity of the hollow mesoporous carbon shell could be fashioned with great success to allow easy flow of reactants and products **[183, 187]**

3.4. On the porosity of hollow carbon spheres

The concept of using nanoreactors in chemical and catalytic reactions is relatively new in the nanotechnology initiative; it is however a very promising field for performing chemical reactions whereby mass transport limitations can be imposed on the reactions of interest **[188-191]**.

Of these nanoreactors, hollow carbon spheres have received great attention over the years. This is because of their variable functionality that has attracted interest from many research fields for technological and scientific applications. The hollow carbon spheres have found applications in batteries, as electrodes for use in supercapacitors, gas adsorption systems, for use as nanoreactors in catalysis and in drug delivery systems **[188, 192-196].** The structural architecture of these materials give them a distinct space in material science in relation to carbon materials such as carbon nanotubes/fibers and even solid carbon spheres. The reason is that even though the hollow carbon spheres have a carbon shell which gives them almost all the advantages offered by carbon nanomaterials, it is however the hollow interior of these materials that can be exploited, this added factor gives them the interesting properties for potential use in many fields of science and technology.

It's because of the hollow morphology that tailoring the porosity of these materials has become an important aspect in the synthesis of hollow carbon spheres that will allow easy and controllable access of reactants in and out of the hollow carbon spheres.

3.4.1. Types of pores observed in hollow carbon spheres

The main method for analysing the pore structures of hollow carbon spheres in the literature is by the use of nitrogen adsorption-desorption (Figure 3.4). It is with these techniques that the total surface area of the material can be estimated using the BET (Braunner-Emmet-Teller) equations. The pore size distributions are also calculated using DFT (density functional theory) techniques or the BJH (Barret-Joyner-Halenda) and other several equations using data obtained from the material's adsorption isotherms **[178, 197-199]**.

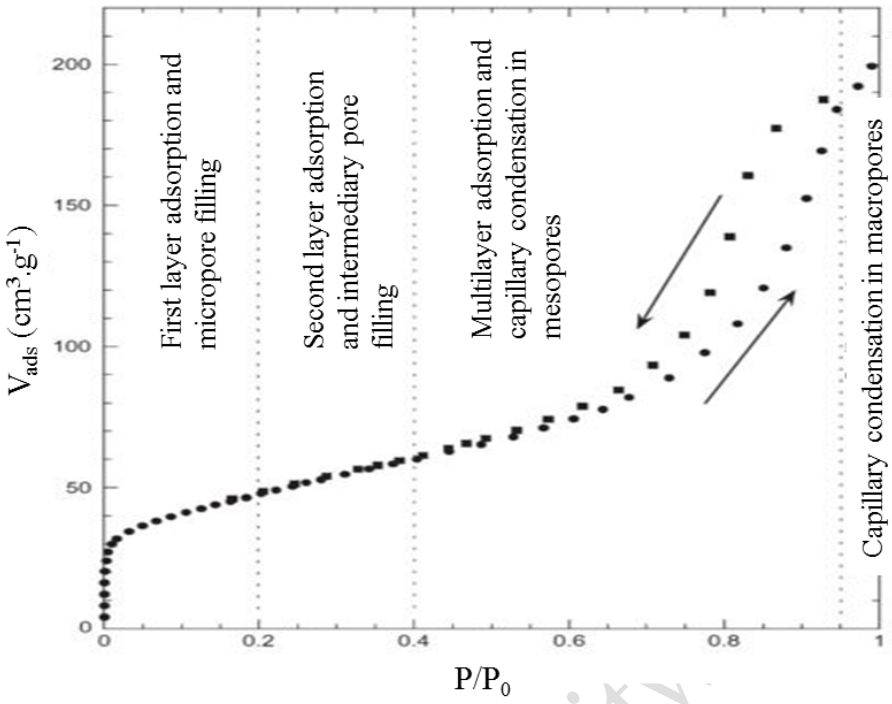

Figure 3. 5: Adsorption isotherm and its general features descriptive of the analyzed material **[199]**.

Several studies have reliably employed these techniques to accurately study and distinguish the hollow carbon sphere porosity. For example, Nongwe et al. **[198]** were able to decipher the difference in the hollow carbon porosity using N_2 adsorption-desorption. The material had different pore size distributions that varied with the synthesis procedure employed. One material showed significant mesoporosity as evidenced by type IV adsorption and pore size distribution calculated by the BJH method (pore diameter of ~ 5.7 nm) and the carbon shell structure from TEM analysis images, while the other hollow carbon spheres displayed a type II adsorption isotherm indicating significant the nonporosity of the carbon shells in question.

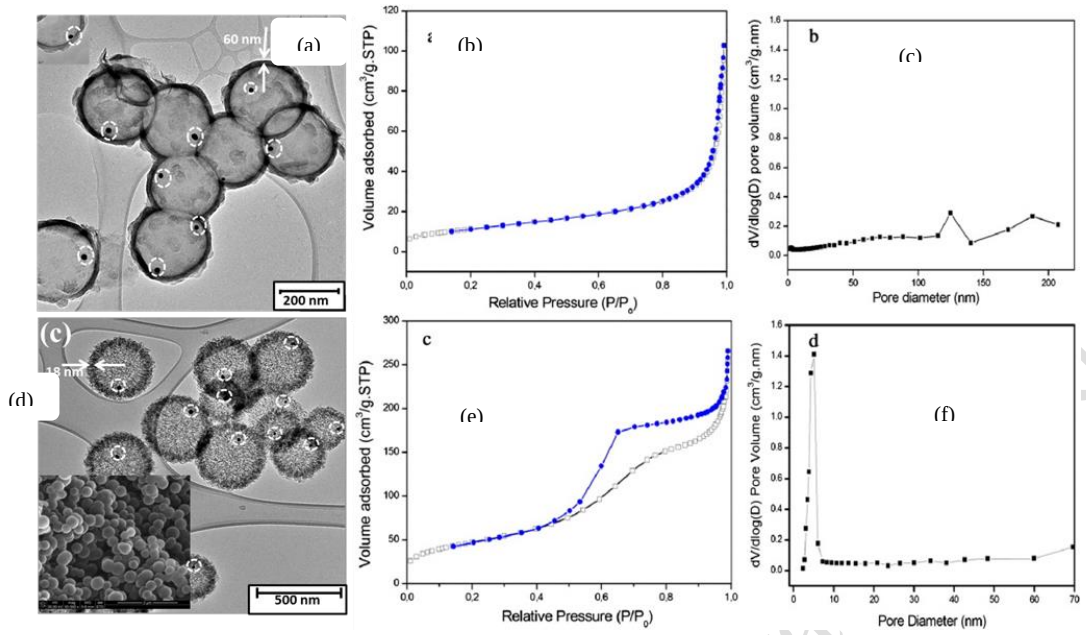

Figure 3.6: TEM images, N_2 adsorption-desorption isotherms and BJH pore size distribution of non-porous hollow carbon spheres (a,b,c) and mesoporous hollow carbon spheres (d,e,f), adapted from **[198]**.

In essence the hollow carbon spheres can be produced with a myriad of pore structures. Non-porous, microporous, mesoporous and macro-porous materials have been synthesized based on the templates and the types of porogen that were employed **[178, 180, 198]**. Hollow carbon materials with interlinked pores are often prepared due to the inability of the current synthesis procedures to adequately control the porosity of the resulting carbon shells. Nonetheless, hollow carbon spheres with > 90 % mesoporisity have been prepared by Qiao et al. **[180]** with the carbon materials exhibiting type-IV adsorption isotherms. Fang et al. **[200]** was able to prepare hollow carbon spheres with a high surface area (639 $m^2.g^{-1}$) that is predominantly microporous (i.e., pore size < 2 nm) as observed by the pore size distribution analysis using the BJH method. Mesoporous hollow carbon spheres (SA = 1286 m^2g^{-1}) were also synthesized using a modified from the one that was used to make the microporous spheres. The broad pore size distribution was centred on 30 nm, an observation that was also confirmed by TEM analysis. An example of hollow carbon spheres with both micro and mesopores was revealed by Zhang et al. **[195]**. In the abovementioned study porous hollow carbon spheres with a BET surface area of 1520 $m^2.g^{-1}$ were prepared. The materials displayed a wide pore size distribution in the range of 1-25 nm as evidenced by the BJH and adsorption (combination of Type I and IV) isotherm plots. Xu et al. **[201]** fabricated ultrahigh surface area (SA_{BET} = 3022 $m^2.g^{-1}$) hollow carbon nanospheres. These spheres displayed a type I and IV N_2 adsorption isotherm with the high surface area originating from the micro and mesopores at 0.6, 1.2 and 2.5 nm.

The porosity of the spheres can be controlled to some extent. In general type I/IV nitrogen N_2 adsorption-desorption isotherms are observed for most of the hollow carbon spheres synthesized to date. They usually have high surface area. This shows that hollow carbon spheres with micro-mesopore arrangements can be easily prepared. Nonetheless, predominantly nonporous, microporous and mesoporous hollow carbon spheres have also been fabricated.

3.4.2. Tailoring of the hollow carbon sphere porous nature

As described above, hollow carbon spheres can and have been fashioned with different pore structures. It however should be noted that the different pores can only be attained when different synthetic procedures are used. This can be done by varying the template (hard, soft or self-template), type of pore-former and even the carbon precursor. In this section several ways in which porosity of hollow carbon spheres can be manipulated will be described (see Table 3.1 and Figure 3.7).

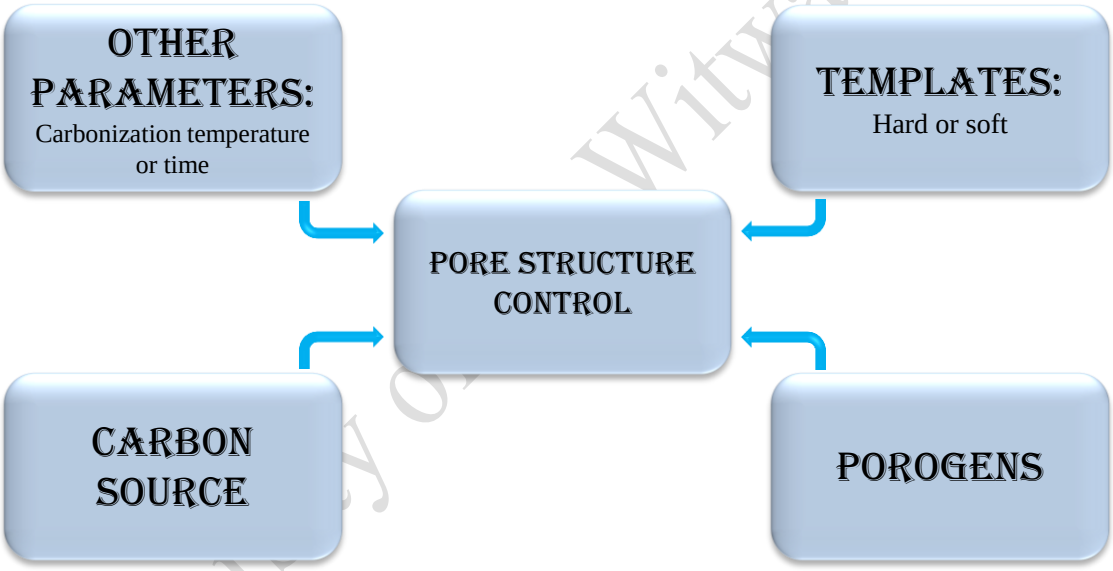

Figure 3. 7: Methods that can be exploited to control hollow carbon spheres pore structure.

3.4.2.1. Control using templates

The use of templates in the synthesis of hollow carbon spheres is indispensable. It is the template that shapes the resulting morphology of the hollow sphere **[152, 176, 177, 198, 202]**. It is thus not unprecedented that even the porosity of hollow carbon spheres can be tuned using the template. Stöber silica spheres are the most commonly used template and have been modified in several ways to make sure that the porosity of hollow sphere can be tailored to be either porous or non-porous. For example, Chen et al. **[192]**, managed to synthesize mesoporous hollow carbon spheres by a chemical vapour deposition method using solid silica spheres modified with a mesoporous silica shell (SiO_2@mSiO_2, C18TMS

used as a surfactant). The MHCSs fabricated at 800 ℃ with shell thickness of 90 nm had a high surface area of 948 $m^2.g^{-1}$ and a pore size distribution of 1.22 and 1.46 nm due to the use of the mesoporous template. It has also been observed that the use of silica spheres without any modification, using a porous shell, results in the formation of nonporous hollow carbon spheres with low a specific surface areas of less than 50 $m^2.g^{-1}$ **[176, 198].** The Stöber silica spheres in most cases are modified using surfactants such as CTAB/CTAC and C18TMS to give a highly porous silica template which can therefore be used to make the porous hollow carbon spheres **[184, 202]**.

Another spherical template that has been commonly used is the polystyrene sphere. This template can be easily removed by annealing at high temperatures after coating with a carbon shell without the need to use strong acids or bases. The microporous hollow carbon spheres result because the template decomposition leaves the hollow carbon sphere void **[178].** Han et al. **[203]** managed to prepare highly microporous hollow carbon spheres with a surface area of 213 $m^2.g^{-1}$ using polystyrene spheres as the hard template and aniline as the carbon source. Soft template methods not only avoid complex synthetic routes but can also be used to control the hollow carbon sphere porosity based on the self-assembly of the surfactants. The pore size distribution of the hollow carbon spheres is dictated by the type of surfactant used. Wang and co-workers **[187]** formed a soft template emulsion using P123 and sodium oleate (i.e, non-ionic and ionic surfactants). Subsequent the hydrothermal polymerization of dihydrobenzoic acid and formaldehyde on the soft-template, followed by annealing in an Ar environment gave hollow carbon spheres with Pt nanoparticles encapsulated inside. Microporous hollow carbon spheres (BET SSA = 540 $m^2.g^{-1}$) with a small amount of mesopores at 3.1 nm were obtained. The ionic surfactants are known to template micropores and small mesopores while the non-ionic surfactants template large mesopores **[204]**. The microporous nature of the above mentioned hollow carbon spheres can then be attributed to the use of the amount and type of ionic surfactant relative to the non-ionic surfactant that is used. This was demonstrated by Yang et al. **[205]** when using a non-ionic surfactant (Pluronic F127) as a soft template to prepare mesoporous hollow carbon spheres (SSA = 431 $m^2.g^{-1}$) with an average pore size of approximately 10 nm. In this case the carbon shell was hydrothermally prepared on a soft template using α-cyclodextrin as the carbon source followed by carbonization under Ar at 900 ℃.

3.4.2.2. Pore size control using porogens

Pore formers such as surfactants have successfully been used to form robust high surface area hollow carbon spheres. In this synthetic procedure the porogen is mixed with a carbon precursor to form pores. As the carbon precursor precipitates onto the template **[194, 206],** the porogen helps in forming porous channels perpendicular to the resulting shell**.** He and co-workers used the method to make highly porous hollow carbon spheres, PolyDADMAC was used at the pore-forming agent and resorcinol-formaldehyde as the carbon source. Mesoporous carbon with a N_2 type IV adsorption isotherm was obtained with a high

surface area of up to 1055 $m^2.g^{-1}$ and a pore size of 4.3 nm **[194]**. A cationic surfactant like CTAB has also been employed to give hollow carbon spheres with sufficient porosity. Fang et al. **[200]** synthesized foam-like hollow carbon spheres using a combination of resorcinol-formaldehyde and CTAB. The carbon had a BET surface area of 639 $m^2.g^{-1}$, with a predominantly microporous pore structure which is due to the use of the cationic surfactant.

Qiao and co-workers **[180]**, prepared different carbon spheres using a silica assisted method with the TEOS as the silica source and hexdecyltrimethylammonium chloride as the template and porogen. Solid, hollow and yolk shell carbon spheres (achieved by varying the TEOS/resorcinol ratio) were obtained after carbonization and removal of silica. It was observed that all the resulting carbon spheres are mesoporous (as shown by N_2 adsorption-desorption isotherm, type IV and TEM analysis) with surface areas greater than 600 $m^2.g^{-1}$. These results thus showed that the CTAC (which was kept constant for all the three composites) played a big role in forming mesopores on the carbon sphere surface. Large non-ionic surfactants have also been used to control the porosity of hollow carbon spheres. In a study performed by Tang et al. **[207],** mesoporous hollow carbon spheres with a pore size of approximately 20 nm and specific surface area of 427 $m^2.g^{-1}$. A diblock copolymer PS-b-PEO was used as the porogen and dopamine as carbon precursor. The porogen formed micelles on the polydopamine during its formation around the silica template that led to a generation of large observable (by SEM imaging) mesopores on the resulting carbon shell after carbonization and template removal by etching (Figure 3.8).

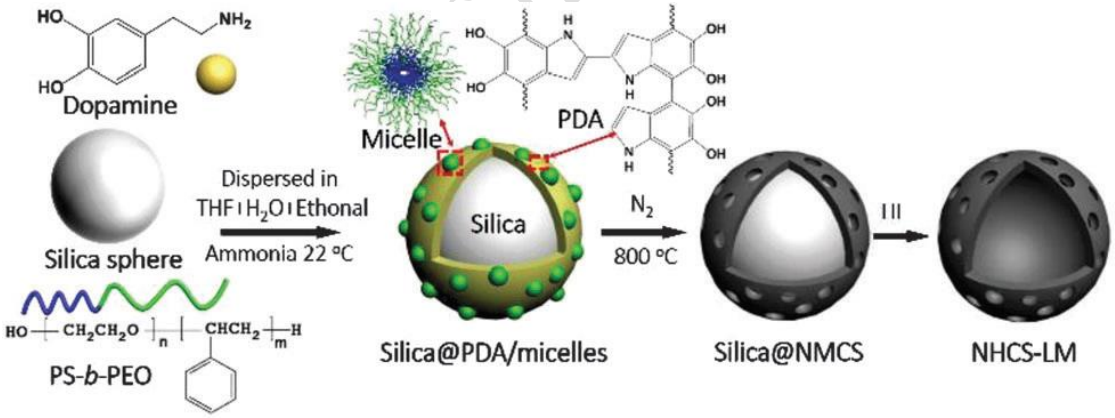

Figure 3. 8: Schematic showing the influence of pore-formers/porogen (PS-b-PEO) on the porosity of the resulting hollow carbon spheres **[207]**.

3.4.2.3. Control Using the Carbon Source

The effect of carbon source on hollow carbon spheres porosity can only necessarily elucidated when the same template has been employed during synthesis.

3.4.2.4. Other pore controlling parameters

Several other synthetic parameters have also been employed to tailor hollow carbon shell porosity and specific surface areas **[176].** Numerous studies have reported on the use of the carbonization temperature to tune the surface area of the hollow carbon spheres and hence the resulting porosity of the material also **[200, 201]**.

Table 3. 1: Comparison of different synthesis method for controlling the pore structure of hollow carbon spheres.

Synthesis method	Template Used	Carbon Source	Porogen/surfactant	Carbonization T, Time (℃, h)	Pore Structure (nm)	Surface Area ($m^2.g^{-1}$)	Ref
Sol-gel	melamine-formaldehyde	Resorcinol-Formaldehyde	CTAB	900,1	Microporous	775	**[208]**
Sol-gel	Stober-silica	Resorcinol-Formaldehyde	CTAB	600,2	Microporous	387	**[209]**
Sol-gel	Stober-silica	dopamine	Diblock copolymer; PS-b-PEO,	800,2	Mesoporous	427	**[207]**
Sol-gel, HTC 100	Stober-silica	Resorcinol-Formaldehyde	-	750, 2	Mesoporous	859	**[210]**
HTC-200	F127-soft template	α-cyclodextrin	-	900,6	Highly microporous-	431	**[205]**
Sol-gel	Silica	RF	CTAC	800,5	Mesoporous	1098−1312	**[180]**
CVD	Silica	Toluene	C18TMS	900,	Mesoporous	202	**[198]**
CVD	Stober silica	Toluene	-	900	Non-porous	40	**[198]**
Hydrothermal-180	Stober silica	Glucose	-	800,2	Micro-meso and macropores	658	**[211]**
Sol-gel	Triton-X100-soft	Aniline and pyrrole	-	900,20	Micro-mesoporous	3022	**[201]**
Sol-gel	Stober silica	RF	CTAB	800,4	Microporous	639	**[200]**
Sol-gel	Aluminosilicate	Phenol and formaldehyde	C18TMS	850,7	Mesoporous (	1230	**[212]**
Sol-gel	Fe impregnated Stober silica	Divinylbenzene and azo-bis-(isobutyronitrile)	C18TMS	1000,4	Mesoporous	1200	**[213]**
Sol-gel	Polystyrene spheres	Poly(cyclotriphosphazene-co-4,40-sulfonyldiphenol)	-	1000,2	Microporous	719	**[214]**
Sol-gel	Silica	Resorcinol-Formaldehyde	-	750,1	Microporous	720	**[215]**
Sol-gel	Silica	Resorcinol-Formaldehyde	-	750, 2	Mesoporous	514	**[216]**

3.4.3. Effect of hollow carbon sphere porosity on catalytic reactions

In this section the effect of hollow carbon spheres porosity on catalytic reactions when the active metal sites are placed inside the carbon nanoreactors is surveyed. Because the catalytic active sites are inside the nanoreactors it is therefore important to have their porosity tailored in such a way that the process would allow the reactants to interact with the encapsulated particles **[188, 198]**. In these systems reactants and products have to move solely through the porous channels, hence a molecule's mobility will be determined by nanoreactor's pores and the molecule of interest effective radius. Several catalytic carbon nanoreactors (i.e. yolk shell or reverse bumpy ball structures) have been tested in different reactions in which the carbon shell pore structure was observed to have significant bearing, particularly on catalytic activity **[198, 217]**. In a study by Nongwe et al. **[198]**, it was observed that a mesoporous carbon allowed easy movement of the reactants (p-nitrophenol) into the Au yolk shell carbon nanoreactor. The nanoreactor with small pores did not allow such free movement of reactants. This gave a very low or no catalytic activity which was attributed to the pore structure of the hollow carbon sphere. This study would therefore suggest that it is absolutely imperative to have hollow carbon nanoreactors with a useful porous structure to exploit the other advantageous properties of hollow carbon spheres in catalysis.

Metal functionalized yolk shell or even reverse bumpy-ball hollow carbon spheres have already been used for applications in many catalytic reactions using predominantly noble metal particles such as Pd **[218, 219]**, Rh **[184],** Ru **[217]**, Pt **[183, 193]** and Au **[175, 202, 220]**. Reactions tested using these nanoreactors include liquid phase reactions such as reduction of nitrophenol **[175, 218-220]**, hydrogenation of olefins **[183],** hydrogenation of aromatic and heterocyclic compound **[184]**, gas phase reactions for CO oxidation **[202]**, or CO hydrogenation in Fischer-Tropsch synthesis **[217]** and even for use as electrocatalysts in fuel cells **[193]**.

All the above mentioned studies used hollow carbon nanoreactors that possessed well defined pore structures (i.e. micro/mesoporous, see Table 3.2), which were sufficient to allow free mobility of reagents.

Table 3. 2: Some of the reaction performed inside carbon nanoreactors using different metals

Catalyst	Catalytic reaction	Pore structure (nm)	Specific Surface area ($m^2.g^{-1}$)	Reactants	Ref
RGO@Pd@HCS	Liquid phase Reduction	-	-	Sodium borohydride and nitrophenol	**[218]**
Pd@HCS	Liquid phase Reduction	-	-	$NaBH_4$ and nitrophenol	**[219]**
AuPt@HCS	Electrocatalysis	Mesoporous	837	electrochemical degradation tests	**[193]**
Rh@HCS	Hydrogenation	Micro/mesoporous (0.4 and 2.9)	1370	aromatic and heterocyclic compounds and hydrogen	**[184]**
Au@HCS	Oxidation	Mesoporous (3.9)	979	CO/O_2	**[202]**

Chapter 4

Material Characterization Techniques, Fischer-Tropsch Synthesis Set-up and equations

3.1. Materials characterization

Different techniques were employed in these studies to obtain a full physico-chemical evaluation of the materials and catalysts. These included the use of transmission electron microscopy (TEM), scanning electron microscopy (SEM) and electron probe microanalysis (EPMA) to evaluate the morphology and in some cases the elemental composition of the new catalysts. Raman and Fourier transform infrared (FTIR) spectroscopies were also employed. Temperature programmed reduction (TPR) and pulse chemisorption were indispensable in the studies. Brunauer–Emmett–Teller (BET) was the main technique use to evaluate the material's surface area and porosity. Powder X-ray diffraction (PXRD) was an important technique for bulk analysis of the materials, especially the different phases found for the catalysts.

The in operando techniques employed in these studies were the in situ powder X-ray diffraction (in situ PXRD) and in situ magnetometer in which the evolution of the catalysts were 'viewed' during activation and catalyst testing.

- What follows is a short but detailed description of each characterization technique and the instrument that was used.
- Detailed sample preparations for each characterization technique are described in individual chapters where the instruments were used.

3.1.1. Transmission electron microscopy (TEM)

This type of electron microscopy technique is the earliest of the microscopies developed for imaging particles in the nanoscale range with high resolution **[221]**. In a TEM instrument a beam of high energy electrons is accelerated downwards from an electron gun through a thin specimen from whom the interaction of the electron beam with the sample is used to visualize its many features (shape, size, chemical composition, etc.).

As the electron beam passes through the instrument column it is focused using a condenser lens into a coherent beam while the condenser aperture reduces spherical aberration. The resulting beam then illuminates the specimen and the transmitted beam, which are is dependent on the specimen density and its transparency to the electron beam. The transmitted beam is focused using an objective lens to form an image on a fluorescent screen or a charge coupled device camera, which is then used to capture the micrographs of the sample (Figure 4.1) **[222]**.

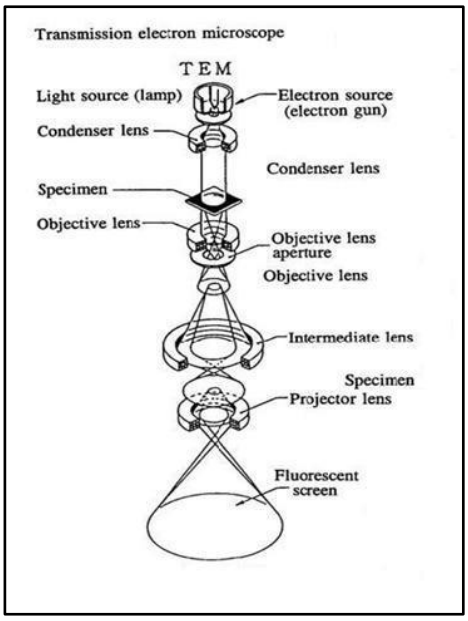

Figure 4. 1: Schematic of main components found in a TEM instrument.

Analysis was performed on a Tecnai spirit (T12) transmission electron microscope operating at 120 kV (Figure 4.2)

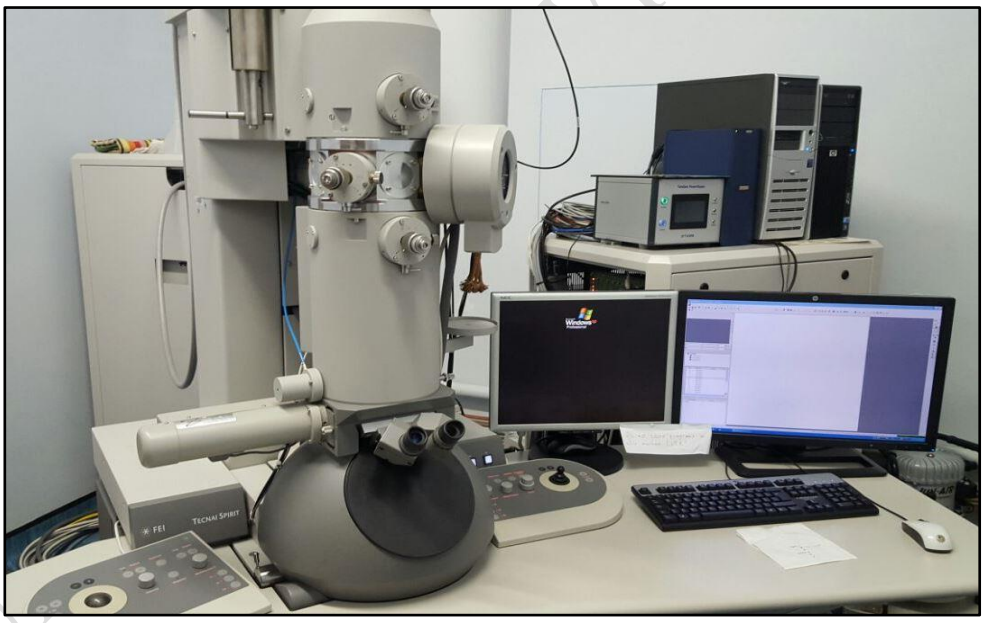

Figure 4. 2: FEI Tecnai T12 TEM instrument.

3.1.2. Scanning electron microscopy (SEM)

Similar to the TEM, SEM instruments use energetic electrons to analyze objects (yielding a more magnified view than obtained by optical microscopy. However, this technique uses a different detection mode than used to collect TEM images. Images in SEM, as the incident electrons strike a specimen several signals are generated. Secondary electrons (SE) or backscattered electrons (BSE) are also produced; these emitted electrons are detected by an electron detector specific for either SE or BSE.

Scanning coils positioned above the objective lens control the electron beam and position the beam onto surface of the sample. This allows scanning of defined area of the sample giving information of the specimen's topography, morphology and composition (Figure 4.3) **[223]**.

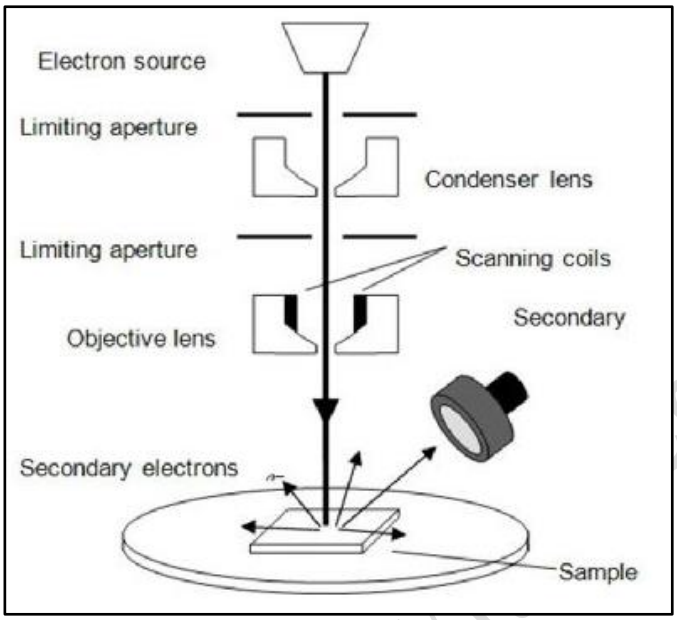

Figure 4. 3: Schematic of main components of a SEM instrument.

SEM analysis was performed on a FEI Nova Nanolab 600 FIB/SEM instrument operating at 30 kV (Figure 4.4).

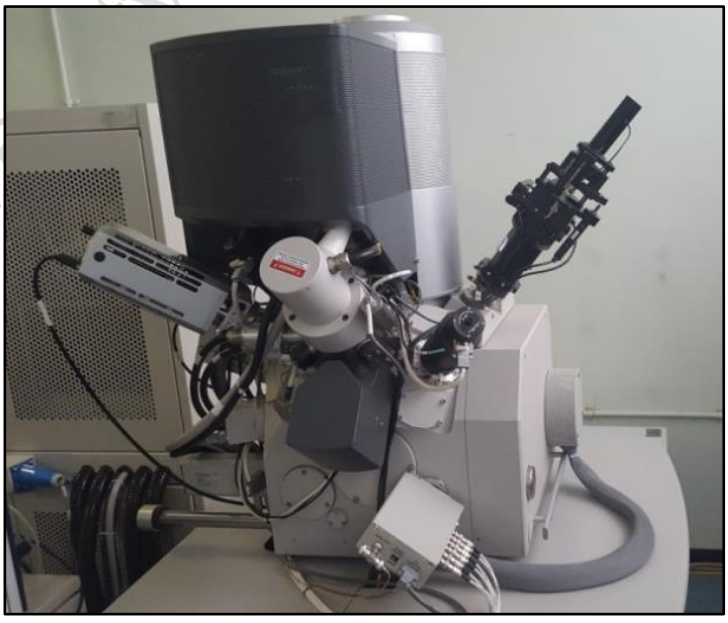

Figure 4. 4: FEI Nova Nanolab 600 FEG-SEM/FIB instrument.

3.1.3. Electron probe micro-analysis (EPMA)

An electron probe micro-analyzer is a microbeam analytical instrument used for an in situ non-destructive chemical analysis of solid samples **[224]**. An EPMA instrument functions like a SEM with an added function for chemical analysis of small areas of the sample by wavelength dispersive spectroscopy (WDS). A wavelength dispersive X-ray spectrometer (WDS) uses crystals that allows for a detection of specific X-ray wavelength or energies **[225]**.

An EPMA instrument is composed of four main parts: (1) an electron source, (2) electromagnetic lenses located in the column of the instrument, (3) sample chamber with movable sample stage, and (4) a multiplicity of detectors arranged around the sample chamber. A diagram of an electron-probe microanalyzer is shown in Figure 4.5.

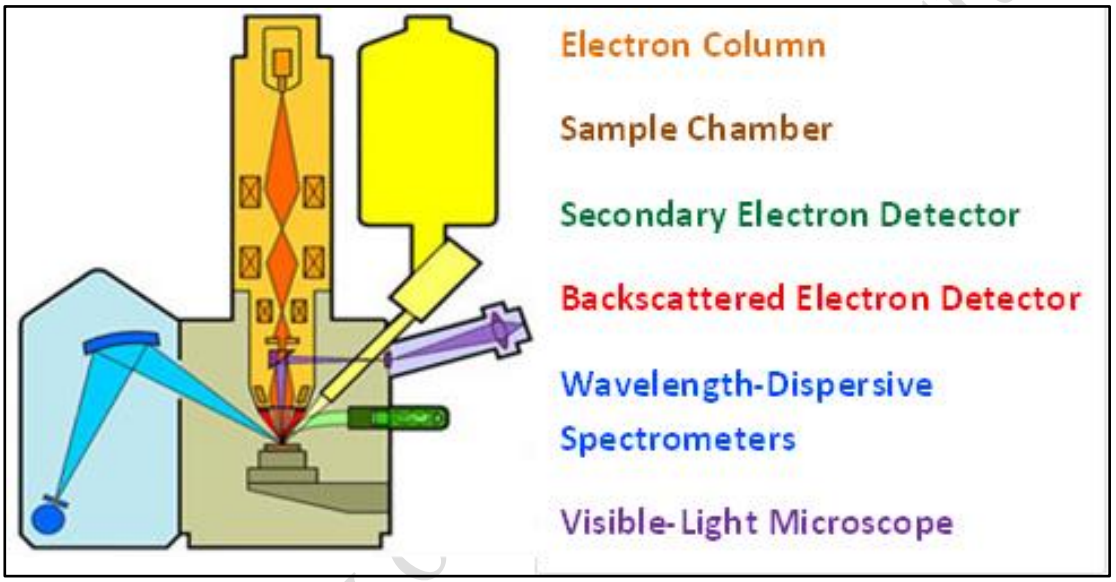

Figure 4. 5: Schematic of an electron probe microanalyzer **[224]**.

EPMA analysis was performed using a CAMECA SX5-FE EPMA, equipped with 5 wavelength dispersive X-ray spectroscopy (WDS) detectors and 12 crystals to select X-ray wavelengths for specific elemental compositions. Elemental mapping was also performed using a FEG-SEM (CAMECA), a component of the EPMA instrument (Figure 4.6).

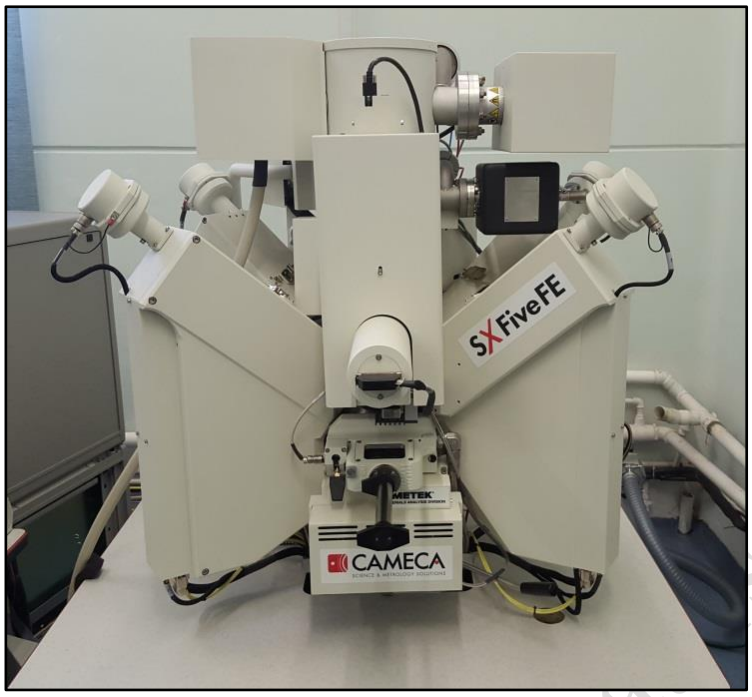

Figure 4. 6: CAMECA SX5-FE EPMA instrument..

3.1.4. Brunauer–Emmett–Teller (BET) analysis

The BET technique uses the BET theory to evaluate the total surface area of a material based on the physical adsorption of an inert gas at constant temperature. The technique focuses on the process of gas phase and absorbed film interchange by approaching the adsorption behaviour of the probe gas kinetically, while assuming that the surface is energetically uniform. For the BET surface area and porosity to be calculated. An adsorption isotherm of a fully degassed material is obtained by adsorbing gases at different pressures, from high vacuum to ambient pressures (Figure 4.7). By using the BET equation (see below) a BET plot is generated to calculate a monolayer volume from the volumetric measurements to calculate the total surface of a material **[197]**.

$$\frac{1}{v\left(P_o/p-1\right)} = \frac{C-1}{v_m C} \times \frac{P}{P_o} + \frac{1}{v_m C}$$

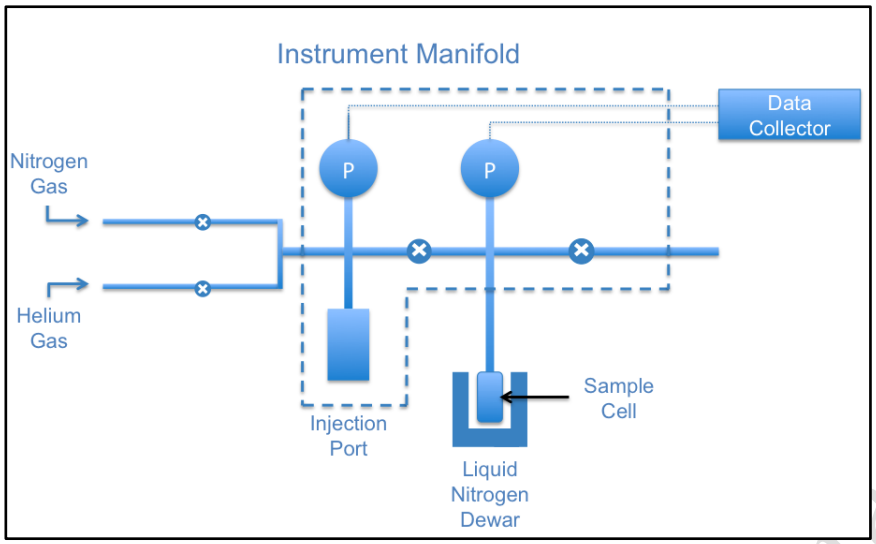

Figure 4. 7: A typical schematic of a gas adsorption instrument **[226]**.

The N_2 adsorption–desorption experiments were conducted at -195 ℃ using a Micromeritics Tristar 3000 surface area and porosity analyzer (Figure 4.8)..

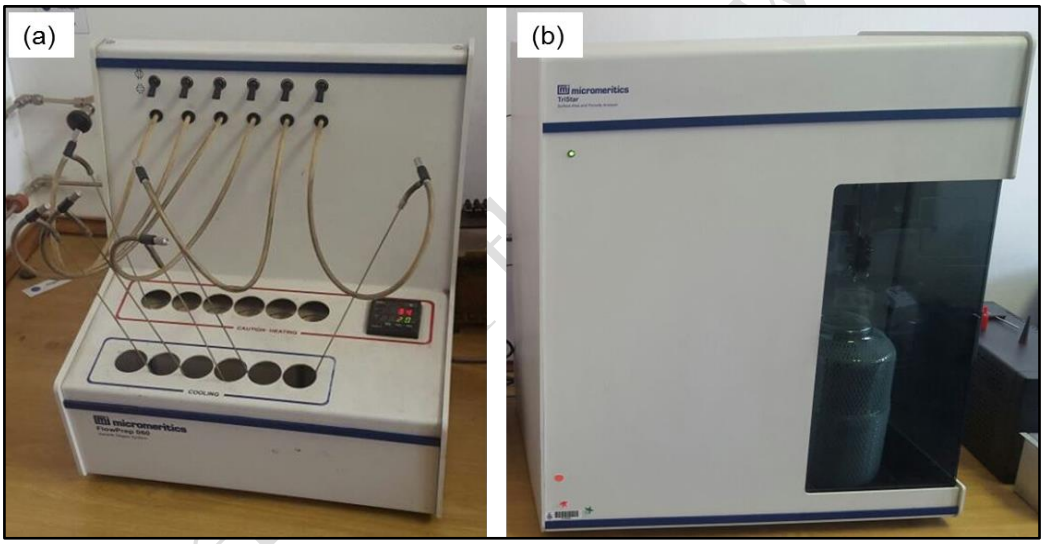

Figure 4. 8: A Micromeritics Tristar 3000 surface area and porosity analyzer.

3.1.5. Chemisorption

The chemisorption techniques are used to determine the degree of metal dispersion, active metal surface area and active particle sizes of catalytic materials. In this technique probe molecules such as hydrogen or carbon monoxide are chemically adsorbed on the surface of the pre-treated catalyst. Specific amounts of the reactive gas are injected in to the sample reactor and the amount that is adsorbed is accurately determined. The adsorbed gas is then used to estimate the metal dispersion of the catalyst and other information that can be extracted from the data **[227, 228]**.

Two chemisorption analysis methods have been used: Static and dynamic adsorption (pulse chemisorption).

In a static adsorption method (Figure 4.9) the sample is evacuated to high vacuum first followed by an injection of known doses of the probe gas in increasing order at different probe gas pressures. After equilibration of the system an adsorption isotherm is generated from which the monolayer gas coverage is calculated **[227]**.

The dynamic method involves a continuous flow of an inert carrier gas flowing over the analyte, while a probe gas is injected in the gas stream via a loop with known volume. Some of the reactive gas is then adsorbed on the catalytic surface and the cumulative sum of the adsorbed gas from the experiment is used to estimate the catalyst dispersion **[227, 229]**.

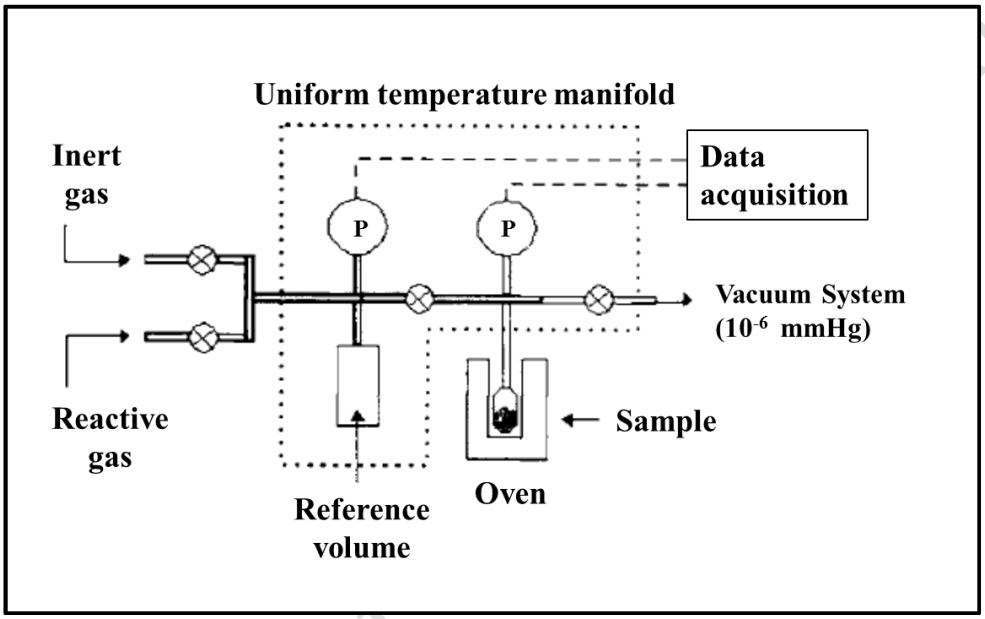

Figure 4. 9: Diagram for static chemisorption method **[230].**

Analysis procedure, pulse chemisorption was performed using the Micromeritics Auto Chem II instrument (Figure 4.10).

Figure 4. 10: Micromeritics ASAP 2020 chemisorption unit.

3.1.6 Temperature programmed reduction (TPR)

TPR is a method used to determine the number of reducible components in catalyst systems. The technique also reveals the temperature at which the reducing species begin to be activated to produce a phase transformation. TPR analysis is performed on a temperature programmed instrumentation that is equipped with a thermal conductivity detector or a mass spectrometer for analyzing the outlet gas. Generally the analysis is performed by flowing hydrogen gas in an inert gas (i.e. 5%H_2/Ar or 5% H_2/N_2) through the sample while the temperature is ramped up to a set value. The resulting catalyst reduction profile is produced as result of monitoring changes in the gas concentration that was fed into the catalyst system **[228]**.

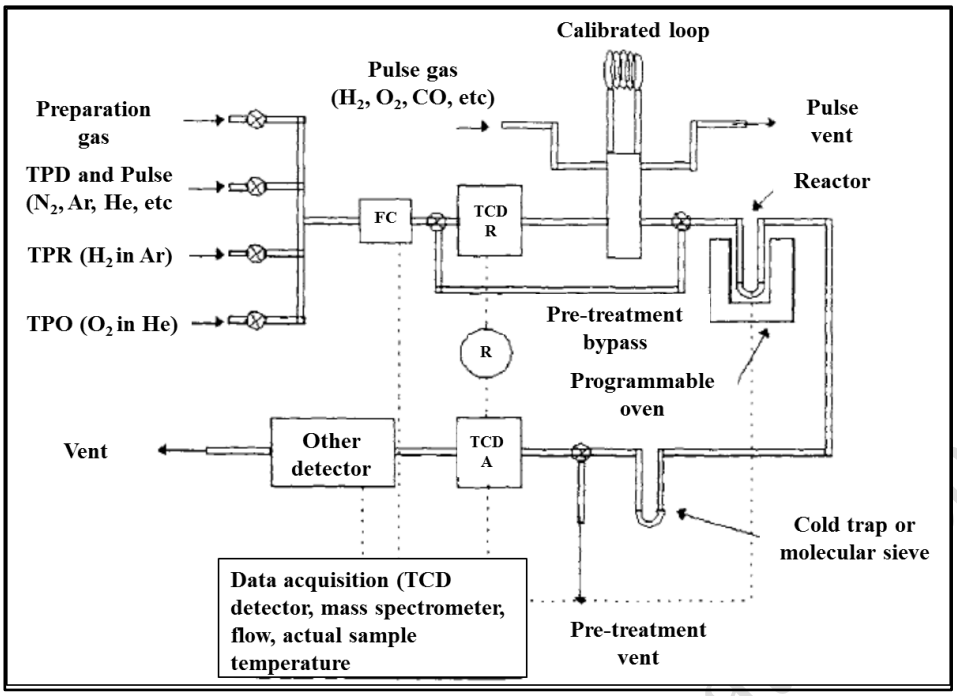

Figure 4. 11: Schematic diagram for pulse chemisorption and temperature programmed analysis **[227, 228]**.

TPR experiments were carried out with a Micromeritics Auto Chem II unit (Figure 4.12).

Figure 4. 12: Micromeritics AutoChem II instrument unit.

3.1.7. Raman spectroscopy

Raman spectroscopy gives details about molecular vibrations in materials that can be used for sample identification. Raman spectroscopy depends on the scattering of monochromatic light which upon interaction with a material can result in four different energy exchanges (absorption, spontaneous emission, stimulated emission and Raman scattering)

During analysis the majority of the light is elastically scattered at the same frequency as the incident source (i.e. Rayleigh scattering), this radiation is filtered out and is not resposible for giving the Raman response. However, the Raman emission occurs when some of the photons (10^{-5}%) are inelastically scattered by the transfer of some of its energy to the material depending on the vibrational energy levels and polarizability of materilal's molecular bonds. The emitted photons can have low or high energy relative to the light source, resulting in what is called the Stokes or anti-Stokes Raman scattering respectively **[231].** The spectrum is collected by detecting these wavelength shifts, and the Rayleigh band is set at 0 cm^{-1} (Figure 4.13).

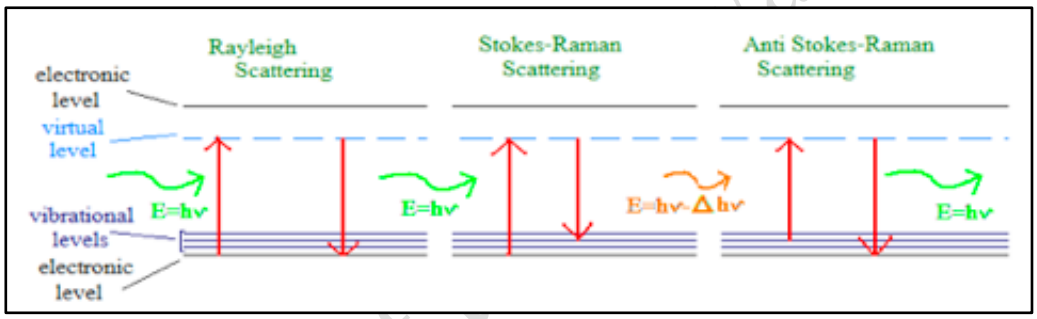

Figure 4. 13: Energy level diagrams in Raman scattering.

Laser Raman spectroscopy (λ = 514 nm) analyses were performed on the materials using a Horiba Jobin-Yvon Raman spectrometer (T64000) (Figure 4.14).

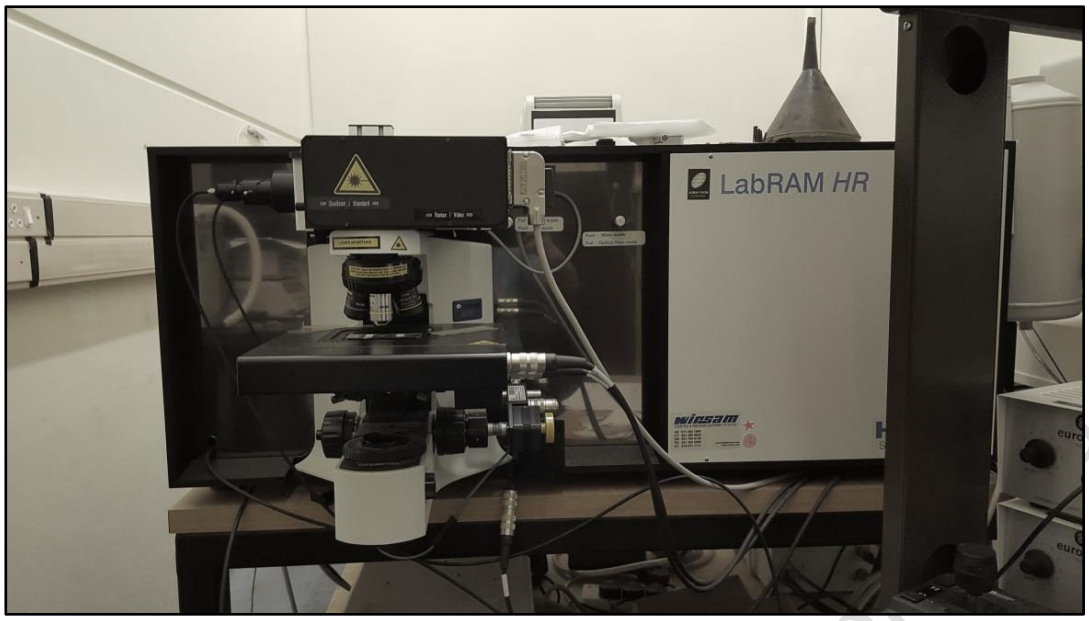

Figure 4. 14: Horiba Jobin-Yvon Raman Spectrometer (T64000).

3.1.8. Fourier transform infrared (FTIR) spectroscopy

This type of vibrational spectroscopy deals with the infrared region of the electromagnetic spectrum. The infrared light interacts with molecules to give qualitative and quantitative details about the materials being analyzed. FTIR spectroscopy measures bond vibrations (i.e. stretch or bend) between two atoms or more whose vibration frequency is dependent on the type of bonding and the atom sizes. Hence, FTIR spectroscopy is one of the main techniques used to determine functional groups in organic and inorganic materials (Figure 4.15) **[232, 233]**.

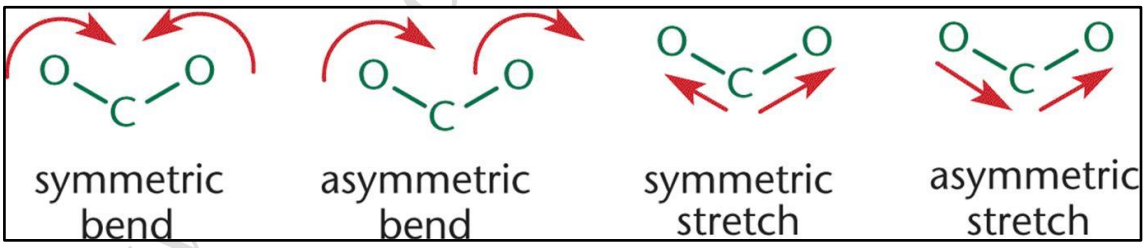

Figure 4. 15: Typical molecular vibrations activated by infrared radiation.

A Brüker Tensor 27 Fourier Transform Infrared spectrometer was used to analyze the surface functionalities of the materials (Figure 4.16).

Figure 4. 16: Bruker TENSOR 27 FTIR Spectrometer.

3.1.9. Thermogravimetric analysis (TGA)

The TGA technique is used to analyze the thermal stability or the behavior of materials under various gaseous environments. The samples mass change (due to decomposition, reduction, oxidation, etc.) is monitored as a function of temperature as it is being ramped up at a set rate. Three types of thermogravimetric analysis have been reported (1) dynamic TGA – sample under continuous increase in temperature, (2) static TGA – sample under constant temperature and (3) quasi static TGA – sample is heated to constant weight at each of a series of increasing temperature regimes **[234]**.

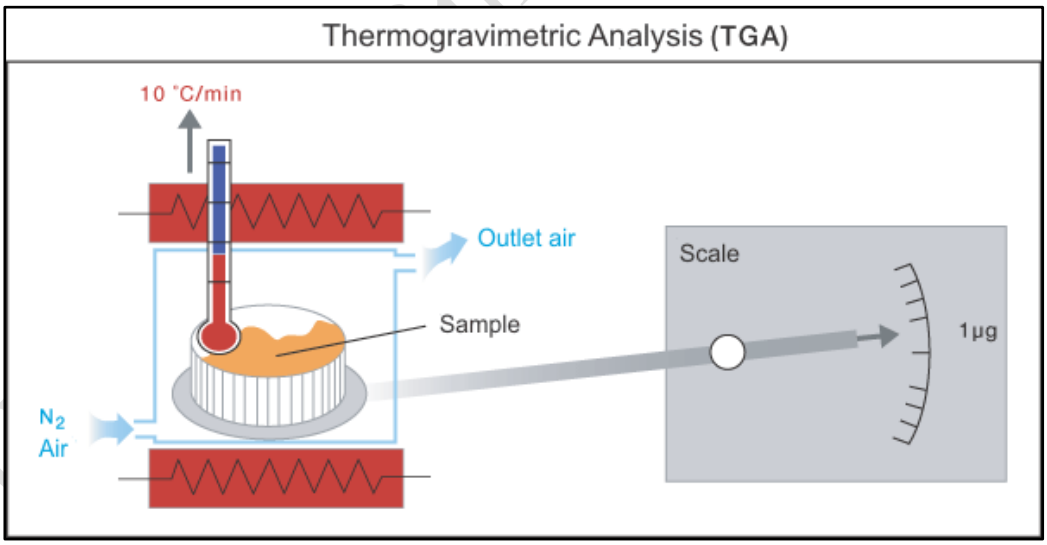

Figure 4. 17: Schematic showing the operating principle for TGA measurements.

A Perkin Elmer TGA 4000 Thermo-gravimetric analyzer was used for thermal analysis (Figure 4.18).

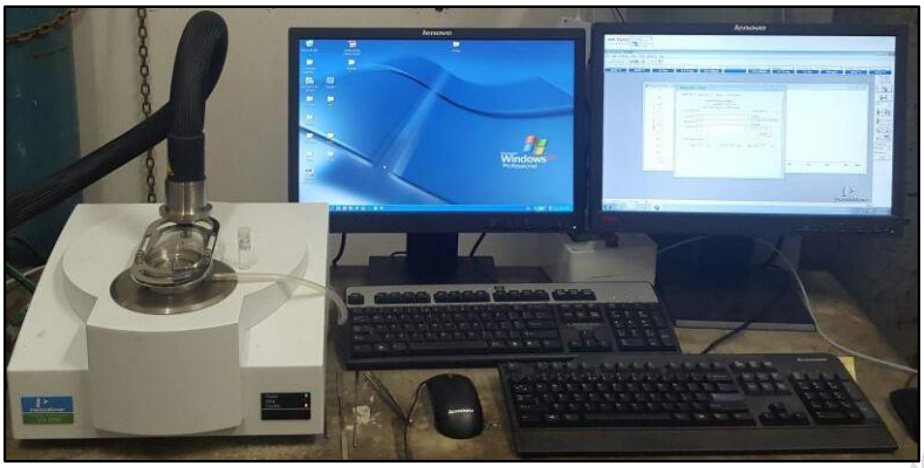

Figure 4. 18: A Perkin Elmer TGA 4000 Thermo-gravimetric analyzer**.**

3.1.10. Powder X-ray diffraction

PXRD is a technique used for a bulk phase analysis of crystalline materials by using monochromatic X-rays **[235]**. This technique was discovered by Max von Laue when he observed that crystalline materials acted as gratings for X-rays due to a planar spacing being almost equal to the X-rays wavelength. The diffraction pattern during analysis results from constructive interference of the diffracted rays after interaction with the analyzed material. The XRD profiles arising from the constructive interference follow the Bragg's law ($n\lambda = 2d \sin\theta$) relating the X-ray wavelength (λ), material lattice crystalline (d) and the diffraction angle (θ) where n is an integer **[236]**.

X-ray diffraction instruments have three main components: (1) an X-ray tube (2) a sample holder and (3) the X-ray detector.

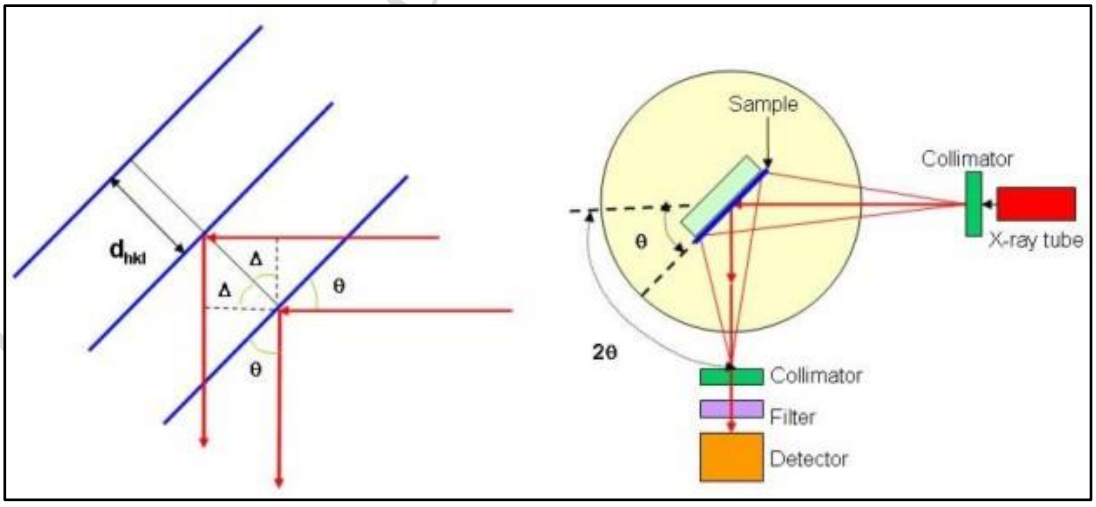

Figure 4. 19: Bragg's schematic and a typical setup on an XRD diffractometer **[236]**.

The bulk composition of the materials was analyzed using a Bruker D2 phaser and a Bruker D8 advance equipped with an Anton-Parr XRK in situ analysis cell.

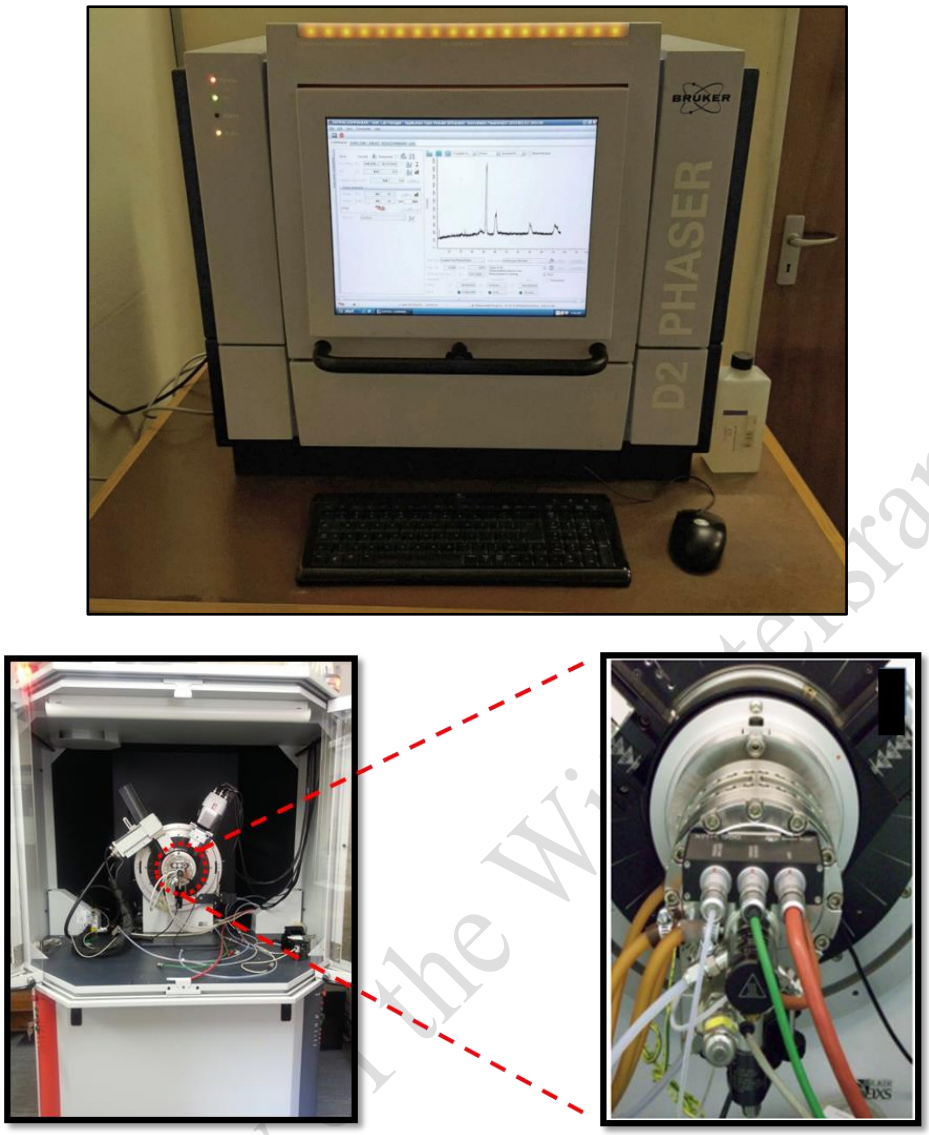

Figure 4. 20: Bruker D2 Phaser and D8 with the in-situ XRK analysis cell.

3.1.10. In situ magnetometer

The in situ magnetometer used in this work has been described in details in these references **[78, 237]**.

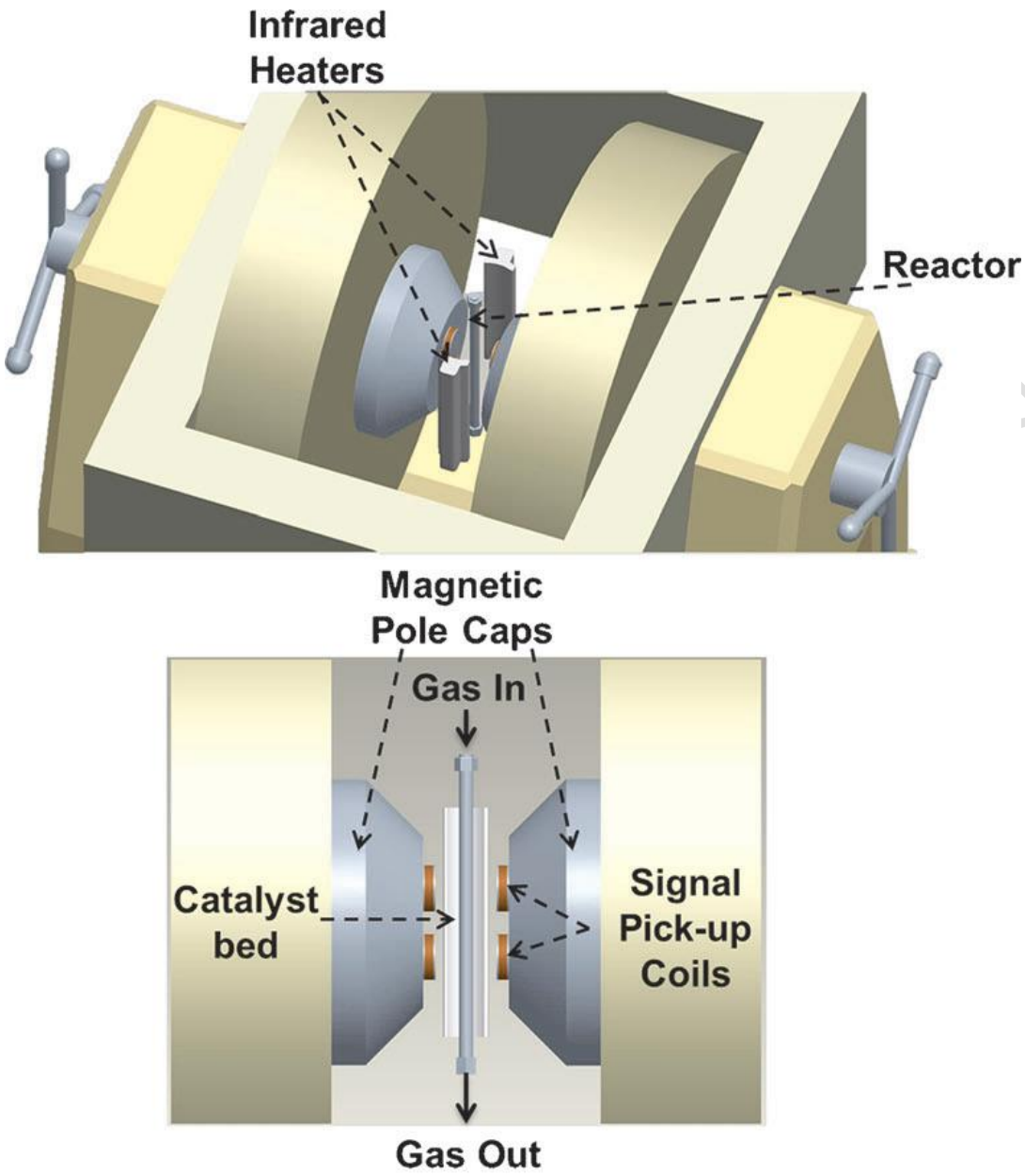

Figure 4. 21: Schematic of the in situ magnetometer **[77]**.

.

3.2. Summary of gases used

Gas	Supplier	Composition (purity)
Helium	AFROX	Baseline 5.0 (> 99.9%)
Hydrogen	AFROX	Baseline 5.0 (> 99.9%)
Nitrogen	AFROX	Baseline 5.0 (> 99.9%)
Argon	AFROX	Baseline 5.0 (> 99.9%)
Oxygen	AFROX	Baseline 5.0 (> 99.9%)
Air	AFROX	Baseline 5.0 (> 99.9%)
Hydrogen in nitrogen	AFROX	~ 5% H_2 and N_2 balance (>99.9%)
Hydrogen in argon	AFROX	~ 5% H_2 and N_2 balance (>99.9%)
Oxygen in argon	AFROX	~ 5% O_2 and N_2 balance (>99.9%)
Syngas (H_2/CO and N_2)	AFROX	~30% CO, 10% N_2 and H_2 balance (> 99.9%)

3.3. Chemical vapour deposition method (CVD) in a horizontally aligned furnace

Synthesis of hollow carbon spheres by carbonization and the annealing of the hollow carbon spheres were performed in a horizontal tube furnace as shown below **[238, 239]**. The gases were supplied into the lab through a gas reticulation system. The furnace heating rate was always kept at 10 ℃.min^{-1}.

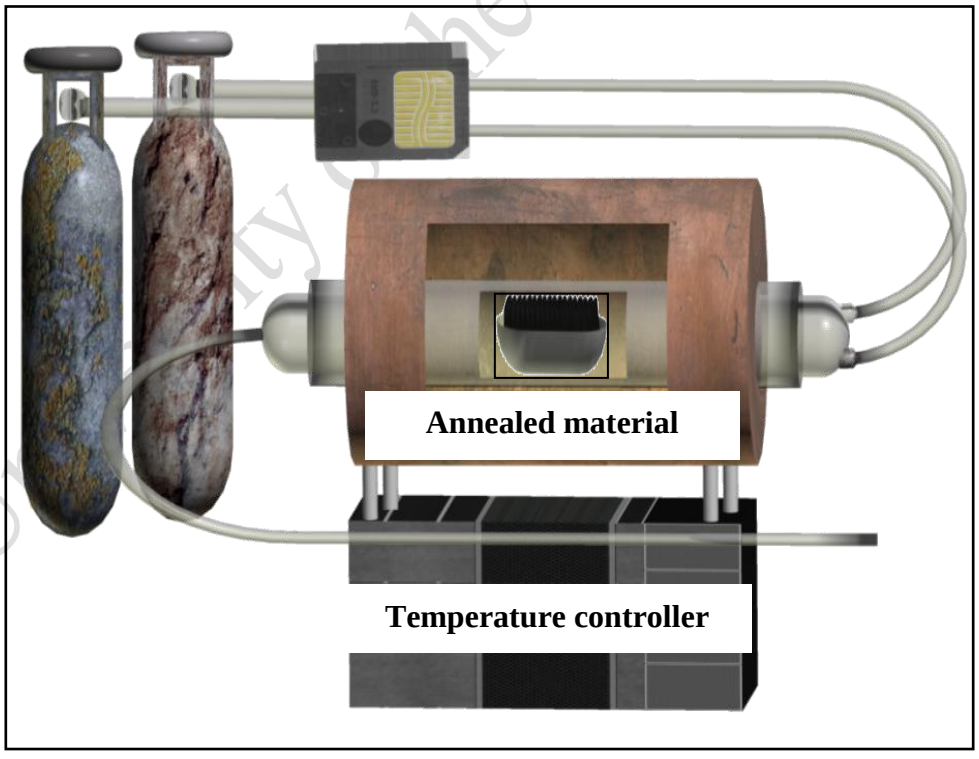

Figure 4. 22: Typical horizontal furnace used for chemical vapor deposition setup.

3.4. Catalyst evaluation

A Fischer-Tropsch synthesis reaction rig and the catalytic reactor are shown schematically below **[240, 241]**. Detailed description of the rig set-up and mass of catalyst used in catalytic testing are included in each individual result chapter.

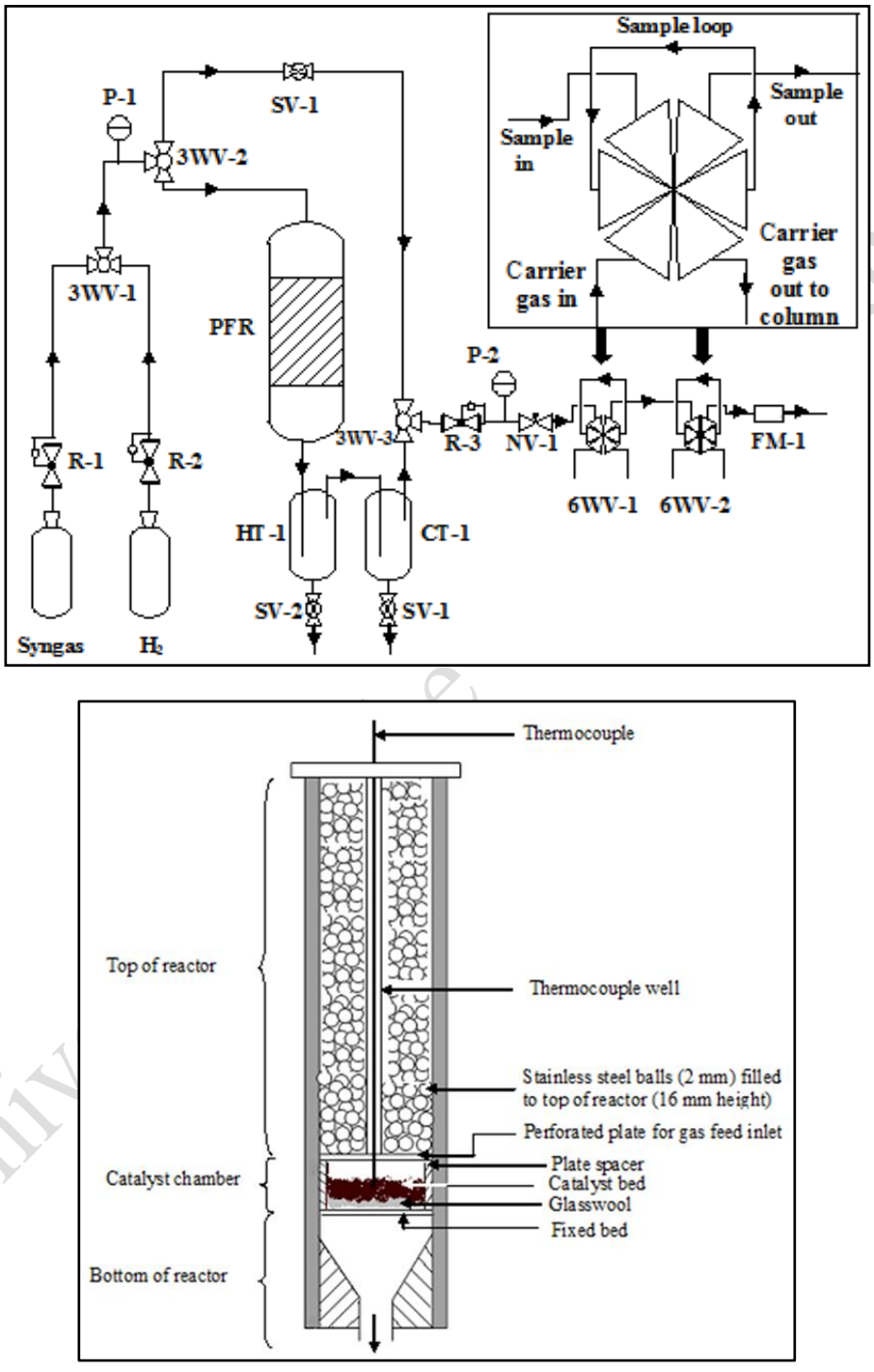

Figure 4. 23: Schematic representation of the rig and a fixed bed reactor setup.

3.5. Conditions for GC Analysis

Online gas chromatograph	
Detector	Thermal conductivity detector (TCD)
Column type	Packed, stainless steel, 2m x 2.2mm, O.D = 1/8"
Stationary phase	Carboxen-1000, 60-80 mesh
Model type	PYE Unicam (Series 204)
Detector temperature	220 ℃
Carrier gas	Argon
Online gas chromatograph	
Detector	Flame ionization detector (FID)
Column type	Packed, stainless steel, 1.5 m x 2.2 mm, O.D = 1/8"
Stationary phase	Porapack q, 80/100 mesh
Model type	Hewlett Packard 5890
Detector temperature	220 ℃
Carrier gas	Nitrogen
Offline gas chromatograph	
Detector	Flame ionization detector (FID)
Column type	30 m x 5 µFT, O.D.= 0.53 mm
Stationary phase	ZB-1
Model type	Varian 3700
Detector temperature	220 ℃
Carrier gas	Nitrogen

3.6. Equations for calculating catalyst activity and selectivity

The equations for evaluating Fischer-Tropsch catalysts performances using data obtained from the offline and online gas chromatographs. Detailed description of these calculations can be found in **[240, 241]**.

Table 4.1: Equation used in the FT calculations

Equation	Details
$\% \text{ CO} = \left[\frac{\text{N}_{\text{co,in}} - \text{N}_{\text{CO,out}} \text{ x Gas contraction}}{\text{N}_{\text{CO,in}}}\right] \text{x } 100$	% CO conversion equation
$\text{F}_{\text{in}} = \text{Gas contarction x F}_{\text{out}}$	The feed inlet flow rate to the reactor
$\text{N}_{\text{C,in}} = \text{F}_{\text{in}}.\text{t}.\text{X}_{\text{CO,in}}$	number of moles of carbon in the feed stream
$\text{N}_{\text{c,out}} = \left[\frac{\text{A}_{\text{C}}}{\text{A}_{\text{C,cal}}}\right].\text{X}_{\text{c,cal}}.\text{F}_{\text{out}}.\text{t}$	number of moles of product for each of the components present in the gas phase
$\text{X}_{\text{HC,i}} = \frac{\text{RF}_{\text{i}}.\text{A}_{\text{HC,i}}}{\text{A}_{\text{C}_2\text{,cal}}}.\text{X}_{\text{C}_2\text{,cal}}$	Hydrocarbon mole fractions, hydrocarbon product areas were corrected relative to C_2H_4 (olefins) and C_2H_6 (paraffins)
$S_i = \left[\frac{N_i}{r_{co}\ .\ t}\right] \times 100\ \%$	Product selectivity
$r_{FTS} = r_{CO} - r_{CO_2}$	Rate of reaction for FTS
$r_{WGS} = r_{CO_2}$	Rate of reaction for water gas shift WGS
$Olefin\ to\ paraffin\ ratio\ i\ = \frac{N_i^=}{N_i^= + N_i^-}$	Olefin to paraffin ratio
Activity = $r_{FTS}/\text{m}_{\text{Co}}$	FT activity

List of abbreviations used in the FT calculations	
$N_{co,in}$	mole fraction of CO in the inlet stream
$N_{co,out}$	mole fraction of CO in the outlet stream
Gas contraction	N_{in}/N_{out} (where N_{in} = the moles of nitrogen from bypass N_{out} = moles of nitrogen during reaction)
F_{in}	the total feed flow rate in mol/s
F_{out}	the reactor exit stream flow rate in mol/s.
$N_{C,in}$	moles of carbon in the feed
t	the total mass balance time
$X_{CO,\ in}$	mole fraction of CO in the feed gas.
A_c	the integrated peak area for component c
$A_{c,\ cal}$	the peak area for the component c in the calibration gas
$X_{c,cal}$	the mole fraction of component c in the calibration gas
RF i	response factor for carbon number *i*
$A_{HC,i}$	integrated peak area for a hydrocarbon with carbon number *i*
$A_{C_2,cal}$	peak area of the C_2 hydrocarbon in the calibration gas
$X_{C_2,cal}$	mole fraction of the C_2 hydrocarbon in the calibration gas
S_i	product selectivity for hydrocarbons
N_i	moles of hydrocarbon containing *i* carbon atoms
r_{co}	rate of CO conversion
r_{CO_2}	rate of carbon dioxide formation
$N_i^=$	moles of olefin containing *i* carbon atoms
N_i^-	moles of paraffin containing *i* carbon atoms

Chapter 5

Ruthenium nanoparticles encapsulated inside porous hollow carbon spheres: A novel catalyst for Fischer–Tropsch synthesis

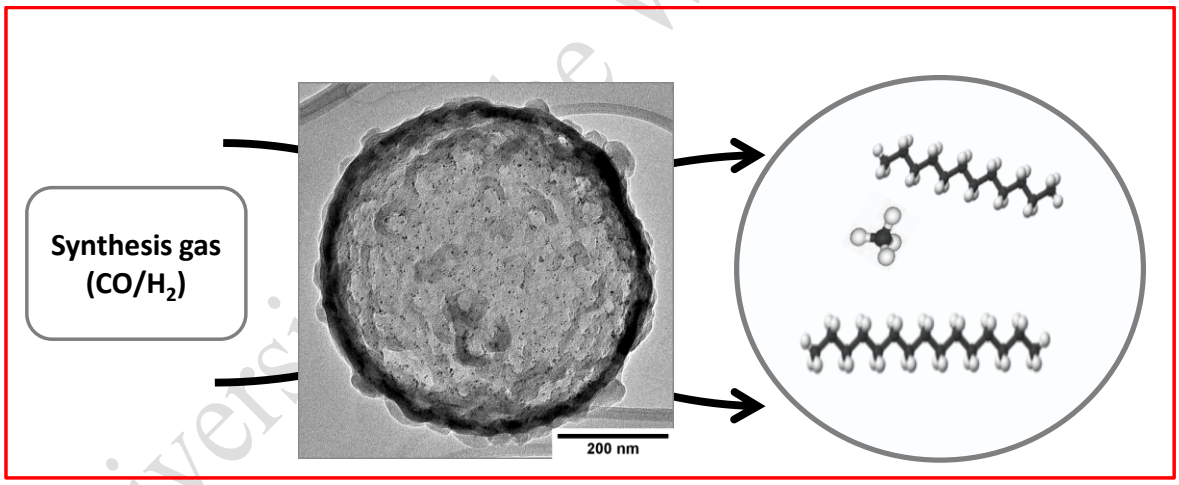

This chapter has been published as: Phaahlamohlaka, T. N., Kumi, D. O., Dlamini, M. W., Jewell, L. L., and Coville, N. J. (2016). Catalysis Today, 275, 76-83.

Supporting information: Appendix A

Abstract: Two novel Ru Fischer–Tropsch (FT) catalysts were made that were supported on the inside of two hollow carbon spheres that differed in terms of their shell porosity. Mesoporous Stöber spheres were made and Ru deposited on the silica. The Ru/silica spheres were encapsulated with carbon deposited by CVD (toluene) or from resorcinol/formaldehyde. Removal of the silica gave Ru@HCS (d_{Ru}= 5.5) and Ru@MHCS (3.2 nm) that had carbon shells (d = ca. 20 nm) with different physicochemical properties as evidenced by the TEM, nitrogen adsorption-desorption, TGA, Raman spectroscopy and XRD measurements. FT studies were performed on the two catalysts (10 bar; 190/220/250 ℃; 2/1 ratio H2/CO). Classical Fischer–Tropsch data was obtained indicating that the catalysts could access the reactants and that FT products could escape from the inside of the spheres (acting as a nanoreactor). Activity data indicated diffusion control of CO/H2into the nanoreactor and selectivity data indicated an alpha value of 0.74–0.78 (220 ℃). Typical product selectivity associated with small Ru particles was observed and the methane content increased with reaction temperature. No substantial Ru sintering occurred below 220 ℃. It is thus seen that the porosity of the two hollow carbon architectures is suitable for the FT polymerization reaction.

5.1. Introduction

Carbon monoxide hydrogenation reactions are an important set of reactions used extensively in the chemical and fuels industry. Two examples include: (i) the Fischer–Tropsch synthesis (FTS) in which carbon monoxide derived from natural gas, coal or biomass **[242, 243]** is converted into liquid hydrocarbons for energy generation and chemicals **[242, 244, 245]** and (ii) the selective methanation reaction used to purify hydrogen that contains CO, for use as a fuel in proton exchange membrane fuel cells **[244, 246].** Generally FT CO hydrogenation reactions have been performed on supported metal catalysts using metals such as Co, Fe, Ru and Ni **[10, 247, 248].** Even though Ru is not cheap relative to other metals, its unique catalytic properties, in particular its high activity in CO hydrogenation reactions and its good stability under different reactions conditions make it a valuable and useful CO hydrogenation catalyst **[249-251].** Most studies on the CO hydrogenation reaction using supported Ru catalysts have been performed on supports such as silica, alumina, titania and various shaped carbon materials **[252-255].** These supports are solid materials with the catalyst particles typically placed on the external support surface, or at best in the pores of the support as found in zeolites or mesoporous materials **[256, 257]**.Preparation and characterization of stable Ru nanoparticles embedded on ordered mesoporous carbon materials have also been applied in FTS **[258]**. In the last decade the possibility of making hollow supports with the metal placed inside the support has become possible **[259, 260]**.The support can then be considered as a nanoreactor **[160, 188, 261]**. Two types of carbon nanoreactors can be envisaged. These are (i) car-bon nanotubes (CNTs); various studies have shown metal particles placed inside CNTs have different catalytic properties to metals placed outside the CNT. The reactant access to the metal particles is determined by the diameter of the CNT (typically >3 nm) **[110, 262, 263]**, (ii) hollow carbon spheres (HCSs); in this case metal nanoparticles are placed inside hollow carbon spheres to form a core-shell or rattle type catalyst. Access to metals placed in these types of nanoreactors is determined by the porosity of the carbon shell which can be mesoporous (2–50 nm) or microporous (<2 nm) **[198, 264]**.The HCSs have emerged as a support material having potential for application as a nanoreactor in heterogeneous catalysis studies. This is because of the relative chemical inertness of carbon which minimizes the metal support interactions, hence allowing easier reducibility and increased metal catalytic activity **[265, 266]**.The compartmentalization of the metal nanoparticles can also limit sintering **[198, 264]**and lead to containment of fragmented catalyst particles **[267]**. The facile ability to control the HCS pore size distribution can be exploited to control access of reactants to metal active sites as well as removal of the products from the hollow core **[180, 187, 194, 200]**. This concept of performing catalytic reactions inside nanoreactors has been demonstrated **[264]** but to date, no reports on the applications of Ru@HCS for gas phase CO hydrogenation reactions (e.g. Fischer–Tropsch synthesis or selective methanation of CO) have been reported. Here we report on the synthesis of Ru@HCS that relies on a hard template method using monodisperse silica spheres as sacrificial templates, a procedure that has proven to be invaluable in the synthesis of hollow nanoreactors **[152, 176, 264]**. These

resulting Ru@HCS structures were tested for CO hydrogenation reactions under typical Fischer–Tropsch conditions. The objective was to determine whether these types of supports could be used in FT synthesis viz. (i) will the carbon shell porosity affect the catalyst activity/selectivity? (ii) Does sintering of the catalysts occur during the reaction? (iii) Can the carbon nanoreactor shell survive the FT catalytic reaction conditions?

5.2. Experimental procedure

5.2.1. Synthesis of modified Stöber spheres

The silica spheres were made by classical procedures using CTAB/TEOS (see Supplementary section **[162, 268]**.

5.2.2. Synthesis of 0.5% Ru/mSiO$_2$

Mesoporous silica spheres (mSiO$_2$; 4 g) were dispersed in 250 mL of deionized water by ultra-sonication. To this mixture was added 0.4 g of urea and 2 mL of 0.1 M $RuCl_3$ solution and the mixture was then sonicated for 30 minutes. Homogenous deposition precipitation of Ru was performed at 95 ℃ for 12 h. The product (ca. 0.5% loaded Ru/SiO2) was then collected by filtration, washed with deionized water and then dried at 100◦C overnight.

5.2.3. Synthesis of Ru@MHCS

Ru/mSiO$_2$ (2 g) and ammonia solution (25%; 1.5 mL) were dispersed in 100 mL of ethanol in a 250 mL beaker. Resorcinol (0.75 g), formaldehyde solution (37%; 1.5 mL), TEOS (1 mL) and CTAB (1 g)mixture in ethanol (50 mL), was added to the first solution and the total mixture then stirred at room temperature for 20 h to form the resorcinol–formaldehyde (RF) polymer around the silica spheres. The red product (Ru/mSiO$_2$@RF) was then collected by centrifugation (4000 rpm, 10 min), washed with acetone and dried at 100 ℃ for 2 h. Carbonization of the Ru/mSiO$_2$@RF was performed at 900 ℃ for 2 h under a flow of argon gas (25–30 mL.min^{-1}) in a horizontal furnace reactor. The silica was then removed by etching at ambient temperature with HF (5% in deionized water) to give Ru@MHCS.

5.2.4. Synthesis of Ru@HCS

The uncalcined Ru/mSiO$_2$ was placed inside a horizontal tube furnace which was heated to 900 ℃ at 10 ℃.min^{-1} under argon. When the desired temperature was reached the argon gas (100 mL.min^{-1}) was bubbled through toluene, at room temperature, for 2 h to coat the Ru/mSiO2composite with a carbon shell. HF solution (5%; 100 mL) was added to the carbon coated Ru/mSiO2 (to produce Ru/mSiO$_2$@C) and the silica template removed at room temperature over 12 h. The material was purified by centrifugation and repeated washing using deionized water and then dried at 100 ℃ to give Ru@HCS. The two catalysts (Ru@HCS and Ru@MHCS) were both heated at 250 ℃ under nitrogen gas at 30 mL.min^{-1} for 2 h prior to use and characterization.

5.2.5. Preparation of Ru supported on hollow carbon sphere catalysts

The $mSiO_2$ was prepared as described above and then coated by carbon using the procedures described in Section 5.2.3 and 5.2.4 (but without Ru) and the silica removed by HF to give MHCS and HCS. Ru/HCS and Ru/MHCS were then prepared by loading 5% Ru onto the hollow carbon spheres by classical homogenous deposition precipitation (see Supplementary section). The two catalysts (Ru/HCS and Ru/MHCS) were heated at 250 ℃ under nitrogen gas at 30 $mL.min^{-1}$ for 2 h prior to use and characterization. All characterization techniques used are reported in the Supplementary section (Supplementary section 5S.4)

5.3. Results and discussion

The general synthesis scheme used to make the Ru supported on hollow carbon spheres is shown in Figure 5.1. Two different car-bon sources were used to modify the surface porosity of the final nanoreactor, but otherwise both methods used similar protocols.

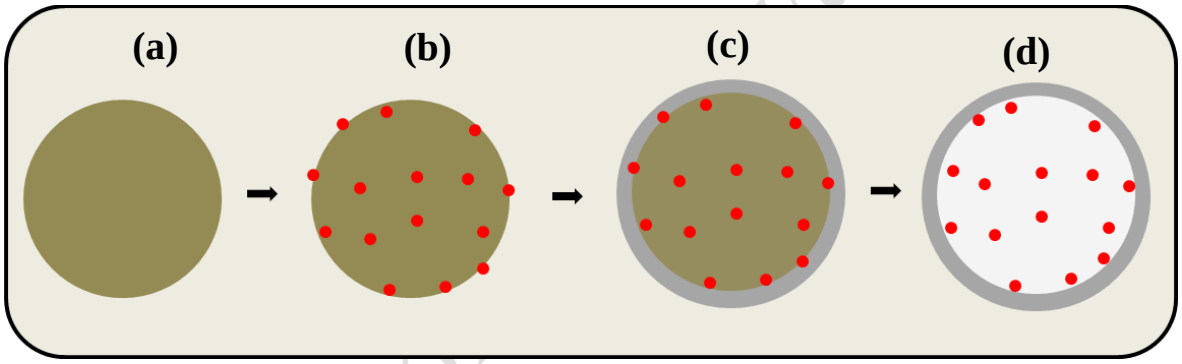

Figure 5. 1: General synthetic scheme for the synthesis of a Ru encapsulated nanoreactor. (a) mSiO2 (b) Ru/mSiO2 (c) Ru/mSiO2@C and (d) Ru@HCS or Ru@MHCS.

5.3.1. Silica spheres and hollow carbon spheres

The silica spheres were prepared by a modified Stöber method. The spheres were then covered by a mesoporous layer using CTAB/TEOS. The covered spheres revealed a uniform particle size (ca. 620 nm) and good dispersion typical of silica spheres prepared by the modified Stöber method **[162, 268]**. It is notable that the mesoporous silica layer on the spheres is uniformly distributed around the silica particle (Figure 5.2). Ru nanoparticles were then loaded on the silica spheres and the silica was then coated with carbon using two different methods. Removal of the silica from both samples gave the hollow carbon shells with different porosities and physicochemical properties which encapsulated the Ru particles. In the first case the silica spheres were completely covered by the resorcinol-formaldehyde polymer which was carbonized to form $Ru/mSiO_2@C$ as confirmed using SEM-EDS mapping (Figure 5S.1). The C Lα1 (densely blue) map clearly showed evidence of total coating by carbon, based on a

random sampling of individual silica spheres that had been coated with the carbon layer. In the second case the Ru/mSiO_2 was coated by carbon from a toluene source. A uniform coating was also observed for the composite consistent with other studies (Figure 5S.2) **[152, 200, 220]**.The hollow carbon spheres from both methods were obtained by etching the silica with HF (5% in water). The hollow morphology of these spheres is visible using transmission electron microscopy showing that the silica material had been removed (Figure 5.3). TGA analysis also confirmed the removal of the SiO_2 (Figure 5.4,b). EDS scans (Figure 5S.3 and 5S.4) of these hollow materials also confirmed that thorough washing of the carbon material after etching ensured that all the fluoride ions were removed. The Ru@MHCS carbon shell showed a shell thickness of 17.8 ± 3.4 nm while the carbon layer thickness for Ru@HCS was observed to be 19.1 ± 4.6 nm (Figure 5S.3,b and 5S.4,b).

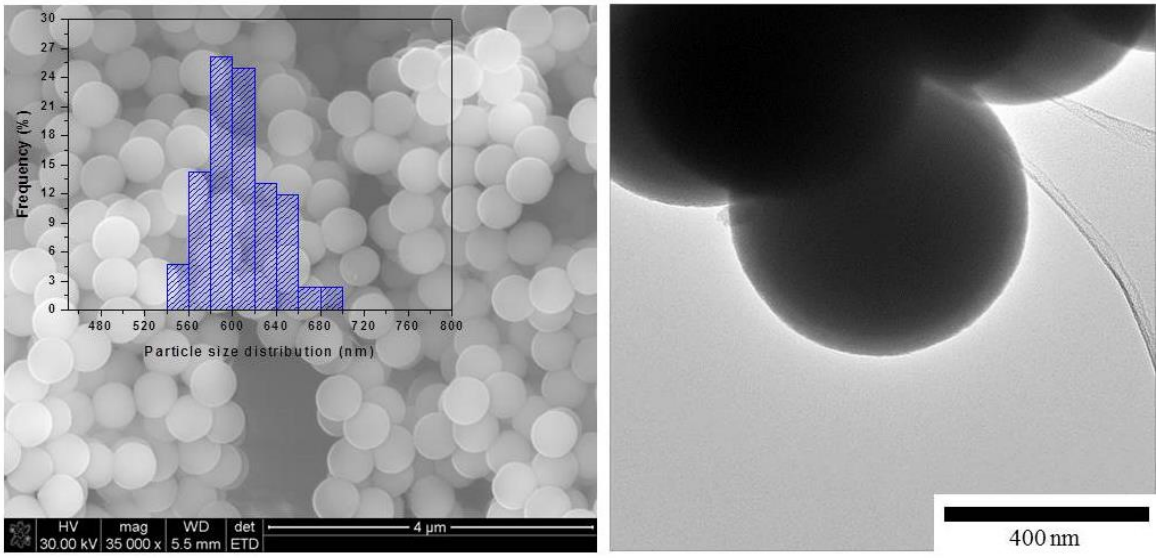

Figure 5. 2: TEM and SEM images and particle size distribution (PSD) of the mesoporous silica spheres.

5.3.2. Catalyst characterization

Metal catalyst dispersion

Figure 5.3 provides TEM images of the Ru catalysts prepared inside the two different hollow carbon spheres. The Ru nanoparticles are seen to be well dispersed inside the carbon shell. The Ru@MHCS dis-played metal nanoparticles in a narrow particle size range (2–6 nm) (Figure 5.3,c). It is however observed that direct carbon coating using toluene leads to particle sizes which are larger and have a wider size distribution (1–13 nm) due to sintering induced by the high temperature treatment of the catalysts in the CVD furnace during the introduction of the carbon source. The average particles size as determined from TEM images for Ru@MHCS and Ru@HCS were calculated to be 3.2 and 5.5 nm respectively (Figure 5.3,c,f).The active Ru particle sizes were estimated using H_2 pulse chemisorption using the metal dispersion of the particles inside the hollow carbon spheres (see Supplementary section). The Ru@MHCS catalyst displayed

a dispersion of 26.9%, while the Ru@HCS catalyst showed the corresponding Ru nanoclusters had a lower dispersion of 11.1% (Table 5.1).The computed active particle sizes were estimated at 4.9 and11.9 nm for Ru@MHCS and Ru@HCS respectively (Table 5.1) **[220, 269]**.The synthesis procedure to make these composites ensured that all Ru nanoparticles remained embedded on the inside walls of the nanoreactors as found by others **[160, 219, 261]**.A transmission electron microscopy tilting experiment was used to determine that the particles were indeed contained inside the hollow carbon spheres (see supplementary, Figure 5S.5). Sintering during reaction which is a common feature of unsupported catalysts should be limited to only those particles within a particular hollow carbon sphere **[186, 270, 271]**. SEM images were used to confirm the homogeneity and large scale coverage of the Ru nanoparticles by the carbon shell. EDX mapping of the samples (Figure 5S.3 and 5S.4) showed only the presence of Ru and carbon, confirming the purity of the samples.

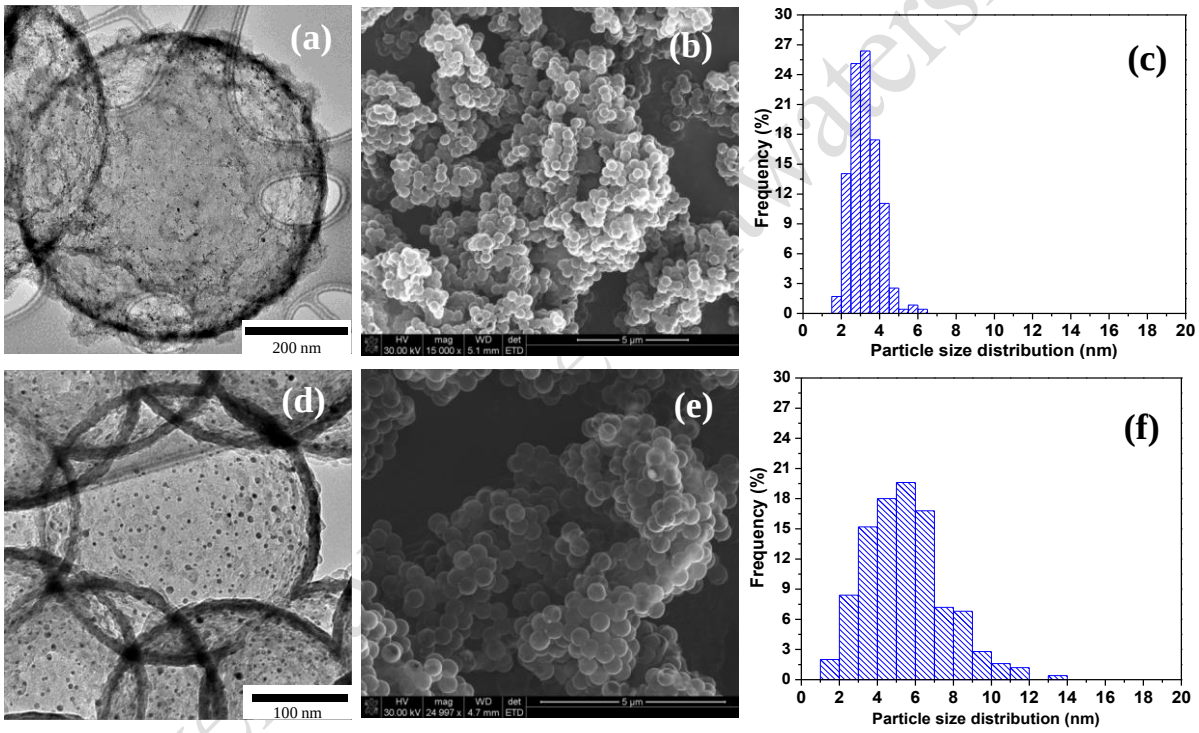

Figure 5. 3: TEM, SEM images and Ru particle size distribution (PSD) of (a,b,c) Ru@MHCS, and (d,e,f) Ru@HCS.

Table 5. 1: Ru content, particle size and pulse chemisorption data for the catalysts.

Sample	Ru dispersion (%)	Particles size (nm)			RuO_2 content (%) /TGA	Ru content (%)
		TEM	Chemisorption	XRD[a]		
Ru@MHCS	27	3.2 ± 0.7	4.9	-	3.22	2.44
Ru@HCS	12	5.5 ± 2	11.1	8.5	2.97	2.26
Ru/MHCS	48	1.8 ± 0.4	2.7	-	5.61	4.26
Ru/HCS	35	1.2 ± 0.3	3.7	-	5.06	3.84

[a]Estimated using the Scherrer equation (K = 0.9).

XRD and TGA analysis

XRD patterns of the Ru@MHCS catalyst (Figure 4,a), shows no notable diffraction pattern for Ru. The two broad peaks seen are due to the amorphous carbon shell; this shows that the carbon is highly defective. However, the Raman spectra (Figure 5S.6) show that the D and G bands of the carbon are readily detected indicating that the material has high sp^2 carbon content **[272, 273]**. This was also confirmed by Raman spectroscopy which showed a lower D-band to G-band ratio of 0.78, compared with Ru@HCS that has an I_D/I_G value of 0.88 hence showing the HCS shell had fewer defects relative to MHCS carbon shell. From the XRD patterns it was observed that the Ru is in a metallic hcp phase (ICSD Coll. Code: 54236, HCP crystal structure). TGA plots displayed in Figure 5.4,b showed that the Ru@HCS with a highly graphitic carbon shell was more thermally stable under air in comparison to the Ru@MHCS. The Ru@MHCS was completely decomposed by oxidation at temperatures in the range of 300–350 ℃ while that of the Ru@HCS decomposed above 400 ℃ (Figure 5S.7). This data thus validated the results observed in the pow-der XRD patterns which showed that the Ru@HCS had a carbon shell with better structural integrity. The TGA plots showed that both the hollow carbon spheres contained a RuO_2 loading of <3% (Table 1) **[274]**. It is assumed that all the SiO_2 has been removed by HF (see EDX data).

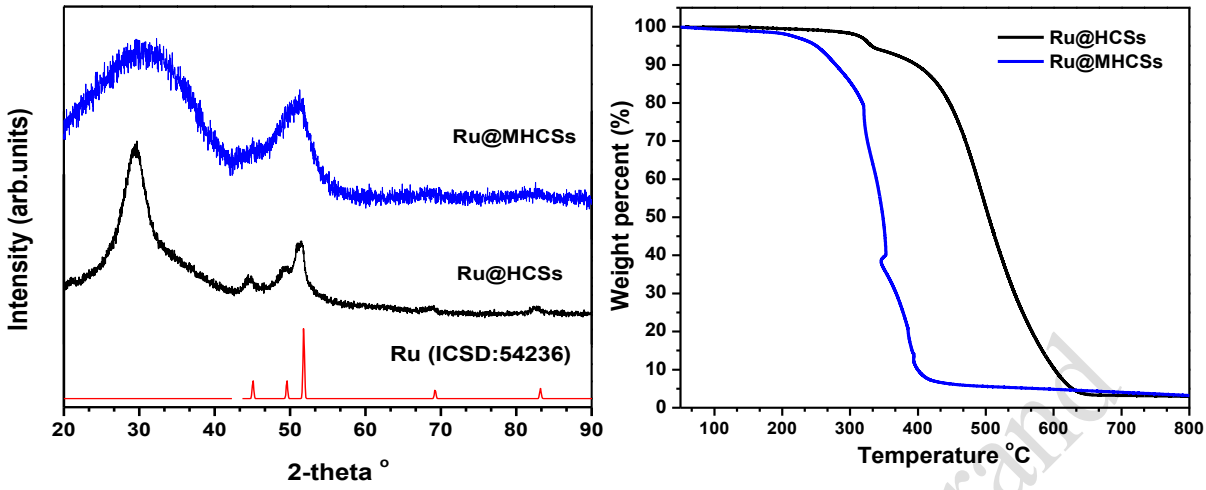

Figure 5. 4: (a) XRD patterns and (b) TGA profiles of the two prepared catalysts.

Nitrogen adsorption-desorption

Figure 5.5 displays the nitrogen adsorption and desorption analysis plots **[275]**. It is notable that Ru@HCS has a pore structure that is predominantly non-microporous and with a low pore volume. The Ru@MHCS displayed the presence of micro and mesopores and the micropore surface area for the catalyst Ru@MHCS was observed to be approximately 15% (135 $m^2.g^{-1}$) of the total BET surface area (Table 5S.1) **[194, 276]**. The Ru@MHCS displayed a high surface area of 944 $m^2.g^{-1}$ while the Ru@HCS had a lower BET surface area of 75 $m^2.g^{-1}$. The pore structures are consistent with studies proposing the use of a surfactant or a porogen during the synthesis procedure to generate mesoporous nanoreactors **[172, 198, 276]**. The porosity of the materials was not expected to be affected by the metal particles (see Table 5S.1 and Figure 5S.8).In summary: the Ru@MHCS and Ru@HCS show very different pore structures (and surface areas) (Table 5S.1).

Characterization data for Ru/HCS and Ru/MHCS

TEM images revealed a high dispersion of Ru nanoparticles on the hollow carbon spheres as evidenced by the particle size distribution, with Ru/HCS and Ru/MHCS having an average particle size of 1.2 and 1.8 nm respectively (Figure 5S.9).XRD data of the Ru supported on hollow carbon spheres showed no Ru diffraction peaks (Figure 5S.10) while TGA profiles were little affected by the Ru and revealed loadings of 3.84% for Ru/HCS and 4.26% for Ru/MHCS (Figure 5S.11). BET data (Table 5S.1) showed an increase in the specific surface area (SSA) of the Ru/HCS (102 $m^2.g^{-1}$) when compared to the plain HCS (82 $m^2.g^{-1}$). The increase suggests that the Ru nanoparticles do not block the pores. Ru/MHCS gave a surface area of 928 $m^2.g^{-1}$ with a reduced pore volume of 0.82 $cm^3.g^{-1}$ in relation to the MHCS (SSA = 941 $m^2.g^{-1}$ and pore volume =

2.05 $cm^3.g^{-1}$). It is envisaged that the Ru nanoparticles can block some of the pores and hence reduce the carbon shell's pore volume and surface area.

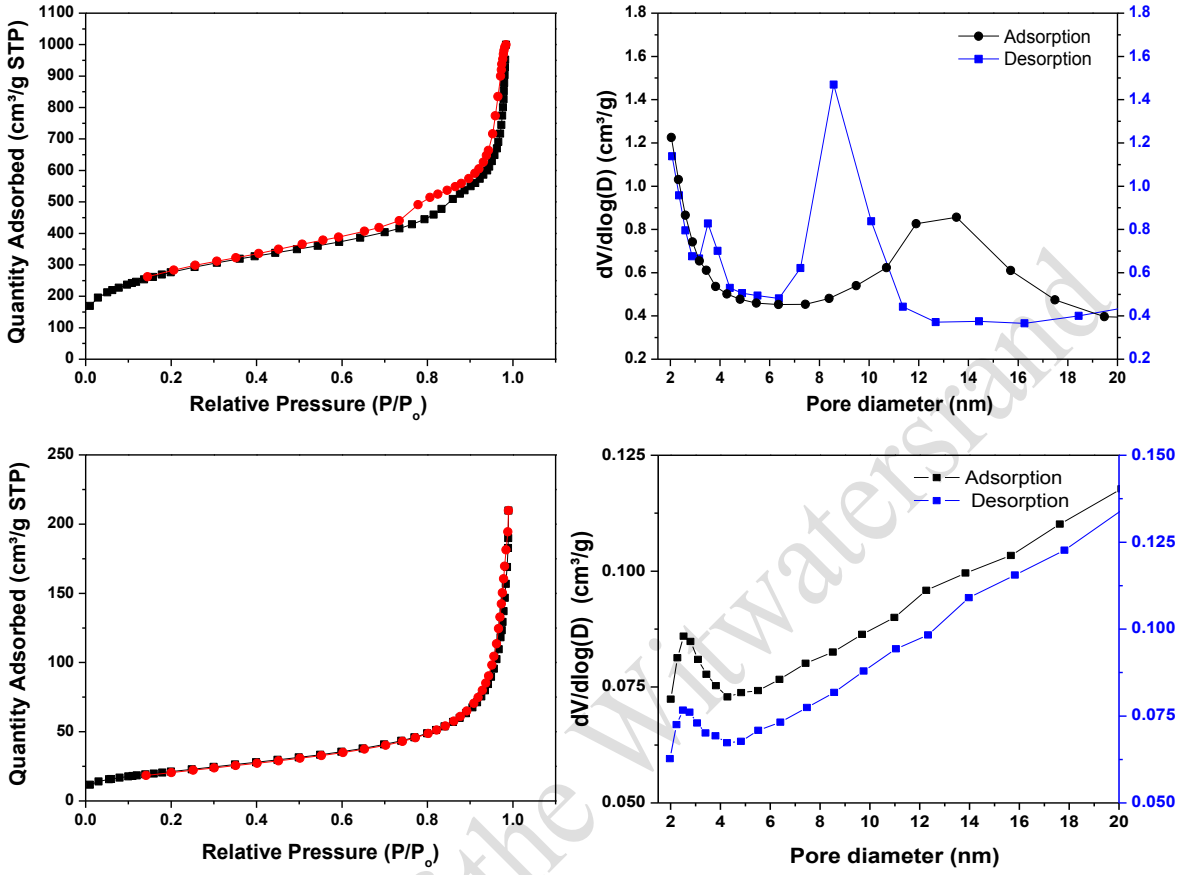

Figure 5. 5: N_2 adsorption/desorption isotherm and pore size distribution curves for, (a,b) Ru@MHCS, and (c,d) Ru@HCS.

5.3.3. Fischer–Tropsch evaluation

Fischer–Tropsch synthesis was performed using Ru supported on the outside of hollow carbon spheres (Ru/MHCS and Ru/HCS) to provide base line information for the study (see Figure 5S.12 and Table 5S.2). Both supports contained catalysts with similar Ru sizes (d = 1.8 and 1.2 nm). Very similar FT activity and selectivity data were obtained for both catalysts indicating that the porous nature of the supports did not impact significantly on the FT data. The FTS data also gave the expected trends with increasing temperature (190, 220 and 250 ℃). The Ru catalysts gave FT activity and selectivity data expected for small particles (Figure 5S.12 and Table 5S.2) such as high CH_4 selectivity that increased with temperature. While little is known about the effect of small Ru particles on FT reactions, a number of studies have appeared that have investigated the effect of larger particle sizes of Ru/supported catalysts (i.e. with the Ru on the surface of a solid support) on the activity/selectivity in the FT reaction and with conflicting results. In a recent publication, the Ru particle size (2.3-0.2 nm) using a 1:1 H_2:CO ratio (260 ℃) was seen (i) not to affect the % CO conversion, (ii) to change the TOF and (iii) to affect the selectivity **[277]**. Steady state isotopic transient kinetic

analysis (SSITKA) data on Ru/Al_2O_3 using an H_2:CO ratio of 10:1 (250 ℃) showed that the TOF for CO consumption also increased as the particle size increased (4-23 nm),reaching a constant value for Ru particles larger than 10 nm. The selectivity changed only marginally with particle size **[278]**. Gas diffusion effects are not expected to be important when Ru is placed on the external surface of a support. When Ru particles are placed inside and outside a CNT, the reducibility and also the activity of the Ru catalysts is different **[263]**.This confinement of the Ru particles affects the catalytic activity as a result of the Ru–C interaction that relates to the carbon curvature in the CNT. This effect is not expected to be seen for the large diameter carbon nanoreactors used in this study. In this study our focus was on whether the pore type/structure and carbon graphitic nature of a hollow carbon sphere would permit the FT reaction to occur as seen by catalyst conversion, activity and FT selectivity data. The FT activity/selectivity of the Ru@HCS and Ru@MHCS catalysts were then measured. The CO conversion with time on stream data for Ru@HCS and Ru@MHCS (ranging from 5 to 30%) are shown in Figure 5S.13 while the activity data are shown in Figure 5.6. It is evident that the Ru in the nanoreactor reacts with the CO and H_2 and that the porous structure allows the syngas to enter the nanoreactor. Thus both nanoreactors allow for reactants to enter the hollow cavities and the products including long chain hydrocarbons, to exit from the nanoreactor.

The Ru@MHCS displayed a higher CO conversion (Table 5.2, Figure 5S.13) and FT activity (Figure 5.6,a) than the Ru@HCS over the temperature range investigated (190, 220 and 250 ℃). The reason for the change in conversion and activity could be due to (i) differences in access of the reactant to the Ru particles, (ii) differences in removal of products from the nanoreactors or (iii) the different particle sizes of the nanoparticles. Increasing the reaction temperature of the catalysts during Fischer–Tropsch synthesis from 190 to 250 ℃ inevitably led to an increase in the Fischer–Tropsch activity of both catalysts: for Ru@MHCS from 3.19×10^{-5} to 5.5×10^{-5} and 9.5×10^{-5} $mol_{CO}.g_{Ru}^{-1}.s^{-1}$ and for Ru@HCS from 1.6×10^{-5} to 2.5×10^{-5} and 4.5×10^{-5} $mol_{CO}.g_{Ru}^{-1}.s^{-1}$ at 190, 220 and 250 ℃ respectively (See Figure 5.6,a).The TOF for the two catalysts (i.e. Ru inside the hollow car-bon spheres) at the three different temperatures was determined(Figure 5.6,b). Similar values for the two different sized catalysts (3-6 nm) were found in the range $6\text{-}23\times10^{-3}$ s^{-1}. The data can be compared with results found by others for Ru/CNT and Ru/Al_2O_3 where TOFs for particles in the 2–6 nm range were found to be 23–50 and $50–75\times10^{-3}$ s^{-1} (250-260 ℃) respectively **[254, 276]**. The values in this study (Ru inside spheres) are about 10 times lower than when the Ru particles are placed outside the supports reported above.

Table 5. 2: Fischer–Tropsch synthesis performance of Ru encapsulated catalysts.

Sample	Reaction Temperature (℃)	CO Conversion (%)	Selectivity (C mol) %			
			C_1	C_2-C_4	C_{5+}	α [a]
Ru@MHCS	190	11.9	10.3	3.9	85.6	-
	220	18.5	18.5	3.3	78.1	0.78
	250	27.8	41.5	2.3	56.3	0.60
Ru@HCS	190	6.9	5.7	5.0	89.3	-
	220	10.1	13.4	3.9	82.7	0.74
	250	17.6	34.9	2.9	62.1	0.67

[a]Based on liquid fraction analysis (C9–C19) using the ASF plot. Fischer–Tropsch reaction conditions: T = 190, 220 and 250 ℃ Psyngas = 10 bar, W/F = 15 g h mol^{-1}.

The values observed in this study were found to be larger than those found for the Ru catalysts placed on the external surface of the support in this study (0.5-3×10^{-3} s^{-1}, see Figure 5S.12). This can be explained by the small size of the Ru catalysts that were placed on the carbon external surface (< 2 nm) (Figure 5S.9). Several studies have shown that small nanosized FT particles have lower surface specific activity than larger particles due to the blockage of the particle surface atoms by CO irreversibly binding to these surface sites, and their low propensity to dissociate CO molecules **[84, 85]**. The observed TOF increase for the Ru supported outside the hollow car-bon spheres, is consistent with other studies which are known to change until the particles reach to a threshold size **[88, 277, 279]**. The Ru encapsulated inside the hollow carbon spheres showed unexpected results (Figure 5.7,b). Ru@HCS with the larger average particle size (5.5 nm) had a lower turnover frequency in relation to Ru@MHCS (3.2 nm). This would suggest that diffusion does impact on the reaction. For the Ru@HCS and Ru@MHCS either the Ru particle size and/or the carbon shell porosity are factors impacting on the FT reaction (CO conversion, activity). From BET analysis and nitrogen adsorption isotherms it was observed that the HCS had low porosity while the MHCS had a higher porosity and a larger surface area. The car-bon shell with the lower porosity either restricted access to the syngas or release of the products. As seen from selectivity data below it appears that the release of products is not the limiting process.

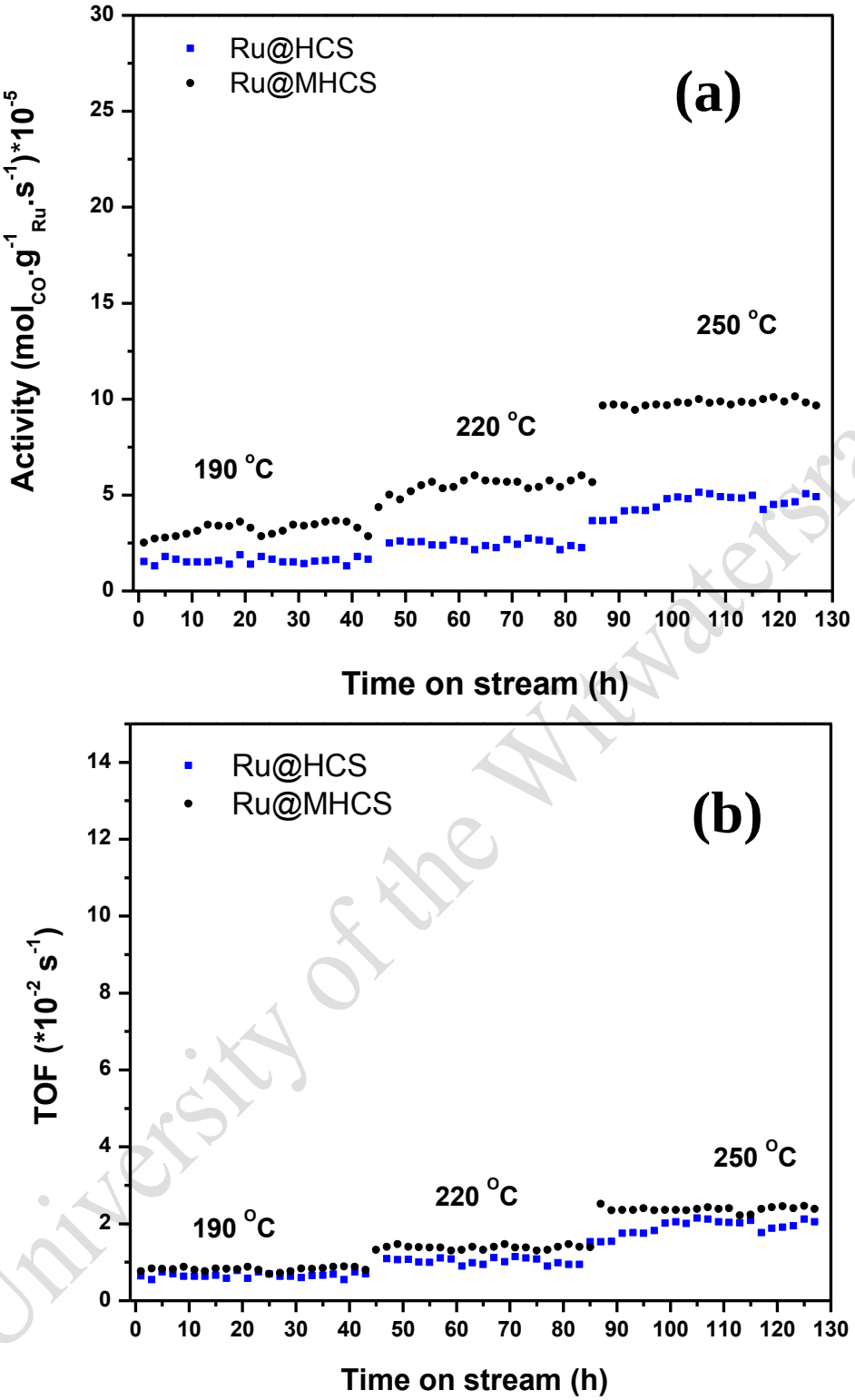

Figure 5. 6: (a) Activity and (b) TOF plots over 130 h TOS of the prepared catalysts at the different reaction temperatures.

Catalyst selectivities

It is well known that the selectivity of FT catalysts varies with CO conversion. This is shown by our own data for the CH_4 selectivity as a function of CO conversion (Figure

5S.14). Thus product selectivity comparisons were made for Ru@MHCS at 190 ℃ with Ru@HCS at 220 ℃ as they had almost similar CO conversions (11.9% and 10.1%). It will be seen that very similar selectivities are observed (Table 5.2).This suggests that the pores and pore structure of the two different hollow carbon sphere supports act similarly in restricting product release. This would indicate that the pore structures either holdup the products in a similar manner or more likely do not holdup the products nor influence the selectivities. Furthermore, the products formed in both catalysts show the typical effect of reaction temperature on the product selectivities (i.e. increased methane formation and decreased C_{5+} selectivity (Supplementary data Figure 5S.15).The product distribution from both the catalysts gave typical ASF plots. The alpha values for Ru@MHCS and Ru@HCS were 0.78 and 0.74 (for the liquid products) respectively at 220 ℃. This again indicates that product release is not held up in either nanoreactor. The catalysts also showed a typical low selectivity (ca. 3–5%) for C_2–C_4 hydrocarbons, this may be due the fact that Ru nanoparticles have high activity in the chemisorption and dissociation of carbon monoxide **[280, 281]**. There was then an abundance of carbon monomers on the catalyst surface that favored chain propagation of these low molecular weight products. The typical deviations of relatively high methane selectivity and a lower yield of C_2–C_4 hydrocarbons, than are predicted from the Anderson–Schulz–Flory (ASF) plot, are also consistent with a classical FT product distribution. It has also been reported that Ru particles and other Fischer–Tropsch metals (e.g. Co) supported on carbon materials tend to give higher methane selectivities at elevated Fischer–Tropsch temperatures in comparison with other catalyst carriers such as titania or ceria **[95, 113]**. Further, the unusually high CH_4 selectivities for Ru could be explained by the relative diffusion rates of H_2 and CO into the HCSs. The higher diffusion of H_2 would lead to a more hydrogenating environment, consistent with the selectivities of hydrocarbons observed. In summary: the two catalysts (Ru@HCS and Ru@MHCS) although showing different porous structures in terms of the carbon shell structure showed quite similar selectivity in terms of the FTS products formed. Most importantly the porosity of the carbon shell does not appear to limit formation and extraction of high molecular weight products from the HCSs that are produced in the FT reaction. The methane selectivity of the Ru/HCS and Ru/MHCS catalysts is large and consistent with small size of the Ru nanoparticles (Table 5S.2) [88, 277]. The methane content also increases, as expected, with temperature. The data for the Ru placed inside the spheres (Ru@HCS and Ru@MHCS) is shown in Figure 5S.15 and Table 5.2. The smaller Ru particles give the larger CH_4 production. Several studies have explained this phenomenon as a result of the lack of necessary ensembles that promote chain growth propagation of the inter-mediate surface methyl monomers thus favoring the termination step and their desorption as methane **[85, 87]**.

Post catalysis analysis

The carbon shell structural integrity was maintained after the FT reaction at 250 ℃, as shown by the TEM images of the spent catalysts (Figure 5S.16). This indicates that the HCSs are mechanically and chemically robust under the FT conditions even when the

carbon shell is thin. Possible sintering of the Ru nanoparticles during FT synthesis was also investigated by TEM analysis of the catalyst after reaction at 220 ℃. This sample was collected and studied after reaction at 190 ℃ (40 h) and 220 ℃ (40 h) (Figure 5S.17). Catalyst sintering was not noted as the particle sizes had not changed (average sizes of 5.8and 3.6 nm for Ru@HCS and Ru@MHCS after reaction). TEM analysis was also performed on both catalysts after reaction at 250◦C.Here it was observed that the particles did undergo agglomeration under the given reaction conditions. The average particle size for Ru@HMCS and Ru@HCS were now observed to be 6.9 nm and 9.7 nm (Figure 5S.16). For comparison the particle growth on the Ru nanoparticles supported on the surface of the carbon shell Ru/MHCS and Ru/HCS, was measured and also found to have increased to 3.7 and 3.2 respectively (Figure 5S.18).

5.3.4. Conclusions

We have demonstrated that ruthenium particles placed inside hollow carbon spheres can be used as catalysts for Fischer–Tropsch synthesis. The carbon shell allowed for access of reactants and products to/from the inside of the hollow carbon spheres. The porosity of the hollow carbon spheres was found to affect the activity and TOF of the encapsulated Ru nanoparticles. It appears that diffusion of CO and H_2 play a role in affecting the activity of the catalysts. The suitability of hollow carbon nanoreactors for high pressure reactions such as used in the Fischer–Tropsch process has been tested. It was found that the porous shell of the carbon is quite stable under the FT conditions and did not buckle of fracture during the process. The shell structure of the hollow carbon spheres remained intact after the Fischer–Tropsch synthesis. The Ru nanoparticles inside the hollow carbon spheres were accessible to the synthesis gas through the porous network of the carbon structures; this was verified by the calculated TOFs and product selectivities. The data indicate that the products can exit the nanoreactor and do not appear to be held up significantly in the reaction. Finally little sintering was observed when low temperature (< 220 ℃) reaction conditions are used. Hence, we have designed a hollow carbon nanoreactor capable of high catalytic activity. The porosity of the hollow carbon spheres was an important factor in determining the activity and TOF of the encapsulated Ru nanoparticles. It appears that diffusion of CO and H_2 play a role in affecting the activity of the catalysts.

Acknowledgements

This work was financially supported by the DST-NRF Centre of Excellence in Catalysis (c*change), and NRF innovation scholarship and the University of the Witwatersrand. We also wish to thank the Microscopy and Microanalysis Unit (MMU) at the University of the Witwatersrand for access to the TEM and SEM instruments.

Chapter 6

Effects of Co and Ru Intimacy in Fischer-Tropsch Catalysts Using Hollow Carbon Sphere Supports: Assessment of the Hydrogen Spillover Processes.

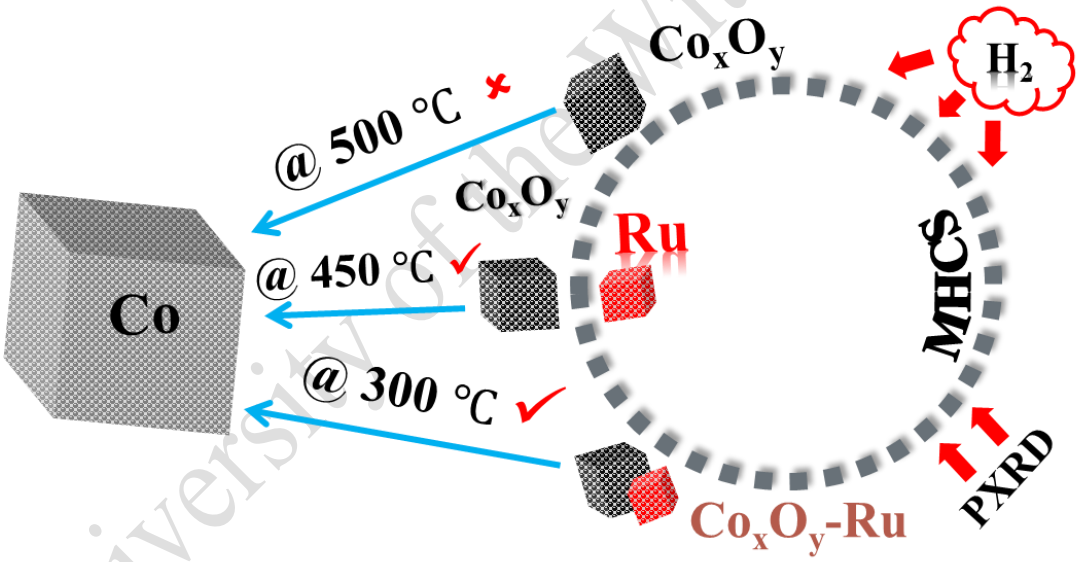

This chapter has been published as: Phaahlamohlaka, T. N., Kumi, D. O., Dlamini, M. W., Forbes, R., Jewell, L. L., Billing, D. G., & Coville, N. J. (2017) ACS Catalysis 7 (3), 1568-1578.

Supporting information: Appendix B

Abstract: Mesoporous hollow carbon spheres (MHCSs) were synthesized (d = 290 nm; carbon shell 20−35 nm), and their hollow morphology was exploited to study the influence of Ru nanoparticle location relative to Co3O4 nanoparticles on the reduction behavior and activity of Co Fischer−Tropsch catalysts. Ru nanoparticles were loaded both inside and outside the MHCS, while Co_3O_4 particles (ca. Co 15 wt % loading) were loaded on the outside of the MHCS. The use of in situ powder X-ray diffraction (PXRD) and temperature-programmed reduction studies on the catalysts indicated the effect of Ru location on the Co_3O_4 reduction pathways. A secondary hydrogen spillover effect was invoked to explain a complete reduction of the Co_3O_4 on Ru@MHCS@Co at 450 ℃. Secondary hydrogen spillover enhanced the CoO to Co transformation by lowering the reduction temperature when compared to the unpromoted catalyst. Primary hydrogen spillover was inferred to explain the complete reduction of Co_3O_4 to Co metal on CoRu/MHCS at 300 ℃. After catalyst activation at 350 ℃, the primary spillover process yielded a catalyst with higher Fischer−Tropsch activity (ca. 2×) than the unpromoted catalyst and the catalysts where Ru and Co were separated by the mesoporous carbon shell. This was partially related to the Co phases that formed on the carbon support during reduction and the catalyst degree of reduction that was reliant on the type of hydrogen spillover process.

6.1. Introduction

Cobalt Fischer-Tropsch synthesis (FTS) catalysts are generally promoted with metals such as ruthenium, platinum, and rhenium in order to enhance the catalytic activity of the cobalt active sites **[92, 99, 137]**. This is believed to occur by a promotion effect in which the added metal assists in lowering the reduction temperatures of the cobalt oxide. The promoter metals are able to dissociate hydrogen gas at lower temperatures and thus lower the reduction temperature of cobalt oxide nanoparticles in comparison to unpromoted catalysts **[20, 131, 282, 283]**. The reducibility of cobalt oxide particles is especially lowered if oxidic supports such as titania and alumina are used. This is due to the increased metal−support interaction (MSI) that makes reduction of the Co_xO_y more difficult, hence the need for reduction promoters **[92, 93]**. These reduction promoters can be classified as electronic promoters since they affect the electronic structure of cobalt particles and they in turn have a significant bearing on the overall cobalt catalytic activity and selectivity **[274]**. The promotion effects, as in many catalytic systems, are dependent on the intimacy (proximity) of the different catalyst components. A case in point is the use of bifunctional catalysts for the hydrocracking of long chain hydrocarbons where the location of the acid and metal sites play a crucial role in the reaction **[284]**. In promoted Co catalysts, the cobalt oxide crystallites can be in direct or indirect contact with a promoter **[136]**, hence several mechanisms to explain the promotion effect of noble metals on the cobalt oxide particles have been proposed **[127, 137]**. One of these involves hydrogen spillover in which a noble metal not only serves as a reduction promoter for the metal oxide (i.e., cobalt oxide) but also plays a role in the reaction selectivity **[131, 283]**. Two types of hydrogen spillover processes can be envisaged (see Scheme 6.1): (1) a primary hydrogen spillover, whereby the promoter (i.e., initiator) is in contact with the cobalt oxide (i.e., acceptor) and dissociated hydrogen atoms can move from the initiator directly to the acceptor, and (2) a secondary hydrogen spillover, in which the initiator and the acceptor materials are separated by some distance and migration of the atomic hydrogen occurs from the initiator to the acceptor via a carrier (or catalyst support) **[23, 127, 135]**. Hydrogen spillover on Fischer−Tropsch catalysts has been typically studied using hybrid catalysts composed of a mechanical mixture of the supported initiator and acceptor **[131, 283, 285]**. The hydrogen spillover and the mobility of the spilled-over hydrogen have been suggested to occur over long distances (up to several millimetres). The effects of such long-range migration of hydrogen may be very small and may not be revealed in Fischer−Tropsch reactions **[131]**. Hydrogen spillover studies involving Co Fischer−Tropsch catalysts have generally been performed on oxidic supports and were observed to offer a limited hydrogen spillover effect over long hydrogen transfer distances. A literature survey by Prins suggests that, in principle, hydrogen spillover on defective materials such as carbon nanomaterials is viable **[23]**. This is because hydrogen can be chemically adsorbed on the carbon defect sites, which are generally present on non-graphitic carbons. As with oxidic carriers heteroatoms such as oxygen

or nitrogen also enhance the ability of carbon materials to facilitate surface diffusion of activated hydrogen species and thus allow secondary hydrogen spillover processes.

Hydrogen spillover studies using noble metals and coinage metals supported on several carbon materials have been reported in numerous studies, either for hydrogen storage or in catalytic reactions **[136, 137, 286]**. Chung and co-workers **[287]**, observed an enhanced hydrogen spillover effect on an oxidized Pd/AC (AC, activated carbon) at room temperature (low and high pressures) with Pd serving as the activator. This effect was also attributed to the presence of oxygen functional groups found on the carbon material, which are thought to facilitate the mobility of the spilled-over hydrogen atoms over long distances. Lueking and Yang **[288]**, invoked hydrogen spillover to explain the ability of multiwalled carbon nanotubes (MWCNTs) containing residual Ni particles to store significantly more hydrogen (0.65%) than MWCNTs, which had all the Ni removed by hot acid reflux at 200 ℃. Their study also suggested that metal−support interactions were important for the spillover process to occur because dry mixing of the MWCNTs and the catalyst did not improve hydrogen spillover. Mesoporous hollow carbon spheres (MHCSs) with their hollow morphology and defective carbon structure could be used to study the extent of hydrogen spillover influence on Ru promoted Co Fischer−Tropsch catalysts. In mesoporous hollow carbon spheres, the pores radiate from inside the cavity through the carbon shell to the outer surface of the MHCS providing easy access for small molecules (e.g., H_2 and CO). Thus, loading of initiator and acceptor metals (i.e., ruthenium and cobalt oxide) inside and outside a defective, porous carbon shell could allow for a study of spillover to delineate the effects of the primary and secondary hydrogen spillover processes **[217, 289]**.
We have chosen to investigate the well-known Ru promoted Co reaction to study the hydrogen spillover effect on MHCS supports. In earlier studies, hydrogen spillover processes have been invoked to explain promoter effects in Ru/Co systems **[290, 291]**. An in situ XAS (X-ray absorption spectroscopy) study by Hong et al. **[274]**, suggested that Ru(IV) ions implanted inside a Co_3O_4 nanoparticle lattice served as a promoter for Co_3O_4 reduction at low temperatures. However, in other studies it has been proposed that Ru nanoparticles, not the ions, were required to be in close proximity to the cobalt oxide particles to effect Ru promotion on Co_3O_4 **[292]**. Recently Sapunov and co-workers **[293]**, reported spillover of hydrogen from Ru nanoparticles supported on hyper-cross-linked polystyrene to explain and elucidate the kinetics of the D-glucose hydrogenation process.

In this study, hydrogen spillover effects on Co Fischer− Tropsch catalysts using MHCS as a physical barrier, where the initiator (Ru) was loaded inside and outside the MHCS while the acceptor (Co_3O_4) was loaded onto the MHCS (with and without Ru), were investigated. The use of two catalysts, CoRu/MHCS and Ru@MHCS@Co (see Scheme 6S.1 for nomenclature used), made possible a separation of primary and secondary spillover processes.

Scheme 6. 1: Hydrogen Spillover Pathways, (a) Primary and (b) Secondary[a]

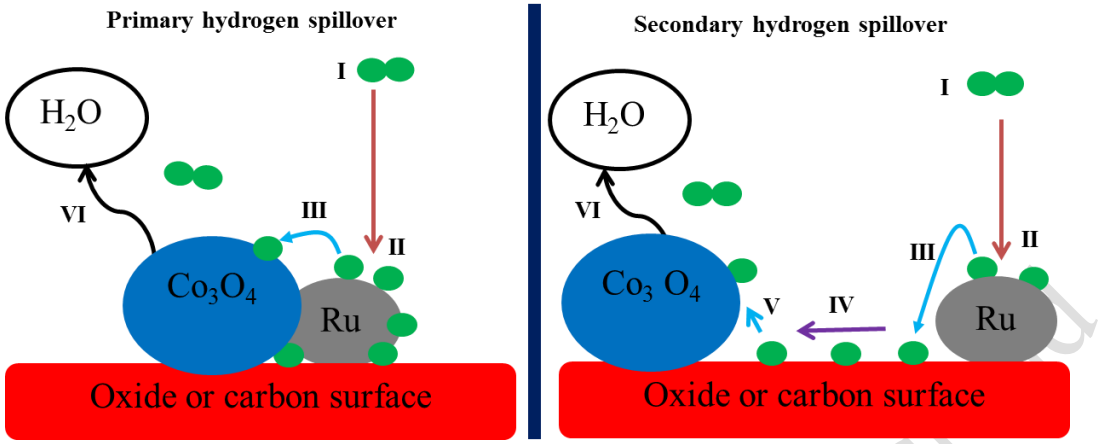

[a]I, Molecular hydrogen; II, dissociative adsorption; III, spillover; IV, hydrogen atom surface migration; V, spillover; VI, reduction and water removal. Adapted from refs **[127]** and **[23]**.

6.2. Experimental section

6.2.1. Sources of chemicals

Tetraethylorthosilicate (TEOS 98%; Aldrich), cobalt nitrate hexahydrate (Aldrich), octadecyltrimethoxysilane (C18TMS; Aldrich), ammonia solution (25%; Fluka), hexadecyltrimethylammonium bromide (CTAB; Aldrich), ruthenium chloride (Aldrich), urea (Promark chemicals), ethanol (98%; Merck), toluene (Merck), HF (40%; Associated chemicals), and nitric acid (55%; Merck) were used as received. Deionized water was used in the experiments.

6.2.2. Synthesis of modified Stöber spheres

Silica spheres were made by adding 50 mL of ammonia solution into a solution of water and ethanol (100 and 800 mL, respectively) **[217, 268]**. This solution was then stirred at room temperature for 10 min. To this solution was slowly added 75 mL of TEOS, and the mixture was stirred for 6 h to form monodisperse Stöber spheres. CTAB (25 g) and TEOS (12.5 mL) in 250 mL of ethanol were then added into the solution containing the Stöber spheres. A thin silica shell formed on the silica to generate a slightly porous silica composite material (SiO_2) while stirring the solution overnight (12 h) at room temperature. The SiO_2 spheres were then harvested by filtration and dried at 100 ℃ for 4 h. This was followed by calcination of the material in air at 500 ℃ for 4 h. This gave a silica yield of approximately 20 g with > 90% yield based on the amount of TEOS used.

6.2.3. Synthesis of 0.2 and 0.5% Ru/SiO_2

Silica spheres (SiO_2; 4 g) prepared above were dispersed in 250 mL of deionized water by ultrasonication. To this mixture was added 0.2 g of urea and 0.8 or 2 mL of 0.1 M $RuCl_3$ solution; the mixture was then sonicated for 30 min. Homogenous deposition precipitation of Ru was performed at 95 ℃ for 12 h. The product (ca. 0.2% or 0.5% loaded Ru/SiO_2) was then collected by filtration, washed with deionized water, and then dried at 100 ℃ overnight.

6.2.4. Synthesis of Ru/SiO_2@mSiO_2 and SiO_2@mSiO_2

The Ru/SiO_2 or SiO_2 (4 g) was dispersed in a water−ethanol solution (50 and 150 mL, respectively) followed by the addition of ammonia solution (3 mL). The mixed solution was then sonicated for 10 min. To this solution was added a mixture of TEOS (5 mL) and C18TMS (1 mL), and the mixture was left stirring for 5 h at room temperature to form a
mesoporous silica shell around the SiO2 or Ru/SiO_2 composites. The resulting product was then collected by filtration, washed with water, and dried at 100 ℃ for 2 h, followed by calcination in static air at 550 ℃ for 4 h.

6.2.5. Synthesis of Ru@MHCS or MHCS

The Ru/SiO_2@mSiO_2 (0.2 or 0.5%) or SiO_2@mSiO_2 was placed in a quartz boat inside a horizontal tube furnace, which was heated to 900 ℃ at 10 ℃/min under argon gas (100 mL min^{-1}). When the desired temperature was reached, argon was bubbled through toluene for 2 h to coat the Ru/ SiO_2@mSiO_2 or SiO_2@mSiO_2 composite with a carbon shell. HF (10%; 100 mL) was added to the carbon coated Ru/SiO_2@mSiO_2 or SiO_2@mSiO_2 to remove the template over 12 h. The HF solution was then decanted followed by purification by centrifugation and repeated washing using deionized water followed by drying at 100 ℃ to give samples that were called 0.2% Ru@MHCS, 0.5% Ru@ MHCS, or MHCS.

6.2.6. Catalyst Preparation: Loading of Co Nanoparticles

Cobalt nanoparticles were loaded onto the Ru@MHCS or MHCS using incipient wetness impregnation. $Co(NO_3)_2 \cdot 6H_2O$ (0.741 g) was dissolved in an appropriate volume of 50:50 water and ethanol solvent mixture, and this solution was then impregnated on the carbon support (MHCS or Ru@MHCS; 1 g) and then dried at 40 ℃ for 12 ,h. The catalyst was then heated under a flow of nitrogen gas (20 mL.min^{-1}) at 100 ℃ for 2 h followed by further heating at 300 ℃ for 2 h. To make sure that all the Co was converted to the Co_3O_4 phase, the catalysts were calcined at 210 ℃ for 2 h under a flow of 5% O_2/Ar gas mixture. The resulting cobalt loading was expected to be 15%. Three catalysts were prepared: Co/MHCS, 0.2% Ru@MHCS@Co (low Ru loading), and 0.5% Ru@MHCS@Co (high Ru loading). A fourth catalyst was made by

adding a Co solution mixed with a Ru solution to give a Co loading of 15% and Ru loading of 0.7%; this was called CoRu/MHCS.

6.2.7. Material characterization

TEM analysis was performed on a Tecnai spirit (T12) transmission electron microscope operating at 120 kV. The samples were dispersed in methanol by ultrasonication and loaded onto a copper grid for TEM analysis. The particle size distribution of the materials formed was determined by counting at least 200 randomly selected particles per sample from different TEM images. Gaussian statistics yielded values for the average particle sizes. SEM analysis was performed on a FEI Nova Nanolab 600 FIB/SEM instrument operating at 30 kV. The samples on a carbon tape were coated with a gold−palladium layer before the analysis. EPMA (electron probe microanalysis) was performed using a CAMECA SX5- FE EPMA, equipped with 5 wavelength dispersive X-ray spectroscopy (WDS) detectors and 12 crystals to select X-ray wavelengths for specific elemental compositions. C, Ru, and Co were mapped during the MD process. Elemental mapping was done using a FEG-SEM (CAMECA), a component of the EPMA instrument. The bulk composition of the catalysts was analyzed using a Bruker D2 phaser equipped with a Lynxeye detector, using a Co−Kα (λ = 0.17889 nm) at 30 kV. The scan ranged from 10° to 90° 2θ in 0.0260° steps. TGA was performed with a Perkin-Elmer STA6000 TGA using high purity nitrogen or air as the purge gas and a heating rate of 10 ℃.min^{-1}. The flow rate of the purge gas was always kept at 20 mL.min^{-1}. N_2 adsorption−desorption experiments were conducted at -195 ℃ using a Micromeritics Tristar 3000 surface area and porosity analyzer. Prior to an experiment, the sample was outgassed at 150 °C for 4 h under nitrogen gas. The BET surface areas were obtained from adsorption data in a relative pressure range from 0.05 to 0.30. The total pore volumes were calculated from the amount of N_2 vapor adsorbed at a relative pressure of 0.99. The pore size distributions were evaluated from the desorption branches of the isotherms using the Barrett−Joyner−Halenda (BJH) method. The micropore surface area and volume were calculated using t-plot data. TPR experiments were
carried out with a Micromeritics Auto Chem II unit. The catalyst (approximately 50 mg) was placed in a quartz tubular reactor, fitted with a thermocouple for continuous temperature measurement. The reactor was heated in a furnace. Prior to the temperature-programmed reduction measurement, the calcined catalysts were flushed with high purity argon at 200 ℃ for 30 min, to remove water or impurities, followed by cooling to ambient temperature. Then, 5% H_2/Ar was switched on, and the temperature was raised at a rate of 10 ℃.min^{-1} from 50 to 850 ℃. The gas flow rate through the reactor was
controlled by three Brooks mass flow controllers and was always 50 mL.min^{-1}. The H_2 consumption (TCD signal) was recorded automatically by a computer. Pulse chemisorption was performed using the Micromeritics Auto Chem II instrument, to compute the number of active sites on the catalysts. The catalyst (ca. 100 mg) was placed in a quartz tubular reactor. The sample was reduced at 350 ℃ for 2 h under a

hydrogen flow of 50 mL.min^{-1}. Before injection of the active gas, the sample was purged using helium gas at 350 °C for 1 h, followed by cooling to ambient conditions. Hydrogen chemisorption (assuming a H_2/Co ratio of 2) was then performed at 150 ℃ using ultrapure hydrogen as the active gas and argon as the carrier gas. O_2 titration was performed using a Micromeritics ASAP 2020 unit after catalyst reduction using high purity hydrogen (50 mL.min^{-1}) at 350 ℃ for 2 h. The samples were cooled to 200 ℃ and then re-oxidized by injecting pulses of high purity oxygen at 200 °C. The extent of reduction was calculated by assuming Co metal was completely converted to Co_3O_4. In-situ PXRD experiments were performed under 5% H2/N2 on a
Bruker D8 Advance fitted with an Anton Paar XRK 900 in situ cell. The diffractometer used a sealed copper tube as the X-ray source operating at 40 kV and 40 mA that provided X-rays with a wavelength of 0.15418 nm in a parallel beam geometry. The Rietveld refinement method was used to analyze the PXRD profiles (fresh and spent catalysts) as described in the Supporting Information (section S1). The Co loading on the MHCS was analyzed using an ICP-OES End on Plasma from Spectro Genesis (Kleve, Germany). A catalyst sample (50 mg) was dispersed in a solution of 5 mL of 55% nitric acid and 40 mL of water to dissolve the Co nanoparticles before analysis.

6.2.8. Evaluation of Fischer−Tropsch Performance

The Fischer−Tropsch synthesis was performed in a fixed-bed microreactor. A gas cylinder containing a H_2/CO/N_2 mixture (~60/30/10 vol %; purity 99.99) was used to supply the reactant gas stream to the catalyst with a specific space velocity of 1800 mL.h^{-1}.g^{-1}. N_2 was used as an internal standard in order to ensure accurate mass balances. Catalyst (0.5 g, sieved through a 150 μm mesh, without pelletizing) was added to the reactor (resulting catalyst bed ~4 cm in length) and reduced in situ at 350 °C for 2 h under a stream of H_2 (1.5 bar at 50 mL.min^{-1}). After reduction, the reactor temperature was decreased to ambient temperature under a hydrogen flow and then heated up to 220 ℃ under synthesis gas at a pressure of 10 bar. A hot trap placed immediately after the reactor was held at 150 °C in order to collect wax. A second trap kept at ambient temperature was used to collect the oil and water mixture. All gas lines after the reactor were kept at 100 °C. The flow was controlled using a metering valve and measured by a bubble meter. The product stream was analyzed online using two gas chromatographs. A thermal conductivity detector (TCD), equipped with a Porapak Q (1.50 m × 3 mm) packed column, was used to analyze H_2, N_2, and CO, and a flame ionization detector (FID), equipped with a Porapak Q packed column, was used for the analysis of the hydrocarbons online. Gas chromatography calibration and product analysis have been described elsewhere (see Chapter 3) **[240]**.

6.3. Results and discussion

6.3.1. Catalyst Preparation and Dispersion

Hollow carbon spheres with a mesoporous structure were prepared with good uniformity by a standard procedure (Figure 6S.1) **[198, 217]**. Ru nanoparticles were placed inside the hollow carbon spheres using a modified method, which was reported in an earlier study **[217]**. It was important to make a porous carbon shell with short dimensions so as to make sure that the spilled-over hydrogen has a short length to travel on the carbon materials. Hence, the hollow carbon spheres had an average particle diameter of 290 nm (Figure 6S.2) and a carbon shell thickness between 20 and 35 nm (Figure 6S.1). SEM analysis of the hollow carbon spheres confirmed their circular morphology and showed that the majority (> 90%) of the MHCS remained intact and were not broken (Figure 6S.1,c) **[198, 204]**. The results presented in Figure 6S.1 confirm that both the empty hollow carbon spheres and the hollow carbon spheres containing the Ru nanoparticles inside the spheres have been successfully synthesized. The encapsulation of the Ru nanoparticles allowed for physical separation of the Ru from the Co by a layer of mesoporous carbon, making the study of hydrogen spillover effects possible. Loading of Co nanoparticles (~15%) on both the MHCS and Ru@MHCS was performed by incipient wetness impregnation (IWI) (Figure 6.1). The Co particle size distributions were obtained from the samples after pre-treatment in nitrogen and 5% O_2/Ar, and they correspond to the cobalt oxide phase (Co3O4). The particle size distribution of the Co_3O_4 nanoparticles for all the catalysts prepared by IWI were in the range of 5−6 nm as determined by transmission electron microscopy analysis (Figure 6.1 and Table 6.1).

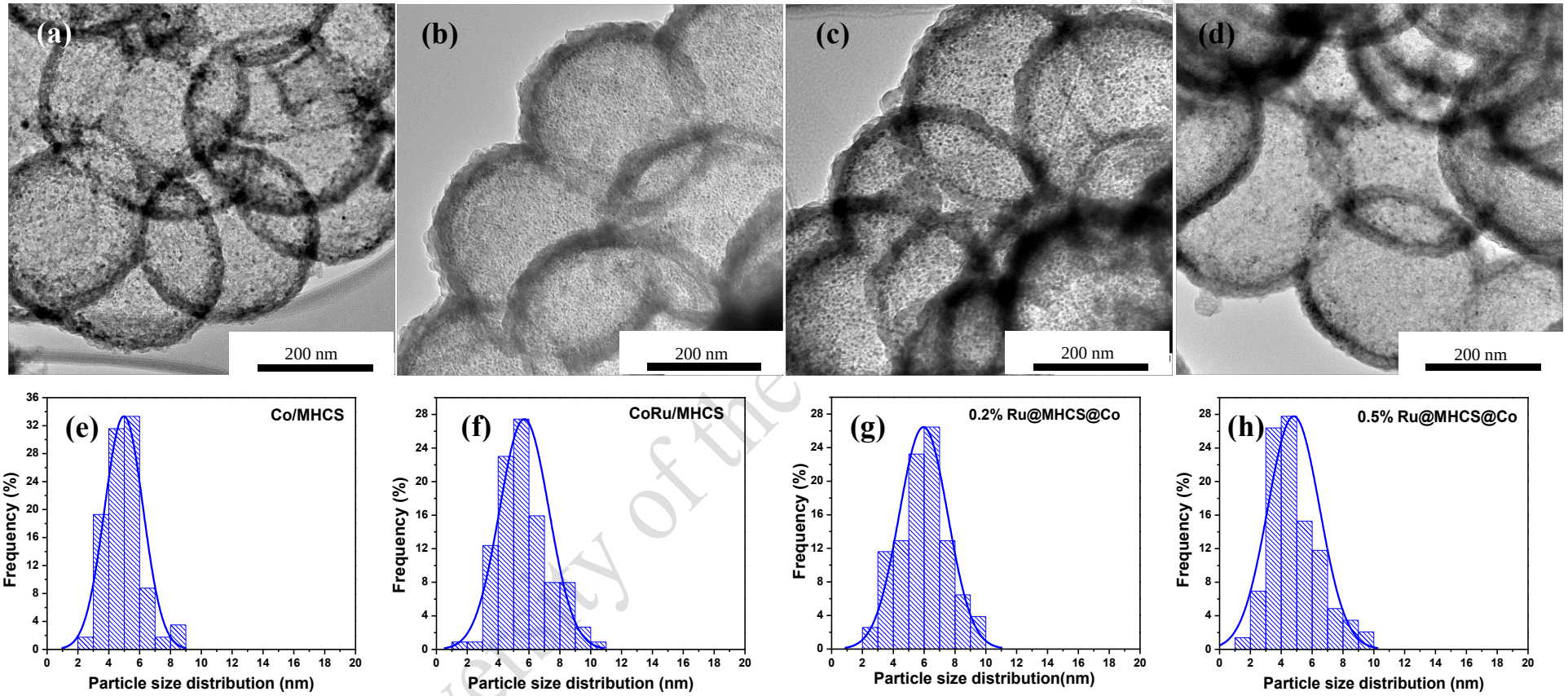

Figure 6. 1: TEM images and particle size distribution of the catalysts: (a,e) Co/MHCS, (b,f) CoRu/MHCS, (c,g) 0.2%Ru@MHCS@Co, (d,h) and 0.5% Ru@MHCS@Co.

Catalyst dispersion using EPMA mapping on the 0.2% Ru@ MHCS@Co catalyst revealed a homogeneous distribution of Co and Ru on the carbon support (Figure 6S.3). WDS data (Figure 6S.3) also confirmed the complete removal of the silica that was used as the template in the synthesis of the hollow carbon spheres. It should be noted that the Ru nanoparticles inside the MHCS could not be easily observed by TEM because of the carbon shell thickness and density together with the small average particles sizes of the Ru. When the carbon coating step was performed by bubbling Ar through toluene for 1 h (instead of 2 h) to give a thinner and less dense carbon shell, the encapsulated Ru nanoparticles in the 0.5%Ru@MHCS could be readily imaged by TEM (see Figure 6S.1,e, d_{Ru} = 4.1 nm). Pulse chemisorption (Table 6.1) analysis revealed that the Co metallic dispersion of the catalysts expressed in terms of a ratio of the H atoms adsorbed to Co atoms increased in the order: Co/MHCS < 0.2% Ru@MHCS ≈ 0.5% Ru@MHCS@Co < CoRu/MHCS. This trend was attributed to the increased degree of reduction (i.e., increased number of Co surface sites) due to the intimate contact between the Ru promoter and the Co (on CoRu/MHCS) with more hydrogen adsorbing on the Ru nanoparticles in Ru@MHCS@Co catalysts than on the Co/ MHCS.

Table 6. 1: Cobalt Content, Particle Size and Pulse Chemisorption Data of the Catalysts.

Sample	dispersion (H:Co)[a]	Co_3O_4 Particle size (nm)		Co content (%wt) /ICP-OES	Ru content (%wt) /TGA
		TEM	XRD[b]		
Co/MHCS	0.011	5.3 ± 1.2	4.8	14.6	0
CoRu/MHCS	0.045	5.6 ± 1.6	4.7	15.4	-
0.2%Ru@MHCS@Co	0.017	5.9 ± 1.5	4.8	14.1	0.9
0.5%Ru@MHCS@Co	0.016	4.8 ± 1.6	4.7	14.8	2.1

[a]Obtained by pulse chemisorption, using a 1:1 ratio of hydrogen atoms to total moles of Co loaded on the sample.
[b]Estimated from the Scherrer equation using Rietveld refinement.

6.3.2. Porosity Analysis Using Nitrogen Adsorption

Porosity analysis of the MHCS and Ru@MHCS with and without Co was performed using nitrogen adsorption−desorption analysis. A typical adsorption isotherm obtained at −195

°C of the materials is included in Figure 6.2. An analysis of all the isotherms show that the MHCS gave a type IV-like adsorption isotherm as given by the IUPAC guidelines **[197]**, with intertwined mesopores centred around a diameter of 3 nm. This indicated that all the carbon shells were mesoporous regardless of whether there were Ru nanoparticles inside. Co loading on the MHCSs did not significantly affect the carbon shell porosity as illustrated by the corresponding pore size distribution (Figure 6.2,b). It is however noted that introduction of Co nanoparticles on the carbon shell did lower the BET surface area, which can be explained by the blocking of some mesopores by Co3O4 nanoparticles thus modifying the carbon shell pore structure (see Figure 3S.4,c and Table 6S.1). This can be seen by the appearance of micropores, which made up less than 5% of the total surface area of the Co3O4 loaded catalysts (Table 6S.1). All MHCS materials showed high BET surface areas due to the mesoporous carbon shell (410−480 $m^2.g^{-1}$). The mesoporosity of the carbon shell was formed as a result of using the mesoporous silica spheres as a template (sections 6.2.4 and 6.2.5), as has also been reported by others [192, 198]. The mesoporous silica template displayed a surface area of 165 $m^2.g^{-1}$ in relation to a surface area of 14 $m^2.g^{-1}$ for the unmodified silica spheres (see Table 6S.1 and Figure 6S.4).

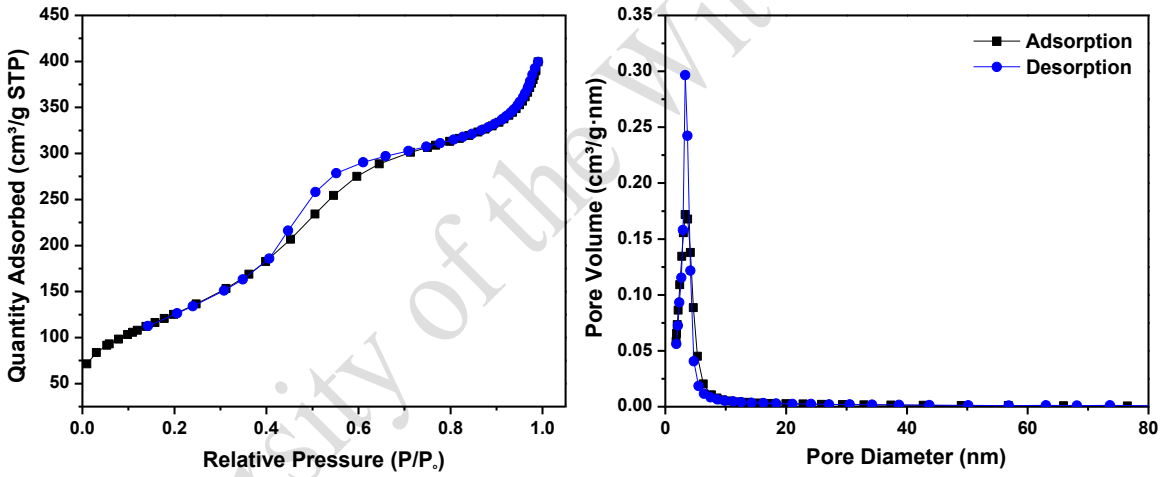

Figure 6. 2: (a) Typical nitrogen adsorption isotherm and (b) BJH pore size distribution of the MHCS and the catalysts (data for Co/MHCS).

6.3.3. PXRD and TGA

Powder X-ray patterns are shown in Figure 6.3,a, for the catalysts that were obtained after calcination in 5% O_2/Ar. The broad distinct peak at 2θ between 28° and 30° is associated with a disordered sp^2 hybridized carbon structure and was observed for all the catalysts **[294]**. A cubic cobalt oxide spinel (Co_3O_4) phase was also observed for all the catalysts, as determined by the characteristic peaks that correspond to the Co_3O_4 phase from the ICSD collection file 9362. The broad peaks for the Co_3O_4 phase confirmed that the loaded

particles were in the nanoscale range, and they also confirmed a narrow size distribution based on the almost symmetric oxide peak shapes **[295]**. The supported nanoparticles crystallite sizes were estimated using the Rietveld Refinement to be in the range of 4.7−4.8 nm (Table 6.1). This was less than the average particle sizes calculated from TEM images. This is not unexpected as the PXRD estimation has been suggested to always underestimate sizes as it is solely based on the diffracting crystallite planes and not the whole particle **[295]**. A hexagonal close packed (hcp) Ru phase was observed for the 0.5% Ru@MHCS and 0.5% Ru@MHCS@Co samples, while Ru in the 0.2%Ru@MHCS was below the detection limit. Thermogravimetric analysis (Figure 6.3,b) was used to study the thermal stability of the catalysts and the carbon support. The analysis was performed in air, with decomposition of carbon via the oxidation of carbon to CO_2. The cobalt oxide nanoparticles catalyze the oxidation of the carbon materials hence lowering the support's decomposition temperature when compared to carbon materials that do not contain cobalt **[255]**. The onset of carbon decomposition for the Co/MHCS occurred at temperatures above 250 °C while for the carbon materials without Co, support decomposition began at around 410 °C for the 0.2% Ru@MHCS and 0.5% Ru@MHCS samples (Table 6.1, Figure 6.3,b).

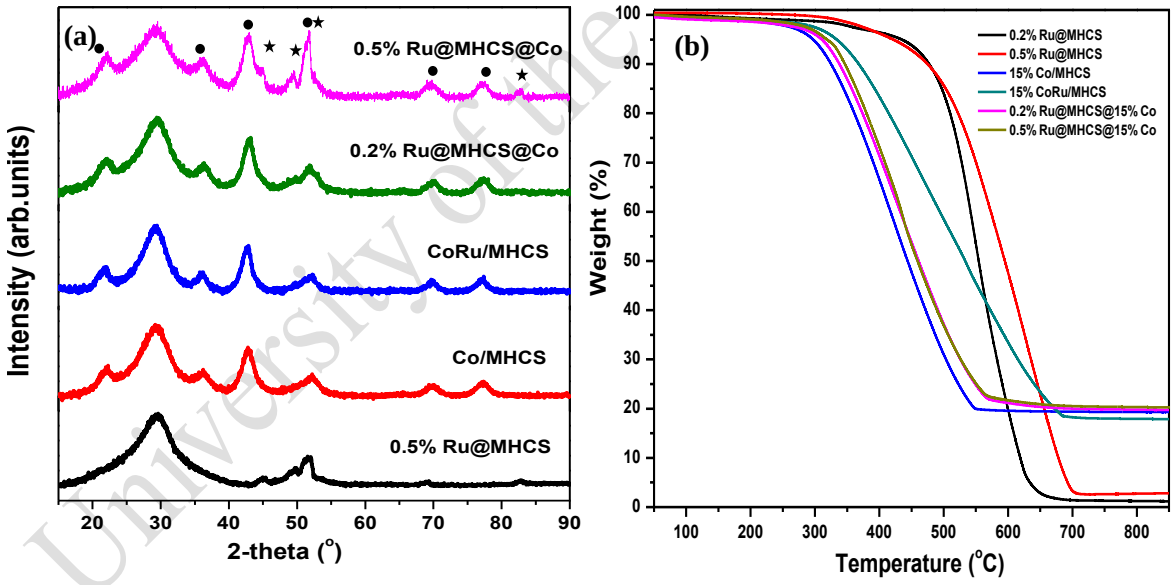

Figure 6. 3: Ex situ PXRD patterns (a) and TGA profiles (b) of the catalysts. Co_3O_4 (●) and Ru (★)

6.3.4. Reduction of Catalysts: in Situ PXRD

To elucidate the reduction behaviour of these Co catalysts an in situ PXRD study was performed. The PXRD patterns were collected at 50 ℃ intervals under hydrogen gas (Figure 6.4; for a full pattern see Figure 6S.5) **[255, 296, 297]**. The behaviour of these catalysts followed the normal reduction for Co_3O_4 with a phase transformation from Co_3O_4 to Co via the CoO intermediate phase. It was however noted that the resulting XRD patterns were influenced by the Ru metal and its location in relation to the Co_3O_4 nanoparticles on the MHCS. For the unpromoted catalyst (Co/MHCS), the Co_3O_4 spinel phase was dominant under the reduction conditions up to 250 ℃, and at this temperature, the Co_3O_4 was completely transformed to a CoO phase. At 250 ℃, the CoO is dominant with the appearance of a small face centered cubic (fcc or α) Co peak. These two phases (CoO and Co) were observed up to 500 ℃ with the CoO phase showing a slight decrease in intensity while the fcc Co peak increased in intensity. It was not possible to completely reduce the entire CoO to Co even at 500 ℃. In situ XRD analysis of the CoRu/MHCS showed that the Co_3O_4 to CoO transition occurred at lower temperature (<200 ℃). At 250 ℃, both hexagonal close packed (hcp or β) and fcc Co phases were evident together with some CoO. The CoO phase disappeared at temperatures >300 ℃. However, the two metallic Co phases (cubic and hexagonal) were observed up to 500 ℃. In situ analysis of cobalt catalysts in which the Ru nanoparticles were loaded on the inside of mesoporous hollow carbon spheres with different nominal Ru loading (0.2% Ru@MHCS@Co and 0.5% Ru@MHCS@Co) was also performed. The Co_3O_4 phase transformation for both these catalysts followed a similar trend that was slightly independent of the Ru loading. It should be noted that for the catalysts with a higher Ru loading the Ru phase was detected at all temperatures from 30 to 500 ℃. In these two catalysts the Co_3O_4 converted to CoO at 200 °C, and more importantly complete conversion from CoO to Co nanoparticles occurred at temperatures between 400 and 450 ℃ to form both fcc and hcp Co phases. The in situ PXRD data (Figure 6.4) allows us to draw conclusions on the hydrogen spillover from Ru to Co. When Ru is in direct contact with Co on the outside of the MHCS a dominant primary spillover effect is expected. This is supported by the finding that the Co_3O_4 is reduced (i) at low temperature to CoO (< 250 ℃) and (ii) is completely reduced to fcc and hcp Co 300 °C by the Ru. Reduction of Co_xO_y is also affected by the relative location of Ru. It is possible that for the Ru@MHCS@Co catalysts, interaction between Co and Ru may take place in the MHCS pores. Incipient wetness impregnation may lead to some Co entering the pores of the hollow carbon spheres; however, the Co particles placed in the pores should still be far removed from the Ru particles when compared to the proximity of the Co and Ru in the CoRu/MHCS catalyst (Figure 6.5). It is to be noted that the carbon shell thickness is 20−35 nm and that the pore dimensions are between 3 and 5 nm (Figure 6.2,b).

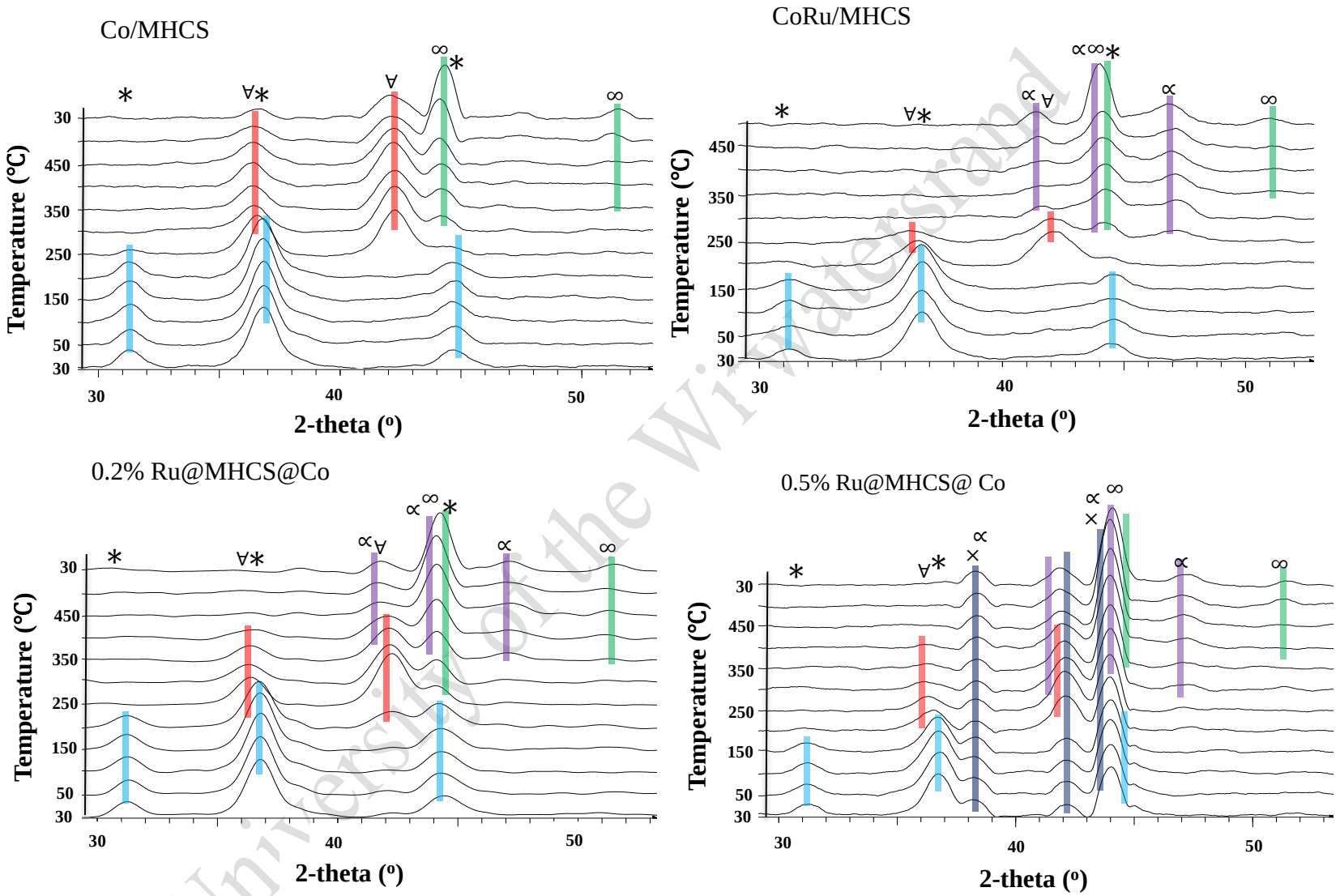

Figure 6. 4: In situ PXRD profiles of the catalysts under reduction conditions Co_3O_4 (*), CoO (∀), α-Co (∞), β-Co (α), Ru (×).

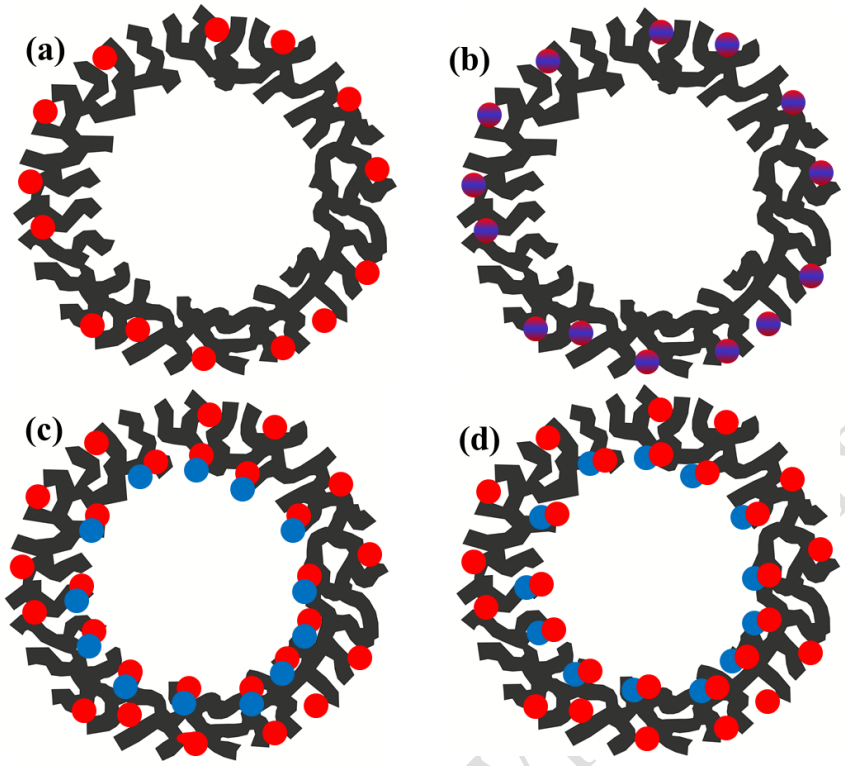

Figure 6. 5: Schematic showing likely Co (red) and Ru (blue) particle distributions on the MHCS support: (a) Co/MHCS, (b) CoRu/MHCS, (c) 0.2% Ru@MHCS@Co and (d) 0.5% Ru@MHCS@Co.

This would suggest that the reduction of the cobalt oxide nanoparticles occurred via a secondary hydrogen spillover effect. Observations to support a secondary hydrogen spillover effect include the following: (i) the catalysts have similar Co particle sizes, hence the effect of size on the reduction behavior of the Co_3O_4 can be ruled out; (ii) the amount of Ru loading on these two catalysts (0.2% Ru@MHCS@Co and 0.5%Ru@MHCS@Co) had the expected impact on their reduction profiles. Thus, the reduction of Co_3O_4 to CoO was complete at temperatures above 200 °C for 0.2% Ru@MHCS@Co and just above 150 ℃ for 0.5% Ru@MHCS@Co consistent with an expected reduction due to a spillover effect dependent on the amount of Ru loaded; (iii) complete reduction at 450 ℃ on the Ru@MHCS@Co catalysts, both the hcp and fcc phases were observed to form upon reduction, with the fcc Co appearing at lower temperatures than the hcp Co; however the fcc Co remained the main Co phase. This indicates that the Ru nanoparticles on a carbon support appear to promote initial formation of fcc Co. The above implies that the Ru promoter effects that are at play on CoRu/MHCS are different from those on Ru@ MHCS@Co and indicates that primary and secondary hydrogen spillover processes can be separated in a Ru promoted Co in carbon support **[118]**. Quantitative phase analysis evaluation by Rietveld refinement (using TOPAS 4.2) of the Co phases on the individual

PXRD profiles (Figure 6.6) was used to calculate the relative abundances of the Co species at each temperature **[296]**. The degree of reduction (DOR) of the catalysts was then estimated as the reduction temperature was increased (Table 6S.3). The estimated DOR at 350 ℃ was 24% for Co/MHCS, 100% for CoRu/ MHCS, 35% for 0.2% Ru@MHCS@Co, and 44% for 0.5% Ru@MHCS@Co. In contrast the Co/MHCS only gave a DOR of 56% at 500 ℃, whereas at this temperature all the other catalysts had a DOR of 100%. The data hence underlines the importance of promoter intimacy for Ru with the Co_3O_4. The Ru promoted catalysts showed hcp Co to fcc Co ratios to be between 0.1 and 0.3. In the case of Co/MHCS, the presence of hcp Co from the PXRD patterns was negligible (Figure 6S.6). The extent of reduction of the catalysts was also determined using oxygen titration after reduction at 350 °C (Figure 6S.7) **[97]**. The re-oxidation of the catalysts was performed at 200 °C to avoid carbon support gasification (see TGA plots, Figure 6S.7,b). The amount of oxygen consumed was based on the usual assumption that Co nanoparticles would convert to the cobalt oxide spinel phase (Co3O4) as supported by XRD analysis of
the oxidized catalyst (Figure 6S.7,b). The CoRu/MHCS had the highest degree of reduction (DOR) (90.2%), while the DORs for 0.2% Ru@MHCS@Co and 0.5% Ru@MHCS@Co were 61.5% and 63.2%. Co/MHCS (62.4%) catalysts had lower values. The data are in agreement with the PXRD data recorded at 350 ℃ shown in Figure 6S.5. The DOR determined using oxygen titration at 350 ℃ shows that without an intimate Co-Ru contact the reduction of the CoO is less affected by encapsulated Ru nanoparticles. Thus, primary hydrogen spillover is invoked to explain the reduction of cobalt oxide on CoRu/MHCS, with the electronic effects determining the Co phase that forms during the process (hcp Co when using a carbon support). For the reduction observed on Ru@MHCS@Co catalysts, secondary hydrogen spillover is invoked to explain the complete phase transformation of the cobalt oxide nanoparticles (to Co) that were loaded on the outside of the hollow carbon spheres. Reduction on these catalysts occurred at higher temperatures, and it is most likely that electronic effects for these catalysts were different from those in CoRu/MHCS. The secondary hydrogen spillover effect requires movement of hydrogen atoms through the carbon shell, which leads to the higher reduction temperatures for the Ru@MHCS@Co catalysts.

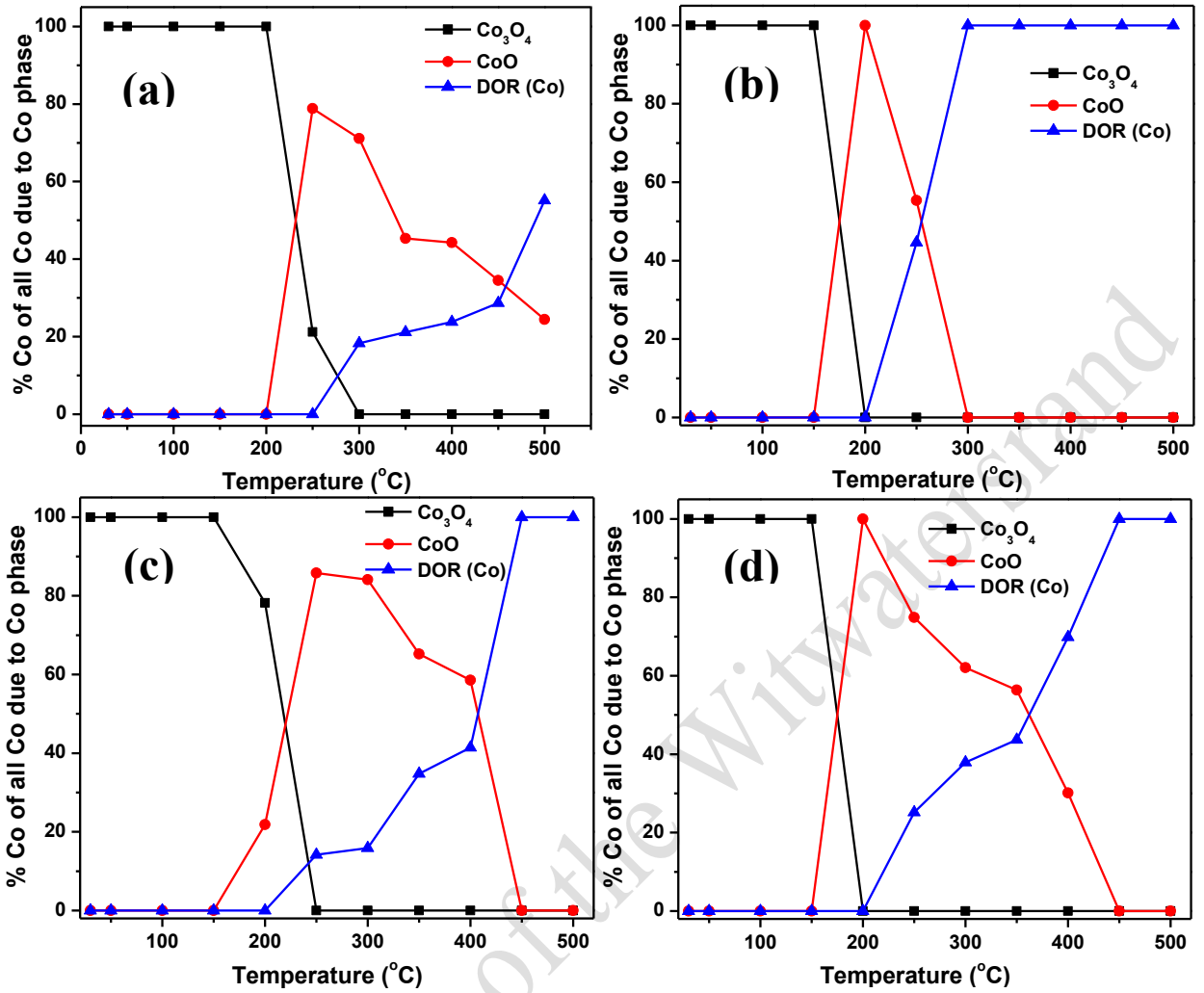

Figure 6. 6: Changes in the Co phase abundance as a function of temperature during in situ PXRD reduction of the catalysts: (a) Co/MHCS, (b) CoRu/MHCS, (c) 0.2% Ru@MHCS@Co, and (d) 0.5% Ru@MHCS@Co.

6.3.5. Temperature-Programmed Reduction Studies

The effect of Ru and its location on the reduction of Co_3O_4 particles was further evaluated using temperature-programmed reduction, and the reduction profiles for the four catalysts are shown in Figure 6.7 (Table 6S.4 shows reduction peak temperatures). After deconvolution, it can be seen that the Co/MHCS and Ru@MHCS@Co catalysts give similar reduction profiles to the reduction of Co_3O_4, but with a shift of the peaks (Table 6S.4). Thus, the stepwise reduction of Co_3O_4 to CoO (ca. 280− 310 ℃) followed by the reduction of CoO to Co (400-430 ℃) was observed. It should be noted that the addition of a higher loading of Ru on Ru@MHCS@Co results in (i) no significant downward or upward shift of the first reduction peak and (ii) a downward shift of the second reduction

peak, when compared to the Co/ MHCS catalyst. In contrast, when the Ru is placed in close proximity to the Co (CoRu/MHCS), the TPR data are quite different with a shift of the first peak to lower temperatures (247 ℃) and a shift of the second reduction peak to higher temperatures (482 ℃). A complete reduction of Co_3O_4 consumes one hydrogen molecule for the first reduction process ($Co_3O_4 + H_2 \rightarrow 3CoO + H_2O$) and three hydrogen molecules for the second ($3CoO + 3H_2 \rightarrow 3Co + 3H_2O$). It is then expected that the Co_3O_4 reduction peaks will be in a ratio of 1:3. However, the peak area ratio of the second reduction peak to the first one was less than one for CoRu/MHCS. This discrepancy can be explained as induced by the Ru promoter, which was in close proximity to the Co oxide nanoparticles. It was therefore assumed that some of the CoO particles were reduced immediately after their formation at the low temperature (247 ℃) to form a Co phase to give the higher consumption of hydrogen as seen in the first reduction peak. This is confirmed by the PXRD profiles presented in Figure 6.4. Other studies have in fact suggested that Ru ions can be doped inside a Co_3O_4 lattice to assist with the oxide reduction at lower temperatures **[274]**. The second peak observed at the higher temperature on this catalyst is probably due to gasification of the carbon support, which is catalyzed by the reduced Co nanoparticles (Table 6S.5). Previous studies have shown that at high temperatures, after complete reduction of the cobalt oxide, the gasification of the carbon support ensues and is catalyzed by the reduced Co nanoparticles **[298]**. Bezemer and co-workers **[299]**, have also suggested that a broad peak at 475 ℃ in their Mn promoted Co catalysts supported on carbon nanofibers was due to the formation of methane, as was confirmed by gas chromatography analysis. Several other studies support our proposal that the Ru promoter affects Co oxide reduction behaviour resulting in a shift of the second reduction peak to low temperatures leading to a possible overlap of the two reduction peaks **[300, 301]**. Irrespective of the exact explanation offered it is clear that placing Ru inside or outside the MHCS leads to substantial changes in the Co oxide reduction behaviour. Reduction profiles in which the Co3O4 nanoparticles and Ru were separated by a carbon shell show that the promoter effects of the Ru were not as prominent as in the catalyst where the two metals are in close proximity (Figure 6.5,c,d). On these catalysts, the first reduction peak occurs at around 300 ℃ and was not changed by the presence of Ru. However, the second reduction peak was shifted to lower temperatures (∼400 ℃) relative to the Co/MHCS (429 ℃) and suggests that a secondary spillover effect occurs to bring about the complete reduction of CoO to Co on the Ru@MHCS@Co catalysts. The TPR profile of a physical mixture of Co/MHCS and Ru/ MHCS showed no discernible shift in the reduction temperature (at 430 ℃) of the corresponding CoO to Co phase transformation (Figure 6S.8)

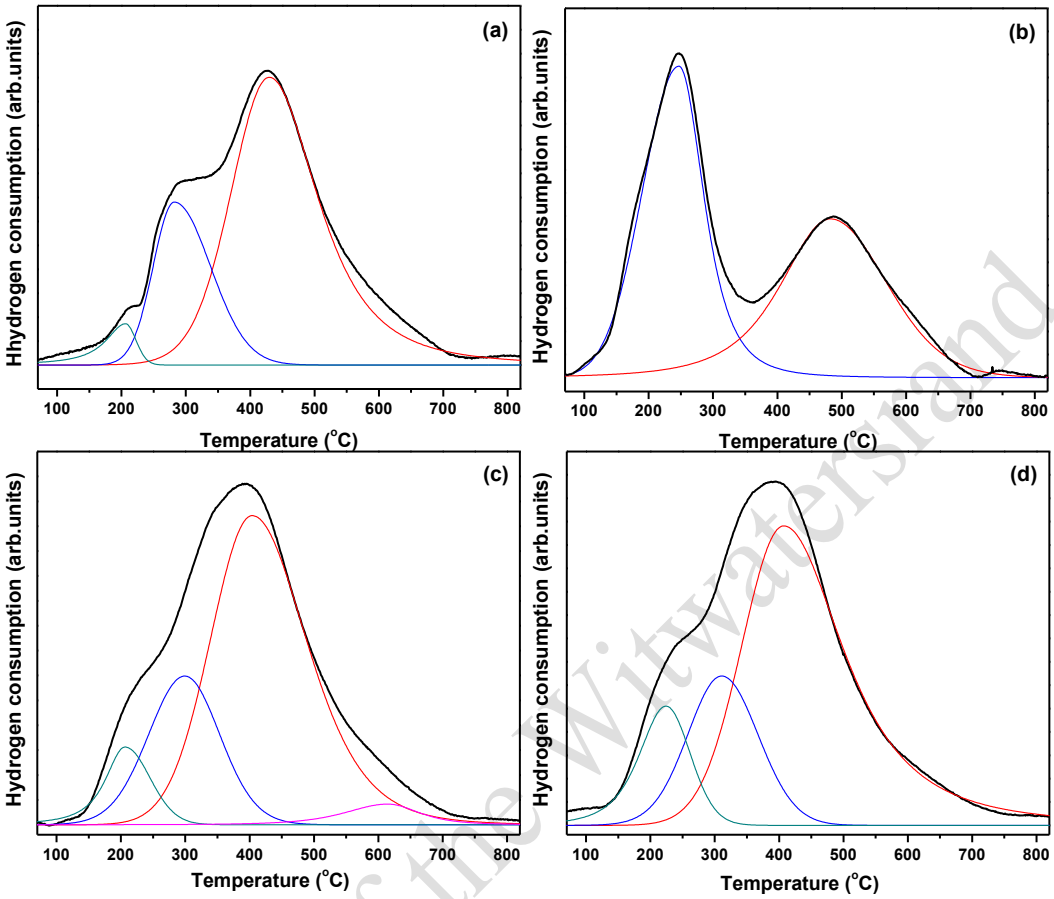

Figure 6. 7: Temperature-programmed reduction profiles of (a) Co/MHCS, (b) CoRu/MHCS, (c) 0.2% Ru@MHCS@Co, and (d) 0.5% Ru@MHCS@ Co.

6.3.6. Fischer−Tropsch Studies

Fischer−Tropsch synthesis over the catalysts was performed at 220 °C at 10 bar pressure for over 100 h on stream (Figure 6S.9). Table 6.2 shows the Fischer−Tropsch activity and product selectivity of these catalysts. CO conversions of these catalysts were between 10% and 20%. Higher FT activity was observed for CoRu/ MHCS at 9.48 $\times 10^{-6}$ $mol_{CO}/g_{Co}.s$, with a calculated activity almost double that of the other three catalysts that had an activity of about 5×10^{-6} $mol_{CO}/g_{Co}.s$. However, the two catalysts with the Ru encapsulated inside the MHCS (i.e., 0.2% Ru@MHCS@Co and 0.5% Ru@MHCS@Co had activities of 5.15×10^{-6} and 5.52×10^{-6} respectively) showed a similar or slightly higher activity with respect to the unpromoted catalyst Co/MHCS (5.13×10^{-6} $mol_{CO}/g_{Co}.s$). The activity of the catalysts can be rationalized based on the reducibility induced by the promoter effects as

determined by the Ru metal **[302]**. The unpromoted catalyst had the lowest FT activity as it had a lower degree of reduction and dispersion of all the catalysts (Table 6.1 and Table 6S.3). The low turnover frequencies observed for the catalysts were attributed to the small Co crystallites that resulted from the reduction process **[82, 85]**. In situ PXRD and oxygen titration studies showed that complete reduction of the cobalt oxide on the CoRu/MHCS catalyst occurred at 300 °C and that reduction at 350 °C prior to Fischer−Tropsch reaction ensured a high reducibility. Further, although the Ru@MHCS@Co could also be completely reduced, this occurred at high temperatures (>350 °C). The lower Fischer−Tropsch activity of these catalysts is attributed to their lower degree of reduction because pre-treatment of these catalysts by hydrogen reduction prior to Fischer−Tropsch synthesis was performed at 350 °C. The lower number of active sites was confirmed by the pulse chemisorption studies, which showed that Co nanoparticles on CoRu/MHCS displayed a higher catalytic dispersion than the other three catalysts. Although secondary hydrogen spillover could be invoked to explain the complete reduction of the two encapsulated Ru catalysts, the secondary spillover process did not significantly enhance the degree of reduction of the catalysts at 350 °C. The higher TOF for the CoRu/MHCS promoted catalysts (as compared to Co/MHCS and Ru@MHCS@Co) is related to the high DOR, and the hcp phase which has a higher intrinsic activity for CO hydrogenation reactions than the fcc Co, which was dominant in Co/MHCS **[303]**. Fischer−Tropsch activity of the catalysts therefore suggests that primary hydrogen spillover (which gives rise to synergistic electronic effects) is effective in giving a highly active Fischer−Tropsch catalyst, while secondary spillover effects are less effective.

Table 6. 2: Fischer−Tropsch Activity and Selectivity.

Sample	CO Conversion (%)	TOF (10^{-4} s)[a]	Activity $\times 10^{-6}$ ($mol_{CO}/g_{Co}.s$)	Selectivity (C mol) %			α
				C_1	C_2-C_4	C_{5+}	
Co/MHCS	11.2	14.2	5.13	20.1	7.9	72.0	0.81
CoRu/MHCS	19.4	35.9	9.48	23.0	13.3	63.7	0.76
0.2% Ru@MHCS@Co	11.9	17.2	5.15	20.8	9.6	69.6	0.75
0.5%Ru@MHCS@Co	12.4	18.8	5.52	22.4	9.2	68.3	0.74

[a]Calculated using the data obtained from Co crystallite sizes of the spent catalysts as determined by Rietveld refinement (Figure 6S.10 and Table 6S.6). Surface atoms were calculated using the Van Hardeveld and Hartog statistical method **[81]**.

All the catalysts gave methane selectivities of approximately 20 mol %, and the gas phase products C_2−C_4 were between 7% and 15%, with the C_{5+} selectivities of the catalysts all above 60 mol % carbon. The catalysts with Co and Ru in direct contact (CoRu/MHCS) yielded higher C_2−C_4 products and lower C_{5+} products. The unpromoted catalyst, Co/MHCS, yielded a higher α value of 0.81, while the promoted catalysts (CoRu/MHCS, 0.2% Ru@MHCS@Co, and 0.5% Ru@MHCS@Co) had α values calculated to be around 0.75. The high methane selectivities can be accounted for by the small cobalt particle sizes. Several studies have suggested that catalysts with small crystallites give high methane selectivity and that in this size regime catalytic selectivity is affected by the small Co nanoparticles **[82, 85, 279]**. The Ru promoter did not impact substantially on the catalytic selectivity (when compared to its effect on Fischer−Tropsch activity) **[290, 291]**. It can be concluded that the Co particle size played a role in affecting the catalytic activity and selectivity, but both the primary and secondary spillover effects did not change the catalytic selectivity.

6.4. Conclusions

Co Fischer−Tropsch catalysts promoted using Ru metal were prepared using mesoporous hollow carbon spheres (MHCSs) as the support. By preferentially placing Ru nanoparticles inside the MHCSs, it was possible to separate the Co and Ru nanoparticles on the carbon support and to study the effect of primary and secondary hydrogen spillover on Ru promoted Co catalysts during reduction and under Fischer−Tropsch conditions. It can be concluded that;

(1) The MHCS was an effective model catalyst support to study the process of primary and secondary hydrogen spillover using Co Fischer−Tropsch catalysts,

(2) in-situ PXRD reduction, TPR studies, and a Fischer−Tropsch catalytic evaluation suggested that a greater reducibility at low temperatures and higher Fischer−Tropsch activity could be obtained for catalysts where the Co and Ru metal were in close proximity to each other (CoRu/MHCS), due to a primary hydrogen spillover effect that enhanced cobalt oxide reduction to give a highly active Co catalyst for use in Fischer Tropsch synthesis,

(3) secondary hydrogen spillover was invoked to explain the complete reduction of cobalt oxide on Ru@MHCS@Co where the Co and Ru were separated by a carbon shell, which occurred at relatively high temperatures resulting in a lower degree of reduction when reduced at 350 ℃, which could explain the lower Fischer−Tropsch activity, when compared to the CoRu/MHCS,

and (4) the catalytic selectivity is correlated with the small Co nanoparticles. The nanoparticles played a significant role in the hydrocarbon product distribution.

Acknowledgments

We thank the NRF, the DST-NRF Centre of Excellence in Catalysis, and the University of the Witwatersrand for financial support. The NNEP is also thanked for an equipment grant. We thank Dr. Mashikoane W. Mogodi for insights relating to the Rietveld refinement analysis.

Chapter 7

Fischer-Tropsch synthesis in a carbon nanoreactor: spillover effect observed on Co@MHCS@Ru

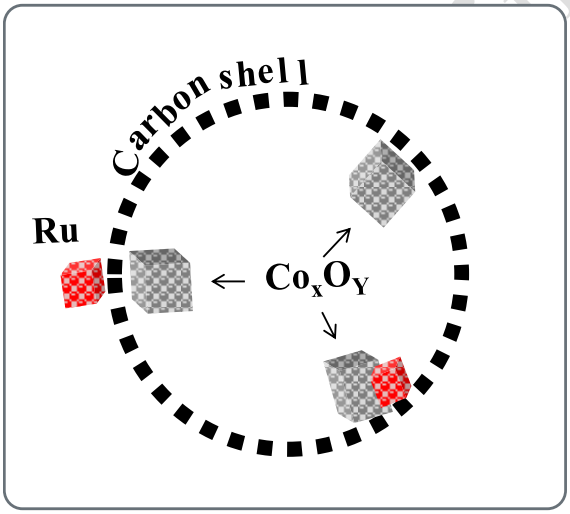

$$Co_3O_4 \rightarrow CoO \rightarrow Co$$

- **Co@MHCS , incomplete reduction @ 500 ℃**
- **Co@MHCS@Ru , complete reduction @ 450 ℃**
- **CoRu@MHCS , complete reduction @ 300 ℃**

Supporting information: Appendix C

Abstract: Hydrogen spillover is thought to be one of the mechanisms by which noble metal promoters enhance cobalt oxide reducibility in Fischer-Tropsch Synthesis. The effect of these metals is attributed to their ability to easily dissociate H_2 molecules at low temperatures to hydrogen atoms that are transferred to the Co_3O_4 nanoparticles via a spillover mechanism. In this study Co and Ru nanoparticles were separated by encapsulating the Co nanoparticles inside a mesoporous hollow carbon sphere support (MHCS) while the Ru was exclusively loaded on the outer surface (i.e., Co@MHCS@Ru). Two other catalysts, unpromoted Co@MHCS and promoted CoRu@MHCS were also prepared. TEM analysis of the materials showed Co_3O_4 particles with an average size between 7.1-7.4 nm and Ru nanoparticle size of 2.6 nm with the MHCS defective carbon shell thickness between 20-30 nm. By using pulse chemisorption, primary hydrogen spillover was invoked to explain the high Co dispersion for CoRu@MHCS in relation to the Co@MHCS@Ru and Co@MHCS dispersion after reduction at 350 ℃. Using in situ PXRD a secondary hydrogen spillover process over the porous carbon was invoked to explain the complete reduction of the Co_3O_4 on Co@MHCS@Ru when compared to unpromoted Co@MHCS. Finally, primary spillover effect was revealed to be more energetically more favourable than a secondary hydrogen spillover effect. Fischer-Tropsch testing of the catalysts showed that the Fischer-Tropsch activity was proportional to the degree of reduction that increased with the Co-Ru intimate contact. The Ru promoter also enhanced the production of paraffinic products and methane.

7.1. Introduction

Fischer-Tropsch catalyst nanoparticles have been promoted by a variety of materials to enhance the number of active sites, enhance the selectivity and stabilize catalysts against deactivation **[20, 304].** Typically these promoters can be classed into two divisions; structural and electronic promoters.

Electronic promoters on Fischer-Tropsch catalysts generally involve the use of the platinum group metals **[92, 118, 304, 305]**. Promotion of cobalt Fischer-Tropsch catalysts by these metals helps in lowering the reduction temperature of the active phase. This is an important aspect to ensure that the Co active phase can attain maximum activity without any significant particle agglomeration during catalyst preparation, especially during the catalyst reduction process **[306]**. It has been observed that the synthesis procedure to make the promoted Fischer-Tropsch catalysts is dependent on the location of the Co and Ru relative to each other. Thus the difference between primary (intimate) and secondary (metal separated from each other) spillover mechanisms is expected to play a role in the catalytic process **[136, 307]**. Ru as a promoter for Fischer-Tropsch catalyst has yielded many significant results whereby both the activity and selectivity of the catalyst's active sites have been improved spillover effects. Trepanier at al **[118],** prepared a Co catalyst (15% loading) on multiwalled carbon nanotubes (MWCNTs) promoted by different loadings of Ru (0.25, 0.5 and 1 %), the Co and Ru metals were co-impregnated on the MWCNT. The prompted catalysts when compared to an unpromoted catalyst showed that the Ru enhanced the cobalt oxide reducibility at lower temperatures (which was especially observed for the second reduction peak corresponding to CoO → Co phase transformation). The Ru promoter also increased metal dispersion by lowering the Co average particle size. This resulted in an increased Fischer-Tropsch activity and the Ru promoter effects induced by changing the Co catalyst morphology yielded low methane and C_2-C_4 selectivity and increased C_{5+} production. In a study by Cook and co-workers **[304],** it was observed the order in which the Co and Ru metals are deposited on the support (La/Al_2O_3) played an important role on the ability of the Ru metal to optimally influence the catalytic activity of the Co metal. When the catalysts was prepared by co-depositing the Co and Ru precursor the catalyst showed a uniform Ru distribution with Co on the support, further the catalyst showed smaller Co crystallites, a higher degree of reduction and low methane selectivity. However, by sequentially loading Co metal followed by the Ru promoter the subsequent catalyst had poor distribution with the reduction temperatures shifted to higher temperatures. Thus the intimate contact between the Co and Ru enhanced the Co Fischer-Tropsch Synthesis activity.

The effect of the Ru promoter location relative to the cobalt oxide nanoparticles in Fischer-Tropsch catalysts can be studied by the use of hollow carbon spheres, such that the catalyst and promoter can be loaded on both sides of the carbon shell thus assuring a spatial

separation between the metals of interests **[217]**. The carbon shell because of its defects can aid the spillover processes.

The synthesis of metal nanoparticles encapsulated inside hollow porous sphere has been ongoing over the years **[289].** The hollow porous spheres have been prepared using different materials such as silica, titania and carbon **[148, 168, 192].** Hollow carbon spheres have been exploited extensively in many studies. The synthesis of metal inside hollow carbon spheres has been achieved by employing the hard template method using modified Stöber silica spheres. Using this method numerous metal nanoparticles have been successfully loaded inside these porous hollow spheres include Pt **[183],** Au **[198],** Pd **[219],** Rh **[184]**. However, a loading of Co or Fe using this process is not possible since SiO_2 template removal by acid also dissolves the Co or Fe nanoparticles thus leaving the hollow carbon spheres empty. Wang et al. **[187],** developed a method for preparing Co nanoparticles inside hollow carbon spheres containing Pt nanoparticles that served as the nucleating agents for the Co2+ ions in the hollow cores. It should however be noted that not all the cobalt nanoparticles were fully incorporated inside the hollow core of the carbon spheres. This because a cobalt precursor was added onto the Pt hollow polymeric sphere before the pyrolysis process from outside resulting in some Co^{2+} ions trapped on the carbon shell's outside surface. The hollow spheres we prepared by a soft template method P123 and sodium oleate (SO) as surfactants. However, this method results in low material yield.

Polystyrene spheres (PSSs) offer an interesting alternative to SiO_2 for use as a hard template in the synthesis of hollow carbon spheres. They can easily be synthesized on a large scale and indeed have been used as templates for the preparation of porous hollow carbon spheres **[176, 178, 308, 309].** Polystyrene spheres offer a softer template when compared to silica spheres because the removal of the polystyrene template after carbon coating does not require harsh conditions (i.e. use of HF). The polystyrene spheres template can be easily removed using a solventless method by heat treatment above 400 ℃ under an inert environment using nitrogen or argon gases. White et al. **[178],** managed to produce well dispersed hollow carbon spheres by coating polystyrene spheres with glucose using a hydrothermal method and then by thermal removal of the PSSs hollow carbon spheres with good porosity and high BET surface area > 350 $m^2.g^{-1}$ could be obtained after annealing and carbonization at temperatures above 500 ℃.

In this study a novel method is presented to encapsulate Co and CoRu nanoparticles inside hollow carbon spheres. The method entails the synthesis of PSSs, loading of Co onto the PSSs and coating by a carbon shell by deposition of a carbonaceous material on the Co/PSSs surface. Finally the PSSs were removed by thermal treatment to give Co@MHCS (CoRu@MHCS) catalyst. These catalysts were then used to evaluate hydrogen spillover effect in Fischer-Tropsch catalysts using Co@MHCS, CoRu@MHCS and Co@MHCS@Ru (where the Co and Ru nanoparticles were separated by the carbon shell)

7.2. Experimental procedure

7.2.1. Chemicals

Styrene (Aldrich), polyvinylpyrollidone (PVP, MW 40 k, Aldrich), cobalt nitrate hexahydrate (Aldrich), ethylene glycol (Aldrich), ammonia solution (25%; Fluka), potassium persulfate (Eimer and Amend), hexadecyltrimethylammonium bromide (CTAB; Aldrich), ruthenium chloride (Aldrich), hydrazine (35%, Aldrich), ethanol (98%; Merck), isopropanol (99%, Merck), nitric acid (55%; Merck), hydrochloric acid (32%, Associated chemical) were used as received. Deionized water was used in all the experiments where water was used.

7.2.2. Synthesis of polystyrene spheres (PSSs)

Styrene (8 mL) and PVP (0.1 g) were dispersed and dissolved (for PVP) in 250 mL of a water-ethanol mixture (water, 200 mL and ethanol 50 mL) by sonication and then stirred for 15 min. To this solution was added potassium persulfate solution (0.15 g in 20 mL water) was added while stirring. The mixture was then heated at 80 ℃ for 27 hours. After cooling the product was then filtered and washed repeatedly using water.

7.2.3. Loading of Co or CoRu on the polystyrene spheres (3% Co/PSSs or 3 %Co 0.2%Ru/PSSs)

PSSs (6 g) were dispersed by sonication for 30 minutes in a 200 ml water ethanol solution (150 and 50 ml respectively). To this solution cobalt nitrate hexahydrate (0.89 g) was added while stirring until it completely dissolved forming a red solution. Deposition of Co nanoparticles was performed by a slow addition of a hydrazine solution (20 ml, 2 M), the solution was left while stirring for 12 hours to ensure complete deposition of the Co nanoparticles. To make the bimetallic CoRu/PSSs composite the cobalt precursor was dissolved together with a $RuCl_3$ solution (11.9 ml, 0.01 M) before nanoparticle precipitation. The Co loading was calculated to be 3% and Ru at 0.2%.

7.2.4. Synthesis of Co or CoRu nanoparticles inside hollow carbon spheres

CoRu/PSSs or Co/PSSs (6 g) and ammonia solution (25%; 4.5 mL) were dispersed by sonication for 30 min in 450 mL of ethanol water solution (300 ml ethanol and 150 ml water). A resorcinol (2.25 g), formaldehyde solution (37%; 4.5 mL) and CTAB (3 g) mixture made in ethanol (150 mL), was then added to the Co/PSSs or CoRu/PSSs mixture and then stirred at room temperature for 20 h to form the resorcinol-formaldehyde (RF) polymer around CoRu/PSSs or Co/PSSs. The resulting composite (CoRu/PSSs@RF or Co/PSSs@RF was then filtered and washed repeatedly with water followed by drying at 80 ℃ for 12 hours. Template removal and carbonization was performed following a one-step procedure inside a horizontal tube by heating CoRu/PSSs@RF or Co/PSSs@RF under a

nitrogen flow (50 ml/min) at 350 ℃ for 1 hour to decompose and remove the polystyrene template. This was followed by the annealing step of the carbon spheres at 600 ℃ for 2 hours under a nitrogen atmosphere. The resulting products were (i.e., **Co@MHCS and CoRu@MHCS, MHCS =porous hollow carbon spheres**)

7.2.5. Preparation of Co@MHCS@Ru

Synthesis of Ru nanoparticles **[310].**

Ruthenium chloride solution (20 ml, 0.01 M) was added ethylene glycol (15 ml) in a round bottomed flask. PVP (0.1 g) was added to this solution while stirring to dissolve the PVP. The Ru nanoparticle synthesis was performed by reduction or the Ru ions using ethylene glycol under reflux at 200 ℃ for 6 hours. The resulting nanoparticles were precipitated using isopropanol and recovered by centrifugation at 15000 rpm while washing with ethanol to remove all ethylene glycol. The clean nanoparticles were dispersed in ethanol (50 ml) and stored at room temperature.

Loading of Ru nanoparticles on Co@MHCS

The Co@MHCS (1.5 g) catalyst was dispersed in in 50 ml ethanol followed by the addition of the dispersed Ru nanoparticles (30 ml). This mixture was sonicated for 30 minutes and then stirred for 12 hours to load the Ru nanoparticles. The catalyst was filtered and washed using ethanol while filtering followed by drying at 100 ℃ overnight.

All the catalysts (Co@MHCS, CoRu@MHCS, Co@MHCS@Ru) were calcined at 210 ℃ under 5% O_2/Ar (50 ml/min) for a further 2 hours to ensure that all the cobalt was converted to Co_3O_4 phase.

7.2.6. Material characterization

TEM analysis was performed on a Tecnai spirit (T12) transmission electron microscope operating at 120 kV. The samples were dispersed in methanol by ultrasonication and loaded onto a copper grid for TEM analysis. The particle size distribution of the materials formed was determined by counting at least 200 randomly selected particles per sample from different TEM images. Gaussian statistics yielded values for the average particle sizes. SEM analysis was performed on a FEI Nova Nanolab 600 FIB/SEM instrument operating at 30 kV. STEM analysis was performed using the JEM 2800 (Scanning) Transmission Electron Microscope using the following instrumental conditions: Voltage (kV) 200; C2 aperture (um) 70 and 40; Bright-field imaging mode using CCD High magnification lattice resolution imaging mode using CCD Dark-field (Z-contrast) imaging in scanning mode using an off-axis annular detector The SE signal was acquired simultaneously with the other STEM images providing topological information of the sample. Compositional analysis was done by X-ray emission detection in the scanning

mode. The samples on a carbon tape were coated with a gold-palladium layer before the analysis. The bulk composition of the catalysts was analyzed using a Bruker D2 phaser equipped with a Lynxeye detector, using a Co-Kα (λ = 0.17889 nm) at 30 kV. The scan ranged from 10-90 2θ in 0.0260 steps. TGA was performed with a Perkin- Elmer STA6000 TGA using nitrogen or air as the purge gas and a heating rate of 10 ℃.min^{-1}. The flow rate of the purge gas was always 20 mL.min^{-1}. N_2 adsorption–desorption experiments were conducted at -195 ℃ using a Micromeritics Tristar 3000 surface area and porosity analyzer. Prior to an experiment, the sample was outgassed at 150 ℃ for 4 under N_2 gas. The BET surface areas were obtained for adsorption data in a relative pressure range from 0.05 to 0.30. The total pore volumes were calculated from the amount of N2 vapor adsorbed at a relative pressure of 0.99. The pore size distributions were evaluated from the desorption branches of the isotherms using the Barrett–Joyner–Halenda (BJH) method. The micropore surface area and volume were calculated using t-plot report data. TPR experiments were carried out with a Micromeritics Auto Chem II unit. The catalyst (approximately 50 mg) was placed in a quartz tubular reactor, fitted with a thermocouple for continuous temperature measurement. The reactor was heated in a furnace. Prior to the temperature-programmed reduction measurement, the calcined catalysts were flushed with high-purity argon at 200 ℃ for 30 minutes, to remove water or impurities, followed by cooling to ambient temperature. Then, 5% H_2/Ar was switched on, and the temperature was raised at a rate of 10 ℃.min^{-1} from 50 to 850 ℃. The gas flow rate through the reactor was controlled by three Brooks mass flow controllers and was always 50 mL.min^{-1}. The H_2 consumption (TCD signal) was recorded automatically by a computer. Pulse chemisorption was performed using the Micromeritics Auto Chem II instrument, to compute the number of active sites on the catalysts. The catalyst (ca. 100 mg) was placed in a quartz tubular reactor. The sample was reduced at 350 ℃ for 2 h under a hydrogen flow of 50 mL.min^{-1}. Before injecting the active gas, the sample was purged using helium gas at 350 ℃ for 1 h, followed by cooling to ambient conditions. Hydrogen chemisorption (assuming a H_2/Co ratio of 2) was then performed at 150 ℃ using ultra-pure hydrogen as the active gas and argon as the carrier gas. The in situ PXRD experiments were performed on a Bruker D8 Advance fitted with an Anton Paar XRK 900 in situ cell. The diffractometer used a sealed copper tube as the X-ray source operating at 40 kV and 40 mA that provided X-rays with a wavelength of 0.15418 nm in a parallel beam geometry. Co loading on the MHCSs was performed using an ICP-OES End on Plasma from Spectro Genesis (Kleve, Germany). A catalyst sample (50 mg) was dispersed in a solution 10 mL 55% nitric acid and 40 mL water to dissolve the Co nanoparticles before analysis.

7.2.7. Fischer-Tropsch Synthesis Evaluation Experiments.

The Fischer–Tropsch synthesis was performed in a fixed-bed micro-reactor. A gas cylinder containing H_2/CO/N_2 mixtures (~60/30/10 vol. % purity: 99.99) was used to supply the reactant gas stream to the catalyst with a flow rate of 15 mL.min^{-1}. N_2 was used as an internal standard in order to ensure accurate mass balances. Catalyst (1 g) was added to the

reactor and reduced in situ at 250 ℃ for 2 hours under a stream of H_2 (1.5 bar at 50 $mL.min^{-1}$). After reduction, the reactor temperature was decreased to ambient temperature under a hydrogen flow, and then heated up to 220 ℃ under synthesis gas at a pressure of 10 bar. All gas lines after the reactor were kept at 100 ℃, and a hot trap placed immediately after the reactor was held at 150 ℃ in order to collect wax. A second trap kept at ambient temperature was used to collect the oil and water mixture. The flow was controlled using a metering valve and measured by a bubble meter. The product stream was analyzed online using two gas chromatographs. A thermal conductivity detector (TCD), equipped with a Porapak Q (1.50 m × 3 mm) packed column, was used to analyze H_2, N_2, CO and a flame ionization detector (FID), equipped with a Porapak Q packed column, was used for the analysis of the hydrocarbons online. Liquid and wax hydrocarbons collected in the knockout pots were analyzed using an offline GC, equipped with a ZB-1 packed column.

7.3. Results and Discussion

7.3.1. Catalyst Structure and Dispersion

SEM images (Figure 7S.1), show the morphology of the composites before carbon coating, the polystyrene spheres (a), after coating (b) and after template removal, for both Co@MHCS (c) and CoRu@MHCS (d). The monodisperse polystyrene spheres (PSSs) were easily coated with the resorcinol-formaldehyde (RF) as can be seen in Figure 7S.1,b and the coated samples showed that the PSSs were almost individually coated with the polymer. Resorcinol and formaldehyde have previously been effectively used to make hollow carbon spheres from Stöber silica sphere templates **[180, 217],** the its polymerization on the PSSs template followed a similar route to that as in SiO_2 spheres. Following the removal of the polystyrene template by heating in nitrogen the resulting hollow carbon spheres took the shape of the template without any significant crumbling (Figure 7S.2). The studies are similar to those by White et al. **[178]**, using a PSS template but resorcinol and formaldehyde were used as carbon source in this study.

The encapsulated Co_3O_4 nanoparticles displayed a good dispersion inside the hollow carbon spheres. Other studies have also shown that the synthetic procedure can be used to prepare encapsulated catalysts using different metals and other materials for making hollow spheres besides carbon **[289]**. No cobalt oxide nanoparticles were expected to be found on the outside of the carbon shell using this procedure. Three catalysts were prepared, (1) Co@MHCS as shown in Figure 7.1, with a Co_3O_4 average size of 7.4 nm, (2) CoRu@MHCS in which the CoRu bimetallic nanoparticles were also encapsulated inside the hollow carbon spheres with an average particle size of 7.1 nm. The particle size distribution was not affected by the Ru promoter.

(3) Co@MHCS@Ru (Figure 7.1, e, f, g and h, Co_3O_4 size = 7.3 nm and Ru size = 2.6 nm). This procedure made sure that all the Ru nanoparticles were located on the outside and Co

on the inside of the hollow carbon spheres and there was no direct contact between Co and Ru metal nanoparticles.

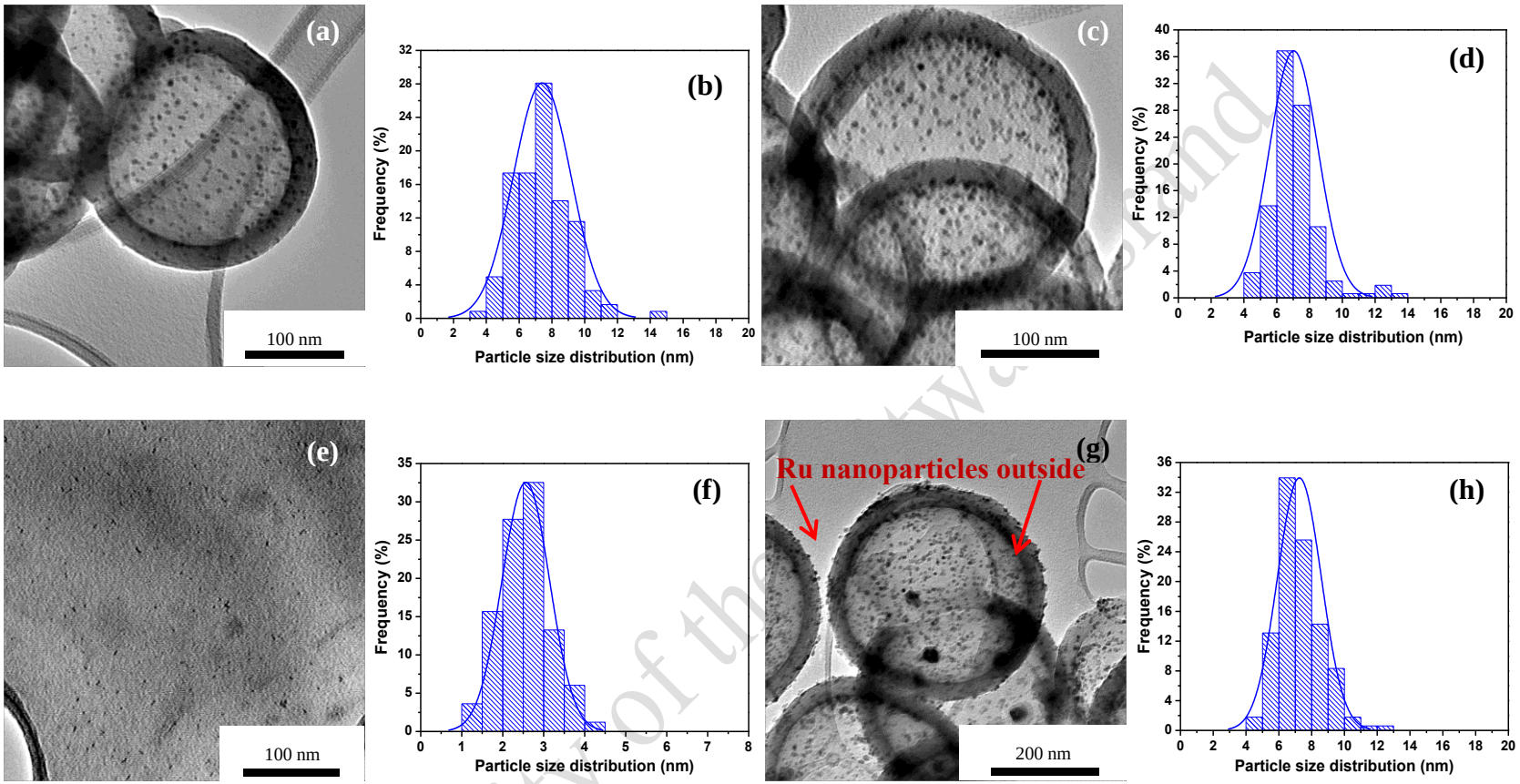

Figure 7. 1: TEM images and particle size distribution of the prepared catalysts together with the presynthesized Ru nanoparticles. (a,b) Co@MHCS (c,d) CoRu@MHCS, (e,f) Ru NPs and (g,h) Co@MHCS@Ru.

STEM analysis of the catalysts revealed the following: For CoRu@MHCS (Figure 7.2,a,b), mainly Co nanoparticle inside the hollow carbon spheres surface which was rough and cratered. An EDX map also showed Ru enrichment in the inner surface of the hollow carbon spheres (Figure 7S.3). On Co@MHCS@Ru, Co particles are found below the carbon surface while Ru particles are on the Carbon surface, seen in the Secondary SE image. Furthermore, a combination of HAADF (transmission) and SE (surface) images clearly showed that the small nanoparticles are on the outer carbon shell surface (Ru as revealed by EDX) while the larger nanoparticles were below the carbon shell surface (Co with oxide as revealed by EDX) (Figure 7.2, c,d and Figure 7S.3).

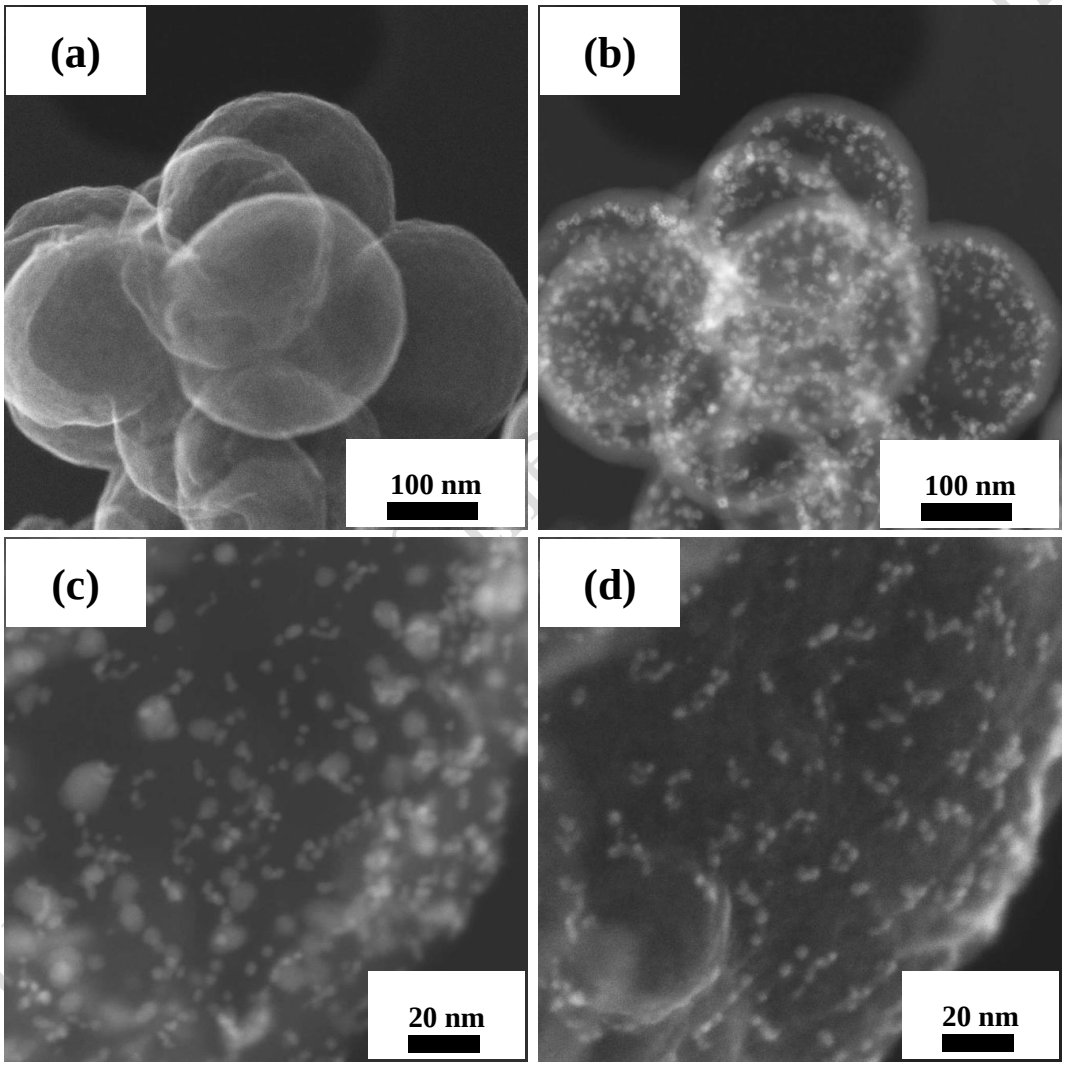

Figure 7. 2: (a,b) SEM and STEM images of the same region on CoRu@MHCS and (c,d) HAADF and secondary electron outer surface of the same region on Co@MHCS@Ru.

EDX lines mapping (Figure 7.3) of the Co nanoparticle on Co@MHCS@Ru revealed the presence of Co element alone without any intimate contact of Co and Ru. However, a similar scan on the CoRu@MHCS catalyst revealed the presence of Co and Ru on the nanoparticle, thus suggesting an intimate contact of the two metals. Using a pair distribution analysis and selected area electron diffraction of the bonds on a highly magnified CoRu nanoparticle (Figure 7S.4), evidence of a Co-O, Co-Co and C-C bonds could be discerned - however, a bimetallic Co-Ru bond was not evident. This hence suggested that the Co and Ru nanoparticles in CoRu@MHCS were mainly in close physical contact. Nevertheless, the existence of a bimetallic CoRu in the catalyst cannot be completely ruled out since only a few CoRu nanoparticles were sampled by this method.

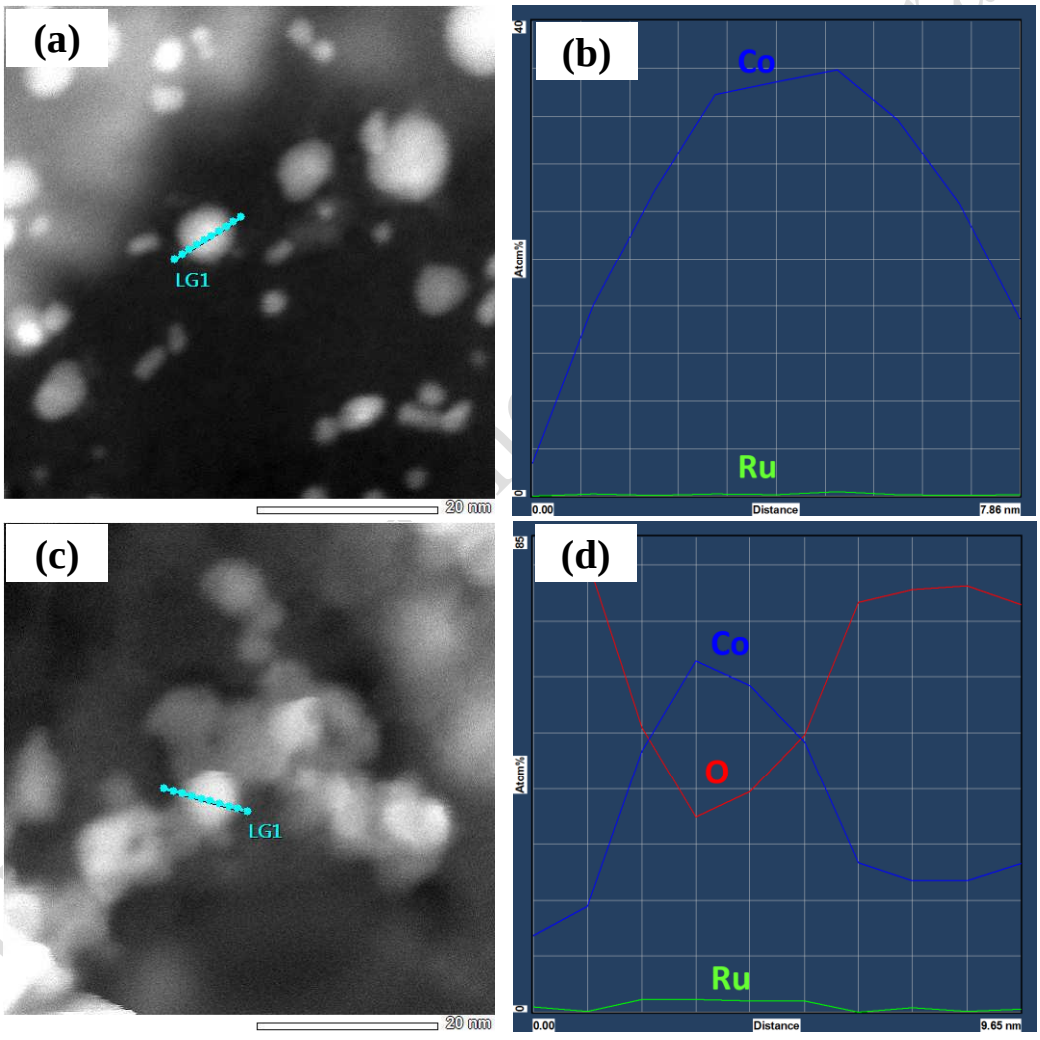

Figure 7. 3: EDX line map of the encapsulated nanoparticles (a,b) Co@MHCS@Ru and (c,d) CoRu@MHCS.

Table 7. 1: Co and Ru content, particle size and pulse chemisorption data of the catalyst composites.

Sample	dispersion (H:Co)[a]	Particle size (nm)		Co_3O_4 and RuO_2 content (%) /TGA	Co loading (%)/ICP	Ru content (%)/ICP
		XRD[b]	TEM			
Co@MHCS	0.007	6.1	7.4	12.46	9.12	-
Co@MHCS@Ru	0.010	6.9	7.3	14.45	9.30	0.27
CoRu@MHCS	0.028	6.2	7.1	13.99	8.99	0.10

[a] Obtained by pulse chemisorption, using a 1:1 ratio of hydrogen atoms to total moles of Co loaded on the sample. [b] Crystallite sizes estimated using Rietveld refinement.

Hydrogen pulse chemisorption at 150 ℃ experimental data is shown in Table 7.1. Higher dispersion (almost double that of Co@MHCS and Co@MHCS@Ru) for CoRu@MHCS was attributed to the intimate contact of the Ru and Co atoms. In this case it suggested that the Ru promoter effects are more pronounced when the particles are in close to one another thus by primary hydrogen spillover the Co_3O_4 nanoparticles were easily reduced with compromising the nanoparticles dispersion and causing metal sintering. However, although the Co@MHCS@Ru had Ru nanoparticles loaded on the outside of the carbon shell its metallic dispersion did not significantly vary from the unpromoted Co@MHCS catalyst (0.007 versus 0.01). This therefore suggested that Ru promoter effects via the carbon shell on the encapsulated Co_3O_4 nanoparticles were not effective in enhancing the reduction degree of the encapsulated nanoparticles, therefore signifying limited hydrogen spillover via the secondary process at the analysis temperature (150 ℃) and reduction temperature (350 ℃).

TGA analysis (Figure 7.4,a) under the flow of air revealed that all the catalysts had similar decomposition profiles with the onset of the carbon consumption via the oxidation step in which the carbon structure is converted to carbon dioxide occurred at approximately 310 ℃. A complete decomposition of the carbon in the catalysts was observed at temperatures between 550-620 ℃. The low decomposition temperature of these carbon materials is attributed to the catalytic effects of the metal nanoparticles which have been observed in our previous study **[112, 217, 255]**. However, hollow carbon spheres prepared using resorcinol formaldehyde as the carbon source has been observed to be highly defective and hence it is not highly thermally stable under an oxidizing environment. The left over residue for these catalysts (between 12-15 %) was then attributed to the cobalt oxide and ruthenium oxide particles, and in doing so we were able to estimate the loading of the aforementioned metals in the three catalysts (see Table 7.1 and Figure 7.4,a). These

loading corresponded well with metallic loading that were obtained using ICP-OES analysis (see Table 7.1). Powder X-ray patterns confirmed the highly defective nature of the hollow carbon shells (i.e. no distinct carbon diffraction peaks), and that the encapsulated nanoparticles had the Co_3O_4 phase (**ICSD collection number 9362**), with the corresponding crystallite sizes as estimated by Rietveld refinement were 6.1, 6.9 and 6.2 nm for Co@MHCS, Co@MHCS@Ru and CoRu@MHCS respectively. Raman spectroscopy (Figure 7S.5) also confirmed the presence of Co_3O_4 nanoparticles (i.e. A_{1g} band around 700 cm^{-1}) inside the hollow carbon spheres **[311, 312]**. The D and G band of the carbon spheres signified a carbon shell with significant defect due the D band broad peak and the G to D band ratio greater than one here highlight a highly defective carbon shell as suggested by Robertson and Ferrari guidelines on the interpretation of amorphous-like sp^2 carbon materials **[313, 314]**.

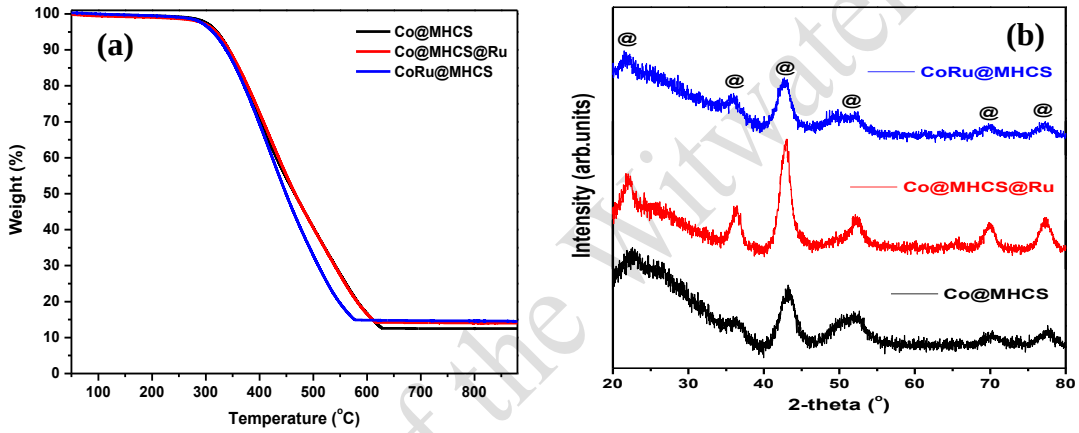

Figure 7. 4: (a) Thermogravimetric and (b) PXRD diffraction data of the catalysts materials, (@) Co_3O_4.

7.3.2. Carbon shell porosity analysis

High porosity in these materials allows for the easy diffusion of reactants and products both into and out of the hollow carbon sphere cavity. The resulting adsorption isotherms of these catalysts suggests that the carbon shell had a pore structure that is type I/IV in nature (Figure 7.5) **[197]** with both micropores and mesopores. This was supported by the high BET surface area between (440-480 $m^2.g^{-1}$) and that > 52 % of the total surface area on the catalysts was due to the microporous nature of the carbon shell (Table 7S.1). This microporosity was also confirmed by the pore size distribution plots, which showed greater nitrogen adsorption at average pore diameters of < 2 nm, although ideally mesopores are the preferred pores because the allow much easier diffusion.

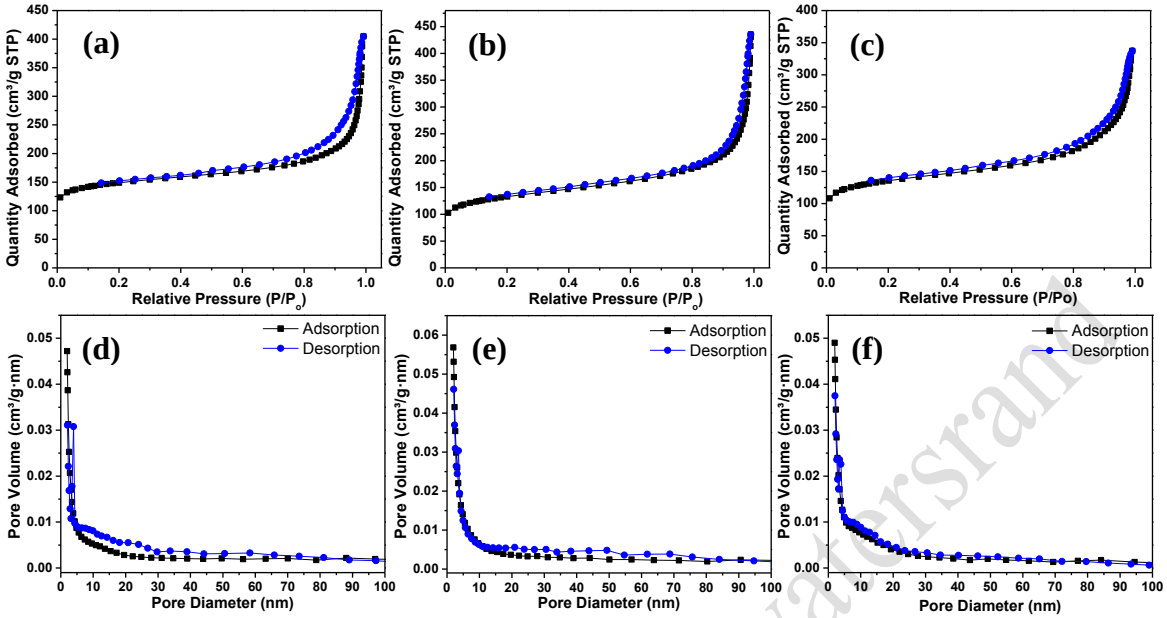

Figure 7. 5: Nitrogen adsorption-desorption isotherms and pore size distribution plots of the catalysts. (a,d) Co@MHCS, (b,e) CoRu@MHCS and (c,f) Co@MHCS@Ru.

7.3.3. Catalyst reduction using in Situ PXRD

Reduction of the catalysts under hydrogen gas was followed in situ using PXRD studies in 50 ℃ intervals from 30 ℃ to 500 ℃ (Figure 7.6, Table 7.2) **[297]**. Distinct reduction profiles were observed for the different catalysts. For the Co@MHCS catalyst displayed a phase transformation from Co_3O_4 to Co via the CoO intermediate. In the reduction the cobalt oxide nanoparticles transformed to CoO at 250 ℃ while the transformation of CoO to fcc-Co began to be more pronounced at 300 ℃ and increased in intensity up to 500 ℃. However the CoO was not completely reduced and consistently appeared with the Co phase. Thus suggests incomplete reduction even at 500 ℃. In contrast for Co@MHCS@Ru complete Co_3O_4 conversion to CoO occurred at 250 ℃ (i.e., between 200 and 250 ℃), while the CoO phase transformation to fcc/hcp Co began at 350 ℃. Complete reduction of the oxide to Co was observed at 450 ℃ both the fcc and hcp Co phases were observed.
Reduction of Co_3O_4 to CoO on CoRu@MHCS was complete at 250 ℃ (similar to Co@MHCS and Co@MHCS@Ru). However, a complete reduction to CoO to Co (fcc and hcp) appeared at 300 ℃, and from 350 ℃ to 500 ℃ the two Co phases were clearly observed in the diffraction patterns. With the fcc phase the dominant Co phase. The reduction profiles of all these catalysts (Co@MHCS, Co@MHCS@Ru and CoRu@MHCS), displayed similar reduction profiles on the conversion of Co_3O_4 to CoO (occurring in the range of 200-250 ℃). This therefore suggests that the Ru promoter regardless of its location relative to the Co_3O_4, did not significantly influence the hydrogen

induced Co_3O_4 conversion to CoO. However, the second reduction process from CoO to Co was visibly different for all the catalysts. These differences can be attributed to the relative location of Ru promoter to the Co nanoparticles. The transformation temperature of CoO on the catalysts increased following this trend, CoRu@MHCS < Co@MHCS@Ru < Co@MHCS. This trend implies that when the Ru promoter was placed further from the CoO nanoparticles the reduction temperature increased. It thus appears that in Co@MHCS@Ru a secondary hydrogen spillover process in which the hydrogen atoms (that were formed by dissociation of H_2 molecules on Ru nanoparticles) were transported via a defective carbon shell to the CoO thus lowering the reduction temperature required to reduce CoO to Co when compared to the CoO on Co@MHCS.

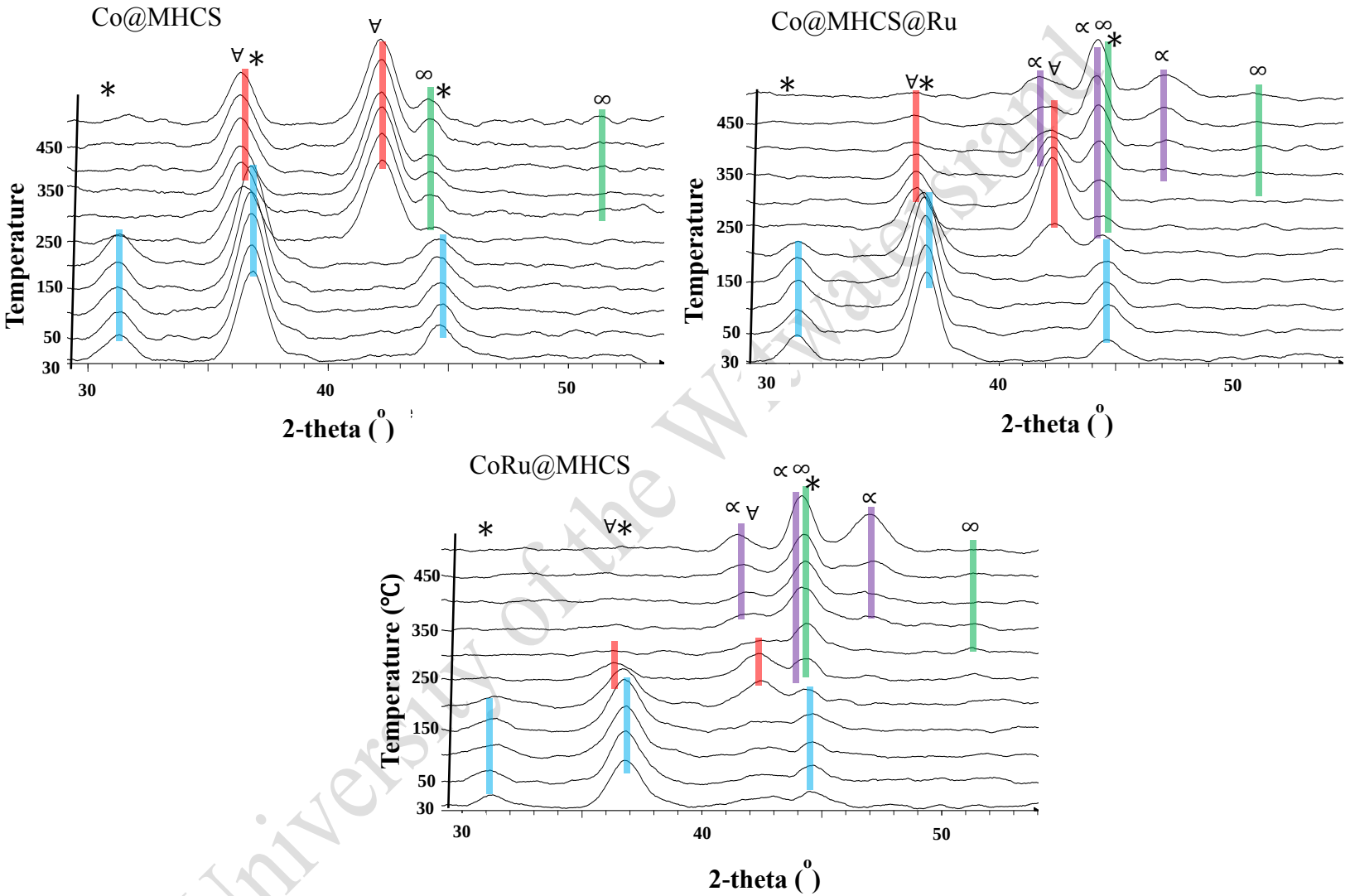

Figure 7. 6: In situ PXRD profiles of the catalysts under reduction conditions. Co_3O_4 (*), CoO (∀), α-Co (∞), β-Co (α).

Table 7. 2: In situ PXRD reduction.

Scan #	Temperature (℃)	Observed Phase		
		Co@MHCS	**CoRu@MHCS**	**Co@MHCS@Ru**
1	30	Co_3O_4	Co_3O_4	Co_3O_4
2	50	Co_3O_4	Co_3O_4	Co_3O_4
3	100	Co_3O_4	Co_3O_4	Co_3O_4
4	150	Co_3O_4	Co_3O_4	Co_3O_4
5	200	Co_3O_4	CoO	Co_3O_4/CoO
6	250	CoO/α -Co	CoO/β-Co	CoO
7	300	CoO/α -Co	CoO/β -Co/α-Co	CoO
8	350	CoO/α -Co	CoO/β -Co/α -Co	CoO/Co
9	400	CoO/α -Co	β -Co/α -Co	CoO/β -Co/α -Co
10	450	CoO/α -Co	β -Co/α -Co	CoO/β -Co/α -Co
11	500	CoO/α -Co	β -Co/α -Co	β -Co/α -Co

[a]hcp cobalt (β -Co) and [b]fcc cobalt (α -Co)

The catalyst degree of reduction was also evaluated from the in situ XRD patterns. This allowed a facile method to obtain the DOR at a specific temperature. Using the Rietveld refinement method, the DOR at 350 ℃ (the T used for the catalyst reduction) was approximately 29% for Co@MHCS, 50% for Co@MHCS@Ru and 100% for CoRu@MHCS at 350 ℃ (Figure 7.5). This can be compared to the actual DOR estimated by oxygen titration assuming a Co to Co_3O_4 transformation which were lower at 21.5, 22.2 and 61.3 for Co@MHCS, Co@MHCS@Ru and CoRu@MHCS respectively (Figure 7S.6 and Table 7S.2) **[97]**. This difference can be attributed to the encapsulating nature of the carbon nanoreactor on the cobalt nanoparticles, in which some of the Co nanoparticles surfaces were not exposed to the oxygen gas as they were embedded inside the carbon shell which had predominantly microporous pore structure. The formation of amorphous Co_xO_y phases that cannot be detected during PXRD measurements can also enhance DOR from Rietveld refinement calculations as compared to the oxygen titration values **[296, 297].** Nonetheless the observed DOR trend on these catalysts suggests a location dependent

effect of the Ru metal toward reduction of cobalt oxide nanoparticles due to the physical barrier separation by the carbon shell.

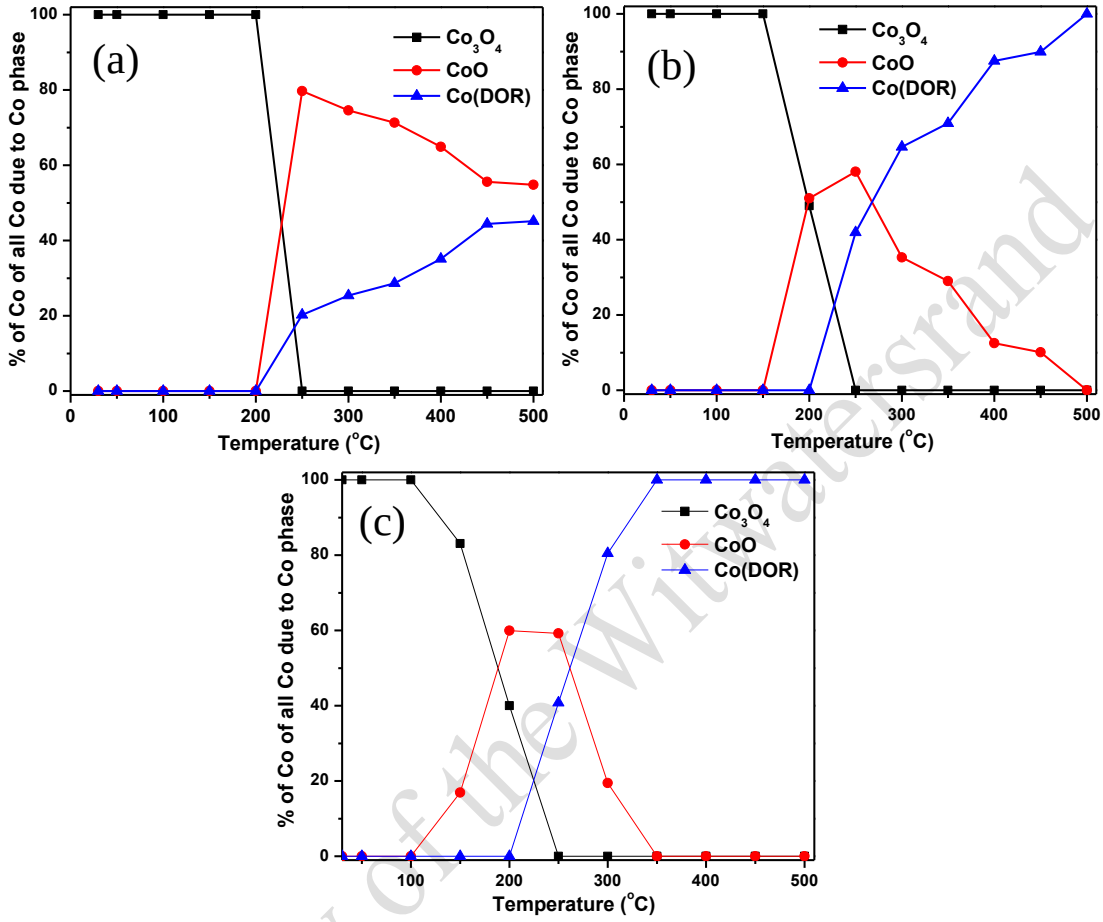

Figure 7. 7: Co phase abundance changes as a function of temperature during in situ PXRD under a hydrogen environment: (a) Co@MHCS, (b)Co@MHCS@Ru, (c) CoRu@MHCS.

These in situ PXRD studies therefore suggest that both primary and secondary hydrogen spillover processes do (or can) serve as Ru promotion processes on Co Fischer-Tropsch catalysts. It should however be noted that based on the observed reduction temperatures (specifically for CoO to Co transformation) the primary spillover is more favoured than secondary hydrogen spillover due to the surface diffusion of hydrogen on the carbon support being a rate limiting step **[136].** Further reduction analysis using temperature programmed reduction (Figure 7.S7 Table 7.S3) suggest similar reduction profiles for the Co@MHCS and Co@MHCS@Ru, with the Co_3O_4 to CoO transformation occurring at 323 and 312 ℃ and the CoO to Co phase transformation occurring at 415 and 414 ℃ respectively. However, the CoRu@MHCS catalyst had a much lower reduction temperature (264 ℃) **[128]**. From the TPR data it can be concluded that the effect of Ru nanoparticles

on the Co oxide nanoparticles reduction using the dynamic characterization technique could not be effectively detected and separated with respect to the unpromoted Co@MHCS. This since the carbon support can be gasified at higher temperatures to form methane whose TCD signal overlaps with the signals that correspond to the hydrogen consumption by the Co oxide phases. The carbon support gasification (see Figure 7S.5 and Table 7S.3, and peak at approximately 700 ℃) was substantial on these catalysts due to the high defect content and low graphitic nature of the hollow carbon shell.

7.3.4. Fischer-Tropsch Analysis

The Fischer-Tropsch evaluation of the catalysts was performed at 220 ℃ and 10 bar pressure (Table 7.3 and Figure 7S.8) after reduction at 350 ℃. In the Fischer-Tropsch study the catalyst activity followed a similar trend (as the catalysts DOR) with respect to CO conversion of 11.8, 12.4, 18.3% for Co@MHCS, Co@MHCS@Ru and CoRu@MHCS respectively. The catalyst turnover frequency increased with the increasing intimacy of the Co and Ru metals (from 14 to 24 $\times 10^{-4}$ s^{-1}). In several other studies it has been shown that by loading the Co and Ru metal using a co-precipitation method or a sequential method the Co and Ru had different contact distances and hence gave affected Fischer-Tropsch activities, that changed with the Co-Ru contact **[128, 304, 315]**. The Co@MHCS and Co@MHCS@Ru with almost similar activity after reduction at 350 ℃ (similar extend of reduction),thus the Ru did not enhance the Co activity owing to Co and Ru separation and the carbon shell length that the spilt-over hydrogen had to travel over its defective structure.

Although the high degree of reduction on CoRu@MHCS due to the primary hydrogen spillover should also lead to high Fischer-Tropsch activity, as evidenced by the Fischer-Tropsch data, the synergistic effect on the Ru promoted Co catalyst cannot be ruled out to explain the observed data. This is due to the proposed positive electronic effects that a Ru promoter affords on Co atoms and the corresponding nanoparticles as it relates to its enhanced ability to dissociate hydrogen and carbon monoxide at higher rates **[128, 315].**

With this observation it can then be concluded that at 350 ℃ the secondary hydrogen spillover process does not help in increasing the catalyst DOR and the subsequent catalysts Fischer-Tropsch activity possibly due to the decreased diffusion rate the spillover hydrogen at this temperatures (i.e. 350 ℃ and 220 ℃). Therefore there was no discernible or significant effect of the Ru promoter on the Fischer-Tropsch activity of Co in the Co@MHCS@Ru catalyst, when compared with the unpromoted Co@MHCS. Because the catalysts had similar Co nanoparticles sizes the difference in activity can be attributed to the extent of catalyst reduction and the type of hydrogen spillover mechanism that was dependent on Co and Ru metal intimacy on the hollow carbon support. The low TOF as it relates to other catalysts in the literature is attributed to the microporous nature of the

hollow carbon spheres since it might lead to diffusion limitations for reactant and the products **[198, 217]**.

Table 7. 3: Fischer-Tropsch Synthesis results.

Sample	CO Conversion (%)	Activity $\times 10^{-6}$ ($mol_{CO}/g_{Co}.s$)	TOF (s^{-1} 10^{-4})	Selectivity (C mol) %		
				C_1	C_2-C_4	C_{5+}
Co@MHCS	11.8	3.64	14	18.7	10.1	71.2
Co@MHCS@Ru	12.4	4.68	18	20.8	8.3	70.9
CoRu@MHCS	18.3	6.07	24	36.4	14.4	49.1

Sample	Olefinicity (%): ($molC_{=}/molC_{-}$)*100%			
	α	C_2	C_3	C_4
Co@MHCS	0.74	21.2	200.8	128.9
Co@MHCS@Ru	0.69	5.66	95.7	59.6
CoRu@MHCS	0.61	6.8	115.3	68.4

Hydrocarbon selectivity (Table 7.3) of the catalysts suggests that the Ru promoter in these studies increased the formation of methane and paraffins. Methane selectivity increased as the Ru and Co nanoparticles intimacy increased; 18.7, 20.8 and 36.8% for Co@MHCS, Co@MHCS@Ru and CoRu@MHCS. Numerous studies have shown that the hydrogen dissociation on noble metal promoters leads to Co Fischer-Tropsch product distribution with high methane selectivity **[131, 139, 305].** The high methane selectivity is however in contrast with several other studies where Co catalysts were promoted by Ru **[316, 317]**. In our study the high methane selectivity was also attributed to the microporosity of these nanoreactors that held up the high molecular weight products leading to their slow rate of effusion. High methane selectivity invariably leads to decreasing C_{5+} selectivity (71.2 for Co@MHCS, 70.9 for Co@MHCS@Ru and 49.1% for CoRu@MHCS), this also corresponded to the decreased ASF values of 0.74, 0.69 and 0.61 respectively. Catalyst olefinicity was evaluated using C_2-C_4 products. The presence of the Ru promoter enhanced the formation of alkanes over alkenes (see Table 7.3). The olefinicity of Co@MHCS@Ru and CoRu@MHCS was low as compared to the Co@MHCS catalyst. The lowering of the olefin content in the product spectrum was attributed to the cleaning effect of the Ru promoter due to its high propensity to dissociate hydrogen - hence the high hydrogen concentration on the catalyst surfaces, that increased the hydrogenation rate of the olefins **[131, 315].**

7.4. Conclusions

We report on the synthesis of a catalytic nanoreactor for application in the Fischer-Tropsch Synthesis using cobalt nanoparticles encapsulated inside hollow carbon spheres. This synthetic method yielded porous catalytic composites whose morphology and defective nature was also exploited to study the effect of hydrogen spillover in the Fischer-Tropsch process. Co and CoRu nanoparticles with similar particles sizes were successfully encapsulated inside the hollow spheres, while a third catalyst was prepared by loading Ru nanoparticles on the outside of Co@MHCS catalysts. This guaranteed Co and Ru separation on the support. The catalyst reducibility (followed by in situ PXRD) was in the order CoRu@MHCS > Co@MHCS@Ru > Co@MHCS and suggests that the secondary spillover over the carbon shell on Co@MHCS@Ru did occur and enhanced the Co_3O_4 reduction. However, this spillover effects was more pronounced at high temperatures. The secondary spillover rate is dependent to the number defects that form on the carbon as the reduction temperature was increased.

The Fischer-Tropsch reaction results suggest that highly hydrogenated products will form due to the Ru on the Co active sites, owing to the hydrogen enriched surfaces included by the hydrogen spillover particularly on Co@MHCS@Ru. On the carbon support the secondary hydrogen spillover did not enhance the catalyst activity as the process did not enhance the catalyst DOR when compared to the unpromoted Co@MHCS catalyst.

Chapter 8

Effect of Water on the Stability of Co Fischer-Tropsch Nanoparticles inside Hollow Carbon Spheres: An In Situ Magnetometer Study

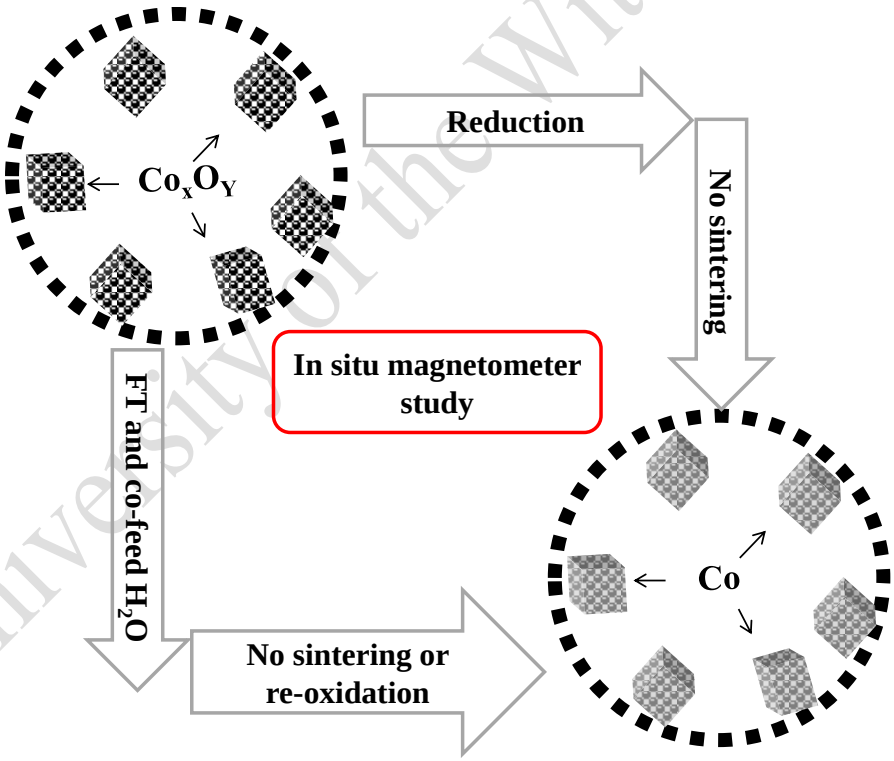

Supporting information: Appendix D

Abstract: Water is understood to be one of the deactivating agents in Co Fischer-Tropsch synthesis, and the development of stable catalysts is of outmost importance. In this study Co and Ru promoted Co nanoparticles (corresponding oxide sizes of 7.7 and 6.1 nm respectively) were encapsulated inside hollow carbon spheres to study their resistance to deactivation by water under simulated Fischer-Tropsch conditions. The in situ magnetometer provided a n ideal instrument to study the catalysts in operando. With this instrument the catalysts showed a maximum DOR of around 60% for both Co@MHCS and CoRu@MHCS, while the Co/MHCS (i.e. Co outside the hollow spheres prepared by normal deposition precipitation method) displayed a maximum DOR of 41%. No re-oxidation of the catalyst was observed at high water levels for all the catalysts. Sintering of the encapsulated Co nanoparticles was quite negligible (< 5%), however it was more pronounced for the catalyst Co nanoparticles loaded on the outside of the hollow carbon spheres (γ > 22%). Our carbon nanoreactors as Fischer-Tropsch catalysts showed more stability against sintering and re-oxidation when compared the Co/MHCS

.

8.1. Introduction

Cobalt Fischer-Tropsch synthesis is at the centre of the modern day gas to liquid (GTL) technology for the beneficiation of syngas from natural gas or biomass to high value products. This involves series hydrogenation reactions of carbon monoxide at elevated pressures and temperatures resulting in the formation of water and hydrocarbons.

Consequently water is the main by-product of the Fischer-Tropsch catalytic process, and has been observed to play a significant role in the behaviour of Fischer-Tropsch catalysts in terms activity, stability and selectivity **[318-320]**. This is because under Fischer-Tropsch reaction conditions the resulting water molecules tend to chemically interact with the catalyst surfaces, causing possible oxidation and restructuring of the catalyst nanoparticles **[66, 67, 78]**. Fratalocchi and co-workers **[320]**, observed after co-feeding water (up to 29 % H_2O content) with syngas on a Co/Al_2O_3 catalysts at 220 ℃ and 25 bar, that (1) water permanently deactivated the catalyst possibly via re-oxidation of the Co active sites and (2) in terms of selectivity water inhibited the hydrogenation kinetics of the catalyst leading to low methane selectivity, increased olefin to paraffin ratio, decreased alcohol content and a higher water gas shift reaction rate. Given that the main deactivation mechanisms on Co Fischer-Tropsch catalysts include sintering and nanoparticles re-oxidation **[19],** it is therefore vital to understand the effect of water on the sintering and oxidation deactivation mechanisms during Fischer-Tropsch synthesis.

In Co Fischer-Tropsch synthesis it has been proposed that the effect of nanoparticle sintering (via Ostwald ripening or particle coalescence) is responsible for approximately 30% of the loss of activity **[63]**. It has also been suggested that vaporized water at higher temperatures (i.e.at Fischer-Tropsch conditions can enhance the sintering processes that happen on catalysts surfaces **[321]**, thus water would generally increases particles together with thermal degradation processes.

Bezemer et al. **[66]**, studied the role of water on Co Fischer-Tropsch catalysts supported on carbon nanofibers (Co nanoparticles average size = 5 nm) using Mossbauer measurements in a flow reactor. The reduced cobalt catalyst was exposed to different H_2O/H_2 ratios of 1, 2, 4, 10 and 30 (at 220℃. 20 bar and relative humidity of 25%). The analysis of the Mossbauer signal showed no oxidation of the nanoparticles. However, when the relative humidity was increased to 62% the Mossbauer spectrum showed a signal loss that corresponded to the presence of super paramagnetic nanoparticles (i.e. small particles). This loss was attributed to the sintering of the smaller nanoparticles. Furthermore, a comparison of the Fischer-Tropsch activity (at 220 ℃, 20 bar and H_2/CO of 2) between the freshly reduced catalyst and one exposed to water were 2.3×10^{-5} and 1.1×10^{-5} $mol_{CO}/g_{Co}.s$ respectively, a decrease in activity attributed to the sintering of the Co nanoparticles from 5 nm to 21 nm by nanoparticle coalescence. An in situ magnetometer study by Claeys and co-workers **[67]**, on a Pt promoted Co catalyst supported on alumina (Co size between 3

and 15 nm) suggested that sintering occurred at by high CO conversions and high water partial pressures in the catalytic reactor under simulated Fischer-Tropsch conditions. They proposed a sintering mechanism in which the particles grew via the cobalt carbonyl species migration facilitated by surface hydroxides on the support. Eschemann and De Jong **[64]**, also correlated the loss of FT activity (at 220 ℃, 20 bar and $H_2/CO = 2$) of a Co catalyst supported on titania at high CO conversion (i.e. high water partial pressures) to catalyst sintering. In their study a Co/TiO_2 catalyst prepared by deposition precipitation with an initial CO conversion of 61.4% and average Co size of 8.0 nm, showed a decrease in activity after 200 hours on stream (with a final cobalt time yield to initial cobalt time yield ratio of 0.72) and a corresponding Co nanoparticle size of 10.1 nm.

It is also possible that high partial pressures of water in Fischer-Tropsch synthesis can result in the re-oxidation of the Co nanoparticles resulting in the formation an inactive Co_x-O_y phase **[320]**. This re-oxidation has been shown both theoretically and experimentally to be prominent on small super paramagnetic Co nanoparticles (< 4.4 nm). Hence, oxidation by water is Co particle size dependent **[76]**. Moritz et al. **[78]**, prepared monodisperse Co_3O_4 nanoparticles of different sizes (2.8, 5.5 and 7.1 nm) on Stöber silica spheres to evaluate their size dependent nature to different concentrations of water that were co-fed with syngas into the reactor (220 ℃ and different H_2O, H_2 and CO pressures). Using an in situ magnetometer the small Co nanoparticles (2.8 nm) was oxidized upon introduction of water (H_2O/H_2 ratio between 0.15 and 50) in the reaction chamber as evidenced by the loss of magnetization of the Co. Upon introduction of water onto the cobalt nanoparticles (average size of 5.5 nm) a significant loss of magnetization occurred when a H_2O/H_2 ratio of 20 was used. The onset of magnetization loss on the 7.1 nm nanoparticles was more prominent at H_2O/H_2 partial pressure ratio of 40 (initial oxidation ensued at H_2O/H_2 ratio of 20). At a H_2O/H_2 ratio of 50, half of the 2.8 nm Co particles were oxidized, while only 4% of the Co was oxidized on the 7.1 nm Co particles. No significant growth in crystallite sizes were observed in this study, this was probably due to low catalysts loading. The oxidation mechanism by water was suggested to be enhanced by CO adsorption and the catalyst support (in this case, silica). And X-ray photoelectron spectroscopy study by Wu et al. **[322]**, showed that a Co foil can be oxidized when it's exposed by water at room temperature, thus alluding to the oxidizing nature of water that forms in situ during Fischer-Tropsch synthesis. However, Bezemer et al. **[66]**, did not observe any oxidation on 5 nm Co nanoparticles supported on carbon nanofibers when water [H_2O/H_2 in the range of 1 to 30] was fed into the reactor at 220 ℃ and 20 bar. However, feeding water without any hydrogen resulted in some oxidation of the nanoparticles, thus - suggesting no oxidation under Fischer-Tropsch synthesis.

The above studies clearly demonstrate that water is a major component that can lower the activity in Fischer-Tropsch synthesis. In this study we present an in situ magnetometer study of Co nanoparticles inside porous hollow carbon spheres to elucidate the stability of

these catalytic nanoreactors against deactivation via water. This was compared to a catalyst where the Co nanoparticles were loaded on the outside of the hollow carbon spheres. This study was performed using simulated Fischer-Tropsch conditions to mimic reaction conditions under typical high CO conversions. Furthermore, ability of the nanoreactors to hold up water molecules inside the hollow carbon spheres to increase encapsulated Co nanoparticles oxidation as compared to Co nanoparticles outside the hollow spheres was also evaluated.

8.2. Experimental procedure

8.2.1. Chemicals

Styrene (Aldrich), polyvinylpyrollidone (PVP, MW 40 k, Aldrich), cobalt nitrate hexahydrate (Aldrich), Ethylene glycol (Aldrich), ammonia solution (25%; Fluka), potassium persulfate (Eimer and Amend), hexadecyltrimethylammonium bromide (CTAB; Aldrich), ruthenium chloride (Aldrich), hydrazine (35%, Aldrich), ethanol (98%; Merck), isopropanol (99%, Merck) were used as received. Deionized water was used in all the experiments where water was required.

8.2.2. Synthesis of polystyrene spheres (PSSs)

Styrene (16 mL) and PVP (0.2 g) were dispersed in 250 mL of a water/ethanol solution (water, 200 mL and ethanol 50 mL) by sonication and then stirred for 15 min. Potassium persulfate solution (0.3 g in 20 mL water) was added to the solution while stirring. The mixture was then heated at 80 ℃ for 24 hours. The product was then filtered and purified by washing with ethanol and then repeatedly using water.

8.2.3. Loading of Co or CoRu on the polystyrene spheres (3% Co/PSSs or 3 %Co 0.2%Ru/PSSs)

PSSs (3 g) were dispersed by sonication for 30 minutes in a 200 mL (water/ethanol solution, 150 and 50 mL respectively). To this solution was added cobalt nitrate hexahydrate (0.445 g) while stirring until it completely dissolved forming a red solution. Deposition of Co nanoparticles was performed by a slow addition of a hydrazine solution (10 mL, 2 M), the solution was left to stir for 12 hours to ensure complete deposition of the Co nanoparticles. To make the bimetallic CoRu/PSSs composite the cobalt and ruthenium precursors (5.95 mL, 0.01 M, $RuCl_3$) were dissolved together and loaded on the PSSs (Co, 3% and Ru at 0.2%).

8.2.4. Synthesis of Co or CoRu nanoparticles inside hollow carbon spheres

CoRu/PSSs, Co/PSSs or PSSs (3 g) and ammonia solution (25%; 2 mL) were dispersed by sonication for 30 min in 200 mL of ethanol water solution (150 mL ethanol and 150 mL water). Resorcinol (1.13 g), formaldehyde solution (37%; 2 mL) and CTAB (1.5 g) in ethanol (150 mL), was then added to the first solution and the total mixture was stirred at room temperature for 20 h to form the resorcinol-formaldehyde (RF) polymer around the CoRu/PSSs or Co/PSSs. The resulting composite (CoRu/PSSs@RF or Co/PSSs@RF was then filtered and washed repeatedly with water followed by drying at 80 ℃ for 12 hours. Template removal and carbonization was performed following a one-step procedure inside a horizontal tube furnace. This was achieved by heating the CoRu/PSSs@RF or Co/PSSs@RF under nitrogen flow (50 mL/min) at 350 ℃ for 1 hour to decompose and remove the polystyrene template followed by annealing of the carbon spheres at 600 ℃ for 2 hours under the nitrogen atmosphere. The resulting products were Co or CoRu nanoparticles inside porous hollow carbon spheres (i.e. **Co@MHCS and CoRu@MHCS**). **MHCS**, empty hollow carbon spheres were prepared in a similar way when the metal was loaded on the polystyrene spheres.

8.2.5. Loading of Co nanoparticles on the outside of hollow carbon spheres (Co/MHCS)

Cobalt nanoparticles (targeting 10% loading) were loaded on to MHCS by a homogeneous deposition precipitation procedure using urea. The MHCS (1 g) were dispersed in 200 mL of water and to this solution was added cobalt nitrate hexahydrate (0.31 g) and urea (0.1 g). The solution was then dispersed by sonication for 10 minutes. Deposition was then performed at 95 ℃ for 18 hours using the slow decomposition of the urea, which served as the precipitating agent. After precipitation the slurry solution was then dried at 65 ℃ using a rotary vapour. The sample was then dried at 100 ℃ in an oven, followed by calcination at 200 ℃ under 5% O_2/Ar.

8.2.6. Magnetic measurements

Detailed descriptions of the analysis technique can be found in references **[67, 78, 237].** Reduction, re-oxidation and sintering under Fischer-Tropsch conditions were performed inside an in situ magnetometer instrument. The fixed bed reactor (diameter = 12.7 mm, maximum pressure up to 50 bar)) was exposed to a field controlled magnet with field strengths of up to $\pm$ 20 kOe (i.e. $\pm$ 2 T). The hollow carbon sphere catalyst (0.1 g) was placed inside the fixed bed reactor. The saturation magnetization of the catalysts measured at 2 T was used to estimate the amount of metallic cobalt and hence the degree of reduction during reduction. This magnetization was also measured during dry and simulated Fischer-Tropsch conditions. Information about particle sintering was obtained by performing a full magnetic analysis over $\pm$ 2 T to obtain the full hysteresis scan from which the remnant

magnetization (i.e. magnetization at 0 T) was used to estimate the nanoparticle size distribution after every set of reaction conditions (see Fischer-Tropsch process conditions below).

8.2.7. Fischer-Tropsch Synthesis evaluation experiments

The catalyst (0.1 g) was reduced at 350 ℃ and 1 bar in the reactor using ultra-pure hydrogen for 2 hours at a gas hourly space velocity of 500 mL/g_{cat}.min. The reactor was then cooled to 220 ℃ under an argon gas flow, followed by a flow of syngas (H_2/CO = 2) with a gas hourly space velocity of 150 mL/g_{cat}.min and reactor pressure at 10 bar, for the dry Fischer-Tropsch synthesis run. To simulate Fischer-Tropsch conditions at high CO conversions the partial pressure of water was incrementally increased by co feeding it with the syngas to model both 70 and 95% CO conversions in the reactor. The oxidation and sintering behavior of the catalysts were monitored for two hours. Finally the reactor was cooled to 50 ℃ under argon and the catalyst passivated using 1% O_2/N_2 for 30 minutes.

Table 8. 1: Reaction conditions under dry and simulated Fischer-Tropsch conditions.

Water level	P_{H2O} (bar)	P_{Syngas} (bar)	P_{H2O}/P_{H2}	Simulated X_{CO} (%)	P_{total} (bar)
0	0	10	0	-	10
1	3.62	10	1	70	13.62
2	6.63	10	8.14	95	16.63

8.3. Results and Discussion

8.3.1. Catalyst characterization

The catalysts (Co@MHCS, CoRu@MHCS and Co/MHCS) were made by a templating procedure in which Co and CoRu nanoparticles were added to PSSs and then covered by a carbon layer made from resorcinol-formaldehyde as the carbon source **[78]**.

Figure 8.1 shows TEM images of the catalysts and their size distributions. The hollow carbon spheres displayed size distributions between 300 and 420 nm and an average carbon shell of 28 nm. Using the hard template synthesis the Co and CoRu nanoparticles were encapsulated inside the hollow carbon spheres for Co@MHCS and CoRu@MHCS and no evidence of nanoparticles on the outside of the hollow carbon spheres was observed. Co@MHCS and CoRu@MHCS had average particle sizes of 7.7 and 6.1 nm respectively. The catalyst Co/MHCS was prepared by precipitation of the cobalt precursor using urea at 95 ℃. The TEM images revealed a large particle size distribution for the Co_3O_4 particles of between 2 and 50 nm (Figure 1c,d). This could be due to the lack sufficient of anchoring sites (i.e. acid groups) on the pre-synthesized spheres and the dominant microporosity on the hollow spheres thus leading to the support's low capacity to take up 10% of the Co metal with good dispersion (see red circles Figure 1,c and d), hence the resulting wide range in catalyst dispersion and a bimodal average particle size centered at 8 nm and 16 nm and an overall average nanoparticle size of 11 nm.

Table 8. 2: Catalysts crystallite sizes and loadings.

Sample	Particle size (nm)		Co_3O_4 content (%) /TGA
	XRD	TEM	
Co@MHCS	5.9	7.7±2.2	11.9
CoRu@MHCS	6.1	6.1±1.3	12.1
Co/MHCS	7.3	11.0 ±6.1	14.7

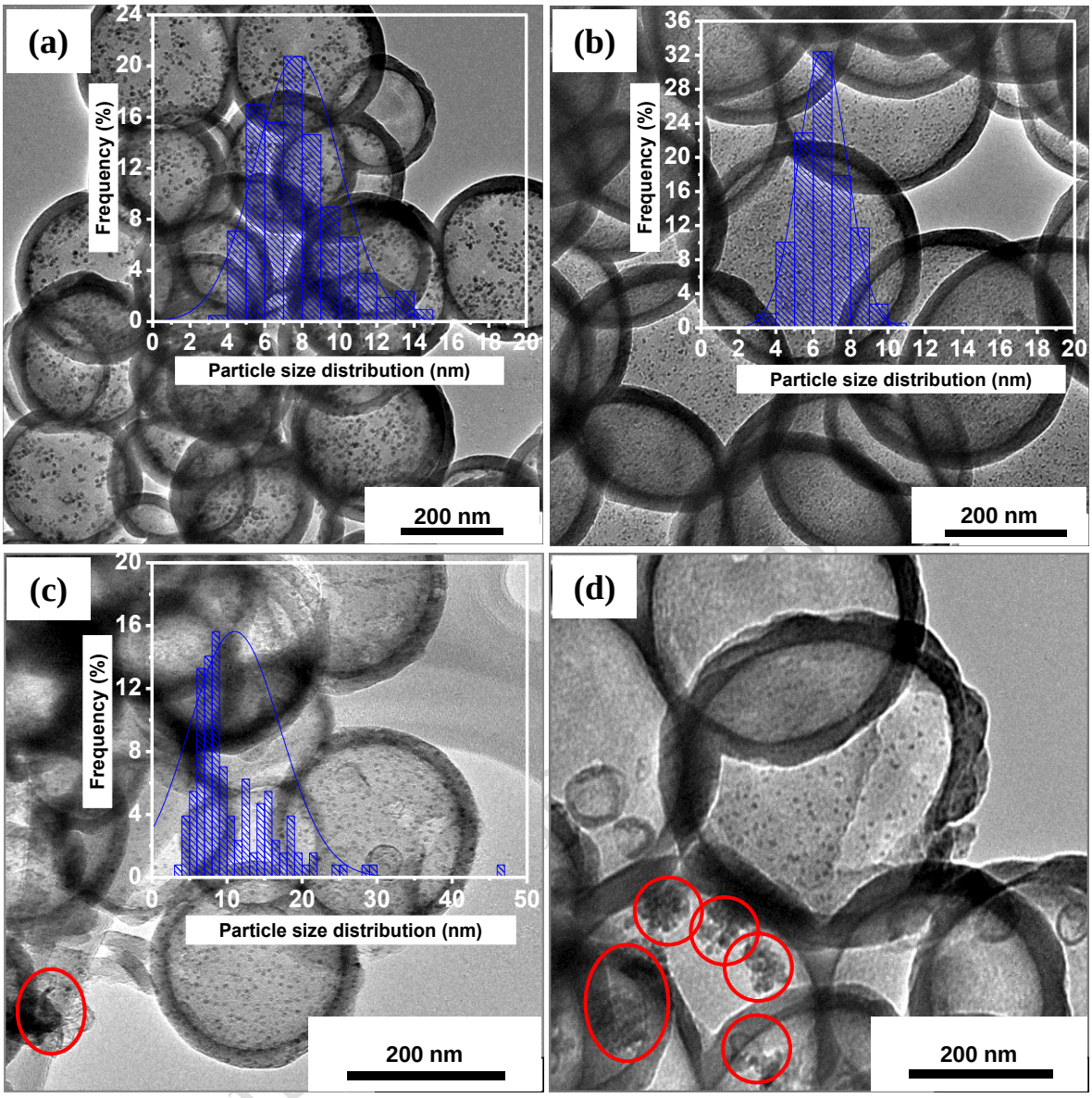

Figure 8. 1: TEM and particle size distributions of the catalysts, (a) Co@MHS, (b) CoRu@MHCS and (c, d) Co/MHCS.

Analysis of the catalysts by PXRD showed the Co catalysts phases to be Co_3O_4 and CoO, indicating that for both the Co@MHCS and CoRu@MHCS full oxidation of the catalysts at 600 ℃ during annealing of the carbon shell had not occurred. This was due to the fact that an inert gas (nitrogen) had been used during the annealing process **[178]**. Only the Co_3O_4 phase was observed on Co/MHCS, after calcination at 200 ℃ in 5% O_2/Ar. Catalyst crystallite sizes were estimated from the PXRD patterns (8.2,a) using the Scherer equation to be 5.9, 6.1 and 7.3 nm similar to with the number based average nanoparticle sizes calculated from TEM the images **[295]**. The TGA profiles shows were used to compute the

amount of Co loaded on the catalysts based on the residual amount of Co_3O_4 left after complete decomposition of the carbon material in air (see Table 2 and Figure 8.2,b).

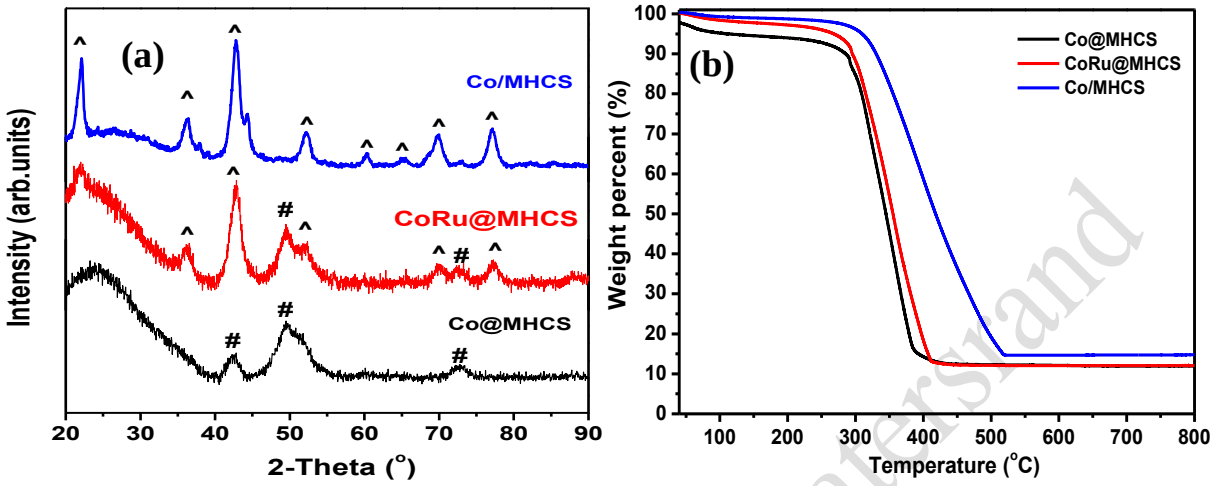

Figure 8. 2: (a) Powder XRD and (b) TGA profiles of the catalysts. Co_3O_4 (^) and CoO (#) phases.

8.3.2. In situ magnetometer measurements

8.3.2.1. In situ catalyst reduction

Catalyst reduction under ultrapure hydrogen was followed in situ using a magnetometer **[78].** Both the Co_3O_4 and CoO are not ferromagnetic at this temperature range and any magnetization observed will be due to metallic cobalt. Thus the magnetization data can be correlated to the catalyst degree of reduction. The method is very sensitive and very small amounts of the Co species can be detected at low temperatures **[323]**. Analysis of the Co@MHCS reduction data (Figure 8.3,a), revealed that the catalysts had approximately 30% of metallic Co prior to reduction with H_2. This value remained relatively constant until a reduction temperature of about 150 ℃ was reached. Then a gradual increase in the degree of reduction that reached a maximum of between 54 and 61% at a reduction temperature of 350 ℃ after 2 hours. A slight increase of the DOR of reduction (to approximately 65 %) after the reactor was cooled to 220 ℃ was also observed. CoRu@MHCS (Figure 8.3,b) displayed a similar reduction pattern. However, the initial metallic content was low at19% degree of reduction. This increased at temperatures just above 150 ℃, reaching up to 57% reduction after 2 hours at 350 ℃ - an increase to approximately 63% DOR occurred upon lowering the temperature to 220 ℃. The presence of metallic Co even before reduction is ascribed to the incomplete oxidation of the Co nanoparticles in the hollow spheres; Co@MHCS surprisingly contained only the CoO phase while a mixture Co_3O_4 and CoO phases were observed on CoRu@MHCS. The early reduction of the CoO phases at 150 ℃ was attributed to the possible hydrogen spillover from the Co nanoparticles that facilitated

their reduction at low temperatures. A further increase in the degree of reduction at 220 ℃ cannot be attributed to any increase in the metallic Co. This is because the magnetic response is also dependent on temperature and the subsequent increase must therefore be due to the temperature change only. From the data below it appeared that the Ru promoter effects did not enhance the CoO reduction. This may relate to the poor mixing and alloying of the Co-Ru because of the incomplete formation of the Co_3O_4 phase were Ru ions can be entrenched inside the oxide lattice **[128],** thus leading to almost similar DOR for both Co@MHCS and CoRu@MHCS.

The reduction profiles for the Co/MHCS (Figure 8.3,c) shows that formation of metallic Co only began at temperatures above 300 ℃, reaching a maximum of 41% degree of reduction after cooling the reactor to 220 ℃. A low rate of reduction is seen when compared to the encapsulated Co nanoparticles, because the catalyst did not have any significant metallic Co before the reduction process.

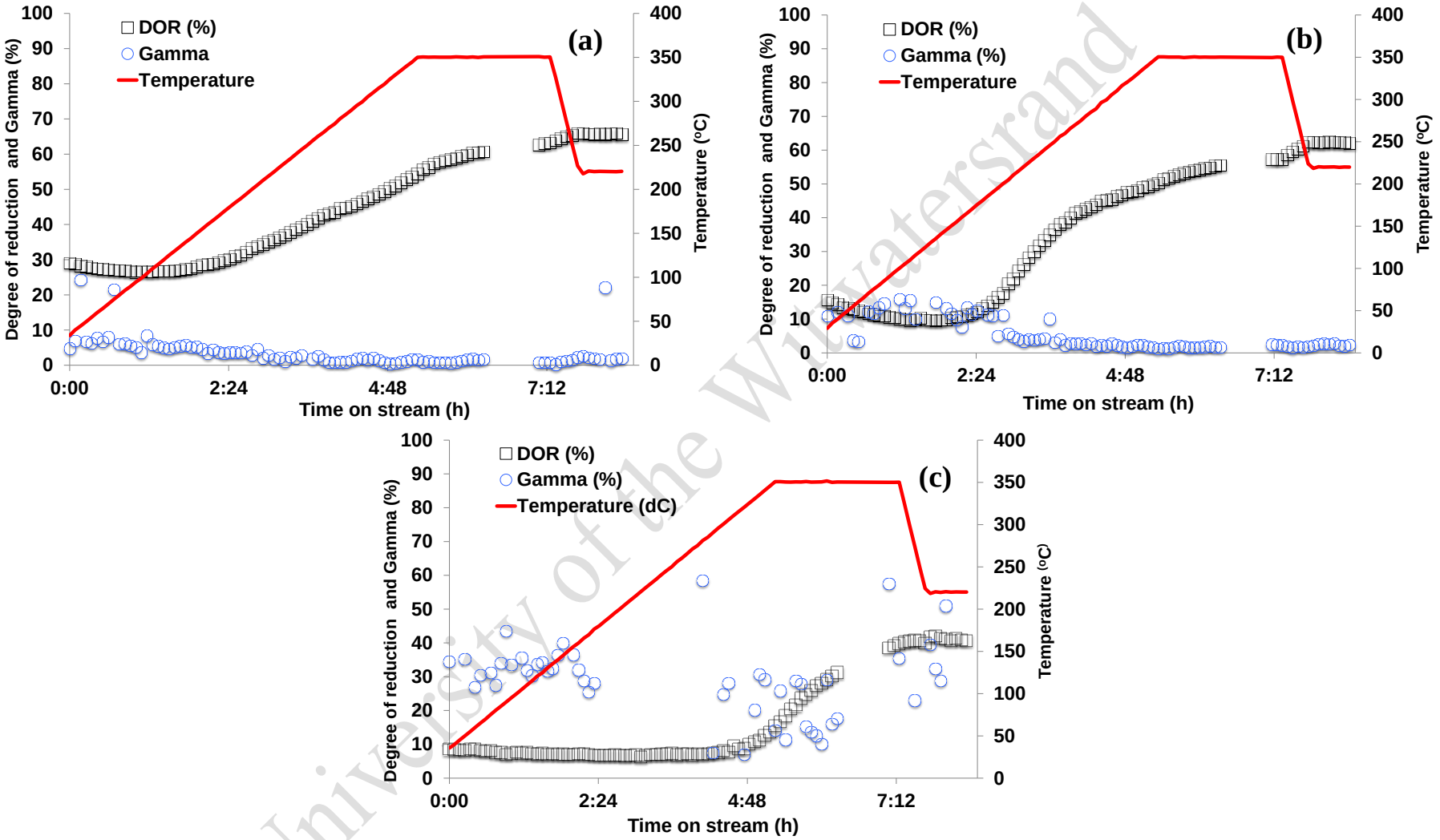

Figure 8. 3: In situ reduction of the catalysts: (a) Co@MHCS, (b) CoRu@MHCS and (c) Co/MHCS.

8.3.2.2. Extend of reduction during dry and wet Fischer-Tropsch conditions

The catalyst degree of reduction using in situ magnetization data was followed during Fischer-Tropsch synthesis (Figure 8.4). After introduction of the syngas a sudden drop in the catalyst magnetization was observed for all the catalysts. This slight drop in DOR has been associated with the adsorption of CO, C and O moieties on the Co catalyst surfaces **[67, 323]**. The catalysts extent of reduction under dry Fischer-Tropsch conditions remained constant with no loss of catalyst magnetization (at water level 1). An increase in the Fischer-Tropsch conversion by simulating high conversions through a co-feeding of water was subsequently performed to evaluate the re-oxidation resistance of the catalysts. At water level one (H_2O/H_2 ratio of 1, 70% CO conversion) the degree of reduction for all the catalysts (Co@MHCS, Co@MHCS and Co/MHCS) were constant time on stream. A further increase of the co-fed water to level 2 (H_2O/H_2 ratio of 8, 90% CO conversion) yielded no decrease in magnetization of the catalysts. However, a slight decrease (< 5% drop) in magnetization can be observed for CoRu@MHCS at this high water levels. This could be correlated with the Co nanoparticle size since the Co nanoparticles in this catalyst were smaller (at < 6 nm) thus they are more prone to re-oxidation at high water levels than larger Co nanoparticles. The evaluation of these catalysts at high water content co-fed with syngas gave results consistent with numerous other studies on the effect of water on Co Fischer-Tropsch catalysts. Bezemer et al. **[66]**, showed that no re-oxidation occurred on the catalysts (Co/CNF, average size > 5 nm) when the catalysts were subjected to water in the presence of hydrogen at process conditions. Furthermore Fischer et al. **[77]**, showed through in situ studies of Co catalysts supported on alumina that there existed a critical Co crystallite size whereby re-oxidation is feasible.

In this study the Co@MHCS catalyst was exposed to the water level one (H_2O/H_2 ratio of 1) followed by Fischer-Tropsch at dry conditions then back to water level one (H_2O/H_2 ratio of 1) (see Figure 8.4, a). It was observed that cycling the catalyst between the wet and dry Fischer-Tropsch conditions did not negatively affect the catalyst degree of reduction. The DOR showed a slight increase after the removal of co-fed water from the syngas. It can thus be deduced that the metallic content of Co catalyst at high Fischer-Tropsch conversions does not easily undergo re-oxidation. This behaviour is not support dependent, as similar results had been obtained with other catalyst supports (i.e. alumina, silica) **[67, 78].** However, the catalyst nanoparticle size can determine the ease of Co nanoparticle re-oxidation at high CO conversion and which is in turn also influenced by the catalyst metal-support interface for very small Co nanoparticles. Furthermore in our study the DOR of the catalysts (under Fischer-Tropsch conditions) was not dependent on the Co nanoparticles location on the hollow carbon spheres supports; as the encapsulated nanoparticles showed similar behaviour to the Co nanoparticles loaded on the outside of the hollow carbon spheres thus also alluding to similar accessibility of water molecules on the different catalysts, possibility because of the hollow carbon sphere significant microporosity (see

Chapter 7, BET results) that can induce some diffusion limitation for water molecules to access the encapsulated Co nanoparticles.

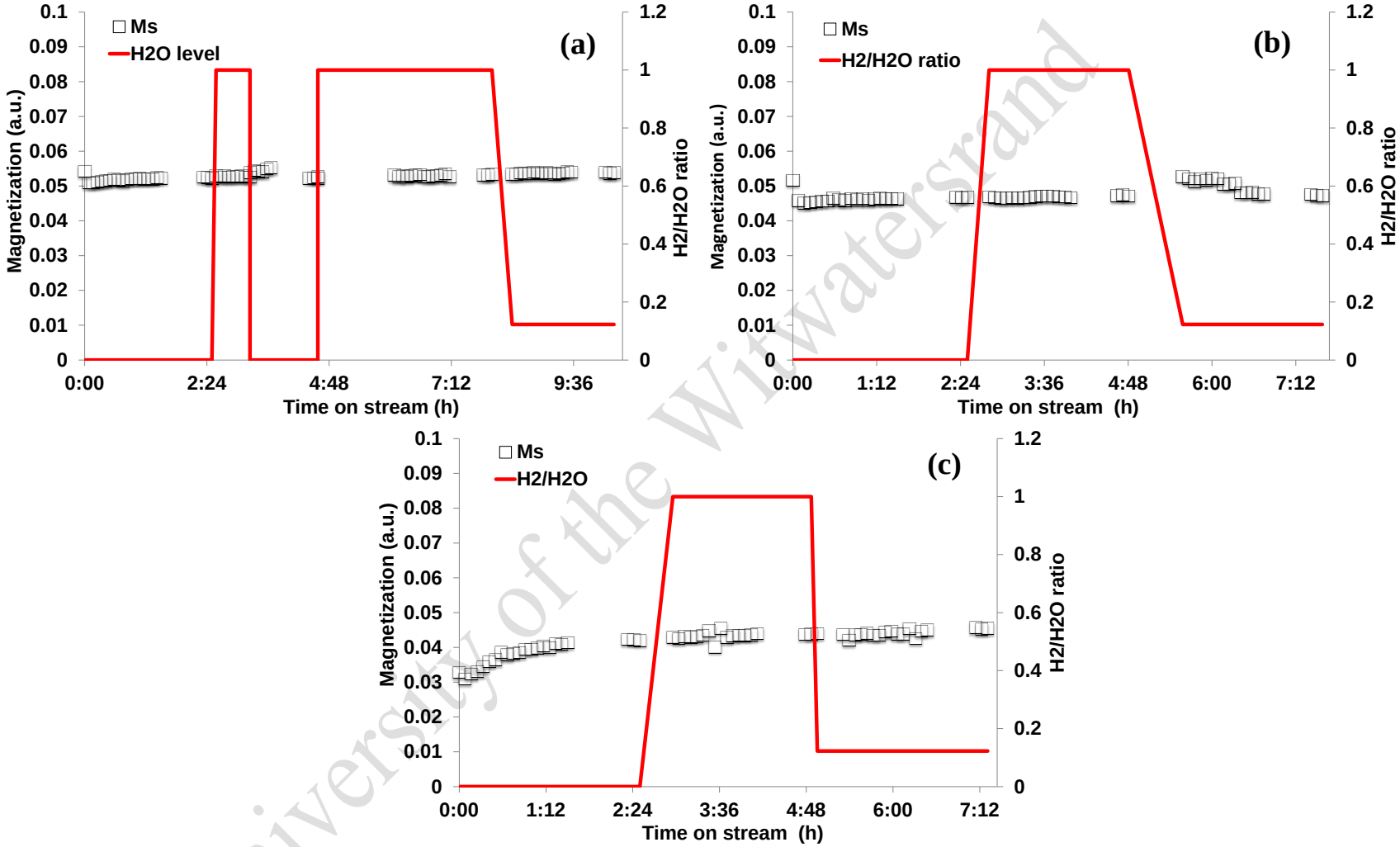

Figure 8. 4: Catalyst magnetization (i.e. degree of reduction) as a function of co-fed water during Fischer-Tropsch: (a) Co@MHCS, (b) CoRu@MHCS and (c) Co/MHCS.

8.3.2.3. Sintering under during reduction, dry and wet Fischer-Tropsch conditions

Particle size evolution of the catalysts were evaluated us using the Langevin method **[67, 78, 237, 323]**, Co@MHCS and CoRu@MHCS's particle size distribution were also extracted from the hysteresis plots (Figure S8.1). For the Co/MHCS this distribution could not be obtained because of the large gamma value corresponding to the percentage of Co with sizes above the critical size for superparamagnetism (see Table 8.3). The crystallite sizes of the catalysts (Co@MHCS, CoRu@MHCS) were analyzed after reduction at 350 and 220 ℃ and also after different Fischer-Tropsch conditions (see Figure 8.5). For Co@MHCS (Figure 8.5,a) the cobalt size range remained at 26 nm under all the conditions. However, after reduction and simulated Fischer-Tropsch condition, the particles size distribution showed an increase in the percentage of Co sizes above 7 nm, implying a loss of the small Co nanoparticles by Ostwald ripening. The increase was small (Table 8.3) and the catalyst average gamma value remained relatively constant below 5 %. CoRu@MHCS (Figure 8.5,b) the size range was calculated to be smaller (17 nm) and showed no growth of Co nanoparticles by Ostwald ripening. This is possibly due to the catalyst's narrow particles size distribution; hence there were no smaller Co nanoparticles that were aggregated with the relatively larger nanoparticles.

The catalyst's average particle size was centred on 5 nm compared to 6 nm on Co@MHCS, whose average size shifted to higher values (≥ 7 nm) at higher water levels (90% CO conversion). CoRu@MHCS average gamma value was less that 3% throughout the catalyst's evaluation signifying the catalyst stability against sintering during harsh Fischer-Tropsch conditions. For the Co/MHCS the particle size evolution could only be tracked using the gamma value. The value was almost 40 % at 220 ℃, this can be taken as discrepancy since the gamma value for all the other was below 25%. However, by considering the gamma value at both the dry and wet Fischer-Tropsch conditions there was increase from 20 % (dry conditions) to just above 24% at Fischer-Tropsch conditions simulated at 90% CO conversion. This suggests a slight growth of the Co nanoparticles supported on the outside of the hollow carbon spheres, when compared to the Co nanoparticles of Co@MHCS and CoRu@MHCS whose gamma value showed an insignificant increase or decrease. The ability of Co nanoparticles to sinter has been suggested to be dependent on the catalyst supports. In their study Claeys et al. **[67]**, postulated that the Co nanoparticles sinter (especially the smaller nanoparticles) via a formation of Co subcarbonyl species on an oxidic support (alumina). Bezemer et al. **[66]** also observed Co nanoparticles sintering during co-feeding of water on a carbon support (graphitic carbon nanofibers). This therefore suggest that the observed sinter resistance of the encapsulated Co nanoparticles can be attributed to geometry of the hollow carbon spheres support as it was formed and healed onto the Co nanoparticles. The nanoparticles embedded on the inside of the support supports which had the capability of limiting their

mobility against the sintering effects induced by water under the Fischer-Tropsch conditions used in the study.

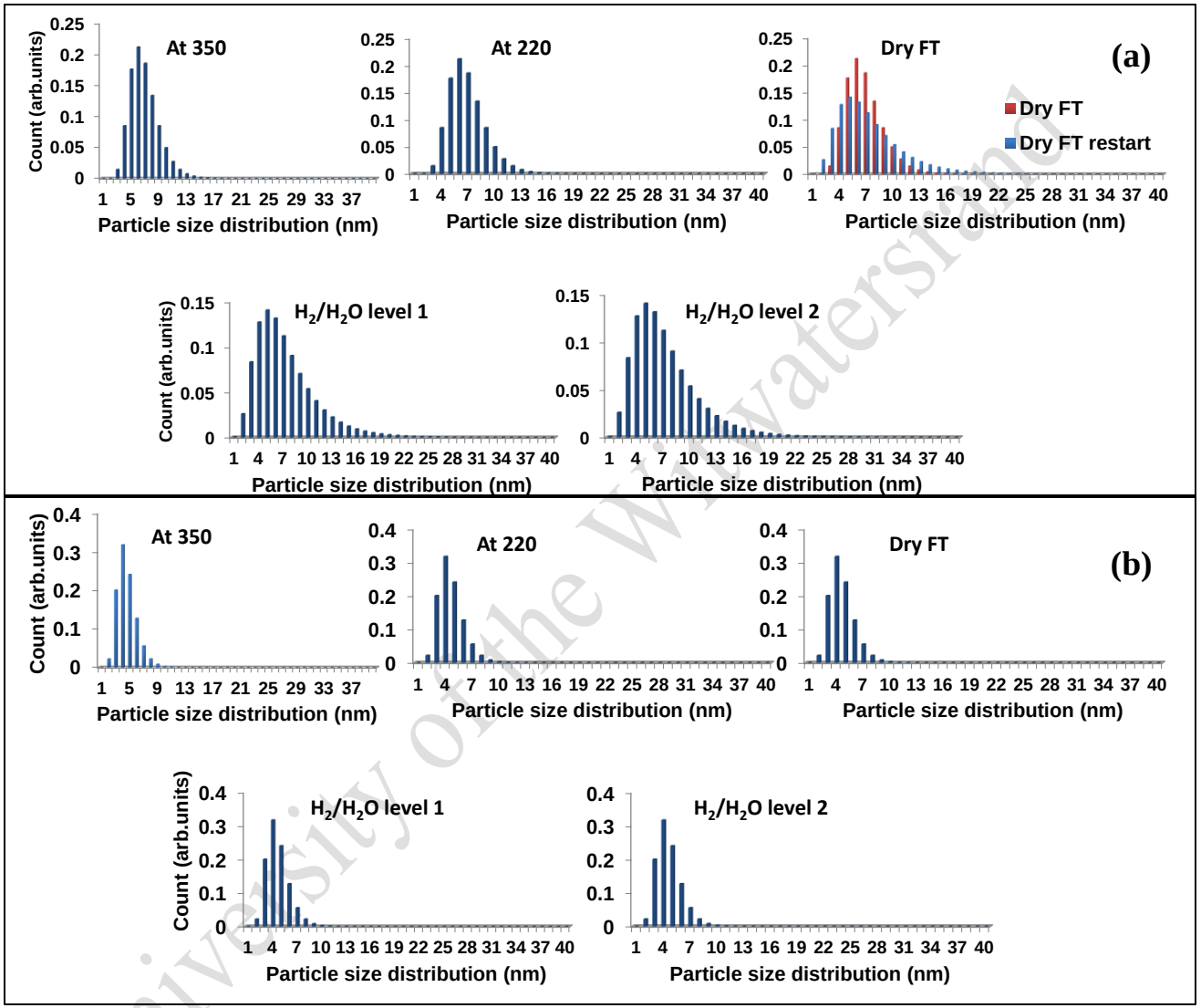

Figure 8. 5: Co particle size distribution after subjecting the catalysts at different reaction conditions, data extracted by the Langevin equation: (a) Co@MHCS and (b) CoRu@MHCS.

Table 8. 3: Particles size distribution as obtained by the Langevin method.

	Particle size range (nm) and Gamma (%)					
	Co@MHCS		CoRu@MHCS		Co/MHCS	
	Range	γ	Range	γ	Range	γ
At 350	26	3.5	17	2.2	-	24.9
At 220	26	4.5	17	2.3	-	39.6
Dry FT	26	4.7	17	2.1	-	20.9
H_2/H_2O level 1	39	4.3	17	2.4	-	22.4
H_2/H_2O level 2	39	4.9	17	1.8	-	24.3

Figure 8.6 shows the change in gamma value with time on stream, as noted above the value represents the fraction of the Co nanoparticles that are above the critical diameter for superparamagnetism to be observed. In this graph below all then gamma values (Co@MHCS, CoRu@MHCS and Co/MHCS) showed a downward trend suggesting an insignificant growth of the Co nanoparticles from the reduction process until the final analysis after subjecting the catalysts to syngas high water content (simulating up to 90% CO conversion).

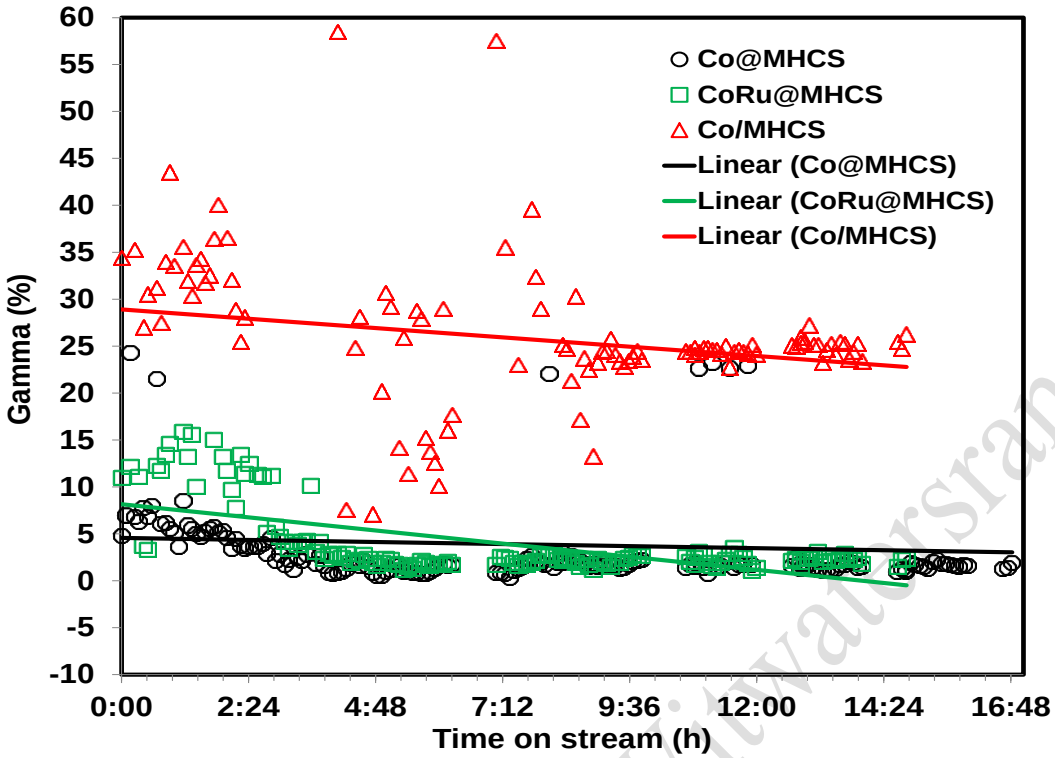

Figure 8. 6: Gamma values of the catalysts as a function of time under different reaction conditions (reduction, dry and wet Fischer-Tropsch).

8.3.2.4. TEM images of the spent catalysts

The passivated spent catalysts were analysed using TEM after Fischer-Tropsch synthesis and their TEM images are shown in Figure 8.7. Co@MHCS and CoRu@MHCS displayed average particle sizes of 6.3 and 5.7 nm compared to observed averages of 6 and 5 nm from the in situ magnetometer studies. This showed that the nanoreactors indeed stabilized the encapsulated Co nanoparticles. The particle size distribution on Co/MHCS (Figure 8.7) remained broad (0-50 nm) hence the particle growth shift could not be easily discerned as for Co@MHCS and CoRu@MHCS.

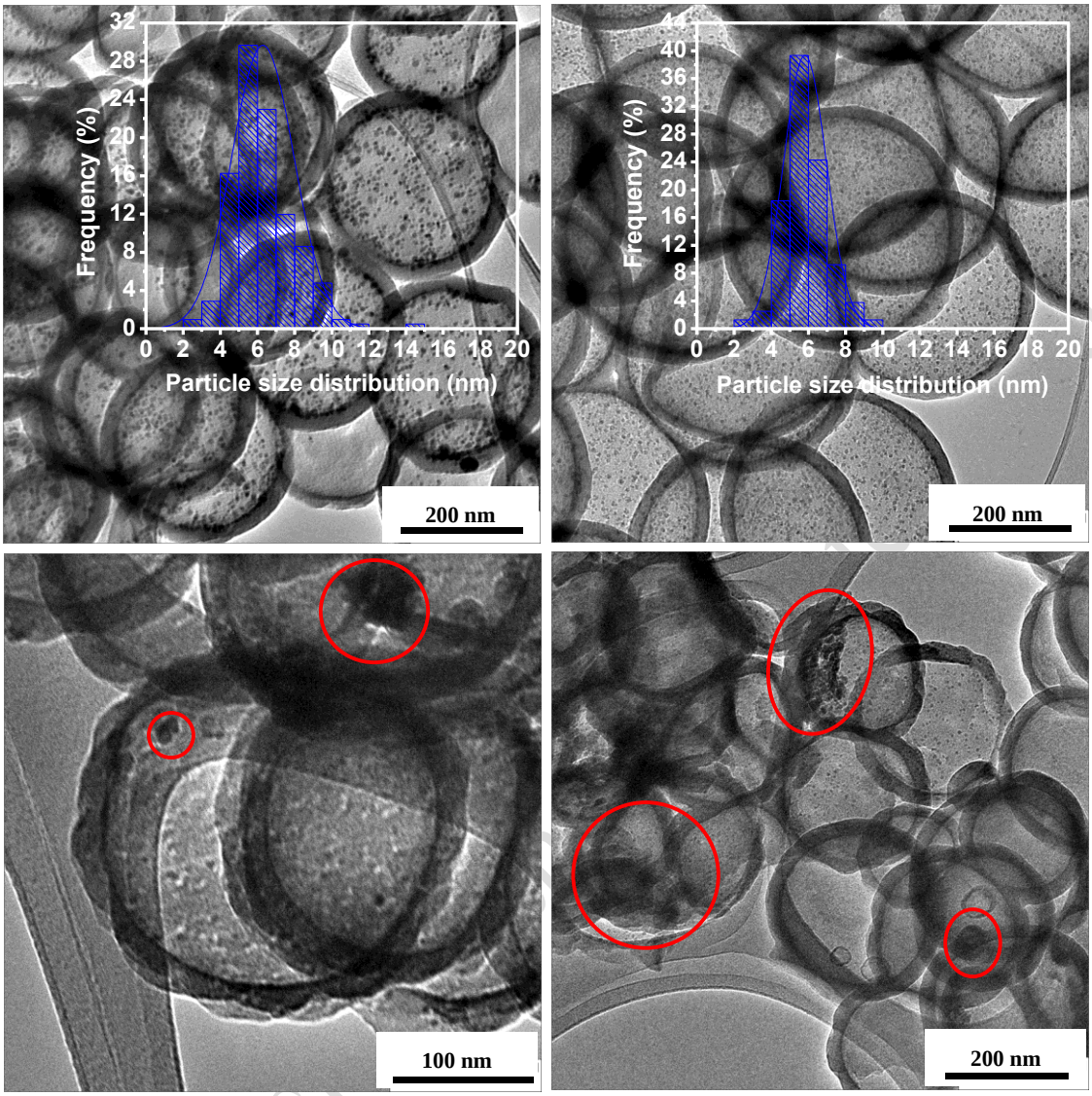

Figure 8. 7: TEM images after in situ magnetometer studies.

8.4. Conclusions

The stability of Co nanoparticles inside and outside hollow carbon spheres was evaluated using an in situ magnetometer under typical Fischer-Tropsch conditions simulating high CO conversions. The Co nanoparticles were not significantly re-oxidized by the co-fed at all the water levels, even up to CO conversions of 90%. The studies confirm that oxidation to CoO of the nanoparticles only occurs on Co nanoparticles with smaller average diameter (<5 nm). In terms of sintering the Co nanoparticle growth on the encapsulated nanoparticles could not be detected. However, the nanoparticles supported on the outside displayed a slight growth which was attributed to the different synthesis procedures used.

The encapsulated nanoparticles appear considerably resistant to sintering due to them being embedded on inside of the hollow carbon spheres shell. The limited sintering was also confirmed by the TEM analysis of the spent catalysts.

Chapter 9

A sinter resistant Co Fischer-Tropsch catalyst supported on Titania; with Ru promoter and mesoporous silica as the structural promoter.

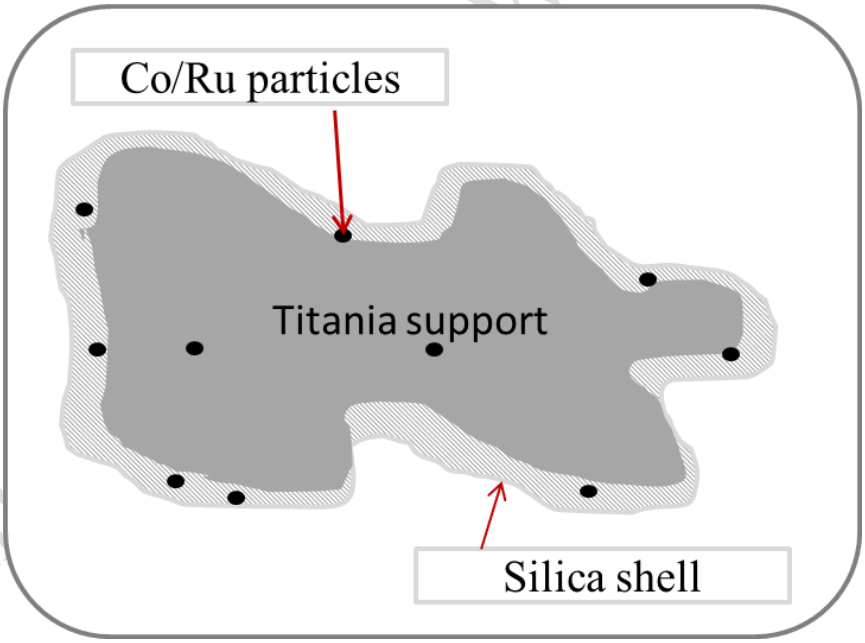

Figure 9. 1: Image showing the $Co/TiO_2@mSiO_2$ three-phase material architecture.

Supporting information: Appendix E

Abstract: One of the pathways responsible for deactivation of Fischer-Tropsch catalysts is the loss of active metal surface area due to nanoparticle agglomeration. To combat this effect efforts have been made to increase the interaction between the metal nanoparticles and the support using materials like silica. Covering supported metal particles with a highly porous layer was used to stabilize Co nanoparticles on titania during reduction and under reaction conditions. In this study Co_3O_4 nanoparticles (size range 8-12 nm) supported on titania were stabilized by coating them with a thin layer of mesoporous silica (~ 4 nm) to make Fischer-Tropsch catalysts that are less prone to sintering ($Co/TiO_2@mSiO_2$). To mitigate the strong metal support interactions brought about by the titania and silica a Ru promoter was loaded together with the cobalt nanoparticles onto the titania ($CoRu/TiO_2@mSiO_2$). Variable temperature XRD studies on the evolution of the Co metal nanoparticles showed that there was no significant particle size growth under reduction conditions in the temperature range from 30 to 600 ℃. Chemisorption studies following reduction under hydrogen at 350 ℃ and 450 ℃ gave results consistent with the in situ XRD data when compared to the Co/TiO_2. Fischer-Tropsch synthesis on the $Co/TiO_2@mSiO_2$ and $CoRu/TiO_2@mSiO_2$ catalysts encapsulated inside the mesoporous silica shell exhibited good catalytic performance without any display of significant mass transport limitations that might arise due to a silica shell coating of the active sites. For these two catalysts the Fischer-Tropsch activity increased with reduction temperature without any significant negative changes in their selectivity due to sintering, while the activity on $Co@TiO_2$ decreased due to Co nanoparticle sintering.

9.1. Introduction

The Fischer-Tropsch synthesis (FTS) is a key technology in the synthesis of liquid hydrocarbons from gaseous feedstock that can be derived from coal, natural gas and biomass **[100, 242]**. Cobalt metal is the preferred active catalyst in the synthesis of these hydrocarbons by FTS in a hydrogen rich syngas **[67, 306, 324, 325]**. The extended interest on the use of cobalt catalyst for FTS is due to the fact that cobalt metal is economically cheaper in comparison to the other high activity Fischer-Tropsch metals (i.e., Ru)**,** and has a comparatively higher Fischer-Tropsch activity and lower propensity to water gas shift reaction than Fe. It is also highly selective to long chain hydrocarbons that can be easily upgraded to other beneficial products by hydrocracking **[242]**.

It is notable that despite almost more than half a century of research on Co metal attempts to control and limit catalyst deactivation during the FT reaction and catalyst treatment is still ongoing **[19, 67, 326]**.

Amongst the main causes of catalyst deactivation, sintering of cobalt particles under the reaction conditions has been proposed to be one of the major contributors in decreasing the Fischer-Tropsch activity of cobalt catalysts **[19, 64, 327]**. Catalyst sintering reduces the metal active surface area and can occur by these two mechanisms (1) particle coalescence or (2) Ostwald ripening **[19]**. To combat the deactivation of FTS catalysts by sintering, efforts have been made to increase the interaction between the metal nanoparticles and the support using strongly interacting materials like silica **[328, 329]**. One possibility is to cover the supported metal particles with a highly porous layer that can reduce sintering and thus stabilize FTS metal particles during reduction and under reaction conditions.

A number of studies are available in the technical literature that discusses the effects of encapsulating or immobilization of active metal particles using porous oxidic layers to prevent metal nanoparticle sintering during catalytic processes **[328, 330-332]**. The positive effect of this confinement against metal particle sintering has been validated using several characterization techniques such as XRD, TEM and chemisorption studies, by comparing the catalysts before and after catalytic process conditions. Lu et al. **[328]**, observed that a silica layer placed on top of a TiO_2 supported Pt catalyst greatly enhanced the sinter resistant capabilities of the system. In this case the silica shell was selectively deposited on the TiO_2 supported to allow sufficient exposure of the metal active sites while serving as a spacer that isolated the individual Pt nanoparticles. The tri-phase (i.e. $Pt/TiO_2@SiO_2$) catalyst displayed good stability up 800 ℃ in air for 20 hours and showed significant activity in p-nitrophenol reduction reaction using sodium borohydride. A TEM analysis study performed by Chen and co-workers for example **[331]**, have shown that the oxide shell coating methodology could also extended to non-noble metal catalysts. CuO nanoclusters with an approximate size of 60 nm synthesized by a solvothermal method and then coated with a mesoporous silica shell were compared with non-coated nanoclusters.

The two nanoclusters were tested for olefin (norbornene) epoxidation over a period of time and a number of cycles. The CuO@meso-SiO_2 remained unchanged after an 8 hour epoxidation reaction, whereas the CuO nanoclusters underwent severe sintering only after 4 hours of reaction. Furthermore, an epoxidation reaction on CuO@mSiO_2 for 720 hours did not show any significant catalyst particle aggregation. Similar procedures for preventing nanoparticle sintering have also been applied for bimetallic catalysts, such as Pt-Co nanoparticles for the oxygen reduction reaction (ORR) **[333]**. Pt_3Co nanoparticles were coated by a silica shell and they were supported on carbon materials. High temperature annealing at 800 ℃ under 10% H_2/Ar to allow sufficient alloying did not show any metal particle agglomeration. The Pt_3Co@SiO_2/C was compared with an uncoated Pt_3Co/C catalyst after annealing at 800 ℃ and showed particles sizes of 3.1 nm and 24.6 nm respectively as (using PXRD) when compared with the original Pt_3Co crystallite sizes in the range of 2-4 nm. This showed that the silica shell served as a structural stabilizer for preserving the original nanoparticle size and that the alloying capability of the material was not hampered. A number of other oxides such as, ceria and titania have also been used to similar effect as structural promoters and stabilizers to reduce metal nanoparticle sintering **[330, 334, 335]**. Reddy et al. **[334]**, used a thin layer of TiO_2 to stabilize Pt nanoparticles supported on silica spheres. The Pt/SiO_2@TiO_2 composite retained its morphology and shape after calcination at 600 ℃ in air with no apparent increase in Pt particle size. A high metallic dispersion of ~ 53 % was retained during a CO oxidation reaction demonstrating that the titania shell still allowed diffusion of reactants These studies therefore demonstrate that coating active metal particles with a protective layer can limit the nanoparticles affinity to sinter during catalysts pre-treatment and testing.

In this study we extend this protocol of preparing Co catalysts for FTS to study the effect of coating the supported cobalt nanoparticles with a mesoporous silica shell to limit the metal agglomeration during reduction and under FT conditions. The activity of uncoated cobalt catalysts was compared with that of cobalt catalysts encapsulated with silica shell to determine whether the increased metal interactions would (1) reduce sintering (2) lower the catalyst catalytic activity.

9.2. Experimental

9.2.1. Chemicals

Titania (TiO_2; Degusa), tetraethylorthosilicate (TEOS 98%; Aldrich), ammonia solution (25%; Fluka), hexadecyltrimethylammonium bromide (CTAB; Aldrich), ruthenium chloride (Aldrich), urea (Promark chemicals), ethanol (98%; Merck), cobalt (II) acetylacetonate (Aldrich), were used as received. Deionized water was used in the experiments.

9.2.2. Preparation of the cobalt supported on titania.

Co/TiO_2

Cobalt particles (10% wt) were loaded on the titania support using homogeneous deposition precipitation. Titania (10 g) was dispersed in 450 mL of water, and cobalt (II) acetylacetonate (4.363 g) and urea (0.4 g) were added and then dispersed by sonication for 20 minutes. Deposition of the Co particles was performed for 18 hours at 95 ℃ using the slow decomposition of the urea, which served as the precipitating agent. After precipitation the slurry solution was then dried at 65 ℃ using a rotary evaporator. The sample was then dried at 100 ℃

$CoRu/TiO_2$

Preparation of the Ru promoted catalyst was prepared using the same method, but in this case the loading was done to give a loading of 9.5% and 0.5% cobalt and ruthenium using cobalt (II) acetylacetonate (4.145 g) and ruthenium chloride solution (0.1M, 4.95 mL).

Calcination of the prepared samples was performed at 250 ℃ under static air for 2 hours.

9.2.3. Coating of the Co/TiO_2 with a mesoporous silica shell

Coating of the Co/TiO_2 catalysts precursors was done using TEOS as the silica source and CTAB as the surfactant. Co/TiO_2 (4 g) was dispersed in 150 mL of ethanol by sonication for 30 minutes. To this solution was added ammonia solution (1 mL). To coat with the silica shell an ethanol solution (50 mL) containing TEOS (2 mL) and CTAB (3 g) was then slowly added into the first mixture while stirring. The resulting solution was aged while stirring at room temperature for 12 hours to allow complete precipitation of the TEOS. The product was then filtered by vacuum filtration and then washed with acetone followed by drying of the solid product at 100 ℃ overnight.

The samples were calcined at 500 ℃ for 4 hours under static air.

The materials obtained were called **$CoRu/TiO_2@mSiO_2$ and $Co/TiO_2@mSiO_2$** (i.e mesoporous silica encapsulated Co or CoRu supported on titania) and **Co/TiO_2** (Co supported on titania).

9.2.4. Material characterization

TEM analysis was performed on a Tecnai spirit (T12) transmission electron microscope operating at 120 kV. The samples were dispersed in methanol by ultrasonication and loaded onto a copper grid. The bulk composition of the catalysts was analyzed using a Bruker D2 phaser equipped with a Lynxeye detector. The radiation used was the Co-Kα at

30 kV. The scan ranged from 10-90^{o} 2θ in 0.0260 steps. N_2 adsorption–desorption experiments were conducted at 195 ℃ using a Micromeritics Tristar 3000 surface area and porosity analyzer. Prior to an experiment, the sample was outgassed at 150 ℃ for 4 h under nitrogen gas. The BET surface areas were obtained from the adsorption data in a relative pressure range from 0.05 to 0.30. The total pore volumes were calculated from the amount of N_2 vapour adsorbed at a relative pressure of 0.99. The pore size distributions were evaluated from the desorption branches of the isotherms using the Barrett–Joyner–Halenda (BJH) method. The micropore area and volume were calculated using the t-plot data. The TPR experiments were carried out with a Micromeritics Auto Chem II unit. The catalyst (approximately 0.1 g) was placed in a quartz tubular reactor which was fitted with a thermocouple for continuous temperature measurement. The reactor was heated in a furnace. Prior to the temperature-programmed reduction measurement, the calcined catalysts were flushed with high-purity argon at 150 ℃ for 1 h, to remove water or impurities followed by cooling to ambient temperature. Then, 5% H_2/Ar was switched on, and the temperature was raised at a rate of 10 ℃.min^{-1} from 50 to 900℃. The gas flow rate through the reactor was controlled by three Brooks mass flow controllers and was always 50 mL.min^{-1}. The H_2 consumption (TCD signal) was recorded automatically by a computer. Pulse chemisorption was performed using the Micromeritics Auto Chem II instrument to give the number of active metal atoms. The catalyst (ca. 0.2 g) was placed in a quartz tubular reactor. The sample was reduced at 350 or 450 ℃ for 2 h under hydrogen flow of 50 mL.min^{-1}. Before injecting the active gas, the sample was purged using helium gas at 350 ℃ for 1 hour, followed by cooling to ambient conditions. Hydrogen chemisorption (assuming a H/Co ratio of 1) was then performed at 150 ℃ using ultra-pure hydrogen as the active gas and argon as the carrier gas.

9.2.5. Evaluation of Fischer-Tropsch Synthesis reaction

The Fischer–Tropsch synthesis was performed in a fixed-bed micro-reactor. A gas cylinder containing H_2/CO/N_2 mixtures (~60/30/10 vol. % purity: 99.99) was used to supply the reactant gas stream to the catalyst at a weight to flow rate (20 mL/min). N_2 was used as an internal standard in order to ensure accurate mass balances. Catalyst (1.5 g) was added to the reactor and reduced in situ at 350 ℃ or 450 ℃ for 2 h under a stream of H_2 (1.5 bar at 50 mL.min^{-1}). After reduction, the reactor temperature was decreased to ambient temperature under a hydrogen flow, then heated up to 220 or 250 ℃ under synthesis gas at a pressure of 10 bar. All gas lines after the reactor were kept at 100 ℃, and a hot trap placed immediately after the reactor was held at 150 ℃ in order to collect wax. A second trap kept at ambient temperature was used to collect the oil and water mixture. The flow was controlled using a metering valve and measured by a bubble meter. The product stream was analyzed online using two gas chromatographs. A thermal conductivity detector (TCD), equipped with a Porapak Q (1.50 m × 3 mm) packed column, was used to analyze

H_2, N_2, CO and a flame ionization detector (FID), equipped with a Porapak Q packed column was used for the online analysis of hydrocarbons. Hydrocarbons collected in the knockout pots were analyzed using an offline GC, equipped with a ZB-1 packed column.

9.3. Results and discussion

9.3.1. Catalyst structure characterization

The Co particle loading was performed using the homogenous deposition precipitation (HDP) method which is one of the common methods employed for catalyst preparation to give uniform particle sizes **[336]**. TEM analysis of the catalyst particles on titania did display a uniform size with an average of about 10.1 nm after calcination at 250 ℃ (Figure 9.2). The target Co loading were ~10%/.

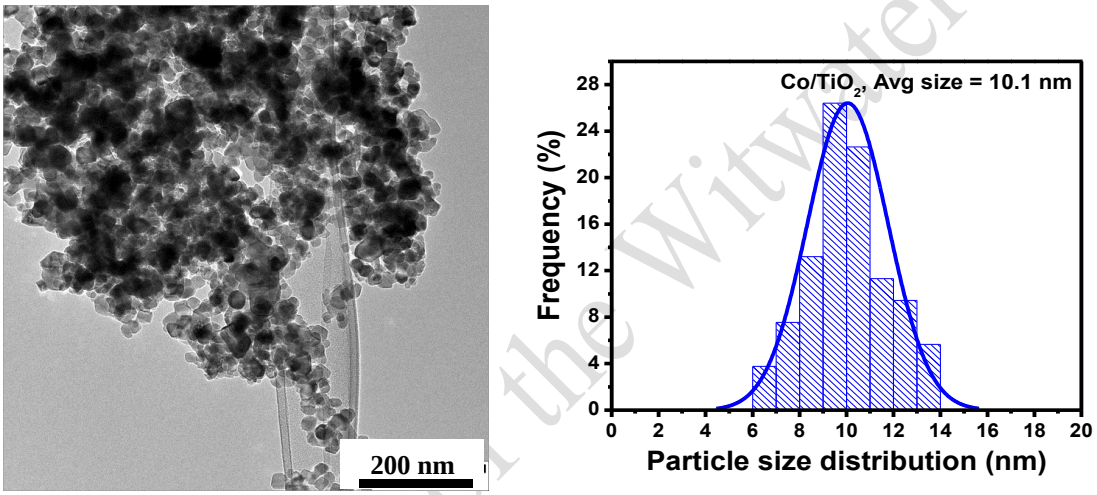

Figure 9. 2: TEM image and Co_3O_4 particle size distribution of Co/TiO_2.

Figure 9.3, shows TEM characterization of the catalysts that were made by adding TEOS/CTAB on the Co and $CoRu/TiO_2$, it quite clear that a successful coverage of the Co/TiO_2 composite with a mesoporous silica shell was attained (Figure 9.3,d) and the silica shell thickness was found to be ~ 4 nm. The coverage of titania with silica shell is well documented in the literature as the oxidic interactions of the silica and titania to form this type of composite is thermodynamically well favoured making the process of coating the Co catalysts a facile one **[337]**. The porogen CTAB was removed from the silica shell by calcination at 500 ℃ for four hours. Little sintering was of the Co_3O_4 occurred on calcination at 500℃ as shown by the XRD line broadening analysis of crystallite sizes (see Figure 9S. 1 and Table in Figure 9S.2). A slight growth of Co_3O_4 catalysts (from 10.3 nm to ~11.8 nm) on the silica coated catalysts during calcination at 500 ℃ presumably during the CTAB removal process. The growth was more significant (from 10.3 nm to 12.9) when the uncoated catalyst (Co/TiO_2) was calcined at 500 ℃ also.

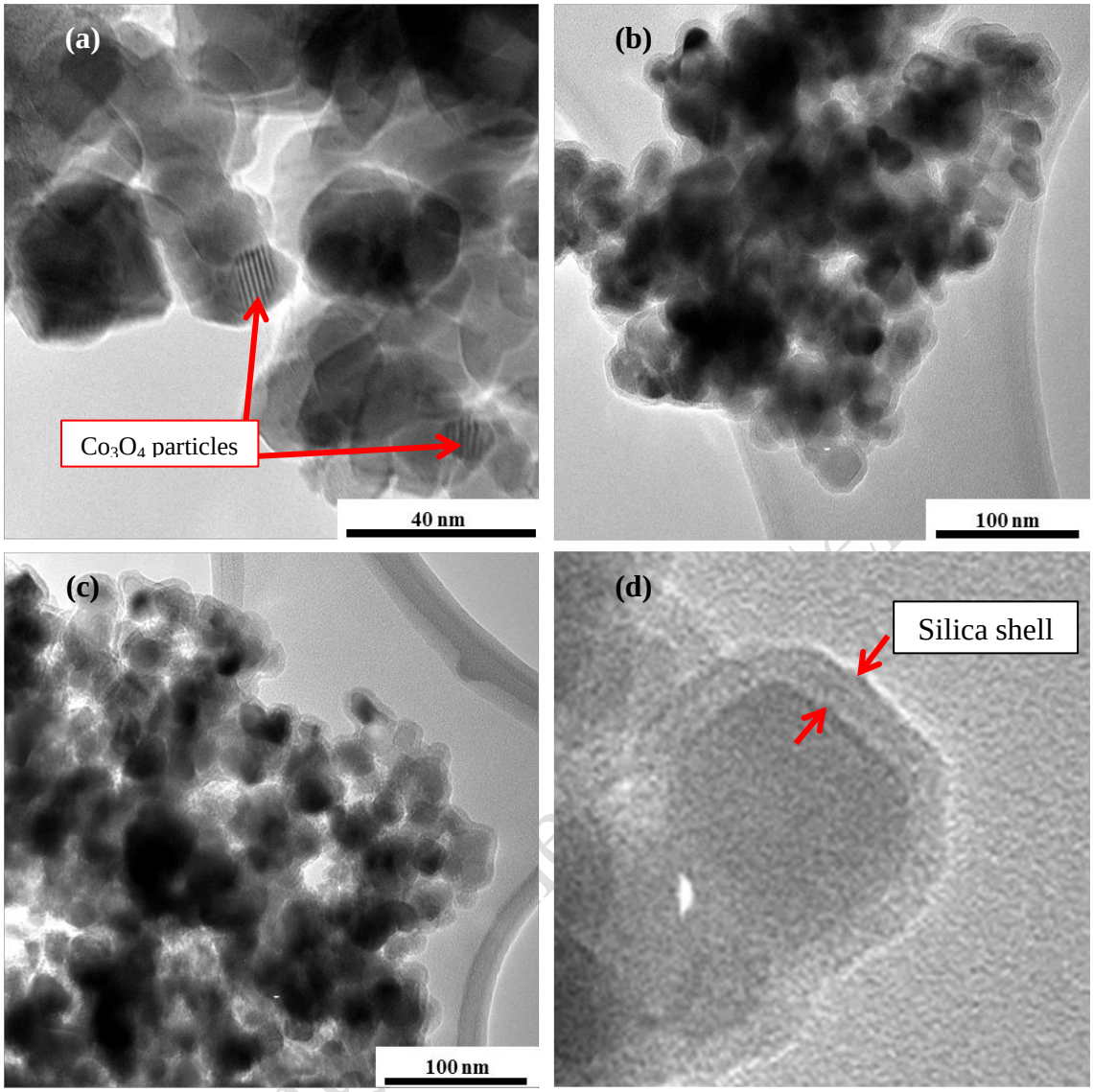

Figure 9. 3: TEM images of the catalysts, (a) Co/TiO_2, (b) $Co/TiO_2@mSiO_2$, (c) $CoRu/TiO_2@mSiO_2$ and (d) the magnified image showing the silica shell on the titania.

Porosity analysis of the catalysts precursors was performed by using the nitrogen adsorption –desorption method (Table 1 and Figure 9S.3). It was observed that the silica coating was indeed mesoporous. This was confirmed by the increased BET surface area of the silica coated Co/TiO_2 catalysts to 103 $m^2.g^{-1}$ and 113 $m^2.g^{-1}$ for $Co/TiO_2@mSiO_2$ and $CoRu/TiO_2@mSiO_2$ respectively when compared to the BET surface area of the uncoated Co/TiO_2 of 56 $m^2.g^{-1}$. It can therefore inferred that the mesoporous silica shell with a thickness of approximately 4 nm and a percentage loading of 11.7% contributed to more than 40 % of the coated catalysts BET surface area. The mesoporous silica shell's surface area alone can be estimated to be > 450 $m^2.g^{-1}$ by using the following equation; $T_{SSA}(m^2/g) = SSA\ (Co/TiO_2) \times \chi_{Co/TiO_2} + SSA\ (mSiO_2) \times \chi_{mSiO_2}$, where T_{SSA} is the total BET

surface area. SSA (Co/TiO_2) and SSA ($mSiO_2$) are the specific surface areas of the Co/TiO_2 and the mesoporous silica shell respectively, while χ (x) is their weight fraction. The increased surface area after coating with the silica confirms that the catalysts are porous enough and the encapsulated Co nanoparticles would be able to interact with the synthesis gas during the Fischer-Tropsch synthesis. Further, the nanoparticle surface mobility would expected to be hindered by the encapsulating effect of the silica shell. The porous nature the silica shell was effected by the porogen [CTAB] that was used during the coating process **[202]**.

Table 9. 1: Co, Ru and SiO_2 loading amounts.

Sample name	BET surface area (m^2/g)	Pore volume (cm^3/g)	Silica loading (%)[a]	Cobalt loading (%)[a]	Ruthenium loading(%)[a]
Co/TiO_2	56	0.289	0	10	0
$Co/TiO_2@mSiO_2$	103	0.398	11.65	8.83	0
$CoRu/TiO_2@mSiO_2$	113	0.348	11.65	8.39	0.44

[a] Estimated based on the amount of material precursor used

9.3.2. Catalyst dispersion

Pulse chemisorption studies were performed to determine the dispersion of Co the nanoparticles on the support at two reduction temperatures (350 and 450 ℃; Table 9.2 and Figure 9S.4). The estimated dispersions were in the range of 1 to 4%. Fischer-Tropsch catalysts supported on oxidic supports are generally observed to have low dispersions **[92]**. It should however be noted that such low dispersions observed are not necessarily due to the active metal sites having large particle sizes but are due to the strong metal support interactions on the metallic sites because of the nature of the metallic supports utilized **[92]**. Because Ru promoter facilitates the reduction of cobalt oxide, $CoRu/TiO_2@mSiO_2$ showed a higher metal dispersion in relation to the $Co/TiO_2@mSiO_2$ composite. It was also observed that for these two catalysts when the reduction temperature was increased to 450 ℃ the cobalt dispersions also increased. In contrast Co/TiO_2 showed high dispersion after reduction at 350 ℃ when compared to $Co/TiO_2@mSiO_2$ (2.19 vs 1.66) at the same temperature, an increase in the reduction temperature to 450 ℃ for Co/TiO_2 resulted in lower catalyst dispersion (1.14% vs 2.09%). This was attributed to some particle

agglomeration of the uncoated Co nanoparticles at 450 ℃ leading to a lower metallic surface area.

Table 9. 2: Pulse Chemisorption at 350 and 450 ℃.

	$CoRu/TiO_2@mSiO_2$		$Co/TiO_2@mSiO_2$		Co/TiO_2	
Temperature (℃)	450	350	450	350	450	350
Active particle size (nm)	25.4	41.2	47.5	59.9	87.4	45.4
Dispersion (%)	**3.92**	**2.41**	**2.09**	**1.66**	**1.14**	**2.19**
Metallic surface area (m^2/g catalyst)	2.23	1.37	1.25	0.993	0.771	1.48
Metallic surface area (m^2/g metal)	26.53	16.35	14.17	11.24	7.705	14.8

9.3.3. Catalyst reduction

9.3.3.1. Temperature programmed reduction (TPR)

TPR studies seek to provide information about the reducibility of the supported cobalt oxide nanoparticles. Displayed in Figure 9.4,a are the reduction profiles of the three catalyst precursors under the flow of 5% H_2/Ar. The TPR profile of Co/TiO_2 showed two distinct reduction peaks as characteristic of the Co oxide spinel phase. These reduction peaks correspond to the following phase transition peaks (i) $Co_3O_4 \rightarrow$ CoO and (ii) CoO $\rightarrow$ Co and 320 ℃ and 490 ℃ respectively. In comparison, the silica shell on the Co titania catalyst increased the reduction temperatures for these transitions (350 and 530 ℃) due to the increased metal support interactions induced by the oxidic silica shell **[92, 306, 338, 339]**. To mitigate this problem reduction promoters using noble metals can be used to lower the reduction temperatures of the catalysts **[20, 306]**. The reduction of the catalyst $CoRu/TiO_2@mSiO_2$ was achieved at lower temperatures of < 400 ℃. This reduction did not occur by formation of a stable CoO intermediate since the two reduction peaks overlap. This can be due to the increased reduction kinetics of the Co oxides that is promoted by the Ru promoter via hydrogen spillover process or even direct Co-Ru interactions **[130, 137, 274]**. The reduction scheme for the catalysts precursors is summarized in Figure 9.4,b showing the dependency of the Co oxides reduction on silica shell and the Ru promoter.

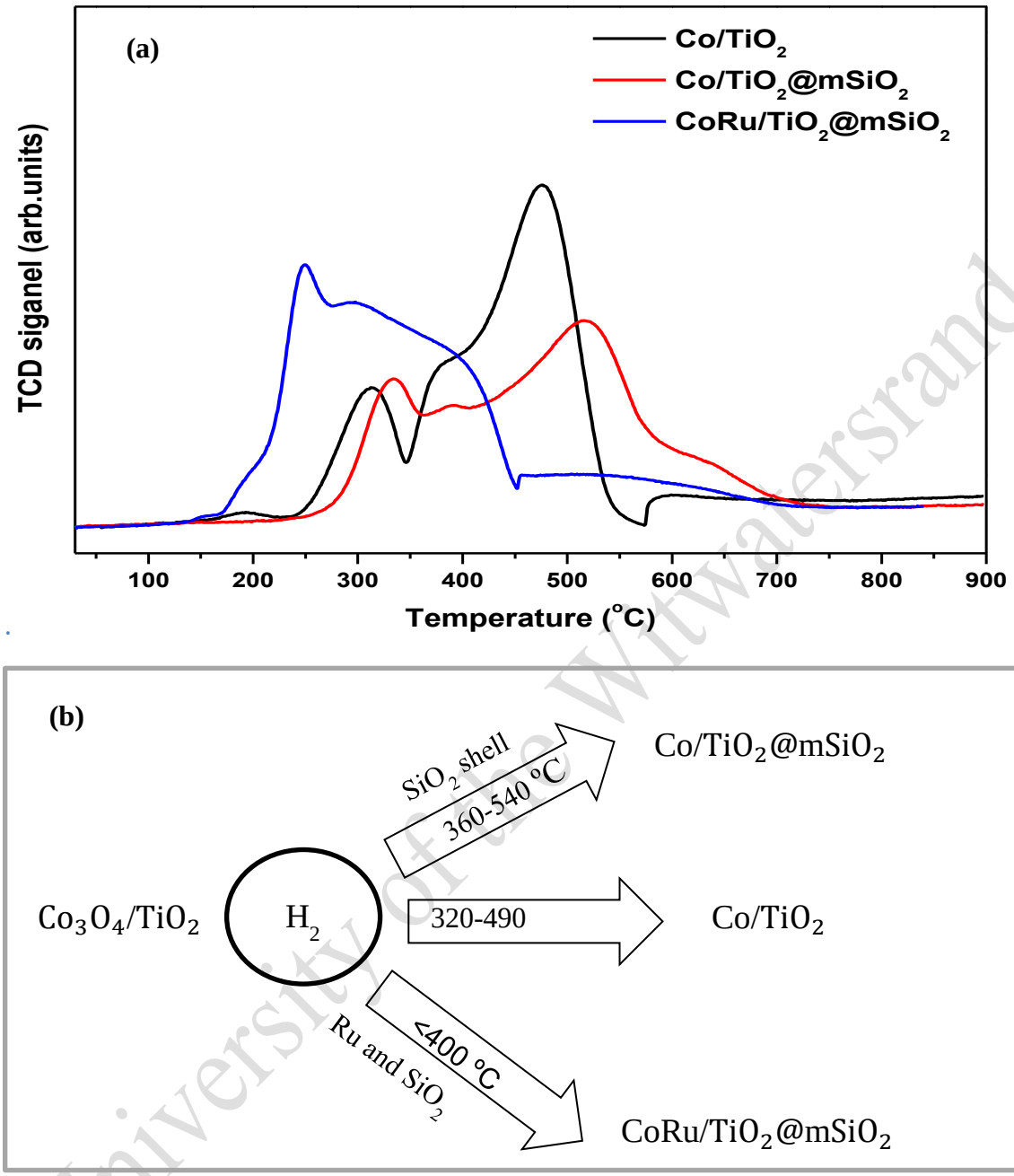

Figure 9. 4: (a) H_2-TPR profiles of the prepared catalysts and (b) a scheme summarizing reduction their behavior

9.3.3.2. In situ PXRD analysis

Phase transformation

The catalysts were studied in operando using variable temperature PXRD to determine the

evolution of the Co particles during the reduction process. This method was also used to ascertain that the silica shell offered some stability to the supported Co nanoparticles against sintering at high reduction temperatures.

The step-wise reduction of the catalysts was monitored under PXRD from 50 to 600 ℃ in 50 ℃ intervals 5% H_2/N_2 gas mixture (Figure 9.5, Figure 9S.5 and Table 9.3). The reduction behaviour of the catalysts validated the one as observed under temperature programmed reduction.

The PXRD patterns showed two Co oxide phase transformation and showed that almost complete reduction of the catalysts occurred below 600 ℃. The anatase phase of the support did not undergo any phase transformation to rutlie under these non-ambient conditions.

The Co/TiO_2 catalysts displayed complete transformation Co_3O_4 to CoO at 300 ℃ while the same transformation for the silica encapsulated Co/TiO_2 commenced at 350 ℃. This transformation was also observed at lower temperatures (250 ℃) for the Ru promoted silica encapsulated Co/TiO_2 (i.e. CoRu/TiO2) possibly due to a hydrogen spillover process taking place and the reduction of the CoO intermediate was also accelerated hence its subsequent conversion to Co at 300 ℃ as detected by in-situ XRD. The reduction process of CoO to Co for Co/TiO_2 and $Co/TiO_2@mSiO_2$ were fully observed at 450 and 500 ℃ respectively.

The Ru promoter reduced the reduction temperature by ±100 ℃ while the use of the $mSiO_2$ as the structural promoter without an reduction promoter raised the reduction temperature of the catalyst up by ± 50 ℃. Figure 4 also displays the relative abundance the Co phases as calculated by Rietveld refinement using the fundamental parameter approach. The degree of reduction (DOR) of these catalysts based on the relative percentage of the Co phase was indeed hampered by the silica shell. These is deduced by considering XRD pattern collected at 450 ℃ for both Co/TiO_2 and $Co/TiO_2@mSiO_2$, at this temperature the catalysts have a DOR of 100 and 13% respectively (Figure 9.6,a and b), hence attesting to an increased metal support interactions on the structurally promoted catalyst. However, this effects were of offset by the Ru promoter as the $CoRu/TiO_2@mSiO_2$'s was observed to be 100% at a lower temperature of 350 ℃ (Figure 4,c) **[92, 339, 340]**.

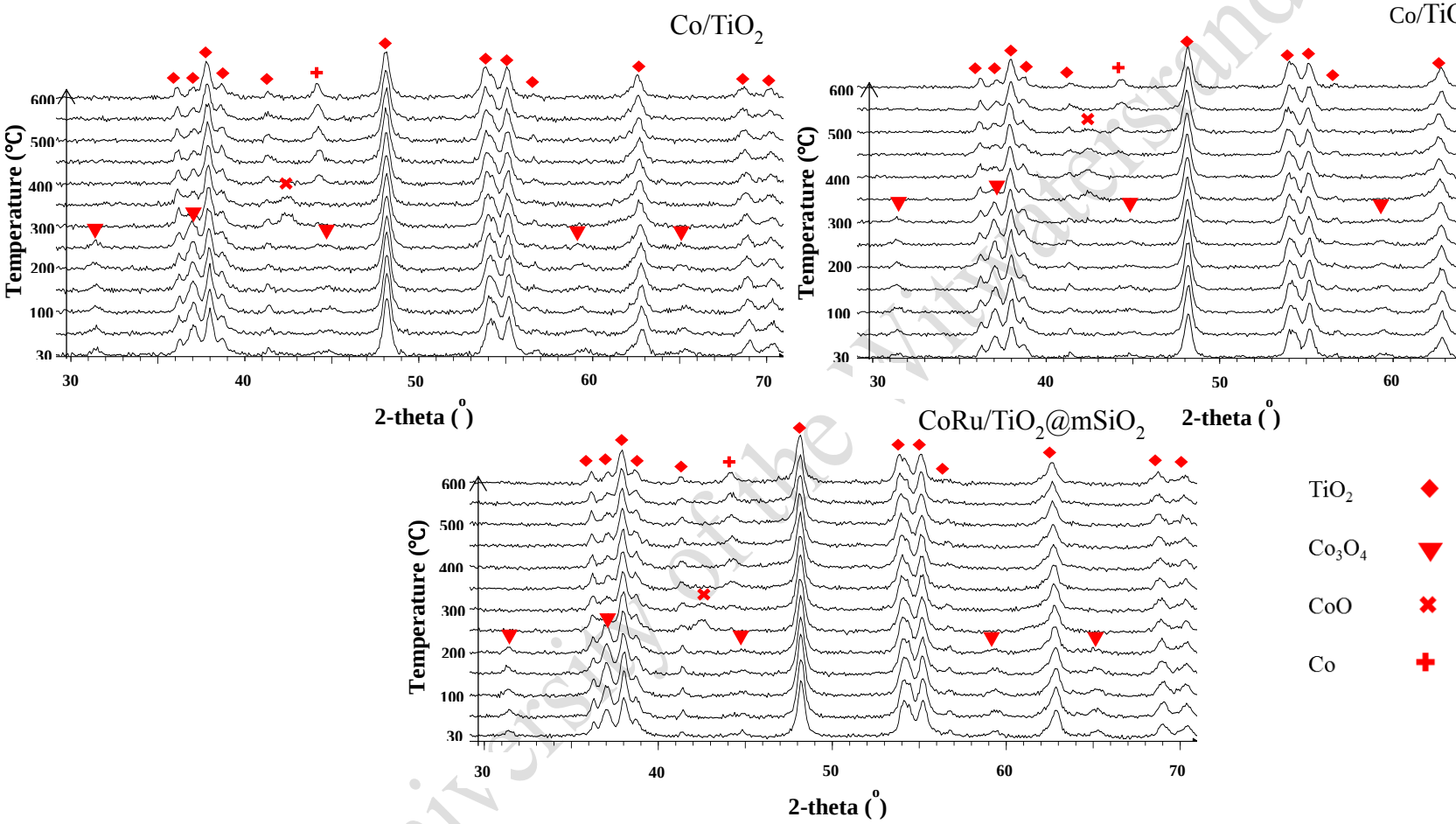

Figure 9. 5: In situ PXRD patterns of the catalysts under reduction conditions at ambient pressure.

Table 9. 3: Observed Co phases during in situ PXRD analysis under reduction conditions.

Reduction temperature (℃)	Co/TiO_2	$Co/TiO_2@mSiO_2$	$CoRu/TiO_2@mSiO_2$
RT	Co_3O_4	Co_3O_4	Co_3O_4
50	Co_3O_4	Co_3O_4	Co_3O_4
100	Co_3O_4	Co_3O_4	Co_3O_4
150	Co_3O_4	Co_3O_4	Co_3O_4
200	Co_3O_4	Co_3O_4	Co_3O_4
250	Co_3O_4	Co_3O_4	CoO
300	Co_3O_4/CoO	Co_3O_4/CoO	CoO/Co
350	CoO	CoO	Co
400	CoO/Co	CoO	Co
450	Co	CoO/Co	Co
500	Co	CoO/Co	Co
550	Co	Co	Co
600	Co	Co	Co

Particle size evolution with reduction

In situ XRD data was collected using an XRK cell and quantitative phase analysis was done by Rietveld refinement (Figure 9S.6) to study the cobalt particle size variation on the three catalysts during reduction (using 5% H_2 nitrogen) from 50 ℃ to 600 ℃ **[296, 297]**. Silica coated catalysts (i.e. $CoRu/TiO_2@mSiO_2$ and $Co/TiO_2@mSiO_2$) did not show significant particle growth during the process (Figure 9.4 and Table 9S.1). When the catalyst precursor was not coated (i.e. Co_3O_4 on titania) the estimated crystallite sizes (calculated using a Rietveld refinement method of the XRD patterns) were in the range of 10 to 12 nm for both $CoRu/TiO_2@mSiO_2$ and $Co/TiO_2@mSiO_2$. After phase transformation to CoO at elevated temperatures the sizes are observed to be around 9.4 nm and between 8.5 and 9.3 nm respectively. Further reduction of these samples to form the Co cubic phase resulted in a further decrease of the estimated sizes to about approximately 7.5 to 8 nm and 9 to 10 nm for $CoRu/TiO_2@mSiO_2$ and $Co/TiO_2@mSiO_2$ respectively. At temperatures above 550 ℃ a slight increase in the Co crystallite sizes was observed indicating modest sintering at elevated temperatures. For the uncoated Co/TiO_2 catalyst the Co particles sizes variation was as follows; Co_3O_4 crystallite size between 10 and 11 nm and around 8 -9 nm for the CoO phase. However, the Co phase was observed to increase from 8.9-16.2 nm at temperatures between 400 to 600 ℃.

The in situ PXRD studies and subsequent refinement of the diffraction patterns showed that due to the increasing strong metal support interactions and possible formation of

amorphous Co with temperature the Co loading decreased with increasing reduction temperature **[296]**.

Growth of the Co crystallites on the silica coated catalysts may also be due to its thickness, as was observed by Lu et al. **[328],** were it was shown that a thicker silica shell offered more nanoparticles stabilization than a thin silica shell when the temperature was ramped up to elevated temperatures (i.e., 800 ℃) , in this case our silica shell was approximately 4 nm, it is possible that the silica was only effective in stabilizing the Co nanoparticles only up 500 ℃.

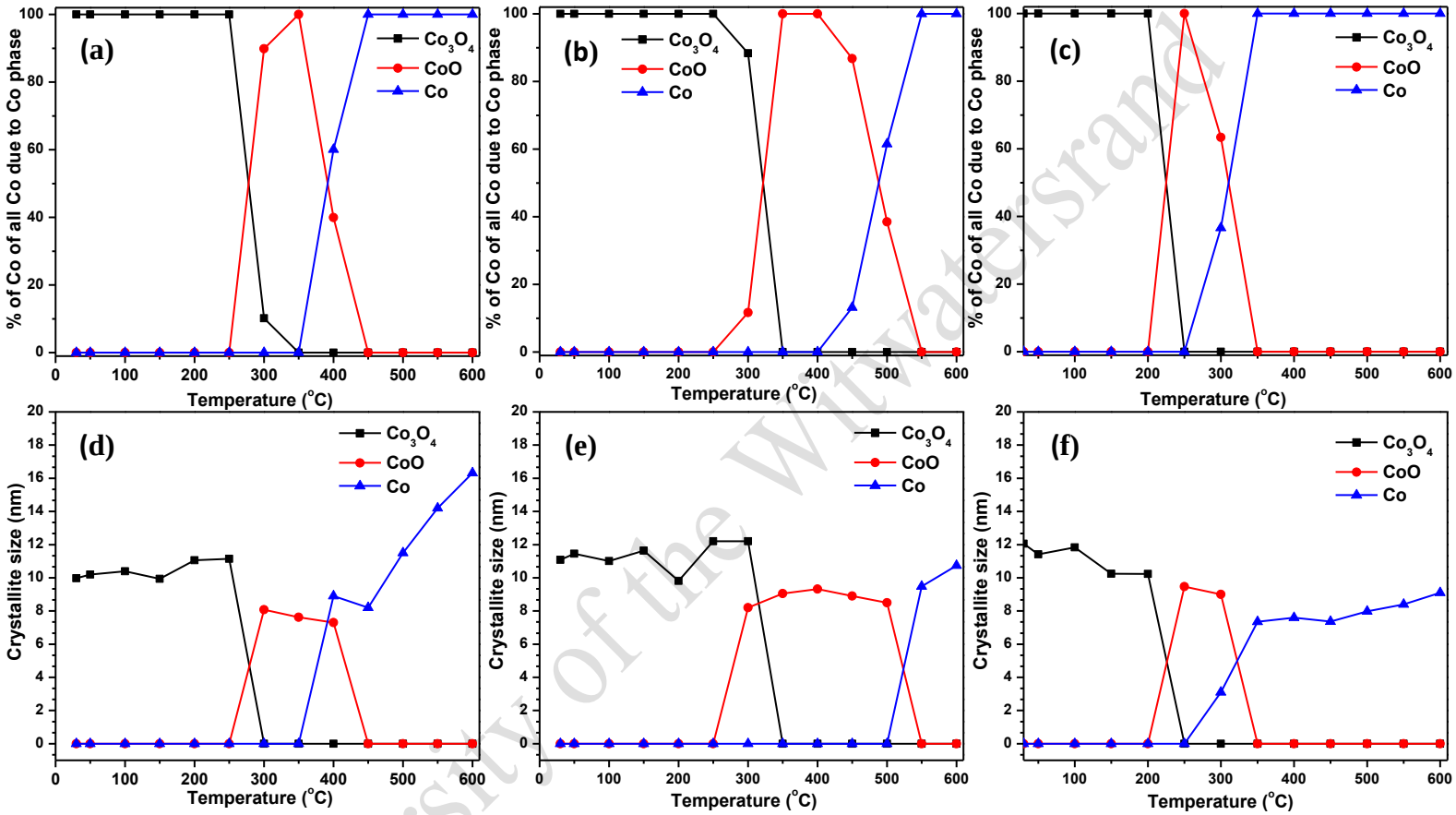

Figure 9. 6: Abundance and crystallite size changes of Co_3O_4, CoO and Co phases during in situ PXRD reduction of the catalysts, Co/TiO_2 (a,d), $Co/TiO_2@mSiO_2$ (b,e) and $CoRu/TiO_2@mSiO_2$ (c,f).

9.3.4. Fischer Tropsch Synthesis Study

Catalysts activities

Evaluation of the FTS activity to decipher the effect of the promoters on the catalysts was performed at 220 and 250 ℃ for 50 hours at each reaction temperature. Pre-treatment of the three catalysts was done by reduction at different temperature (350 and 450 ℃) to observe the effect of the different reduction temperatures on the catalysts activity. Increased FT activity (see Table 9.4) in terms of CO conversion was observed for the catalysts coated with the mesoporous silica structural promoter. It was however observed that when the reduction temperature was increased from 350 to 450 ℃ for the uncoated catalyst precursor (Co/TiO_2) the FT activity of this catalyst decreased from approximately 8.9 % at 220 ℃ and 3.5 % at 250 ℃. The different behaviour of these catalysts is attributed to a possible sintering process of the catalysts particles with increasing reduction temperature because the catalysts precursor Co/TiO_2 did not have a structural promoter. In contrast the increased FT activity for $Co/TiO_2@mSiO_2$ and $CoRu/TiO_2@mSiO_2$ with reduction temperature is due to the increased percentage reducibility at 450 ℃ and stabilizing effect of the silica shell which hindered the propensity of the Co nanoparticles from sintering. It is worth noting that the silica shell did not hinder the mobility of reactants and products because the shell was highly porous. Several studies have shown that increasing reduction temperatures for catalysts can increase the catalytic activity but the problem of catalyst particle sintering remains an issue **[297].**

The above studies therefore indicate that Fischer-Tropsch activity can be increased by enhancing the reducibility of the catalysts while slowing down the activity of metal particle sintering, which in this case was done by coating Co/TiO_2 catalysts using a mesoporous silica shell.

Comparing the activity of the two catalysts $Co/TiO_2@mSiO_2$ and Co/TiO_2 at the reduction of 350 ℃ showed that at this temperature the silica shell plays a significant role in lowering the Co activity which is a result of the silica binding on the Co nanoparticles by strong interactions (lowering the Co active sites).

We can thus conclude that reduction of the Co_3O_4 at 350 ℃ did not induce appreciable sintering of the Co particles on Co/TiO_2 and the resulting difference in catalytic activity on Co/TiO_2 and $Co/TiO_2@mSiO_2$ after reduction at 350 ℃ is due to the coating of the catalyst with the oxidic silica shell, limiting the extend of reduction on $Co/TiO_2@mSiO_2$. This showed that without adequate reduction the silica shell can lower catalytic activity while serving as a sinter resistant agent for the supported metal nanoparticles, $CoRu/TiO_2@mSiO_2$ gave high activity throughout **[328]**. The higher FT activity of $Co/TiO_2@mSiO_2$ over the Co/TiO_2 at 250 ℃ can be explained by further sintering of the uncoated Co/TiO_2 Co nanoparticles upon increasing the reaction temperature from 220 to

250 ℃ which is closer to the Huttig temperature of Co hence the enhanced mobility of the particles **[12, 67]**.

As expected the results indicate that the higher reduction temperature gives a catalyst with a lower dispersion of active metal nanoparticle, due to particle agglomeration. However the effect of the strong metal-support interaction (SMSI) can be overcome by the higher reduction temperature for the coated catalyst precursors. It is therefore seen that the reduction temperature of 450 ℃ was not high enough to produce SMSI between the Co TiO_2 and the silica shell **[341]**.

The increased Fischer-Tropsch activity of the catalysts ($Co/TiO_2@mSiO_2$ and $CoRu/TiO_2@mSiO_2$) after reduction at 450 ℃ showed that the catalysts did not undergo any deactivation by formation of strong metal support interactions. Nobile et al. have shown that for Fe/TiO_2 (Degussa P-25) an increased metal support interactions come into play at reduction temperatures equal or above 450 ℃ **[340].** However, for the catalysts significant interactions that can lower the activity of our catalysts were not observed at 450 ℃ reduction temperatures, this can be due to the fact that the SMSI interactions actions due to the titania support are not the same for supported Co or Fe nanoparticles. The in situ PXRD also showed that the Co nanoparticles did not react with TiO_2 at reduction temperatures up to 600 ℃ with no clear sign of the formation of $CoTiO_3$.

Table 9. 4: Fischer-Tropsch performance of the catalysts.

Sample	Reduction temperature (℃)	Reaction Temperature (℃)	CO Conversion (%)	Activity ($mol_{CO}.g^{-1}_{Co}h^{-1}$)	Selectivity (C mol) %			α^a
					C_1	C_2-C_4	C_{5+}	
$CoRu/TiO_2@mSiO_2$	350	220	31.6	0.024	14.3	12.1	73.5	0.72
		250	53.0	0.053	29.6	23.3	47.1	0.57
	450	220	35.4	0.026	17.4	16.4	66.1	0.72
		250	58.9	0.065	25.8	21.9	52.2	0.67
$Co/TiO_2@mSiO_2$	350	220	17.0	0.010	7.9	5.2	86.8	0.71
		250	41.3	0.032	27.0	21.7	51.2	0.64
	450	220	22.2	0.012	10.1	9.3	80.6	0.74
		250	46.1	0.033	31.3	21.3	47.3	0.63
Co/TiO_2	350	220	27.5	0.014	8.3	10.6	81.0	0.73
		250	36.6	0.021	23.9	15.9	60.1	0.61
	450	220	18.6	0.010	7.7	14.9	77.3	0.74
		250	33.1	0.018	24.5	20.9	54.5	0.59

[a]α - estimated by the ASF equation using liquid alkane products from C_9- C_{20}.

Catalyst reduction time has a significant bearing on the formation of the strong metal support interactions since it was observed that reducing the catalysts at 450 ℃ for 6 hours did not give any FT activity. This effect was observed on Co/TiO_2 reduced at 450 ℃, post synthesis analysis of this catalyst XRD after FT synthesis showed no Co peak or phase, attributed to the formation of mixed metal oxides at the higher reduction temperatures.

Therefore the reduction temperature, time and the ease at which the particles can agglomerate can therefore be the reason why Co/TiO_2 gave SMSI and lower FT activity after reduction at a higher temperature (450 ℃). This phenomenon was not observed for the silica coated catalysts because of the protective shell. Nobile studied the effect of reduction temperature on Fe/TiO_2 and observed that at temperatures $\geq$ 450 ℃, there was an increase in SMSI by titania grain enlargement that lowered the catalyst active sites due to a formation of $FeTiO_x$ **[340]**. Furthermore, work by Duvenhage et al. **[342]**, showed that at reduction temperatures of 400 ℃, a bimetallic $CoFe/TiO_2$ catalyst Fischer-Tropsch activity was lower than that of the catalyst reduced at lower temperature of 300 and 350 ℃. This possibly due to the deactivation mechanism as suggested by Nobile and co-workers **[340]**, a mechanism that would not evident on the silica coated catalysts.
TEM images of the spent catalyst ($CoRu/TiO_2@mSiO_2$, which had the highest activity) of the coated catalysts did not show any silica shell breakage after Fischer-Tropsch synthesis for 100 hours at 220 and 250 ℃ (Figure 9S.7).

Catalysts selectivities

Methane is the most stable Fischer-Tropsch product and tends to form in large quantities on Co catalysts **[31]**. Increased methane selectivity always results in lower selectivity of high molecular weight products (i.e. C_{5+}). Cobalt Fischer-Tropsch catalysts perform optimally (in terms of selectivity) at lower temperatures hence the increased methane selectivity at 250 ℃.
Fischer-Tropsch catalytic measurements showed that the silica coating did not in any extent have a significant effect on the catalysts hydrocarbon selectivity (Table 9.4). High reaction temperatures resulted in high methane selectivity but the space time yield (STY) of the C_{5+} is still to be high when compared to the yield (STY) obtained at 220 ℃ for all the individual catalysts. From these studies we can infer that the SMSI induced on the Co particles do not result in significant differences in catalyst selectivity. The Ru promoted catalyst displayed a higher activity and higher methane. This is because of the Ru nanoparticles by hydrogen spillover (or its promoter effect on the Co nanoparticles) **[131, 274]** increased the hydrogenation rates. This increased the termination step on the C_1 monomers thus lowering the chain growth probability. With increasing CO conversion methane selectivity decreased on $CoRu/TiO_2@mSiO_2$ while it was observed that the methane selectivity increased for $Co/TiO_2@mSiO_2$.

The difference in hydrocarbon selectivity for the catalysts reduced at temperatures of 350 and 450 ℃ can be accounted for by to the increased activity of the catalysts. The selectivity for C_2-C_4 gaseous hydrocarbons (between 5-25%) increased with FT reaction temperature and reduction temperature. The increased activity for the catalyst $CoRu/TiO_2@mSiO_2$ was accompanied by high yields of C_{5+} products (in terms of STY) when compared to the two catalysts which were not Ru promoted despite the high propensity of the Ru promoter to increase the methane fraction in the hydrocarbon products. No specific trend in the hydrocarbon selectivities of the catalysts at Fischer-Tropsch synthesis of 250 ℃ was observed. At this temperature the catalyst $Co/TiO_2@mSiO_2$ gave higher methane selectivity then the $CoRu/TiO_2@mSiO_2$. However, at 220 ℃ the C_{5+} hydrocarbon (in terms of STY) general trend was decreasing with increasing FT activity, together with an increase in methane selectivity.

9.4. Conclusions

This study was aimed at designing stable Co catalysts for Fischer-Tropsch synthesis using a mesoporous silica shell as the stabilizer. A thin layer of silica was successfully coated on the Co nanoparticles supported on TiO_2. Increased metal support interactions that can lower the reducibility of the catalysts were countered by using a Ru promoter. In situ XRD studies under reduction and crystallite size calculations (of the Co phases) by the modified Scherer equation showed that the catalysts reduction followed the classical phase transformation from Co_3O_4 to Co via the CoO intermediate phase and that the crystallite growth under reduction was only observed after complete transformation to Co phase. The growth was more pronounced on the uncoated Co/TiO_2 than on the silica coated catalysts. Fischer-Tropsch catalytic behaviour of the catalysts was consistent with characterization data, and furthermore the Ru promoter helped in giving a highly active sinter resistant catalyst.

Therefore this study then highlights that a triphasic compact nanoreactor can potentially be used in Fischer-Tropsch catalysis without a significant change in the inherent Co nanoparticle activity and selectivity while on the one hand reducing the Co nanoparticles propensity to sinter under reaction conditions and high activity.

Chapter 10

10.1. Conclusions

In this study a synthesis of various catalytic materials to study the effect of hydrogen spillover on Fischer-Tropsch synthesis and Fischer-Tropsch catalyst stability against some deactivation mechanisms was undertaken.

Hollow carbon spheres with controllable porosities were synthesized for use as the nanoreactor and encapsulation of metal nanoparticles inside these hollow carbon spheres yielded nanoreactor endowed with catalytic activity. Ru and Co nanoparticles were successfully encapsulated inside the hollow carbon spheres, however the preparation method required different synthesis technique because of the high solubility of Co in acids when compared to Ru.

With these catalysts (i.e. Me@MHCS, Me = Ru or Co) Fischer-Tropsch synthesis could be performed inside the hollow carbon sphere interior without noticeable diffusion limitations of the reactants and products (this includes high molecular weight hydrocarbons). The Me@MHCS catalysts were robust and could withstand pressures up to 20 bar and temperatures under Fischer-Tropsch reaction conditions without fracturing and losing the hollow morphology.

The hollow morphology of the carbon spheres was exploited to study the hydrogen spillover process by supporting the Ru (initiator) and the Co (acceptor) on different sides of the porous carbon shell.

In the first study (**Chapter 5**) Ru nanoparticles encapsulated inside the mesoporous hollow carbon spheres where shown to enhance the reduction of Co oxide loaded on the outside of the hollow spheres. Secondary hydrogen spillover was invoked to explain the complete reduction of the Co oxide nanoparticles relative to the unpromoted nanoparticles. Furthermore, in the study above it was postulated that some Co nanoparticles could be in direct contact with the Ru nanoparticles owing to the method that was used to load the Co nanoparticles(**Chapter 6**) . In a subsequent work a complete and sure exclusive separation of the two metals was achieved to effect of hydrogen spillover in Fischer-Tropsch synthesis. This was done by developing a new method for encapsulating Co nanoparticles inside the hollow carbon spheres using polystyrene templates. With pre-synthesized Ru nanoparticles loaded outside the hollow carbon spheres (to make Co@MHCS@Ru,

Chapter 7) secondary hydrogen spillover was inferred to explain the complete reduction of this catalyst when compared to unpromoted Co@MHCS.

In both studies it was however observed that the secondary hydrogen spillover was not energetically more favoured than the primary hydrogen spillover process, possibly due to (i) the energy required for the transport of hydrogen atoms on the carbon support from the initiator to the acceptor, and (ii) the concentration of defects increased with high reduction temperatures.

With regards to the Fischer-Tropsch performance of the different catalysts the Ru promoter intimacy with the Co nanoparticles was shown to play a significant role. Hence, the CoRu (direct metal contact) had higher activity than the Co@MHCS@Ru catalysts followed by the unpromoted catalysts. This difference in activities could be related primarily to the degree of reduction of the catalysts, with an increase in the extent of reduction increasing with the Co and Ru intimacy. The Ru promoter enhanced the formation of saturated hydrocarbons more than the unpromoted catalyst.

It was also observed that the carbon nanoreactors stabilized the encapsulated metal nanoparticles against sintering better when the Co nanoparticles were loaded on the outside of the hollow spheres. Ru nanoparticles inside the hollow spheres (**Chapter 5**) showed less metal agglomeration after Fischer-Tropsch synthesis at 220 ℃ than after Fischer-Tropsch reaction at 250 ℃. Furthermore the stability of Co inside hollow carbon spheres studied using an in situ magnetometer under Fischer-Tropsch conditions with high CO conversions (up to 90%) simulated by co-feeding water showed that the Co nanoparticles did not undergo any significant deactivation by oxidation or sintering (**Chapter 8**). However, a slight growth of the Co nanoparticles was observed on Co supported on the outside of hollow carbon spheres.

Lastly a compact nanoreactor using Co supported on titania was designed and tested in Fischer-Tropsch synthesis to evaluate its sinter resistant nature (**Chapter 9**). The catalyst encapsulated by a porous silica shell showed good stability under reduction conditions at temperatures up to 500 ℃. However, the silica shell lowered the catalyst reducibility, a setback that was counteracted by adding a reduction promoter in the form of Ru. The nanoreactor ($Co/TiO_2@mSiO_2$ and $CoRu/TiO_2@mSiO_2$) activity increased with reduction temperature while that of the uncoated catalyst Co/TiO_2 decreased with increasing reduction temperature (from 350 to 450 ℃). These differences could be attributed to the uncoated Co catalyst absence of the silica and subsequent support mobility that resulted in growth of the Co nanoparticles. An increase in the metal support interactions by the titania grain enlargement at higher reduction temperatures also played a role.

10.2. **Outlook**

This work revealed that hollow carbon morphology can play a vital role in understanding the behaviour of Fischer-Tropsch catalysts and for designing new effective catalysts.

(i) Of further interest will be the use of the hollow carbon spheres doped with different heteroatom (i.e. nitrogen) to study hydrogen spillover on Fischer-Tropsch catalysts. Strong acid functionalization to increase OH^- groups on the carbon surface should also enhance the material's hydrogen transporting capabilities due to increased defects.

(ii) Hollow spheres made of titania, silica and alumina would be of great interest in elucidating the effect of catalyst supports enhancing the hydrogen spillover process during the Fischer-Tropsch synthesis process. This can also be studied using other promoters such as platinum and rhenium.

(iii) The hollow carbo sphere morphology can also be used to study the Fischer-Tropsch metal particle size effect by making yolk shell nanostructures with a single nanoparticle encapsulated inside individual hollow spheres. This would allow the study of nanoparticles that would not sinter and with limited metal support interactions as the nanoparticle would be free to move inside the hollow sphere.

(iv) A further coating of the Me@MHCS catalyst with an acidic zeolite shell can give bifunctional catalysts that can be used to control the Fischer-Tropsch catalyst selectivity for a one step synthesis of liquid fuels.

Chapter 5: Supporting information

Appendix A

Ruthenium nanoparticles encapsulated inside porous hollow carbon spheres: A novel catalyst for Fischer-Tropsch synthesis

5S.1. Sources of chemicals

Tetraethylorthosilicate (TEOS 98%; Aldrich), formaldehyde (37%; Aldrich), resorcinol (Merck), ammonia solution (25%; Fluka), hexadecyltrimethylammonium bromide (CTAB; Aldrich), ruthenium chloride (Aldrich), urea (Promark chemicals), ethanol (98%; Merck), toluene (Merck), HF (40%; Associated chemicals) were used as received. Deionized water was used in the experiments.

5S.2. Synthesis of modified Stöber spheres.

The silica spheres were made by adding 10 mL of ammonia solution into a solution of water and ethanol (20 mL and 200 mL respectively) **[162, 268]**. This solution was then stirred at room temperature for 10 minutes. To this solution was slowly added 15 mL of TEOS and the mixture stirred for 6 h to form monodisperse Stöber spheres. CTAB (5 g) and TEOS (2.5 mL) in 50 mL of ethanol was added into the solution containing the Stöber spheres. A mesoporous silica shell formed on the silica to generate a mesoporous silica composite material ($mSiO_2$) after stirring the solution overnight (12 h) at room temperature. The $mSiO_2$ spheres were then harvested by filtration and dried at 100 ℃ for 4 h. This was followed by calcination of the material in air at 500 ℃ for 4 h. This gave a silica yield of approximately 4.5 g. with a greater than 95% yield based on the TEOS used.

5S.3. Preparation of Ru supported on hollow carbon sphere catalysts.

The $mSiO_2$ was prepared as described above and then coated by carbon using the procedures described in section 5.2.4 and 5.2.5 (but without Ru) and the silica removed by HF to give MHCS and HCS. Ru/HCS and Ru/MHCS were then prepared by loading 5% Ru onto the hollow carbon spheres by homogenous deposition precipitation. The deposition was performed as follows; hollow carbon spheres (MHCS or HCS, 1 g) were dispersed in 200 mL of deionized water by ultra-sonication. To this mixture was added 0.1 g of urea and 4.95 mL of 0.1 M $RuCl_3$ solution. Homogenous deposition precipitation of Ru was performed at 95 ℃ for 12 h. The product was collected by filtration, washed thoroughly with deionized water and then dried at 100 ℃ overnight. The two catalysts (Ru/HCS and Ru/MHCS) were heated at 250 ℃ under nitrogen gas at 30 mL/min for 2 h prior to use and characterization.

5S.4. Material characterization

TEM analysis was performed on a Tecnai spirit (T12) transmission electron microscope operating at 120 kV. The samples were dispersed in methanol by ultrasonication and loaded onto a copper grid. The particle size distribution of the materials formed was determined by counting at least 200 particles per sample by random selection from different TEM images. Gaussian statistics yielded values for the average particle sizes. SEM analysis was performed on a FEI Nova Nanolab 600 FIB/SEM instrument operating

at 30 kV. The sample loaded on a carbon tape was coated by a gold-palladium layer before the analysis. The bulk composition of the catalysts was analyzed using a Bruker D2 phaser equipped with a Lynxeye detector. The radiation used is the Co-Kα at 30 kV. The scan ranged from 10-90 2θ in 0.0260 steps. TGA was performed with a Perkin- Elmer STA6000 TGA using nitrogen or air as the purge gas and a heating rate of 10 ℃.min^{-1}. Raman spectroscopy analysis was performed using a Bruker, Senterra Raman spectrometer with a wavelength of 540 nm. The flow rate of the purge gas was always 20 mL.min^{-1}. N_2 adsorption–desorption experiments were conducted at -195 ℃ using a Micromeritics Tristar 3000 surface area and porosity analyzer. Prior to an experiment, the sample was outgassed at 150 ℃ for 4 h under nitrogen gas. The BET surface areas were obtained for adsorption data in a relative pressure range from 0.05 to 0.30. The total pore volumes were calculated from the amount of N_2 vapor adsorbed at a relative pressure of 0.99. The pore size distributions were evaluated from the desorption branches of the isotherms using the Barrett–Joyner–Halenda (BJH) method. The micropore area and volume were calculated using the t-plot data. Pulse chemisorption was performed using the Micromeritics Auto Chem II instrument to give the number of active metal atoms. The catalyst (ca. 100 mg) was placed in a quartz tube reactor. The reactor was heated in a furnace. Prior to the analysis, the calcined catalysts were flushed with high-purity argon at 150 ℃ for 1 h, to remove water or impurities followed by cooling to ambient temperature. The sample was reduced at 250 ℃ for 2 h under a hydrogen flow of 50 mL.min^{-1}. Before injecting the active gas the sample was purged using helium gas while cooling the sample to ambient temperature. Hydrogen chemisorption (assuming an stoichiometric factor of 2) was then performed at 75 ℃ using ultra-pure hydrogen and argon as the carrier gas.

Particles sizes (d_{Me}) were estimated using the equation $d_{Me} = 6\times10^2\times Mw/\rho\sigma N_A D$, where M_w (101.07 g.mol^{-1}) is the metal atomic weight, ρ (12.410 g.cm^{-3}) is the Ru density, σ (0.0614 nm^2.atom^{-1}) is the atomic surface area of Ru, N_A (6.022 $\times10^{23}$ mol^{-1}) is Avogadro's number, and D is the Ru percentage dispersion **[269]**. It should be noted that nanoparticle dispersion can also be estimated using average particle sizes as obtained from TEM. In this case the using a simplified equation $D = 1.33/d_{TEM}$ we observed that the computed dispersions were higher than those estimated by pulse chemisorption. The different Ru particle sizes (and dispersion) relative to the average particles estimated by TEM can be accounted for by increased interaction of the Ru nanoparticles with the carbon shell and also the nature of the carbon shell's porosity. The second method however assumes that all the surface atoms are exposed which is normally not the case for supported catalysts. The synthesis procedure to make these composites ensured that all Ru nanoparticles remained embedded on the inside walls of the nanoreactors. This synthetic procedure to make embedded catalysts has been reported by other authors using silicon oxide nanoreactors where Pd in a nanoreactor was successfully employed as a catalyst in Suzuki coupling reactions **[160, 219, 261]**. A transmission electron microscopy tilting experiment was also used to determine that the particles were indeed contained inside the

hollow carbon spheres (see supplementary, Figure 5S.5). Samples were tilted around a single axis in the range -25^{o} to +25^{o}. The study also confirmed that the Ru nanoparticles were supported on the inside wall of the carbon nanoreactors and did not move freely inside the nanoreactors. Thus, sintering during reaction which is a common feature of unsupported catalysts should be limited to only those particles within a particular hollow carbon spheres **[186, 270, 271]**. SEM images were used to confirm the homogeneity and large scale coverage of the Ru nanoparticles by the carbon shell. EDX mapping of the samples (Figure 5S.3 and 5S.4) showed only the presence of Ru and carbon, confirming the purity of the samples.

5S.5. XRD and TGA analysis

The defects observed on the carbon material are thus attributed to a high content of topological defects that leads to the amorphous nature of the carbon spheres (C5, C7, C8 carbon rings) **[343]**. This would be expected for carbon materials formed by annealing a resorcinol-formaldehyde polymer since the carbon was not formed in a stepwise bottom-up synthesis typically used to make highly graphitized carbon nanomaterials with limited defects. In contrast the sharper XRD pattern for Ru@HCS indicates the presence of both Ru and carbon diffraction patterns. The sharper peaks for carbon arise because coating by chemical vapor deposition using toluene occurs at higher temperatures leading to a more graphitic carbon layer **[176, 344]**. This was also confirmed by Raman spectroscopy which showed a lower D-band to G-band ratio of 0.78, compared with Ru@MHCS that has an I_D/I_G value of 0.88. The D band can be used to qualitatively measure the degree of disorder on the carbon material while the G band measures the structural order of the sp^2 carbon material **[272, 345]**. From the XRD patterns it was observed that the Ru is in a metallic hcp phase (ICSD Coll.Code: 54236, HCP crystal structure).

TGA plots displayed in Figure 5.4,b showed that the Ru@HCS with a highly graphitic carbon shell was more thermally stable under air in comparison to the Ru@MHCS. The Ru@MHCS was completely decomposed by oxidation at temperatures in the range of 300-350 ℃ while that of the Ru@HCS decomposed above 400 ℃ (Figure 5S.7). This data thus validated the results observed in the powder XRD patterns which showed that the Ru@HCS had a carbon shell with better structural integrity. The TGA plots showed that both the hollow carbon spheres contained a Ru loading of < 3% (Table 5.1). From the TGA plot the Ru content was determined as the resulting RuO_2 that formed during oxidation of the material at high temperatures does not transform to the volatile RuO_4 at temperatures less than 800 ℃ **[274]**. It is assumed that all the SiO_2 has been removed by HF (see EDX data).

5S.6. Evaluation of Fischer-Tropsch performance

The Fischer–Tropsch synthesis was performed in a fixed-bed micro-reactor. A gas cylinder containing $H_2/CO/N_2$ mixtures (~60/30/10 vol. % purity: 99.99) was used to supply the

reactant gas stream to the catalyst at a weight to flow rate (W/F) of 15 g.h.mol^{-1}. N_2 was used as an internal standard in order to ensure accurate mass balances. Catalyst (0.5 g) was added to the reactor and reduced in situ at 250 ℃ for 2 h under a stream of H_2 (1.5 bar at 50 mL.min^{-1}). After reduction, the reactor temperature was decreased to ambient temperature under a hydrogen flow, then heated up to 190, 220 and 250 ℃ under synthesis gas at a pressure of 10 bar. All gas lines after the reactor were kept at 100 ℃, and a hot trap placed immediately after the reactor was held at 150 ℃ in order to collect wax. A second trap kept at ambient temperature was used to collect the oil and water mixture. The flow was controlled using a metering valve and measured by a bubble meter. The product stream was analyzed online using two gas chromatographs. A thermal conductivity detector (TCD), equipped with a Porapak Q (1.50 m × 3 mm) packed column, was used to analyze H_2, N_2, CO and a flame ionization detector (FID), equipped with a Porapak Q packed column, was used for the analysis of hydrocarbons online. Hydrocarbons collected in the knockout pots were analyzed using an offline GC, equipped with a ZB-1 packed column.

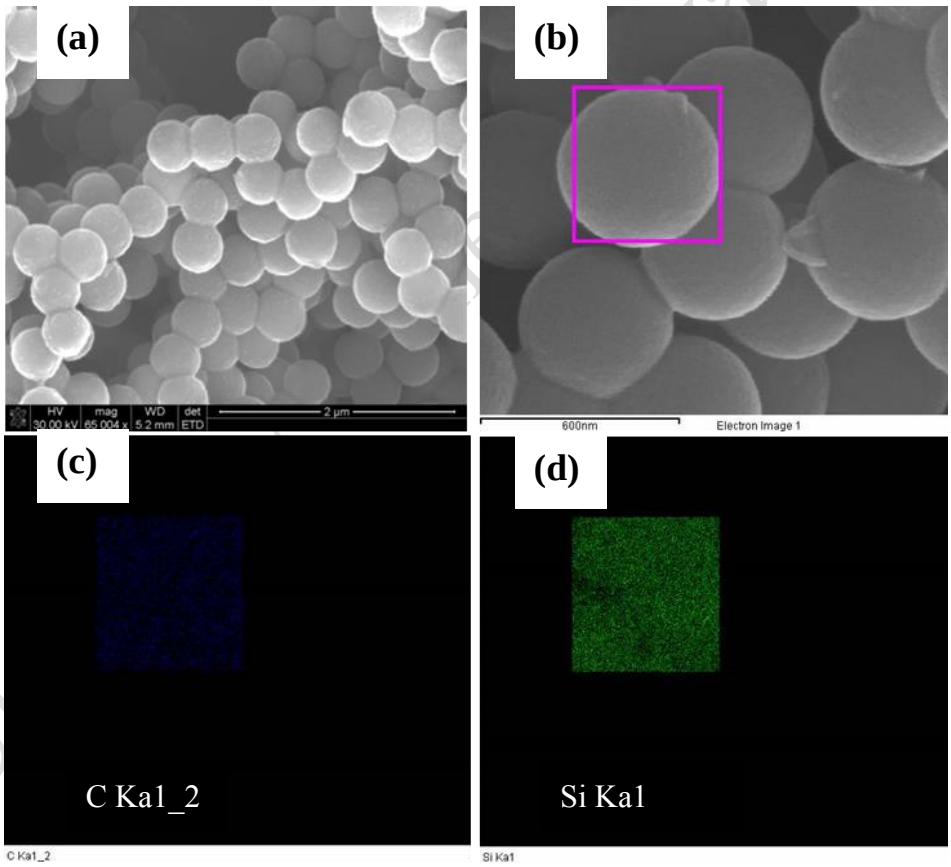

Figure 5S. 1: SEM image and the EDS maps of the 0.5%Ru/mSiO2@C for Ru@MHCS. (a) SEM image of Ru/SiO_2@MHCS, (b) Selected area for EDX mapping (c) EDX map for carbon and (d) EDX map for silica. (Ru was below detection limit).

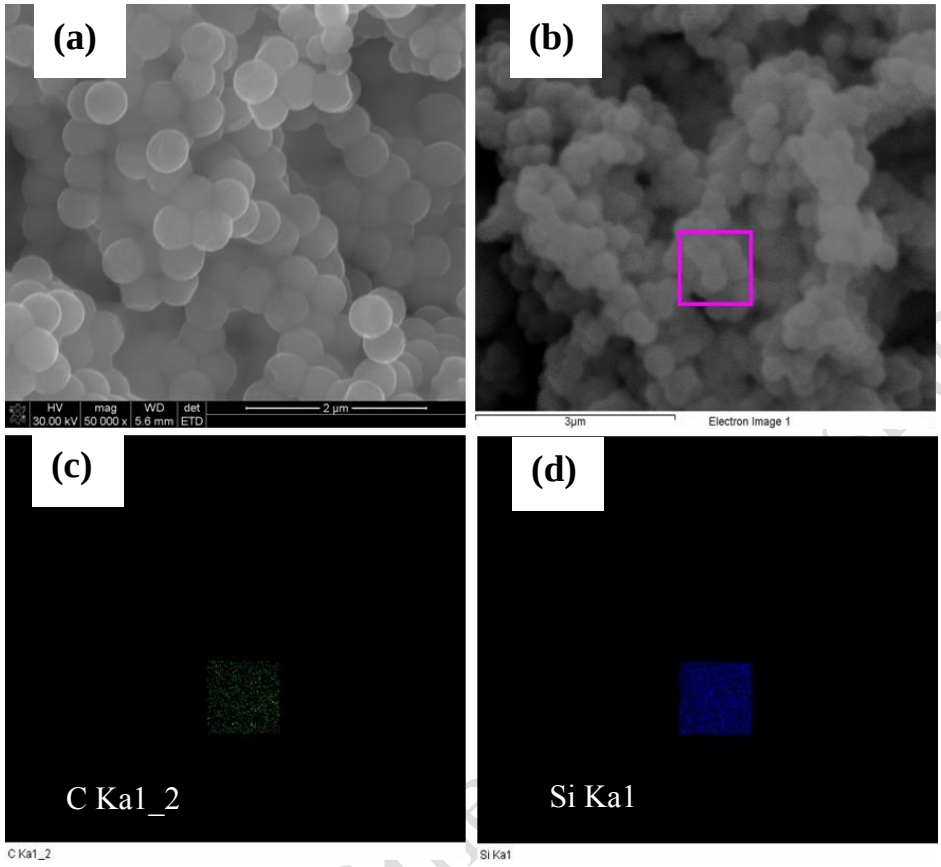

Figure 5S. 2: SEM image and the EDS maps of the 0.5%Ru/mSiO_2@C for Ru@HCS. (a) SEM image of Ru/SiO_2@HCS, (b) Selected area for EDX mapping (c) EDX map for carbon and (d) EDX map for silica.

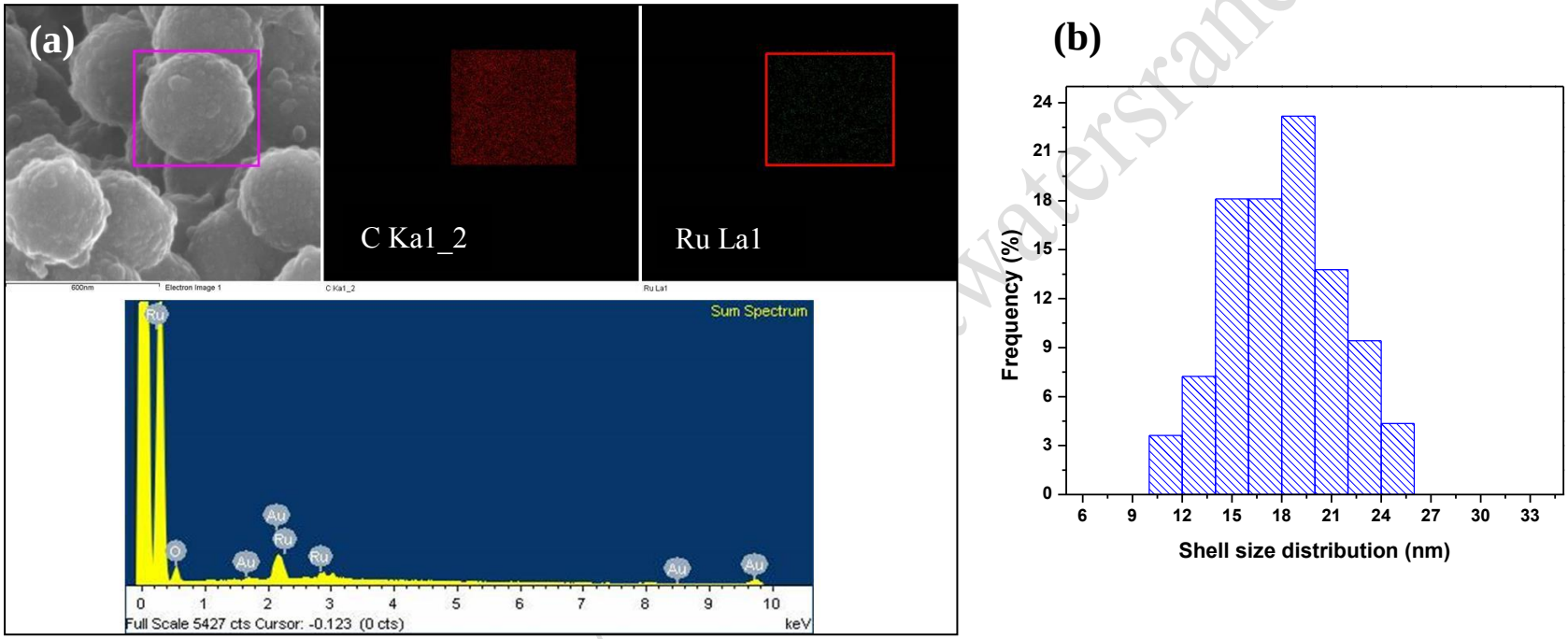

Figure 5S. 3: EDS map (a) of Ru@MHCS displaying the presence and the distribution of Ru inside the hollow carbon spheres and the corresponding carbon shell size distributions (b). Gold signal is due to the gold coating used during sample preparation.

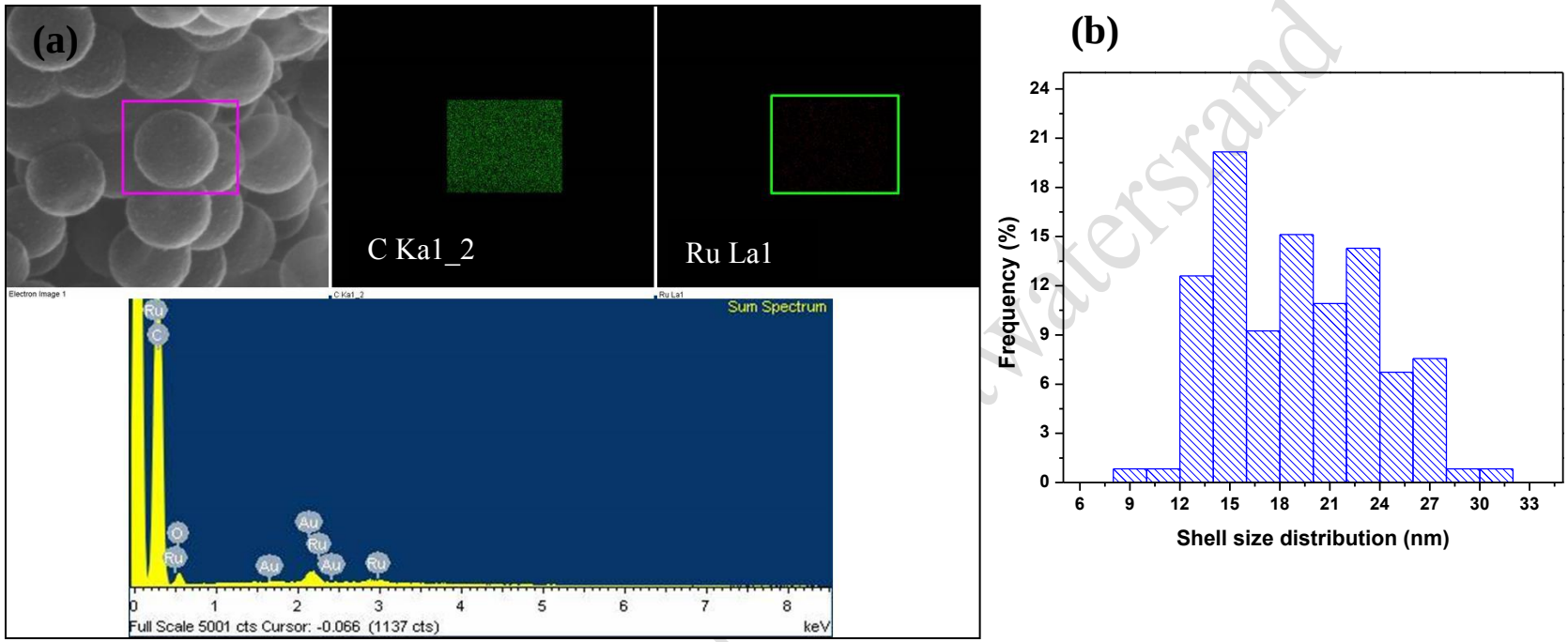

Figure 5S. 4: Figure S 4: EDS map of Ru@HCS (a) displaying the presence and the distribution of Ru inside the hollow carbon spheres and the corresponding carbon shell size distributions (b). Gold signal is due to the gold coating used during sample preparation.

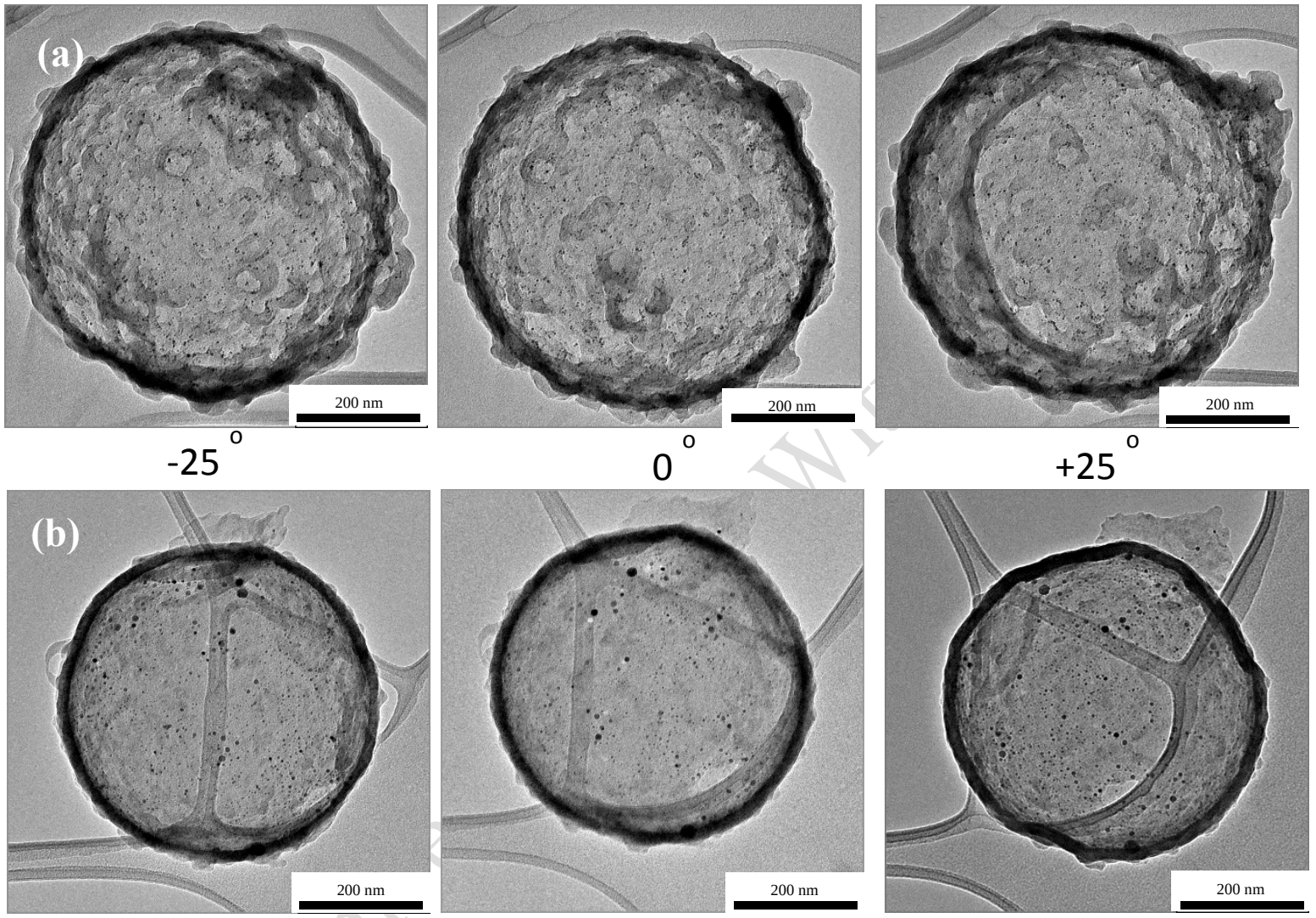

Figure 5S. 5: TEM images of the catalysts taken at different tilting angles (for the same carbon sphere) Ru@MHCS (a) and Ru@HCS (b), obtained by single axis tilt.

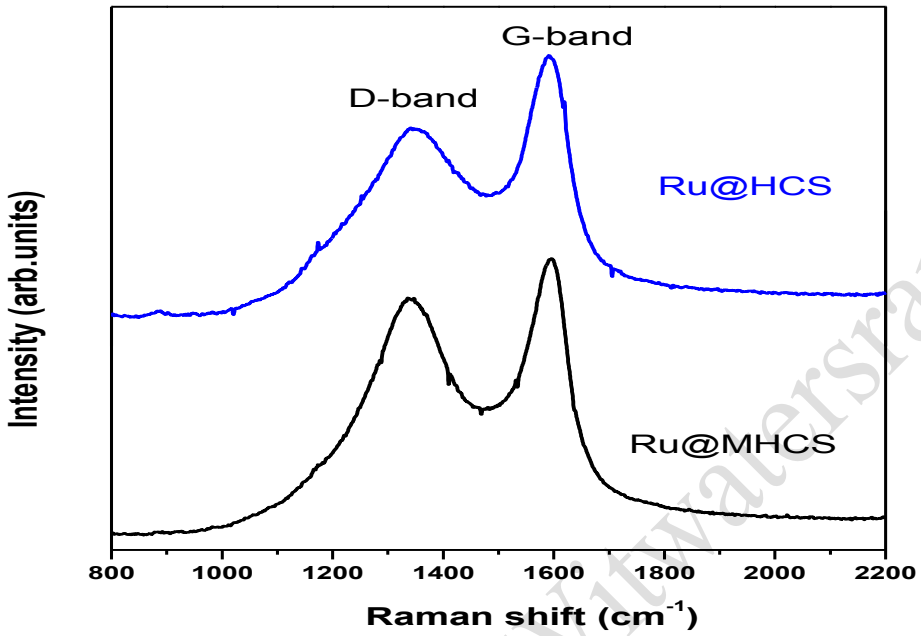

Figure 5S. 6: Raman spectra of the catalysts.

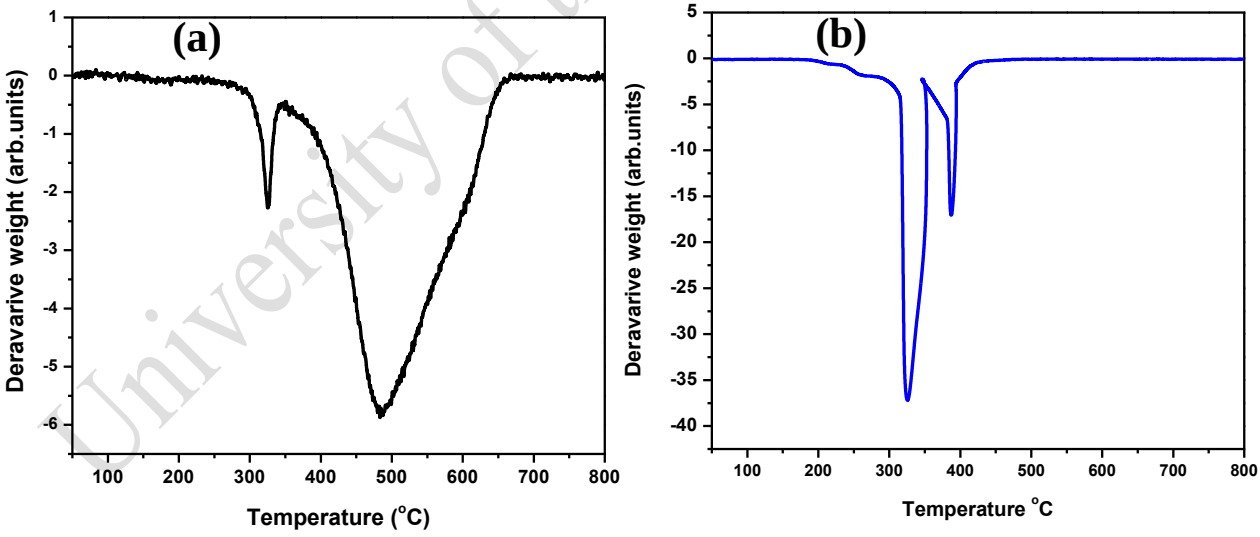

Figure 5S. 7: Differential thermogravimetric plots of the catalysts showing the major temperature regimes whereby there is a higher decomposition of the catalysts material under the flow of air, Ru@HCS (a) and Ru@MHCS (b).

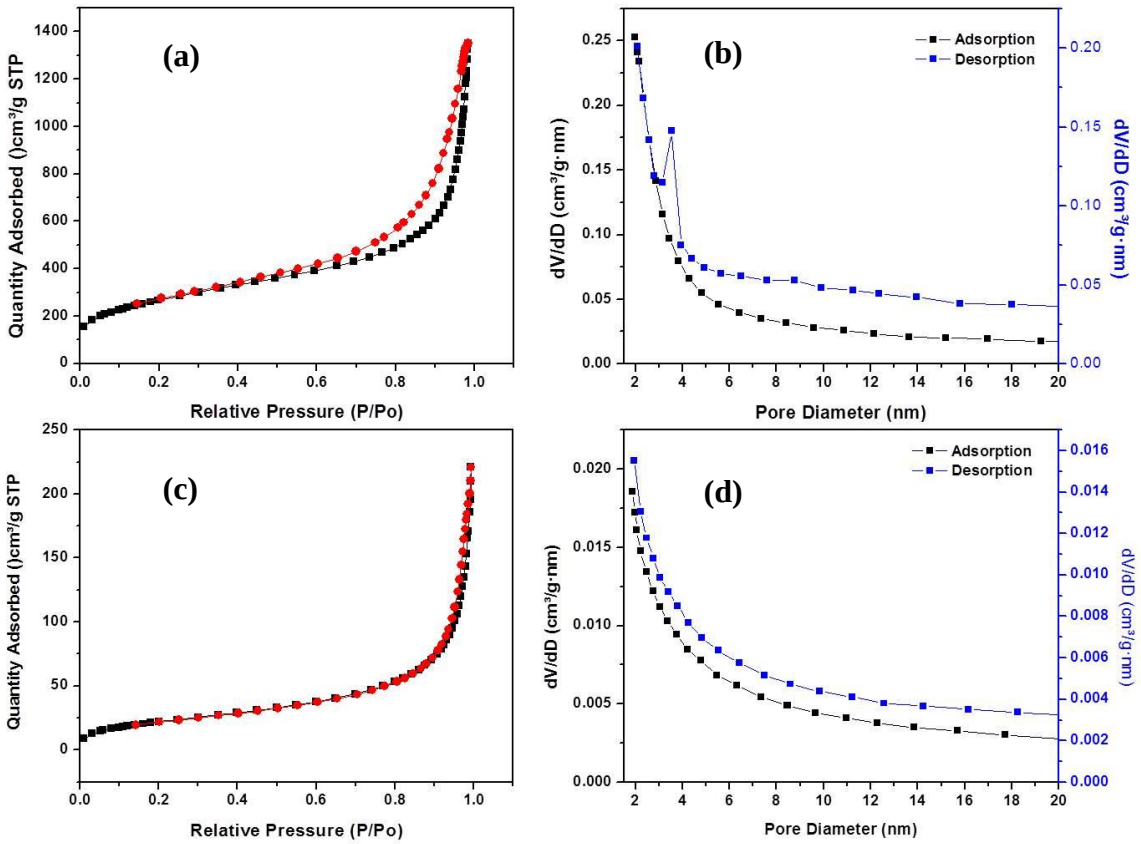

Figure 5S. 8: N_2 adsorption/desorption isotherm and pore size distribution curves of the MHCS (a,b), and HCS (c,d) empty spheres.

Table 5S: 1: N_2 adsorption/desorption data.

Sample name	BET surface area (m^2/g)	Micropore area (m^2/g)	Pore volume (cm^3/g)
MHCS	941	37	2.05
HCS	82	-	0.32
Ru@MHCS	944	135	1.47
Ru@HCS	75	1.44	0.27
Ru/MHCS	928	81	0.82
Ru/HCS	102	11	0.27

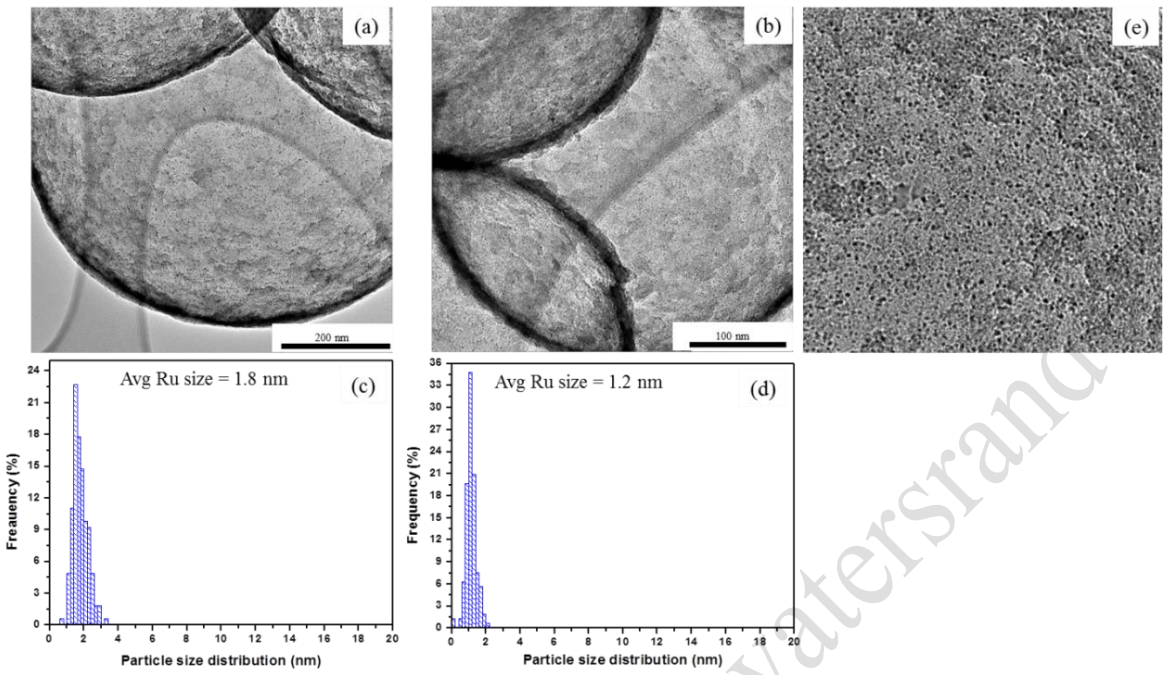

Figure 5S. 9: TEM images and Ru particle size distributions (PSD) of Ru/MHCS (a,b) and Ru/HCS (c,d) catalysts and (e) Magnified view of the Ru particles on the carbon surface.

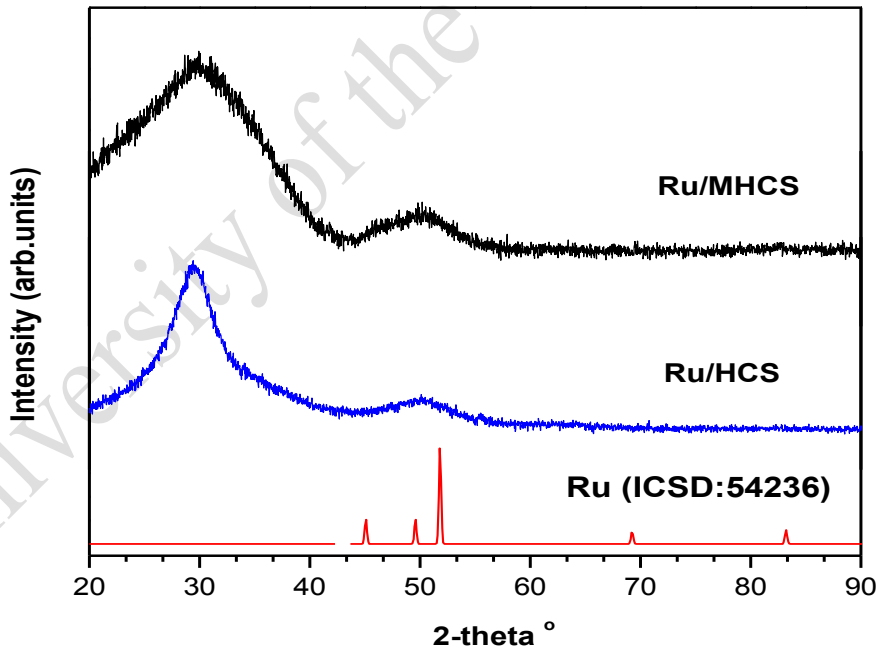

Figure 5S. 10: PXRD patterns of the supported Ru catalysts, Ru nanoparticles are too small and could not be detected by XRD diffraction

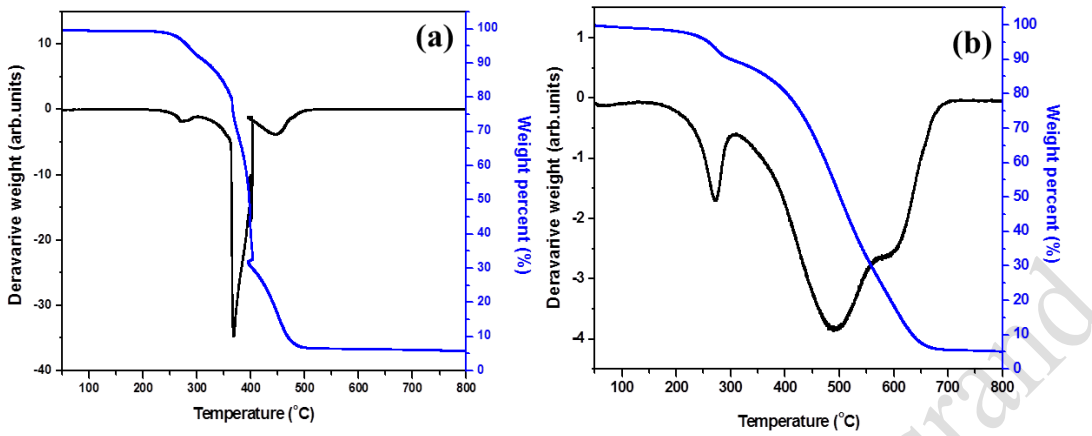

Figure 5S. 11: TGA and differential thermogravimetric profiles of the catalysts Ru/MHCS (a) and Ru@HCS (b).

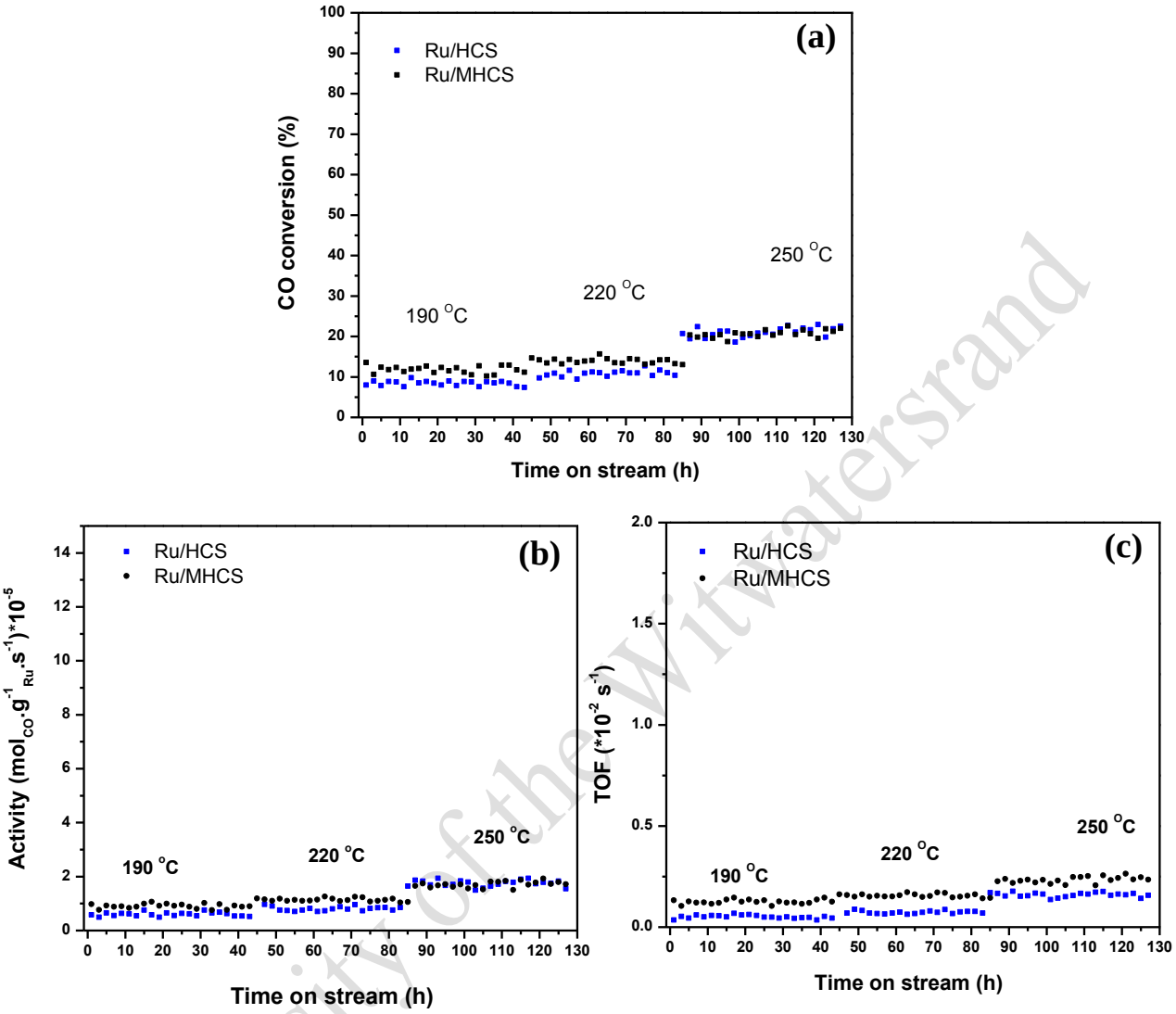

Figure 5S. 12: Plots showing the (a) CO conversion, (b) activity and (c) turnover frequency of the Ru nanoparticles supported outside the hollow carbon spheres under the Fischer-Tropsch synthesis process.

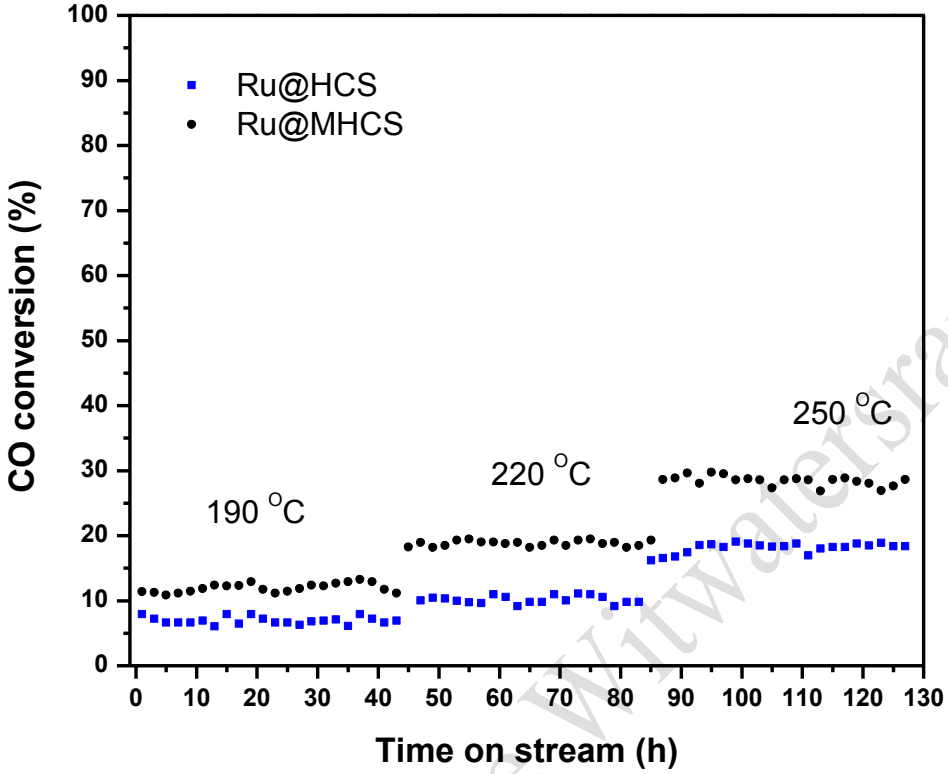

Figure 5S. 13: Plots showing the CO conversion under the Fischer-Tropsch synthesis process.

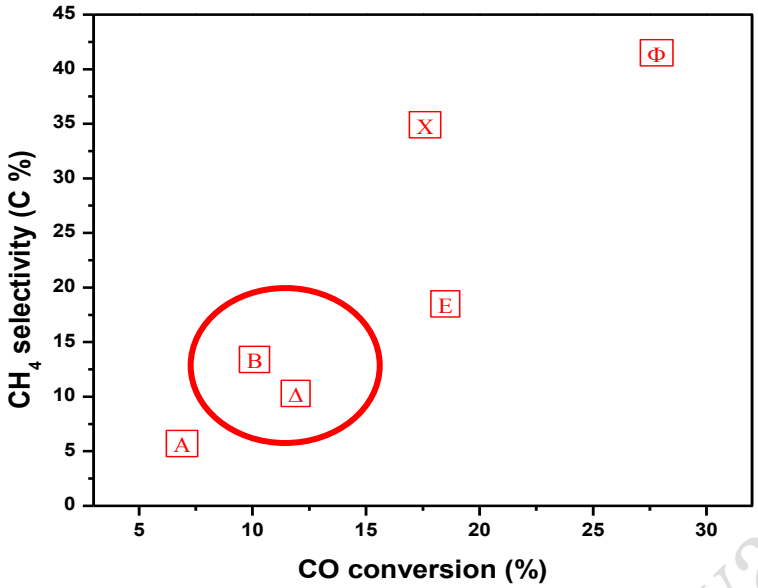

Figure 5S. 14: Methane selectivity versus CO conversion plot for both catalysts, Ru@HCS (A, Δ, X) and Ru@MHCS (B, E, φ) at reaction temperatures 190, 220 and 250 ℃.

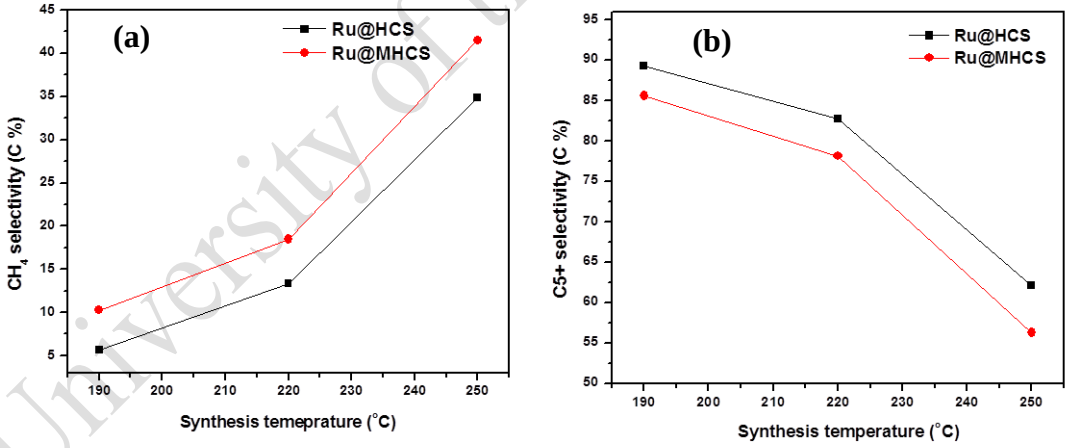

Figure 5S. 15: Product selectivities (a) methane and (b) C5+ hydrocarbons.

.

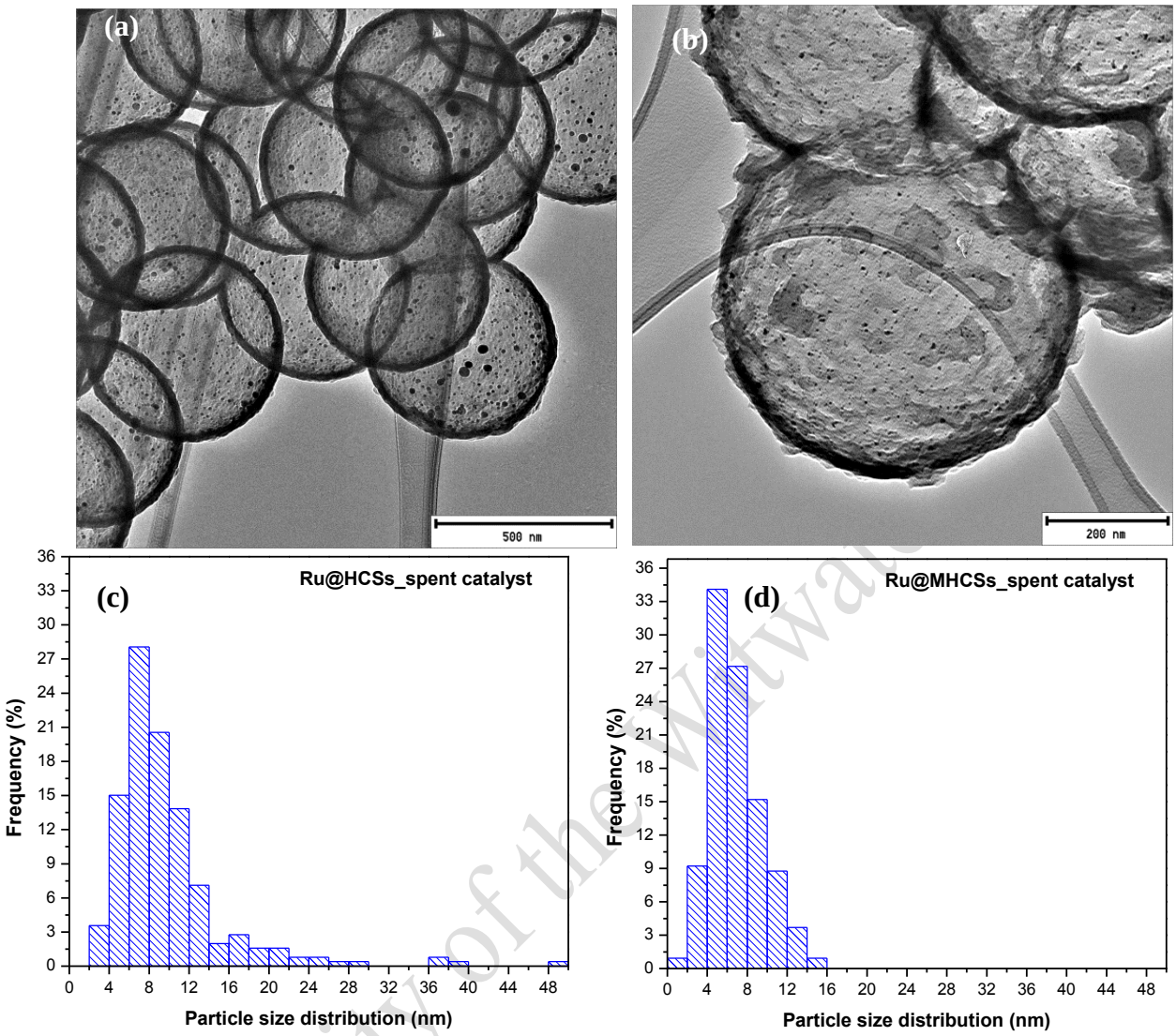

Figure 5S. 16: TEM images and particle size distribution of spent catalysts after Fischer Tropsch synthesis at 190, 220 and 250 ℃. Ru@MHCS (a,c) and Ru@HCS (b,d).

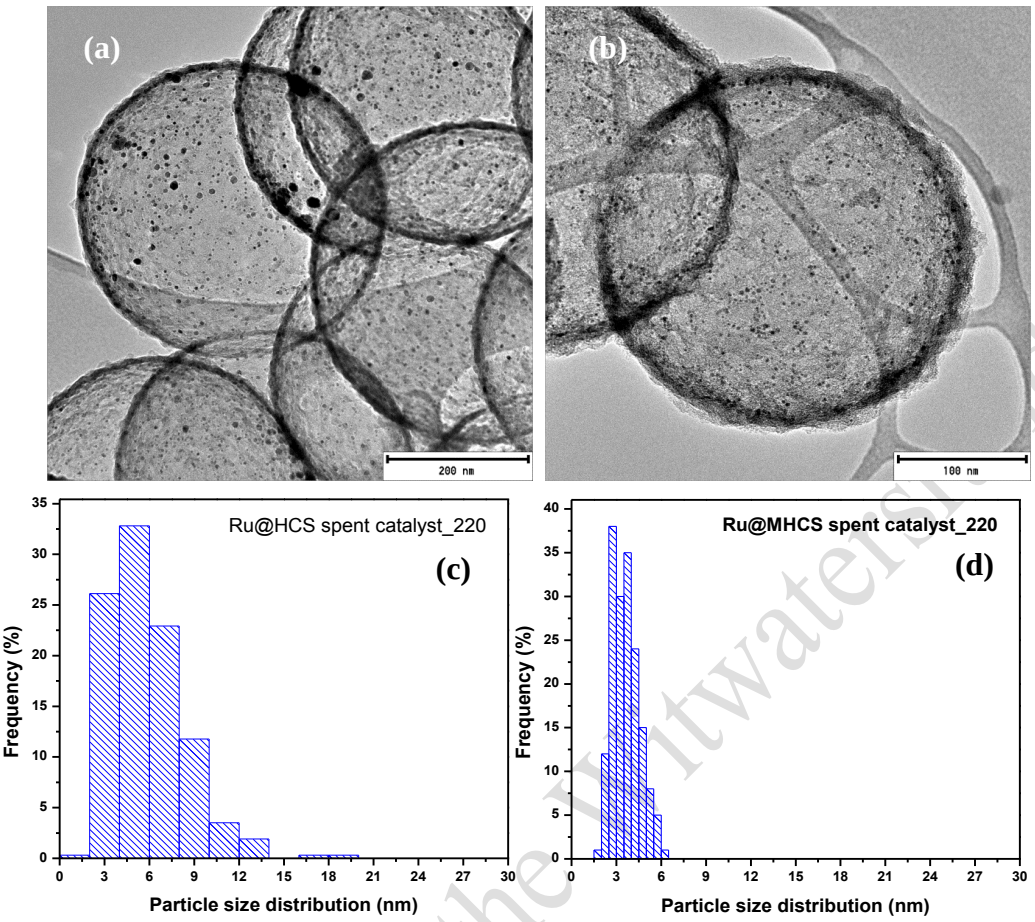

Figure 5S. 17: TEM images and particle size distribution of spent catalysts after Fischer-Tropsch synthesis at 190 and 220 ℃. Ru@HCS (a,c) and Ru@MHCS (b,d).

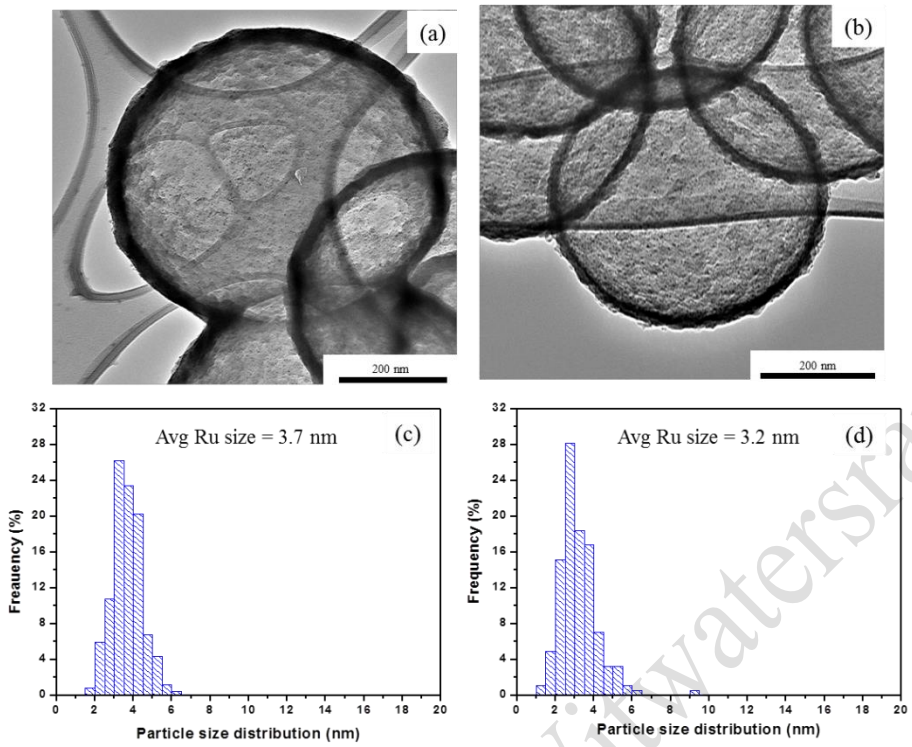

Figure 5S. 18: TEM images and particle size distribution of spent catalysts after Fischer-Tropsch synthesis at 190, 220 and 250 ℃. Ru/MHCS (a,c) and Ru/HCS (b,d).

Table 5S: 2: Fischer-Tropsch Synthesis performance of the supported Ru catalysts.

Sample	Reaction Temperature (℃)	CO Conversion (%)	Selectivity (C mol) %		
			C_1	C_2-C_4	C_{5+}
Ru/MHCSs	190	11.7	17.2	5.2	77.1
	220	13.9	31.4	6.1	62.5
	250	20.4	71.8	4.2	24.0
Ru/HCSs	190	7.8	16.0	4.9	78.9
	220	10.6	39.4	5.1	55.4
	250	20.9	66.5	5.6	27.4

Fischer-Tropsch reaction conditions: T = 190, 220 and 250 ℃ $P_{syn.gas}$ = 10 bar, W/F = 15 g.h.mol^{-1}.

Chapter 6: Supporting information

Appendix B

Effects of Co and Ru intimacy in Fischer-Tropsch catalysts using hollow carbon sphere supports: assessment of the hydrogen spillover processes

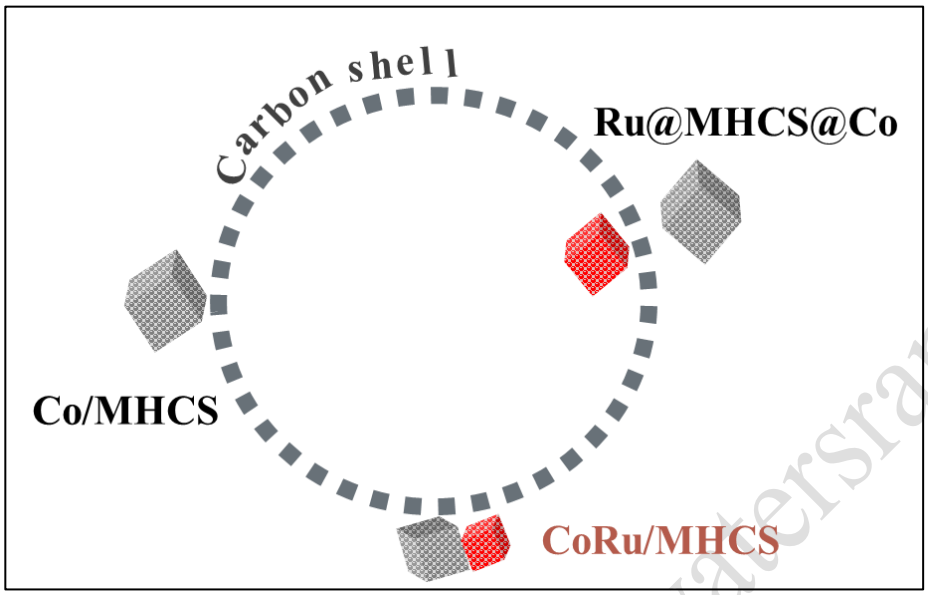

Scheme 6S. 1: Catalyst schematic and their corresponding nomenclature.

6S 1. Rietveld refinement method

Quantitative phase analysis (QPA) using Rietveld refinement **[346]**, was performed using the fundamental parameters approach in TOPAS 4.2 software. **[347, 348]** The derivation of the algorithms used in TOPAS 4.2 to calculate phase loading (in percentage) in each of the experiments has been presented elsewhere. **[235]** The fundamental parameters approach involved the determination of a peak-profile function (taking into account peak broadening due to instrumentation parameters), based on user input and the PXRD powder diffraction scans, which were refined by a least-squares procedure until a reasonable fit is achieved. Crystallite size determination from diffraction data was attained by using the in-built Scherrer equation. The model refined in Rietveld's method includes parameters related to the instrument, phase concentration, particle size, lattice constants and other parameters related to the materials being refined, all these values can then be extracted once a successful Rietveld refinement has completed.**[297]**

These CIF files [downloaded from https://icsd.fiz-karlsruhe.de/search/basic.xhtml] were used for the refinement: Carbon support (graphite-2H, database_code_ICSD **31170**), Co_3O_4 (database_code_ICSD **9362**), CoO (database_code_ICSD **9865**), Co(fcc) (database_code_ICSD **44989**), Co(hcp) (database_code_ICSD **44990**) and Ru (database_code_ICSD **54236**).

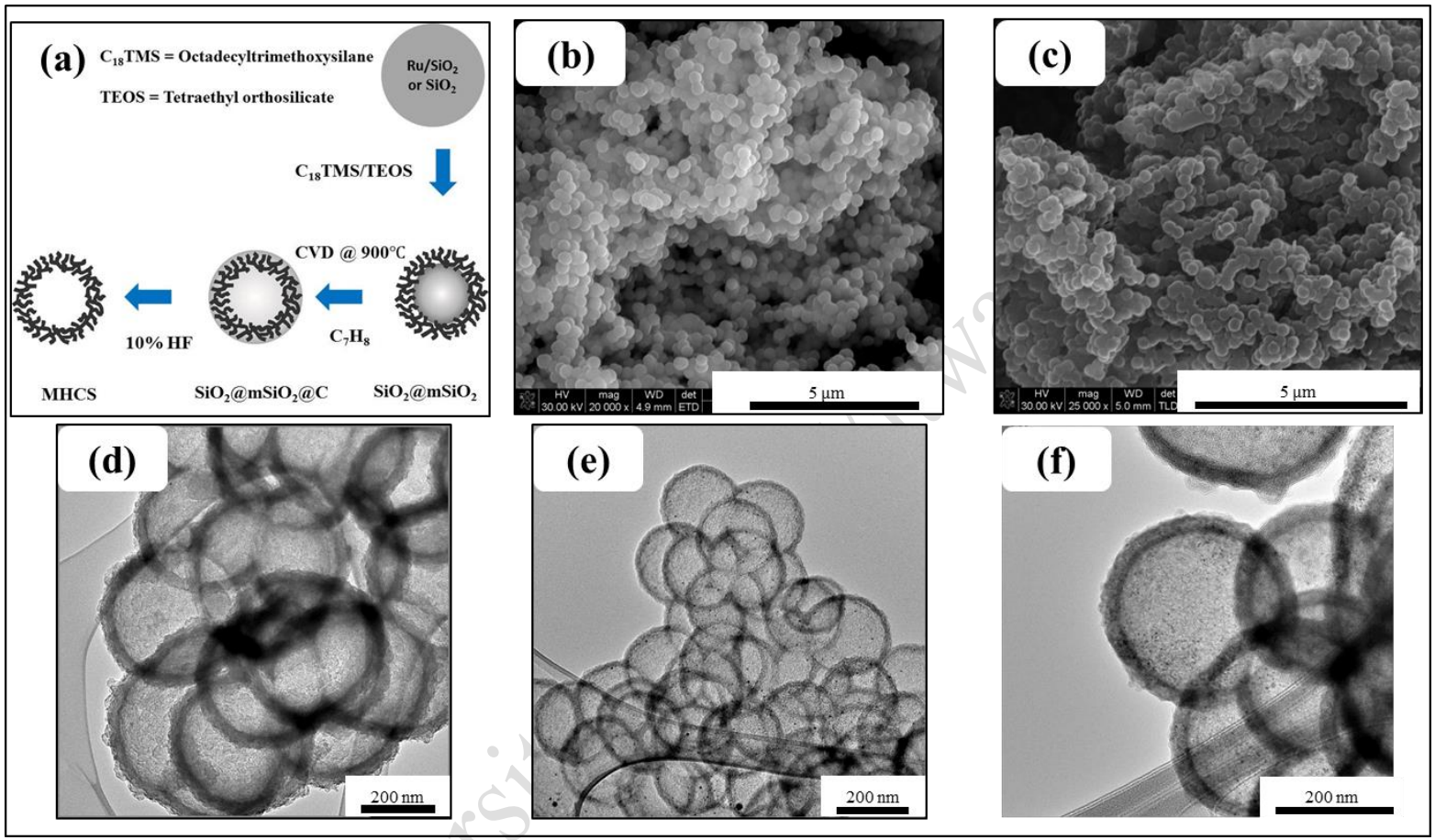

Figure 6S. 1: (a) General scheme for synthesis of the mesoporous hollow carbon spheres with or without Ru inside. (b) SEM images of the silica (or Ru on silica) spheres template before carbon coating, (c) SEM images of mesoporous hollow carbon spheres (MHCS) after template removal of the silica template and TEM images of: (d) the empty mesoporous hollow carbon spheres (MHCS), (e) Ru nanoparticles inside the MHCS (i.e., Ru@MHCS, after bubblig toluene for one hour during carbonization) and (f) an image of Co nanoparticles loaded outside MHCS of Ru@MHCS giving 0.2% Ru@MHCS@Co.

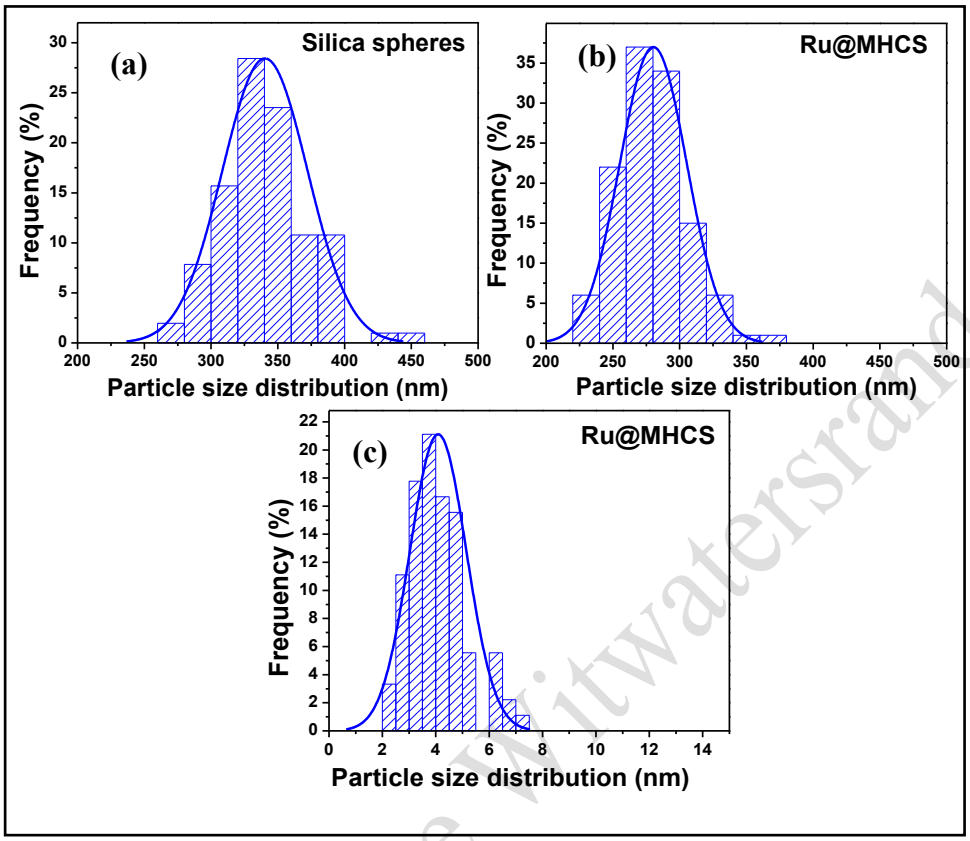

Figure 6S. 2: Size distributions of: (a) the silica spheres, (b) MHCS for Ru@MHCS and (c) Ru nanoparticles for Ru@MHCS

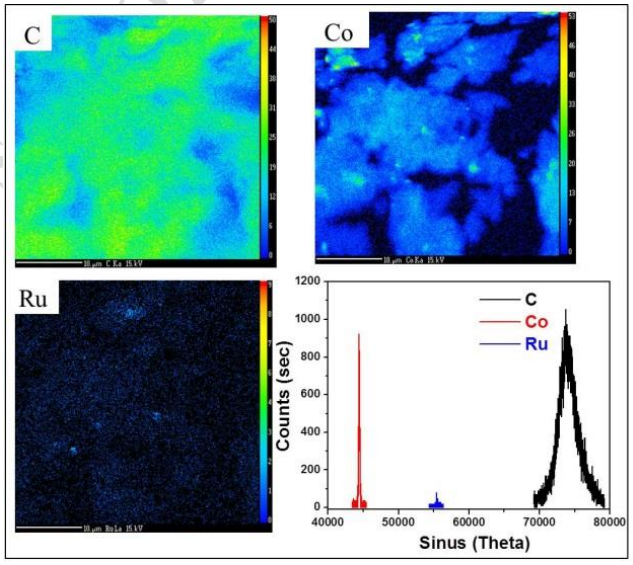

Figure 6S. 3: EPMA mapping and WDS spectra of Ru@MHCS@Co showing the distribution and relative abundance of C, Co and Ru on the sample.

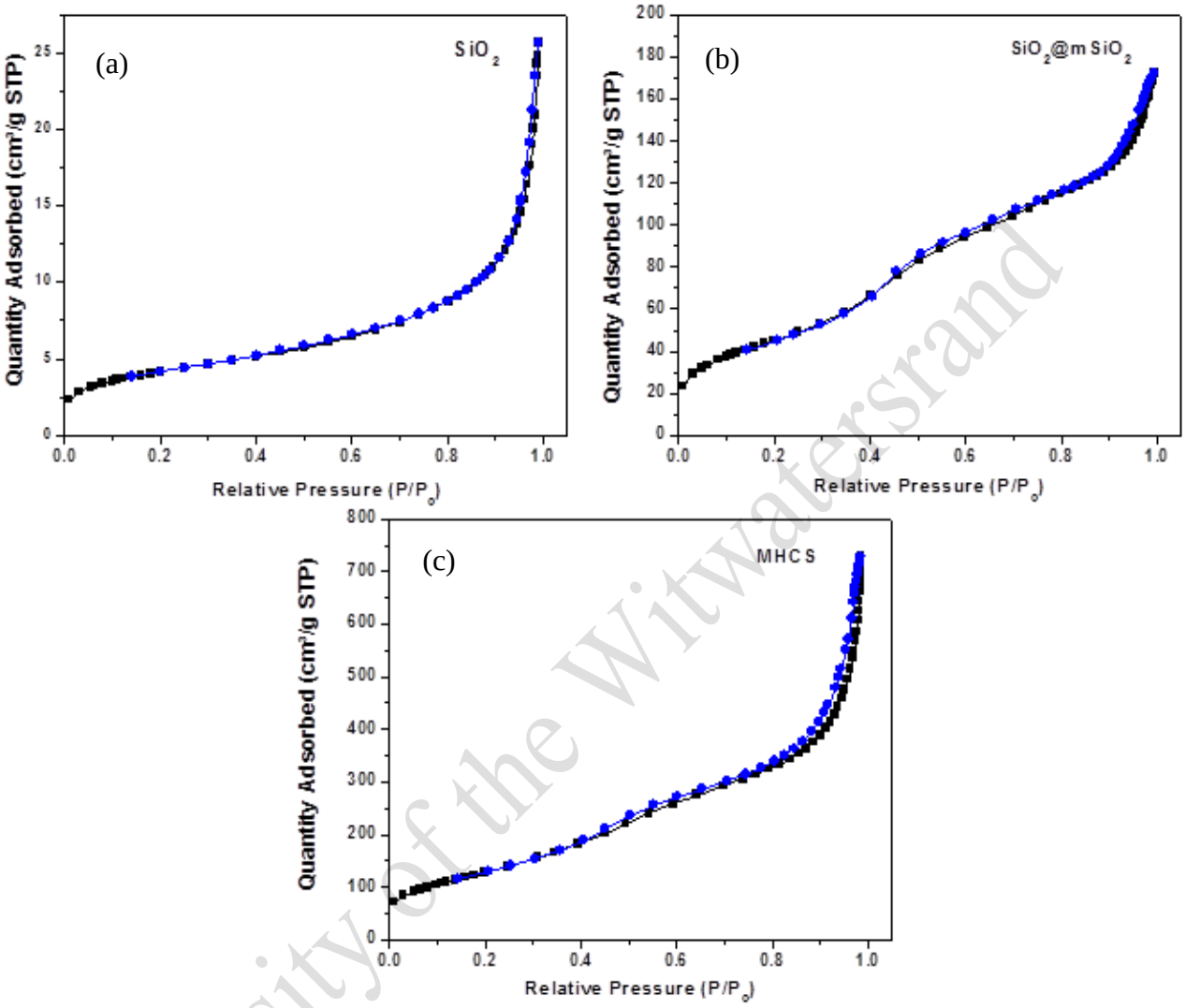

Figure 6S. 4: Nitrogen adsorption isotherms of the silica sphere templates and the resulting hollow carbon spheres.

Table 6S. 1: BET surface area, pore volume and pore diameter of the catalysts.

Sample name	BET surface area/ m^2/g	Micropore area/m^2/g	Pore volume/ cm^3/g	Pore diameter /nm
SiO_2 (Stober spheres)	14	-	0.04	10.6
SiO_2@mSiO_2	165	-	0.27	6.4
MHCS	472	-	1.15	7.8
0.2% Ru@MHCS	462	-	0.65	4.4
0.5% Ru@MHCS	485	-	0.71	5.1
0.2%Ru@MHCS@Co	433	5	0.77	6.8
0.5%Ru@MHCS@Co	421	-	0.55	4.6
CoRu/MHCS	416	20	0.95	9.1
Co/MHCS	425	12	0.86	8.3

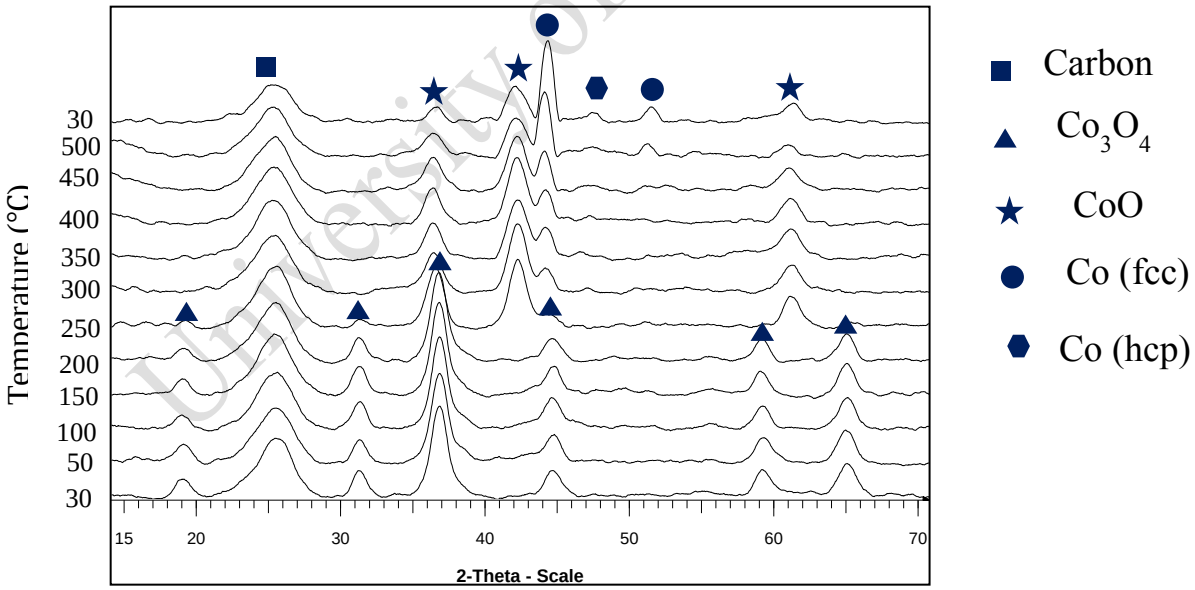

Figure 6S. 5: Typical full in situ PXRD scan of the catalysts (i.e., Co/MHCS) under a flow of 5% H_2/N_2 gas.

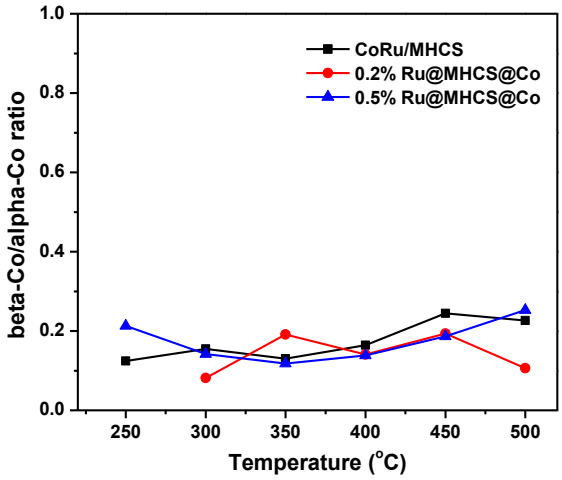

Figure 6S. 6: Co (hcp) to Co (fcc) ratio as calculated using Rietveld refinement QPA.

Table 6S. 2: Co phases changes under in situ PXRD reduction, hcp cobalt (β-Co) and fcc cobalt (α-Co).

Temperature (℃)	Sample phase			
	Co/MHCS	CoRu/MHCS	0.2% Ru@MHCS@Co	0.5% Ru@MHCS@Co
30	Co_3O_4	Co_3O_4	Co_3O_4	Co_3O_4
50	Co_3O_4	Co_3O_4	Co_3O_4	Co_3O_4
100	Co_3O_4	Co_3O_4	Co_3O_4	Co_3O_4
150	Co_3O_4	Co_3O_4	Co_3O_4	Co_3O_4
200	Co_3O_4	CoO	Co_3O_4/CoO	CoO
250	Co_3O_4/CoO	CoO/β-Co	CoO/Co	CoO/Co
300	CoO/α-Co	β -Co/α-Co	CoO/α -Co	CoO/β -Co/α -Co
350	CoO/α -Co	β -Co/α -Co	CoO/β -Co/α -Co	CoO/β -Co/α -Co
400	CoO/α -Co	β -Co/α -Co	CoO/β -Co/α -Co	CoO/β -Co/α -Co
450	CoO/α -Co	β -Co/α -Co	β -Co/α -Co	β -Co/α -Co
500	CoO/α -Co	β -Co/α -Co	β -Co/α -Co	β -Co/α -Co
30	CoO/α -Co	β -Co/α -Co	β -Co/α -Co	β -Co/α -Co

.

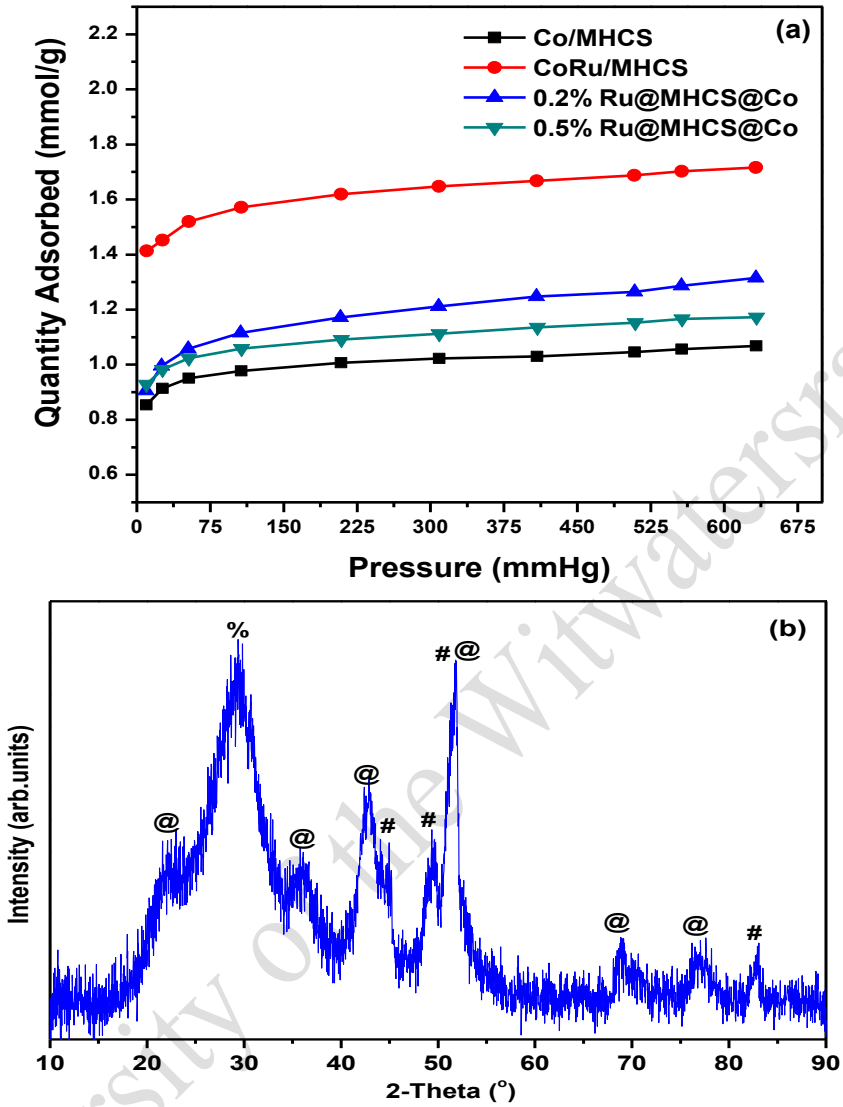

Figure 6S. 7: Oxygen titration adsorption isotherms of the catalysts used for calculating a catalysts degree of reduction obtained at 200 ℃ (a) and the resulting PXRD pattern of the spent re-oxidized catalyst. Carbon (%), Co_3O_4 (@) and Ru (#) (b).

Table 6S. 3: DOR values of the catalysts.

Catalyst	Degree of reduction (O_2 – titration)/%	Degree of reduction (XRD)/%
Co/MHCS	62.4	24
CoRu/MHCS	90.2	100
0.2% Ru@MHCS@Co	61.5	35
0.5% Ru@MHCS@Co	63.2	44

Table 6S. 4: Peak parameters of the TPR profiles after deconvolution.

Sample	Nitrate decomposition /℃	Peak 1 # /℃	Peak 2 ^ /℃	Integrated area ratios ($A_{CoO \rightarrow Co}/A_{Co3O4 \rightarrow CoO}$)
Co/MHCS	206	282	429	2.93
CoRu/MHCS	-	247	482	0.89
0.2%Ru@MHCS@Co	206	299	403	2.85
0.5%Ru@MHCS@Co	224	306	405	3.54

attributed to $Co_3O_4 \rightarrow CoO$, ^ attributed to $CoO \rightarrow Co$, except in the case of CoRu/MHCS where this peak is probably due to support gasification catalysts by metallic Co.

Table 6S. 5: Hydrogen consumption estimated from TPR peaks.

Sample	Peak 1 #/ mmol/g	Peak 2 ^ / mmol/g	Total hydrogen consumption/ mmol/g	DOR(%)[a]
Co/MHCS	1.10	3.23	4.33	131
CoRu/MHCS	2.35	2.10	4.46	128
0.2%Ru@MHCS@Co	1.44	4.10	5.53	173
0.5%Ru@MHCS@Co	1.24	4.41	5.65	168

[a]DOR > 100% due to support gasification at higher temperatures, therefore not true representative of the catalyst DOR.

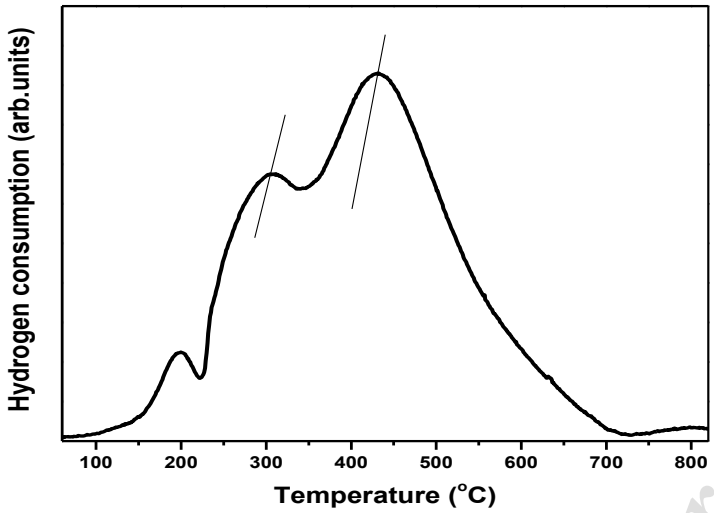

Figure 6S. 8: TPR profile of 5% Ru/MHCS + 15% Co/MHCS (1: 4 wt/wt) physical mixture.

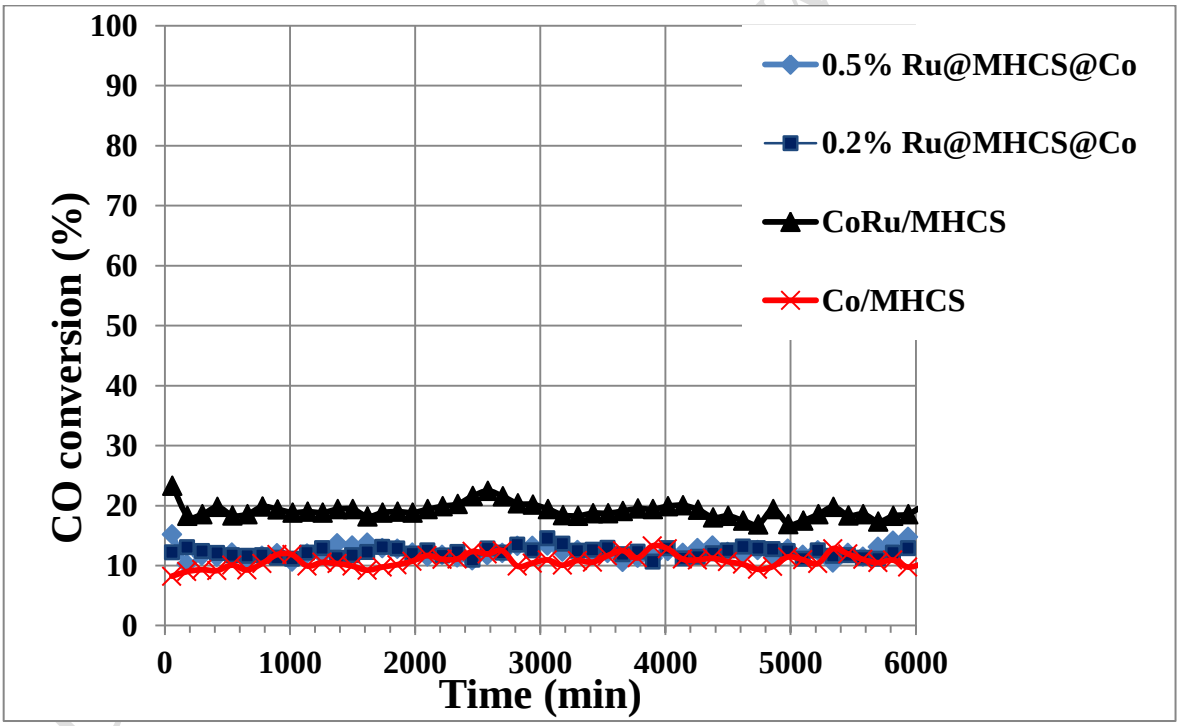

Figure 6S. 9: CO conversion plots of the different catalysts over 100 hours Fischer-Tropsch reaction time on stream.

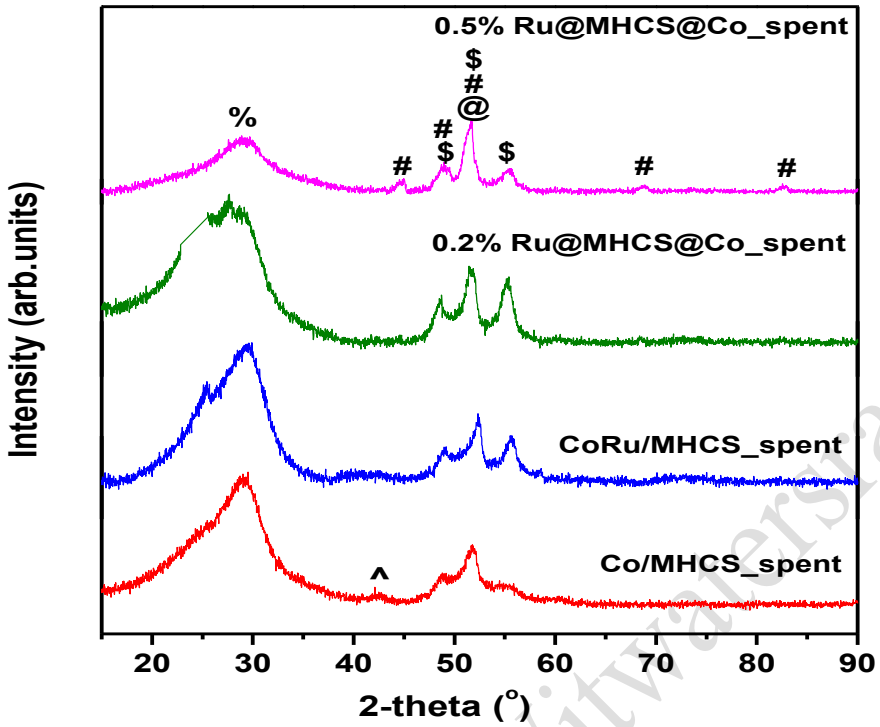

Figure 6S. 10: PXRD patterns of the fresh and spent catalysts, Carbon (%), hcp Co($), fcc Co (@) and Ru (#), CoO (^) . XRD patterns obtained after passivation of the catalysts in the reactor at room for 0.5 hour using 5% O2/Ar (15 mL.min-1) gas mixture.

Table 6S. 6: Co crystallite sizes before and after Fischer-Tropsch synthesis as calculated using Rietveld refinement.

Sample	Co_3O_4 crystallite size before FT /nm	Co crystallite size after FT /nm ***(% relativeWt)***		
		α-Co	β-Co	CoO
Co/MHCS	4.8	5.5 ***(74.4)***	4.6 ***(19.7)***	4.4 ***(5.8)***
CoRu/MHCS	4.7	7.1 ***(62.2)***	5.6 ***(37.8)***	-
0.2%Ru@MHCS@Co	4.8	6.5 ***(61.3)***	5.6 ***(38.6)***	-
0.5%Ru@MHCS@Co	4.7	6.4 ***(69.1)***	3.7 ***(30.9)***	-

Chapter 7: Supporting information

Appendix C

Fischer-Tropsch synthesis in a carbon nanoreactor: spillover effect observed on Co@MHCS@Ru

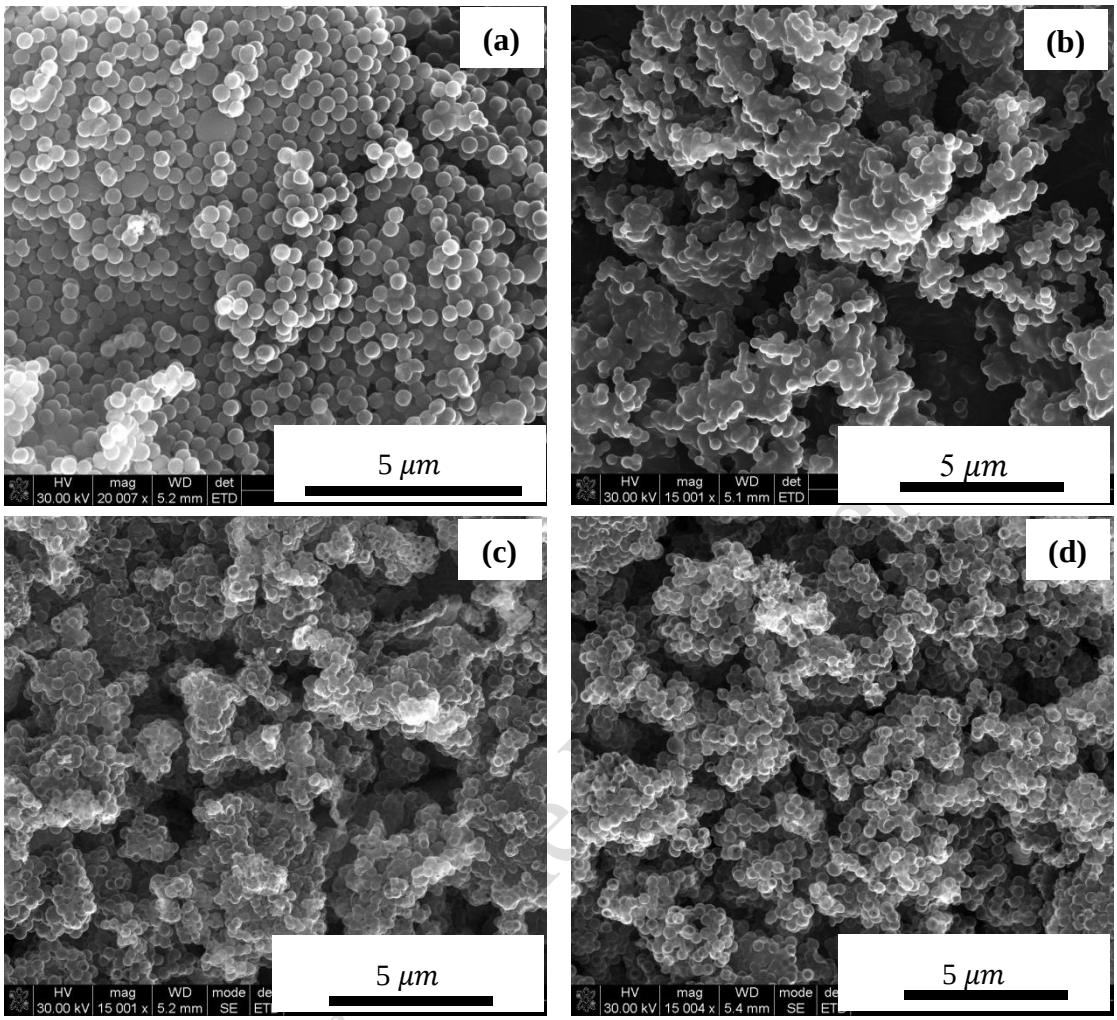

Figure 7S. 1: SEM of PSSs template loaded with Co nanoparticles (a), PSS@C after carbon coating (b), Co@MHCS (c) and CoRu@MHCS (d).

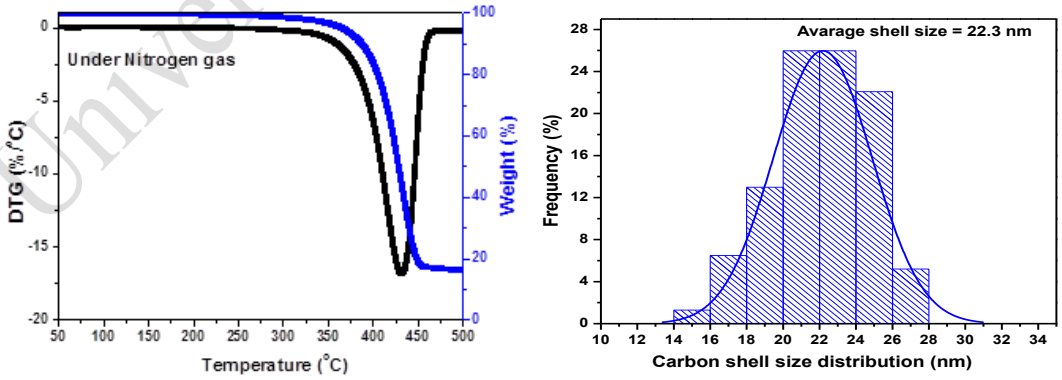

Figure 7S. 2: TGA profile of PSS@RF showing the onset of the polystyrene decomposition and the resulting hollow carbon spheres shell size estimation.

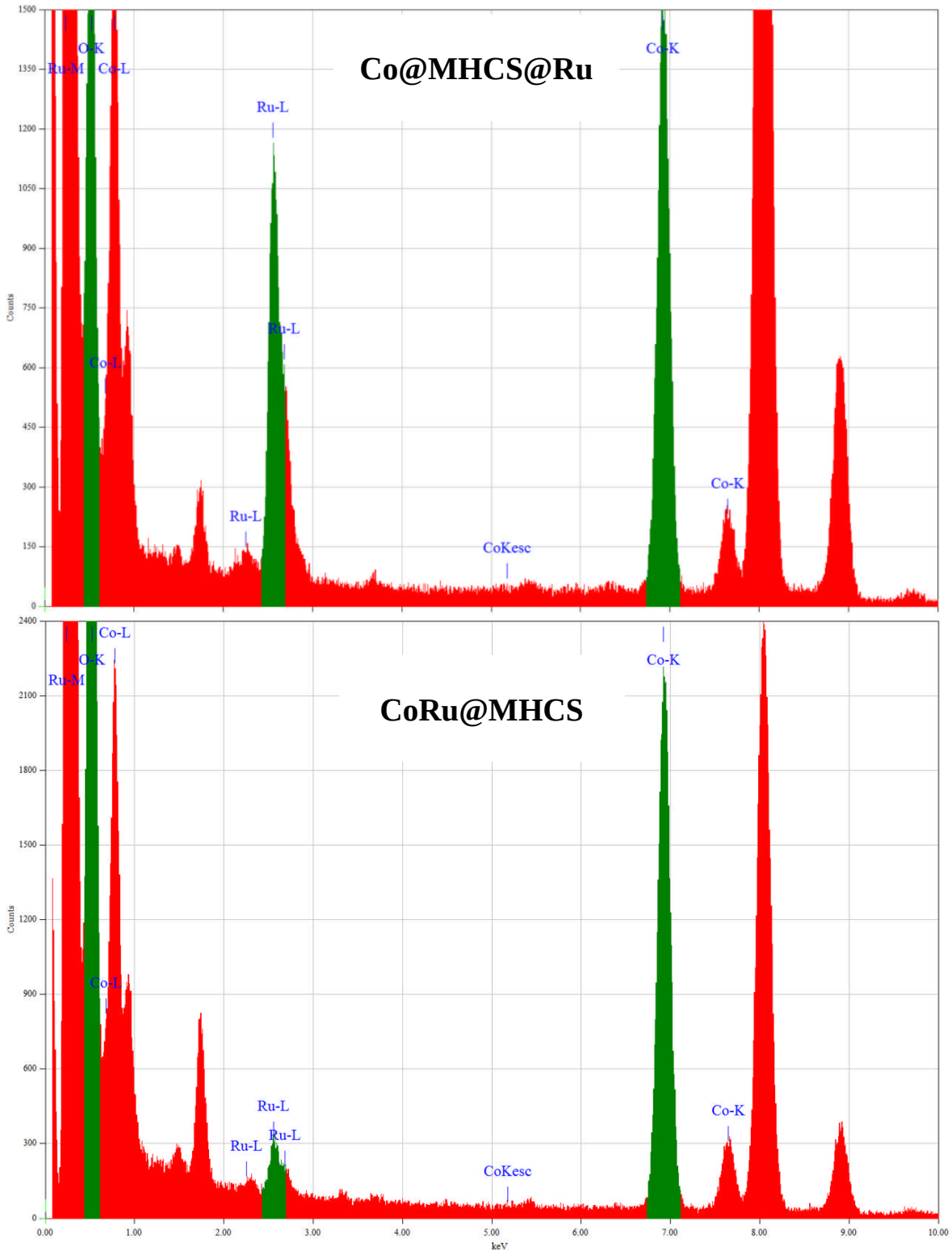

Figure 7S. 3: EDX profiles of the catalysts.

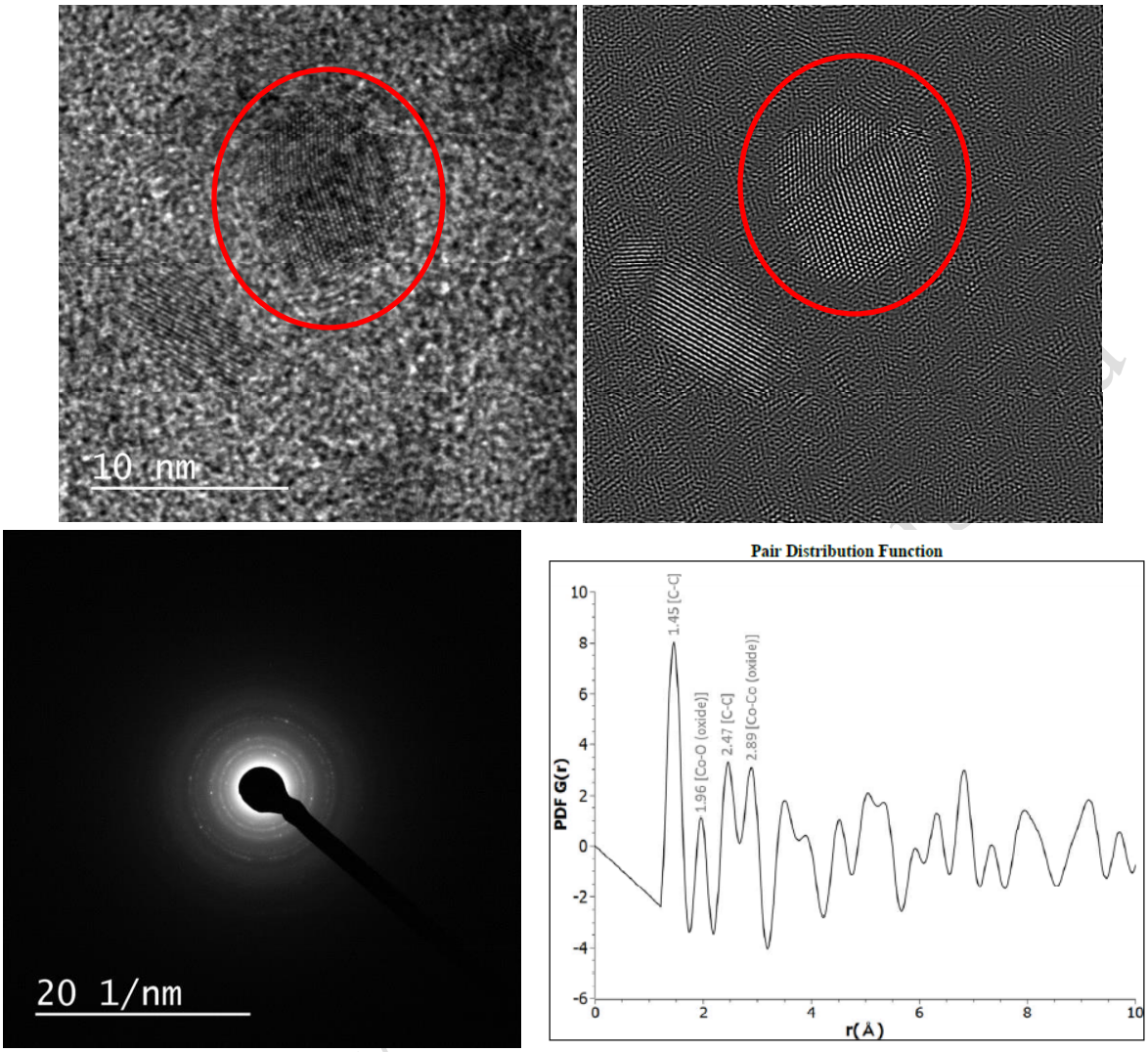

Figure 7S. 4: High resolution EM images, selected area diffraction and PDF plot of the encapsulated nanoparticles on CoRu@MHCS.

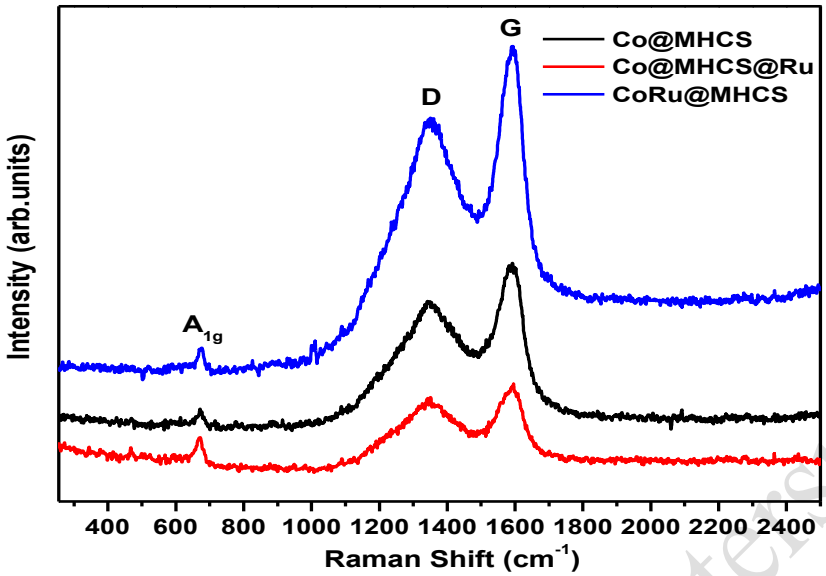

Figure 7S. 5: Raman spectra of the catalysts showing Co3O4 and carbon excitation bands.

Table 7S. 1: Materials BET surface area. micropore surface area and pore volume.

Sample name	BET surface area (m^2/g)	Micropore area (m^2/g)	Pore volume (cm^3/g)	Pore diameter (nm)
PSSs	2	-	0.005	-
PSSs@RF-C	12	-	0.04	13.8
Co@MHCS	483	322	0.59	4.9
CoRu@MHCS	438	232	0.55	6.1
Co@MHCS@Ru	443	265	0.52	4.7

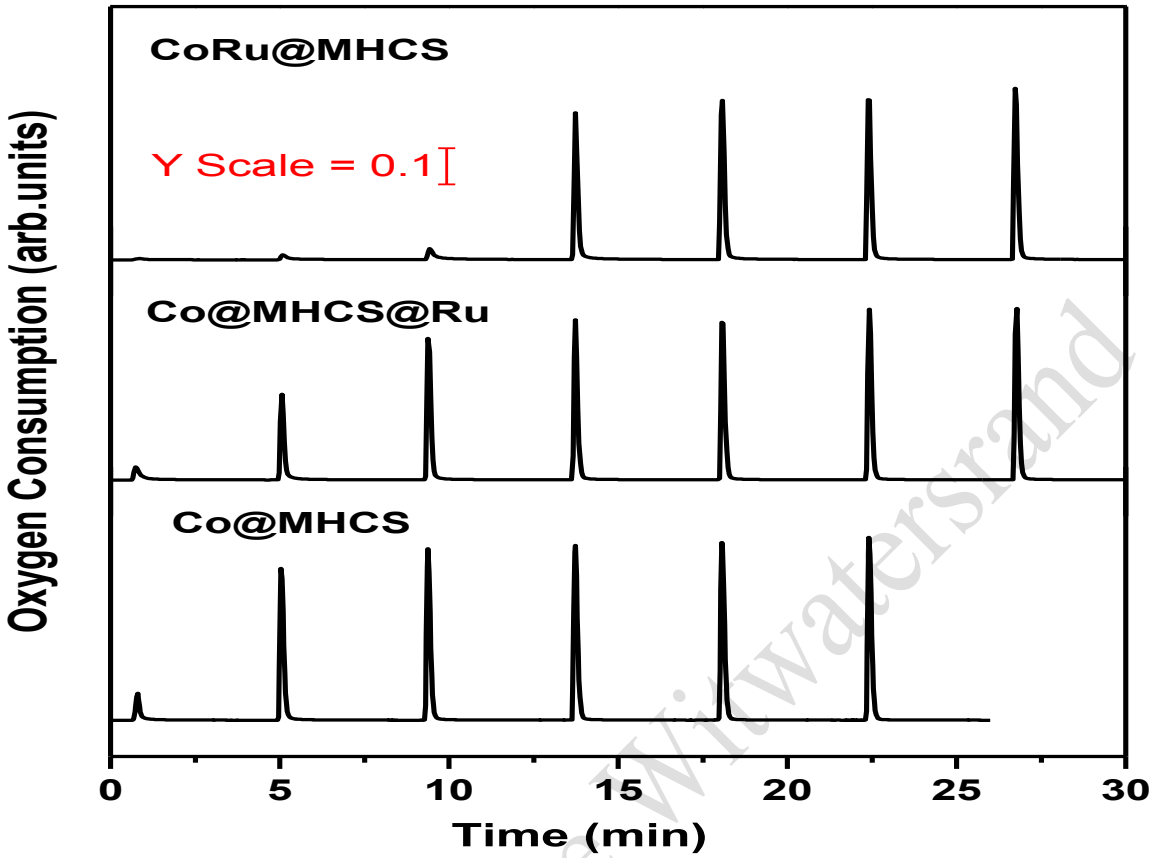

Figure 7S. 6: Oxygen pulse chemisorption for Co bulk oxidation at 200 ℃.

Table 7S. 2: Extend of reduction as evaluated from in situ XRD and oxygen titration experiments.

Catalyst	Degree of reduction (O_2 –pulse)/%	Degree of reduction (XRD)/%
Co@MHCS	21.5	28.7
Co@MHCS@Ru	22.2	49.9
CoRu@MHCS	61.3	100

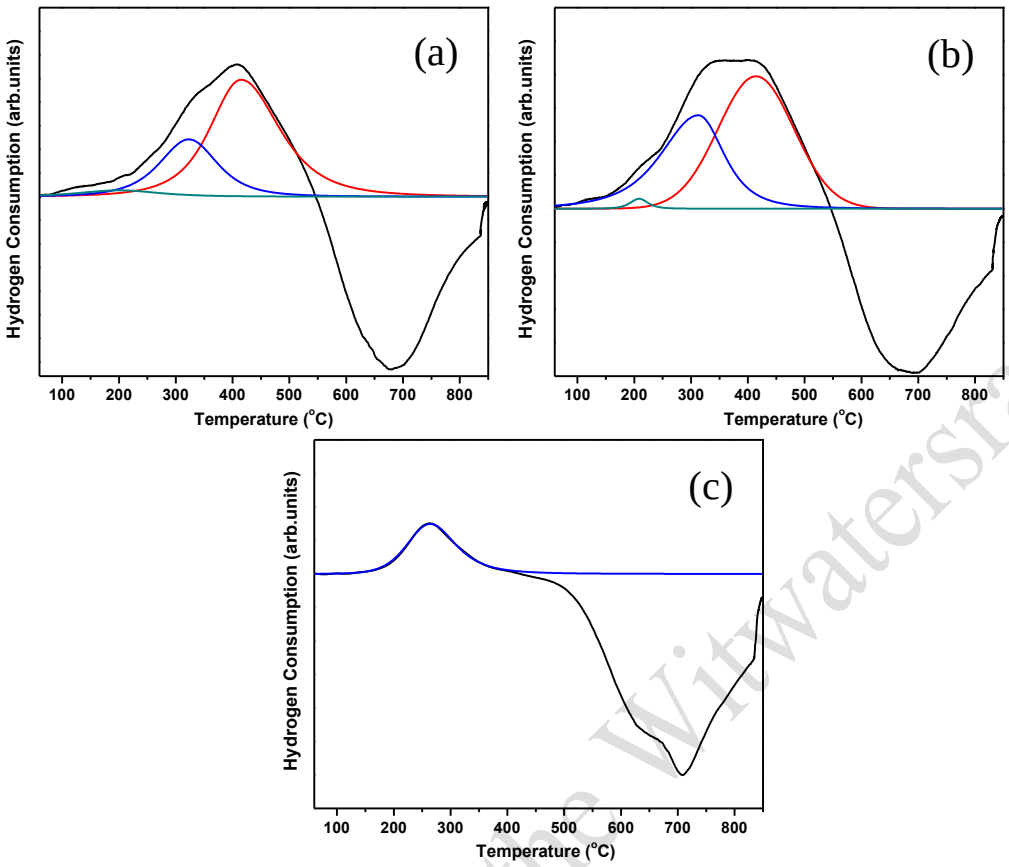

Figure 7S. 7: Temperature programmed reduction (TPR) of the catalysts, Co@MHCS (a), Co@MHCS@Ru (b) and CoRu@MHCS (c).

Table 7S. 3: Peak parameters of the TPR profiles after deconvolution.

Sample	$Co_3O_4 \rightarrow CoO$ (°C)	$CoO \rightarrow Co$ (°C)	Integrated area ratios ($A_{CoO \rightarrow Co}/A_{Co3O4 \rightarrow CoO}$)
Co@MHCS	323	415	2.4
Co@MHCS@Ru	312	414	1.6
CoRu@MHCS	264 (corresponding to $Co_3O_4 \rightarrow Co$)		

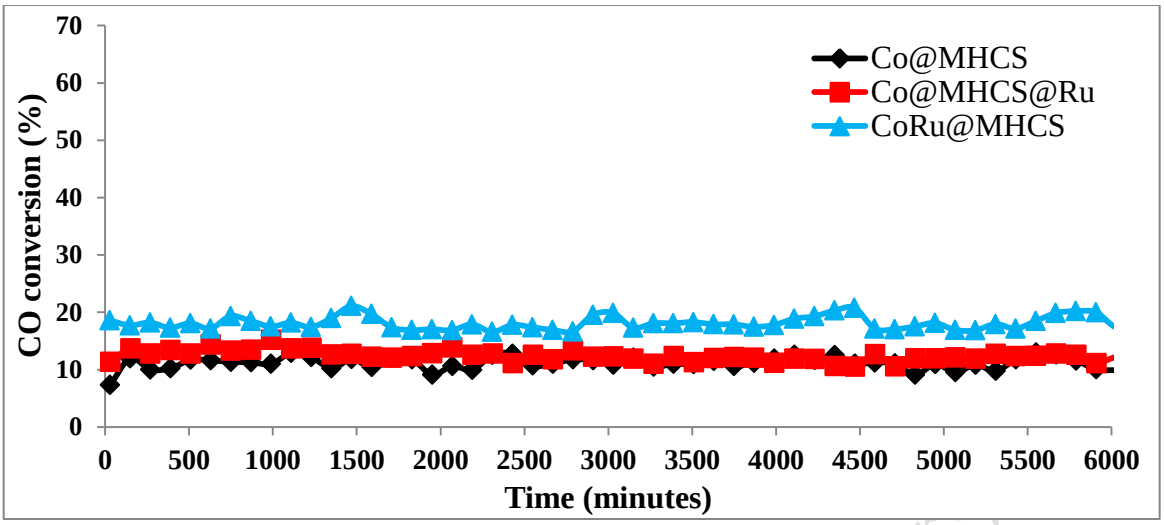

Figure 7S. 8: CO conversion plots of the catalysts over 100 hours Fischer-Tropsch synthesis test.

Chapter 8: Supporting information

Appendix D

Effect of Water on the Stability of Co Fischer-Tropsch Nanoparticles inside Hollow Carbon Spheres: An In Situ Magnetometer Study

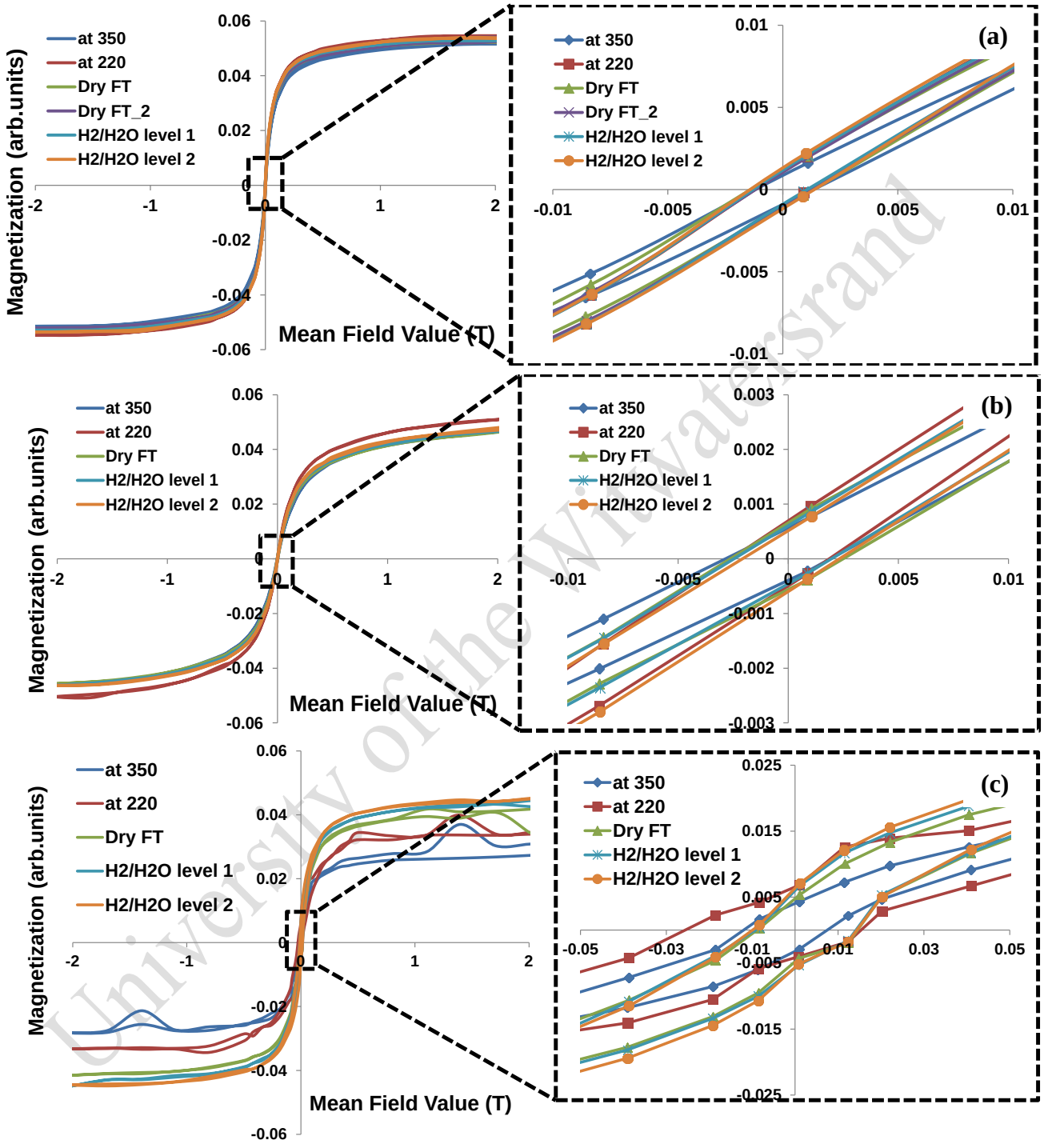

Figure 8S. 1: Catalysts hysteresis loops after different reaction conditions. (a) Co@MHCS, (b) CoRu@MHCS and (c) Co/MHCS.

Chapter 9: Supporting information

Appendix E

A Sinter Resistant Cobalt Fischer-Tropsch Catalyst Supported on Titania; With Ru as an Electronic Promoter And Mesoporous Silica as The Structural Promoter.

9S.1. In Situ PXRD analysis and Rietveld analysis details.

X-ray diffraction experiments were performed on a Bruker D8 Advance fitted with an Anton Paar XRK 900 in situ cell. The diffractometer used a sealed copper tube as the X-ray source operating at 40 kV and 40 mA that provided X-rays with a wavelength of 0.15418 nm in parallel beam geometry.

Quantitative Rietveld refinement **[346]**, was performed using the fundamental parameters approach in TOPAS 4.2 software **[347, 348]**. The derivation of the algorithms used in TOPAS 4.2 to calculate phase loading (in percentage) in each of the experiments has been presented elsewhere **[235]**. The fundamental parameters approach involved the determination of a peak-profile function (taking into account peak broadening due to instrumentation parameters), based on user input and the PXRD powder diffraction scans, which were refined by a least-squares procedure until a reasonable fit is achieved. Crystallite size determination from diffraction data was attained by using the in-built Scherrer equation. The model refined in Rietveld's method includes parameters related to the instrument, phase concentration, particle size, lattice constants and other parameters related to the materials being refined, all these values can then be extracted once a successful Rietveld refinement has completed.

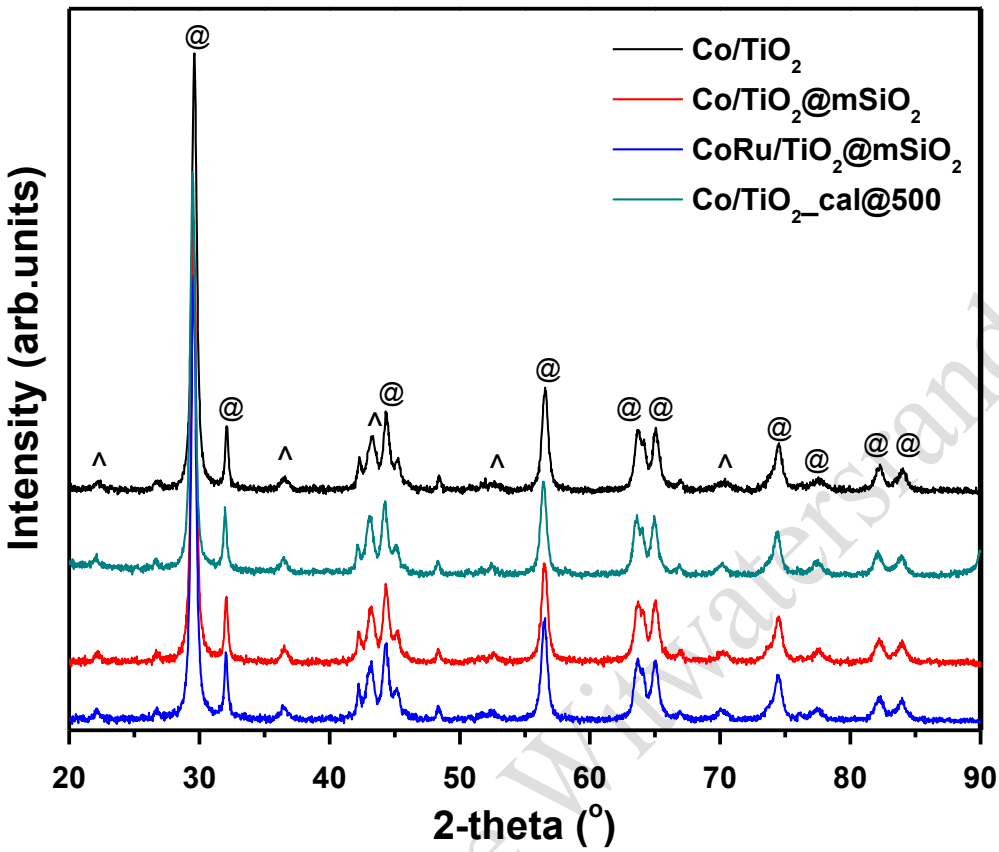

Figure 9S. 1: Ex situ PXRD patterns of the catalysts, TiO_2 (@) and Co_3O_4 (^).

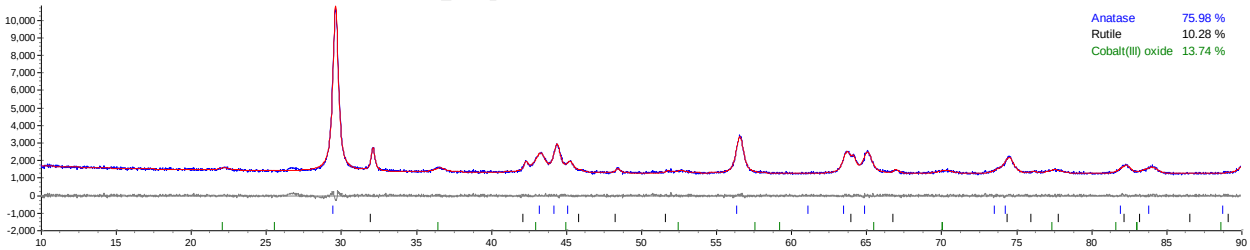

Sample name	RwP	Anatase		Rutile		Cobalt(III)oxide	
		Loading (%)	Crystallite size (nm)	Loading (%)	Crystallite size (nm)	Loading (%)	Crystallite size (nm)
$CoRu/TiO_2@mSiO_2$	3.00	74.8	19.7	13.6	25.2	11.61	11.9
$Co/TiO_2@mSiO_2$	2.96	76.8	19.8	12.3	24.9	10.92	11.8
Co/TiO_2_Cal@500	2.86	76.5	20.6	11.39	27.6	12.15	12.9
Co/TiO_2	2.79	77.2	20.4	10.6	29.6	12.20	10.3

Figure 9S. 2: Rietveld refinement pattern of the ex situ XRD profiles and the quantitative phase analysis (QPA) data relating to the refined phases present in the catalyst.

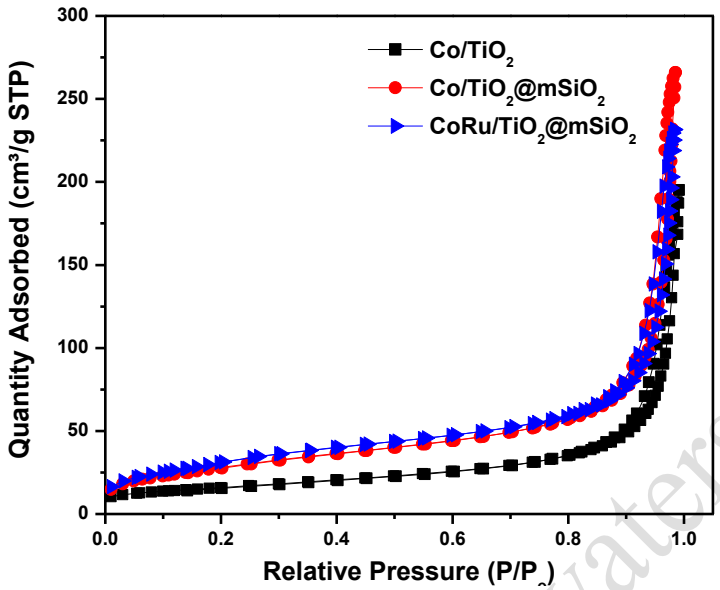

Figure 9S. 3: N_2 adsorption/desorption isotherm of the catalysts used to calculate their BET surface area.

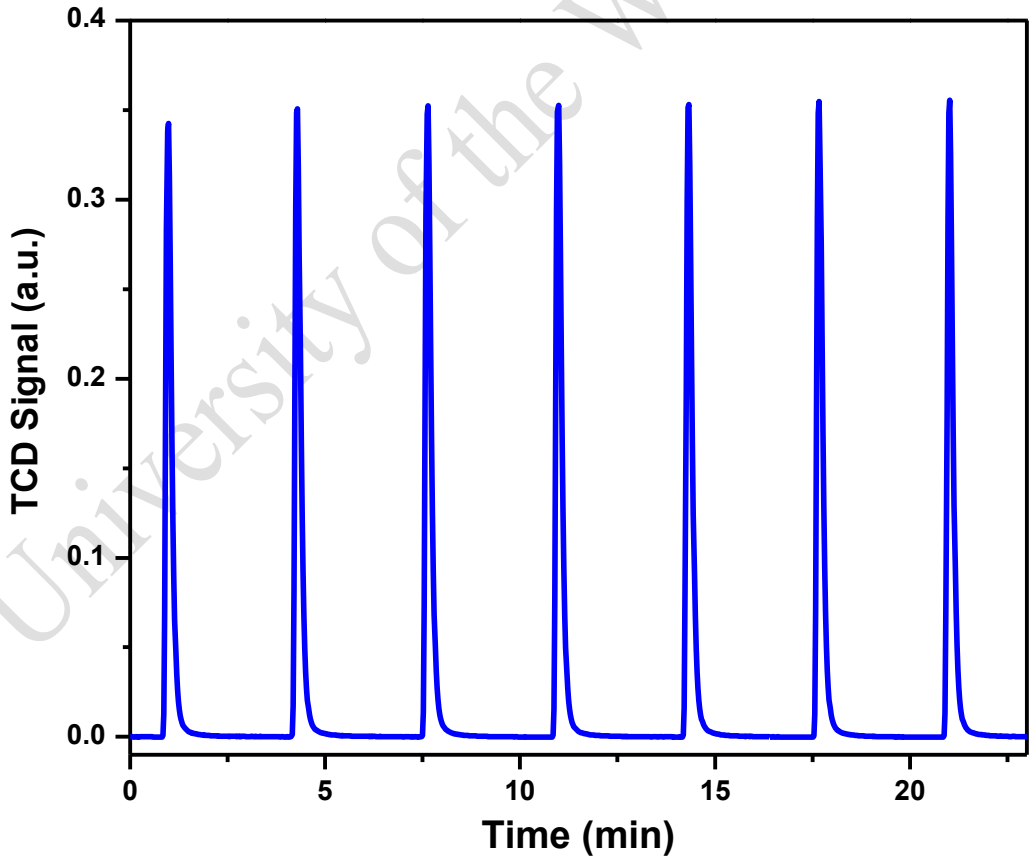

Figure 9S. 4: Typical hydrogen pulse chemisorption trace of the catalysts at 150 ℃.

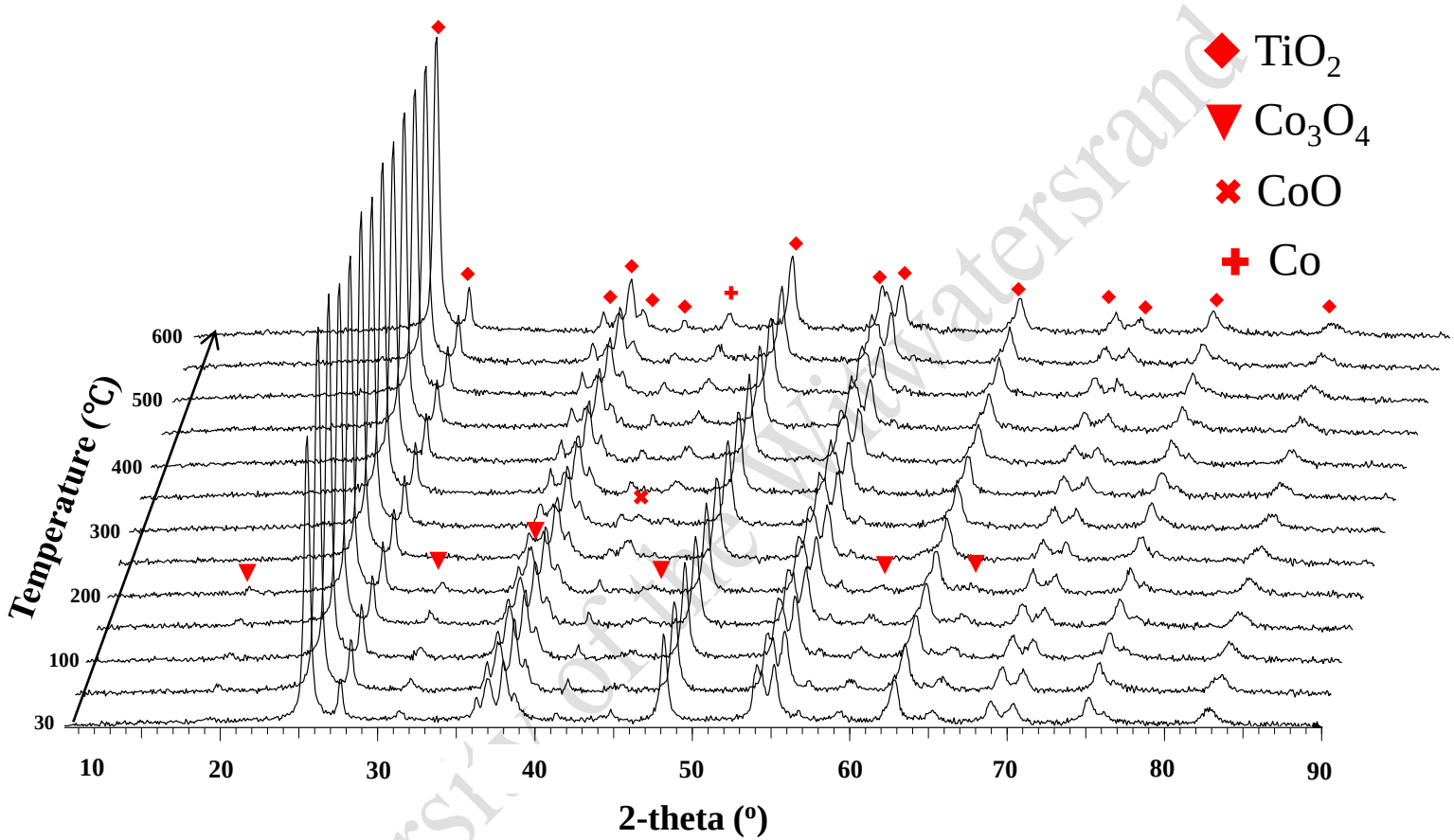

Figure 9S. 5: Typical in situ PXRD scans of the catalysts under reduction conditions, full pattern from Bragg angle 10-90^{o}, measurements taken at 50 ℃ intervals up to 600 ℃.

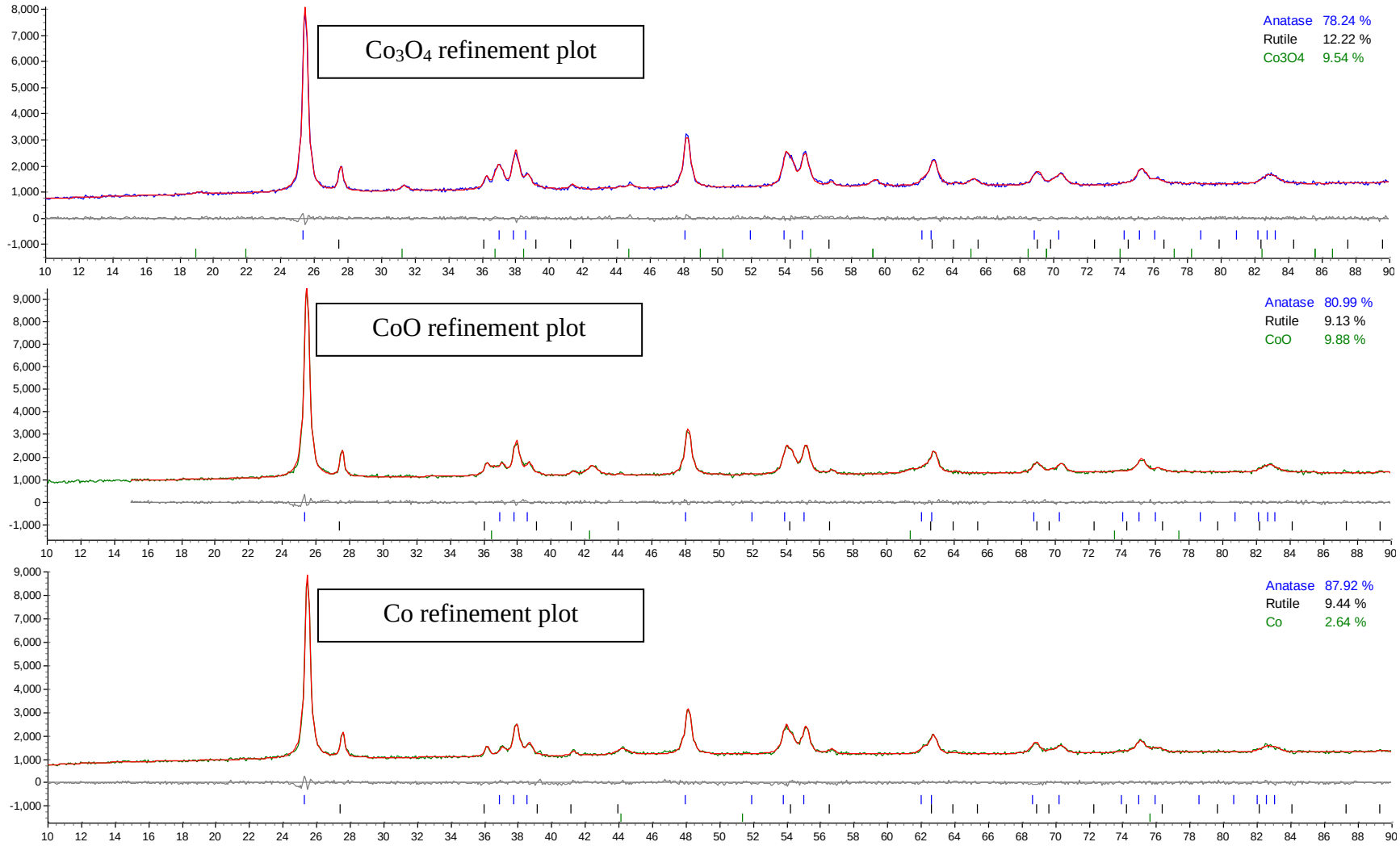

Figure 9S. 6: Typical quantitative Rietveld refinement graphs (red plot) showing the fitted PXRD model on to the experimental PXRD pattern. The model was used to calculate the crystallite sizes of the cobalt oxide and cobalt phases. For Co_3O_4 phase (a), CoO (b) and Co (c).

Table 9S. 1: Co phase and particle size changes under in situ PXRD reduction as calculated using Rietveld refinement.

Scan #	Temperature	Sample phase Co/TiO_2					
		$CoRu/TiO_2@mSiO_2$		$Co/TiO_2@mSiO_2$		Co/TiO_2	
1	30	12.06	Co_3O_4	11.08	Co_3O_4	9.98	Co_3O_4
2	50	11.42	Co_3O_4	11.45	Co_3O_4	10.19	Co_3O_4
3	100	11.84	Co_3O_4	11.01	Co_3O_4	10.39	Co_3O_4
4	150	10.24	Co_3O_4	11.64	Co_3O_4	9.94	Co_3O_4
5	200	10.23	Co_3O_4	9.82	Co_3O_4	11.06	Co_3O_4
6	250	9.47	CoO	12.2	Co_3O_4	11.14	Co_3O_4
7	300	9.0/3.1	CoO/Co	12.2/8.2	Co_3O_4/CoO	/8.08	Co_3O_4/CoO
8	350	7.35	Co	9.05	CoO	7.62	CoO
9	400	7.6	Co	9.32	CoO	7.3/8.9	CoO/Co
10	450	7.36	Co	8.9	CoO/Co	8.2	Co
11	500	7.98	Co	8.5	CoO/Co	11.5	Co
12	550	8.4	Co	9.478	Co	14.2	Co
13	600	9.1	Co	10.7	Co	16.32	Co

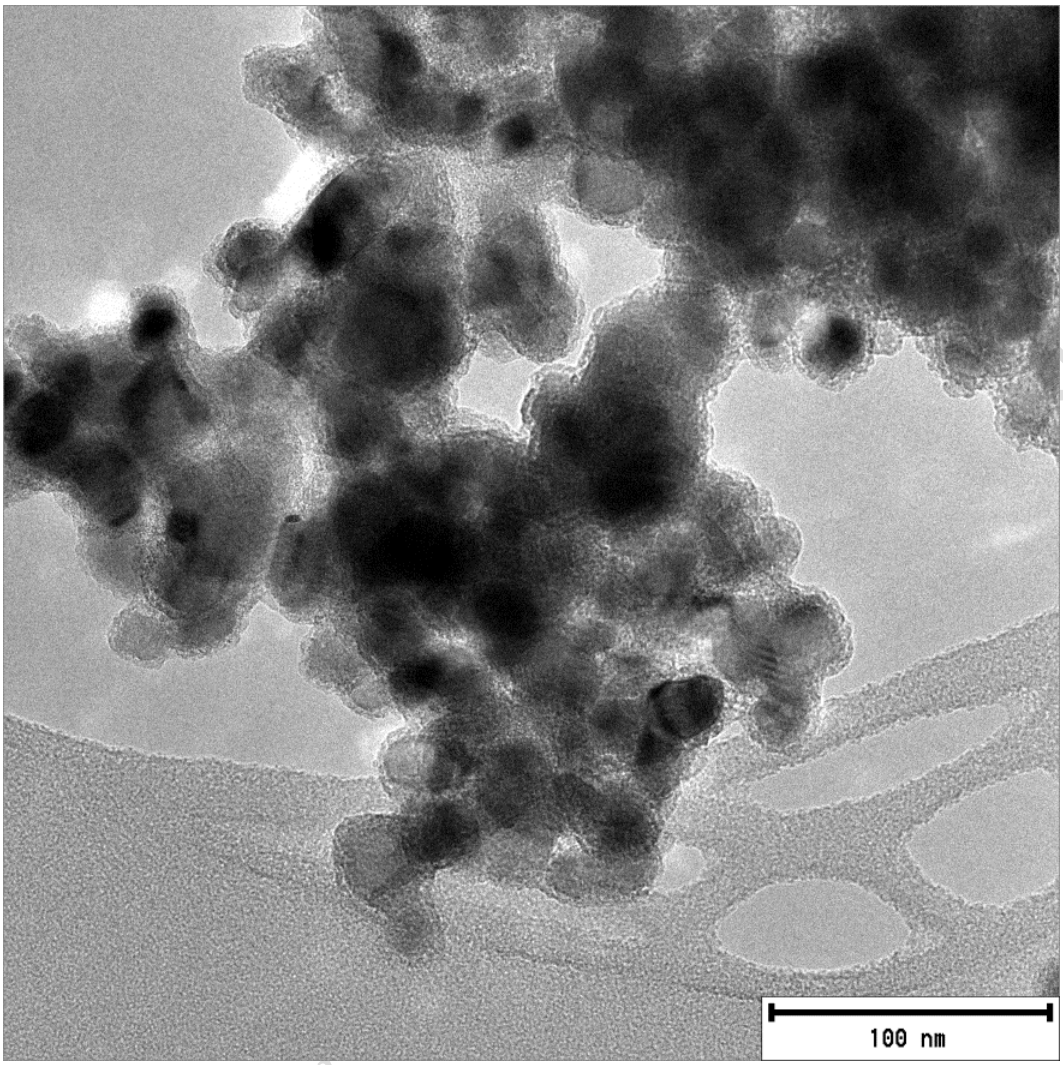

Figure 9S. 7: TEM image of the CoRu/TiO_2@mSiO_2 after Fischer-Tropsch synthesis at 250 ℃.

References

1. **The drivers of global energy demand growth to 2050** [https://www.mckinseyenergyinsights.com/insights/the-drivers-of-global-energy-demand-growth-to-2050/]
2. **Operations and Refinery** [http://www.petrosa.co.za/innovation_in_action/Pages/Operations-and-Refinery.aspx]
3. De Klerk A: **Fischer-Tropsch Refining**. University of Pretoria Pretoria South Africa; 2008.
4. Espinoza R, Steynberg A, Jager B, Vosloo A: **Low temperature Fischer–Tropsch synthesis from a Sasol perspective**. *Applied Catalysis A: General* 1999, **186**(1):13-26.
5. Steynberg A: **Introduction to fischer-tropsch technology**. *Studies in surface science and catalysis* 2004, **152**:1-63.
6. Minderhoud JK, Sie ST: **Process for the preparation of middle distillates from syngas**. In.: Google Patents; 1986.
7. Fechete I, Wang Y, Védrine JC: **The past, present and future of heterogeneous catalysis**. *Catalysis Today* 2012, **189**(1):2-27.
8. Armor JN: **A history of industrial catalysis**. *Catalysis Today* 2011, **163**(1):3-9.
9. Ertl G, Knözinger H, Weitkamp J: **Handbook of heterogeneous catalysis**. 1997.
10. Schulz H: **Short history and present trends of Fischer–Tropsch synthesis**. *Applied Catalysis A: General* 1999, **186**(1):3-12.
11. Khodakov AY, Chu W, Fongarland P: **Advances in the development of novel cobalt Fischer− Tropsch catalysts for synthesis of long-chain hydrocarbons and clean fuels**. *Chemical reviews* 2007, **107**(5):1692-1744.
12. Davis BH, Occelli ML: **Advances in Fischer-Tropsch synthesis, catalysts, and catalysis**: CRC Press; 2009.
13. Zhong L, Yu F, An Y, Zhao Y, Sun Y, Li Z, Lin T, Lin Y, Qi X, Dai Y: **Cobalt carbide nanoprisms for direct production of lower olefins from syngas**. *Nature* 2016, **538**(7623):84-87.
14. Galvis HMT, Bitter JH, Khare CB, Ruitenbeek M, Dugulan AI, de Jong KP: **Supported iron nanoparticles as catalysts for sustainable production of lower olefins**. *Science* 2012, **335**(6070):835-838.
15. Zhang Q, Kang J, Wang Y: **Development of novel catalysts for Fischer–Tropsch synthesis: tuning the product selectivity**. *ChemCatChem* 2010, **2**(9):1030-1058.

16. Shafiee S, Topal E: **When will fossil fuel reserves be diminished?** *Energy policy* 2009, **37**(1):181-189.
17. Maggio G, Cacciola G: **When will oil, natural gas, and coal peak?** *Fuel* 2012, **98**:111-123.
18. Lan W, Chen G, Zhu X, Wang X, Xu B: **Progress in techniques of biomass conversion into syngas**. *Journal of the Energy Institute* 2015, **88**(2):151-156.
19. Tsakoumis NE, Rønning M, Borg Ø, Rytter E, Holmen A: **Deactivation of cobalt based Fischer–Tropsch catalysts: a review**. *Catalysis Today* 2010, **154**(3):162-182.
20. Morales F, Weckhuysen BM: **Promotion effects in Co-based Fischer-Tropsch catalysis**. *Catalysis* 2006, **19**(1).
21. Nabaho D, Niemantsverdriet J, Claeys M, Van Steen E: **Hydrogen spillover in the Fischer-Tropsch synthesis**. 2016.
22. Psofogiannakis GM, Froudakis GE: **Fundamental studies and perceptions on the spillover mechanism for hydrogen storage**. *Chemical Communications* 2011, **47**(28):7933-7943.
23. Prins R: **Hydrogen spillover. Facts and fiction**. *Chemical reviews* 2012, **112**(5):2714-2738.
24. Karim W, Spreafico C, Kleibert A, Gobrecht J, VandeVondele J, Ekinci Y, van Bokhoven JA: **Catalyst support effects on hydrogen spillover**. *Nature* 2017, **541**(7635):68-71.
25. Liu J, Wickramaratne NP, Qiao SZ, Jaroniec M: **Molecular-based design and emerging applications of nanoporous carbon spheres**. *Nature materials* 2015, **14**(8):763-774.
26. Bell AT: **The impact of nanoscience on heterogeneous catalysis**. *Science* 2003, **299**(5613):1688-1691.
27. Van de Loosdrecht J, Botes F, Ciobica I, Ferreira A, Gibson P, Moodley D, Saib A, Visagie J, Weststrate C: **Fischer-Tropsch synthesis: catalysts and chemistry**. In: *Comprehensive Inorganic Chemistry II, Edition: 2.* Edited by Reedijk J, Poeppelmeier K: Elsevier; 2013: 525-557.
28. Henrici-Olivé G, Olive S: **The Fischer-Tropsch Synthesis: Molecular Weight Distribution of Primary Products and Reaction Mechanism**. *Angewandte Chemie International Edition in English* 1976, **15**(3):136-141.
29. Rogner H-H: **An assessment of world hydrocarbon resources**. *Annual review of energy and the environment* 1997, **22**(1):217-262.
30. Traa Y: **Is a renaissance of coal imminent?—challenges for catalysis**. *Chemical Communications* 2010, **46**(13):2175-2187.
31. Van Der Laan GP, Beenackers A: **Kinetics and selectivity of the Fischer–Tropsch synthesis: a literature review**. *Catalysis Reviews* 1999, **41**(3-4):255-318.

32. Davis BH: **Fischer–Tropsch synthesis: current mechanism and futuristic needs**. *Fuel Processing Technology* 2001, **71**(1):157-166.
33. Dry ME: **Practical and theoretical aspects of the catalytic Fischer-Tropsch process**. *Applied Catalysis A: General* 1996, **138**(2):319-344.
34. Jager B, Espinoza R: **Advances in low temperature Fischer-Tropsch synthesis**. *Catalysis Today* 1995, **23**(1):17-28.
35. Friedel R, Anderson R: **Composition of synthetic liquid fuels. i. product distribution and analysis of c5-c8 paraffin isomers from cobalt catalyst**. *Journal of the American Chemical Society* 1950, **72**(5):2307-2307.
36. Flory PJ: **Molecular Size Distribution in Linear Condensation Polymers1**. *Journal of the American Chemical Society* 1936, **58**(10):1877-1885.
37. Sie S, Senden M, Van Wechem H: **Conversion of natural gas to transportation fuels via the Shell Middle Distillate Synthesis process (SMDS)**. *Catalysis Today* 1991, **8**(3):371-394.
38. Puskas I, Hurlbut RS, Pauls RE: **Telomerization Model for Cobalt-Catalyzed Fischer-Tropsch Products**. *Journal of Catalysis* 1993, **139**(2):591-601.
39. Huff Jr GA, Satterfield CN: **Evidence for two chain growth probabilities on iron catalysts in the Fischer-Tropsch synthesis**. *Journal of Catalysis* 1984, **85**(2):370-379.
40. Gaube J, Klein H-F: **Studies on the reaction mechanism of the Fischer–Tropsch synthesis on iron and cobalt**. *Journal of Molecular Catalysis A: Chemical* 2008, **283**(1):60-68.
41. Wojciechowski B: **The kinetics of the Fischer-Tropsch synthesis**. *Catalysis Reviews Science and Engineering* 1988, **30**(4):629-702.
42. Puskas I, Hurlbut R: **Comments about the causes of deviations from the Anderson–Schulz–Flory distribution of the Fischer–Tropsch reaction products**. *Catalysis Today* 2003, **84**(1):99-109.
43. Teng B, Chang J, Wan H, Lu J, Zheng S, Liu Y, Liu Y, Guo X: **A Corrected Comprehensive Kinetic Model of Fischer–Tropsch Synthesis**. *Chinese Journal of Catalysis* 2007, **28**(8):687-695.
44. van der Laan GP, Beenackers AA: **Hydrocarbon selectivity model for the gas-solid Fischer-Tropsch synthesis on precipitated iron catalysts**. *Industrial & Engineering Chemistry Research* 1999, **38**(4):1277-1290.
45. Iglesia E, Reyes SC, Madon RJ: **Transport-enhanced α-olefin readsorption pathways in Ru-catalyzed hydrocarbon synthesis**. *Journal of Catalysis* 1991, **129**(1):238-256.
46. Madon RJ, Iglesia E: **The Importance of Olefin Readsorption and H< sub> 2</sub>/CO Reactant Ratio for Hydrocarbon Chain Growth on Ruthenium Catalysts**. *Journal of Catalysis* 1993, **139**(2):576-590.

47. Kuipers EW, Vinkenburg IH, Oosterbeek H: **Chain Length Dependence of α-Olefin Readsorption in Fischer-Tropsch Synthesis**. *Journal of Catalysis* 1995, **152**(1):137-146.
48. Zimmerman W, Bukur D, Ledakowicz S: **Kinetic model of fischer-tropsch synthesis selectivity in the slurry phase**. *Chemical Engineering Science* 1992, **47**(9–11):2707-2712.
49. Schulz H: **Trends in research and development of coal conversion to liquid fuels and basic chemicals in Europe**. *Pure and Applied Chemistry* 1979, **51**(11):2225-2241.
50. Odian G: **Principles of polymerization**: John Wiley & Sons; 2004.
51. Shetty S, van Santen RA: **CO dissociation on Ru and Co surfaces: the initial step in the Fischer–Tropsch synthesis**. *Catalysis today* 2011, **171**(1):168-173.
52. Davis BH: **Fischer–Tropsch synthesis: reaction mechanisms for iron catalysts**. *Catalysis today* 2009, **141**(1):25-33.
53. Ojeda M, Nabar R, Nilekar AU, Ishikawa A, Mavrikakis M, Iglesia E: **CO activation pathways and the mechanism of Fischer–Tropsch synthesis**. *Journal of Catalysis* 2010, **272**(2):287-297.
54. Weststrate C, Van Helden P, Van De Loosdrecht J, Niemantsverdriet J: **Elementary steps in Fischer–Tropsch synthesis: CO bond scission, CO oxidation and surface carbiding on Co (0001)**. *Surface Science* 2016, **648**:60-66.
55. Brady III RC, Pettit R: **Mechanism of the Fischer-Tropsch reaction. The chain propagation step**. *Journal of the American Chemical Society* 1981, **103**(5):1287-1289.
56. Nijs HH, Jacobs PA: **New evidence for the mechanism of the Fischer-Tropsch synthesis of hydrocarbons**. *Journal of Catalysis* 1980, **66**(2):401-411.
57. Inderwildi OR, Jenkins SJ, King DA: **Fischer− Tropsch mechanism revisited: alternative pathways for the production of higher hydrocarbons from synthesis gas**. *The Journal of Physical Chemistry C* 2008, **112**(5):1305-1307.
58. Storch HH, Anderson RA, Golumbic N: **The Fischer-Tropsch and related syntheses**, vol. 6: Wiley New York; 1951.
59. Zhuo M, Tan KF, Borgna A, Saeys M: **Density functional theory study of the CO insertion mechanism for Fischer− Tropsch synthesis over Co catalysts**. *The Journal of Physical Chemistry C* 2009, **113**(19):8357-8365.
60. Schweicher J, Bundhoo A, Kruse N: **Hydrocarbon chain lengthening in catalytic CO hydrogenation: evidence for a CO-insertion mechanism**. *Journal of the American Chemical Society* 2012, **134**(39):16135-16138.
61. Xiang Y, Chitry Vr, Liddicoat P, Felfer P, Cairney J, Ringer S, Kruse N: **Long-chain terminal alcohols through catalytic CO hydrogenation**. *Journal of the American Chemical Society* 2013, **135**(19):7114-7117.

62. Moodley DJ: **On the deactivation of cobalt-based Fischer–Tropsch synthesis catalysts**. *American Chemical Society, Division of Petrochemical Chemistry* 2008, **53**:122-125.
63. Saib A, Moodley D, Ciobîcă I, Hauman M, Sigwebela B, Weststrate C, Niemantsverdriet J, Van de Loosdrecht J: **Fundamental understanding of deactivation and regeneration of cobalt Fischer–Tropsch synthesis catalysts**. *Catalysis Today* 2010, **154**(3):271-282.
64. Eschemann TO, de Jong KP: **Deactivation Behavior of Co/TiO2 Catalysts during Fischer–Tropsch Synthesis**. *ACS Catalysis* 2015, **5**(6):3181-3188.
65. Xie J, Torres Galvis HM, Koeken AC, Kirilin A, Dugulan AI, Ruitenbeek M, de Jong KP: **Size and Promoter Effects on Stability of Carbon-Nanofiber-Supported Iron-Based Fischer–Tropsch Catalysts**. *ACS Catalysis* 2016, **6**(6):4017-4024.
66. Bezemer GL, Remans TJ, van Bavel AP, Dugulan AI: **Direct evidence of water-assisted sintering of cobalt on carbon nanofiber catalysts during simulated Fischer− Tropsch conditions revealed with in situ Mössbauer spectroscopy**. *Journal of the American Chemical Society* 2010, **132**(25):8540-8541.
67. Claeys M, Dry M, van Steen E, van Berge P, Booyens S, Crous R, van Helden P, Labuschagne J, Moodley D, Saib A: **Impact of process conditions on the sintering behavior of an alumina-supported cobalt fischer–tropsch catalyst studied with an in situ magnetometer**. *ACS Catalysis* 2015, **5**(2):841-852.
68. Borg Ø, Hammer N, Enger BC, Myrstad R, Lindvåg OA, Eri S, Skagseth TH, Rytter E: **Effect of biomass-derived synthesis gas impurity elements on cobalt Fischer–Tropsch catalyst performance including in situ sulphur and nitrogen addition**. *Journal of Catalysis* 2011, **279**(1):163-173.
69. Wilson J, de Groot C: **Atomic-scale restructuring in high-pressure catalysis**. *The Journal of Physical Chemistry* 1995, **99**(20):7860-7866.
70. Banerjee A, Navarro V, Frenken JW, van Bavel AP, Kuipers HP, Saeys M: **Shape and Size of Cobalt Nanoislands Formed Spontaneously on Cobalt Terraces during Fischer–Tropsch Synthesis**. *The journal of physical chemistry letters* 2016, **7**(11):1996-2001.
71. Karaca H, Hong J, Fongarland P, Roussel P, Griboval-Constant A, Lacroix M, Hortmann K, Safonova OV, Khodakov AY: **In situ XRD investigation of the evolution of alumina-supported cobalt catalysts under realistic conditions of Fischer-Tropsch synthesis**. *Chemical Communications* 2010, **46**(5):788-790.
72. Moodley D, Van de Loosdrecht J, Saib A, Overett M, Datye A, Niemantsverdriet J: **Carbon deposition as a deactivation mechanism of cobalt-based Fischer–Tropsch synthesis catalysts under realistic conditions**. *Applied Catalysis A: General* 2009, **354**(1):102-110.

73. Sudsakorn K, Goodwin JG, Jothimurugesan K, Adeyiga AA: **Preparation of Attrition-Resistant Spray-Dried Fe Fischer− Tropsch Catalysts Using Precipitated SiO2**. *Industrial & engineering chemistry research* 2001, **40**(22):4778-4784.
74. O'Brien RJ, Xu L, Bao S, Raje A, Davis BH: **Activity, selectivity and attrition characteristics of supported iron Fischer–Tropsch catalysts**. *Applied Catalysis A: General* 2000, **196**(2):173-178.
75. Herranz T, Deng X, Cabot A, Guo J, Salmeron M: **Influence of the cobalt particle size in the CO hydrogenation reaction studied by in situ X-ray absorption spectroscopy**. *The Journal of Physical Chemistry B* 2009, **113**(31):10721-10727.
76. van Steen E, Claeys M, Dry ME, van de Loosdrecht J, Viljoen EL, Visagie JL: **Stability of nanocrystals: thermodynamic analysis of oxidation and re-reduction of cobalt in water/hydrogen mixtures**. *The Journal of Physical Chemistry B* 2005, **109**(8):3575-3577.
77. Fischer N, Clapham B, Feltes T, van Steen E, Claeys M: **Size-Dependent Phase Transformation of Catalytically Active Nanoparticles Captured In Situ**. *Angewandte Chemie International Edition* 2014, **53**(5):1342-1345.
78. Wolf M, Kotzé H, Fischer N, Claeys M: **Size dependent stability of cobalt nanoparticles on silica under high conversion Fischer-Tropsch environment**. *Faraday Discussions* 2016.
79. Bezemer GL, Bitter JH, Kuipers HP, Oosterbeek H, Holewijn JE, Xu X, Kapteijn F, van Dillen AJ, de Jong KP: **Cobalt particle size effects in the Fischer− Tropsch reaction studied with carbon nanofiber supported catalysts**. *Journal of the American Chemical Society* 2006, **128**(12):3956-3964.
80. van Helden P, Ciobîcă IM, Coetzer RL: **The size-dependent site composition of FCC cobalt nanocrystals**. *Catalysis today* 2016, **261**:48-59.
81. Van Hardeveld R, Hartog F: **The statistics of surface atoms and surface sites on metal crystals**. *Surface Science* 1969, **15**(2):189-230.
82. Fischer N, Van Steen E, Claeys M: **Structure sensitivity of the Fischer–Tropsch activity and selectivity on alumina supported cobalt catalysts**. *Journal of catalysis* 2013, **299**:67-80.
83. Wang Z-j, Skiles S, Yang F, Yan Z, Goodman DW: **Particle size effects in Fischer–Tropsch synthesis by cobalt**. *Catalysis today* 2012, **181**(1):75-81.
84. Tuxen A, Carenco S, Chintapalli M, Chuang C-H, Escudero C, Pach E, Jiang P, Borondics F, Beberwyck B, Alivisatos AP: **Size-dependent dissociation of carbon monoxide on cobalt nanoparticles**. *Journal of the American Chemical Society* 2013, **135**(6):2273-2278.
85. Den Breejen J, Radstake P, Bezemer G, Bitter J, Frøseth V, Holmen A, Jong Kd: **On the origin of the cobalt particle size effects in Fischer− Tropsch catalysis**. *Journal of the American Chemical Society* 2009, **131**(20):7197-7203.

86. Xiong H, Motchelaho MA, Moyo M, Jewell LL, Coville NJ: **Correlating the preparation and performance of cobalt catalysts supported on carbon nanotubes and carbon spheres in the Fischer–Tropsch synthesis**. *Journal of Catalysis* 2011, **278**(1):26-40.
87. Welker CA: **Ruthenium based Fischer–Tropsch synthesis on crystallites and clusters of different sizes**. *Department of Chemical Engineering, PhD, University of Cape Town, Cape Town* 2007.
88. Quek X-Y, Pestman R, van Santen RA, Hensen EJ: **Structure sensitivity in the ruthenium nanoparticle catalyzed aqueous-phase Fischer–Tropsch reaction**. *Catalysis Science & Technology* 2014, **4**(10):3510-3523.
89. Carballo JMG, Yang J, Holmen A, Garcia-Rodriguez S, Rojas S, Ojeda M, Fierro JLG: **Catalytic effects of ruthenium particle size on the Fischer–Tropsch Synthesis**. *Journal of Catalysis* 2011, **284**(1):102-108.
90. Park J-Y, Lee Y-J, Khanna PK, Jun K-W, Bae JW, Kim YH: **Alumina-supported iron oxide nanoparticles as Fischer–Tropsch catalysts: Effect of particle size of iron oxide**. *Journal of Molecular Catalysis A: Chemical* 2010, **323**(1):84-90.
91. González-Carballo JM, Pérez-Alonso FJ, Ojeda M, García-García FJ, Fierro JLG, Rojas S: **Evidences of Two-Regimes in the Measurement of Ru Particle Size Effect for CO Dissociation during Fischer–Tropsch Synthesis**. *ChemCatChem* 2014, **6**(7):2084-2094.
92. Jacobs G, Das TK, Zhang Y, Li J, Racoillet G, Davis BH: **Fischer–Tropsch synthesis: support, loading, and promoter effects on the reducibility of cobalt catalysts**. *Applied Catalysis A: General* 2002, **233**(1):263-281.
93. Storsæter S, Tøtdal B, Walmsley JC, Tanem BS, Holmen A: **Characterization of alumina-, silica-, and titania-supported cobalt Fischer–Tropsch catalysts**. *Journal of Catalysis* 2005, **236**(1):139-152.
94. Khodakov AY, Griboval-Constant A, Bechara R, Zholobenko VL: **Pore size effects in Fischer Tropsch synthesis over cobalt-supported mesoporous silicas**. *Journal of Catalysis* 2002, **206**(2):230-241.
95. Koh T, Koo HM, Yu T, Lim B, Bae JW: **Roles of Ruthenium–Support Interactions of Size-Controlled Ruthenium Nanoparticles for the Product Distribution of Fischer–Tropsch Synthesis**. *ACS Catalysis* 2014, **4**(4):1054-1060.
96. Jacobs G, Chaney JA, Patterson PM, Das TK, Davis BH: **Fischer–Tropsch synthesis: study of the promotion of Re on the reduction property of Co/Al 2 O 3 catalysts by in situ EXAFS/XANES of Co K and Re L III edges and XPS**. *Applied Catalysis A: General* 2004, **264**(2):203-212.
97. Li J, Coville NJ: **The effect of boron on the catalyst reducibility and activity of Co/TiO 2 Fischer–Tropsch catalysts**. *Applied Catalysis A: General* 1999, **181**(1):201-208.

98. de Smit E, Swart I, Creemer JF, Hoveling GH, Gilles MK, Tyliszczak T, Kooyman PJ, Zandbergen HW, Morin C, Weckhuysen BM: **Nanoscale chemical imaging of a working catalyst by scanning transmission X-ray microscopy**. *Nature* 2008, **456**(7219):222-225.
99. Diehl F, Khodakov AY: **Promotion of cobalt Fischer-Tropsch catalysts with noble metals: a review**. *Oil & Gas Science and Technology-Revue de l'IFP* 2009, **64**(1):11-24.
100. Xiong H, Jewell LL, Coville NJ: **Shaped Carbons As Supports for the Catalytic Conversion of Syngas to Clean Fuels**. *ACS Catalysis* 2015, **5**(4):2640-2658.
101. Fu T, Li Z: **Review of recent development in Co-based catalysts supported on carbon materials for Fischer–Tropsch synthesis**. *Chemical Engineering Science* 2015, **135**:3-20.
102. Lam E, Luong JH: **Carbon materials as catalyst supports and catalysts in the transformation of biomass to fuels and chemicals**. *ACS Catalysis* 2014, **4**(10):3393-3410.
103. Zhu J, Holmen A, Chen D: **Carbon nanomaterials in catalysis: proton affinity, chemical and electronic properties, and their catalytic consequences**. *ChemCatChem* 2013, **5**(2):378-401.
104. Tavasoli A, Sadagiani K, Khorashe F, Seifkordi A, Rohani A, Nakhaeipour A: **Cobalt supported on carbon nanotubes—A promising novel Fischer–Tropsch synthesis catalyst**. *Fuel Processing Technology* 2008, **89**(5):491-498.
105. Schulte HJ, Graf B, Xia W, Muhler M: **Nitrogen-and Oxygen-Functionalized Multiwalled Carbon Nanotubes Used as Support in Iron-Catalyzed, High-Temperature Fischer–Tropsch Synthesis**. *ChemCatChem* 2012, **4**(3):350-355.
106. Motchelaho MA, Xiong H, Moyo M, Jewell LL, Coville NJ: **Effect of acid treatment on the surface of multiwalled carbon nanotubes prepared from Fe–Co supported on CaCO 3: correlation with Fischer–Tropsch catalyst activity**. *Journal of Molecular Catalysis A: Chemical* 2011, **335**(1):189-198.
107. Chinthaginjala J, Seshan K, Lefferts L: **Preparation and application of carbon-nanofiber based microstructured materials as catalyst supports**. *Industrial & engineering chemistry research* 2007, **46**(12):3968-3978.
108. Deshmukh AA, Mhlanga SD, Coville NJ: **Carbon spheres**. *Materials Science and Engineering: R: Reports* 2010, **70**(1):1-28.
109. Coville NJ, Mhlanga SD, Nxumalo EN, Shaikjee A: **A review of shaped carbon nanomaterials**. *South African Journal of Science* 2011, **107**(3-4):01-15.
110. Pan X, Bao X: **The effects of confinement inside carbon nanotubes on catalysis**. *Accounts of chemical research* 2011, **44**(8):553-562.
111. Chen W, Fan Z, Pan X, Bao X: **Effect of confinement in carbon nanotubes on the activity of Fischer− Tropsch iron catalyst**. *Journal of the American Chemical Society* 2008, **130**(29):9414-9419.

112. Xiong H, Moyo M, Motchelaho MA, Tetana ZN, Dube SM, Jewell LL, Coville NJ: **Fischer–Tropsch synthesis: Iron catalysts supported on N-doped carbon spheres prepared by chemical vapor deposition and hydrothermal approaches**. *Journal of Catalysis* 2014, **311**:80-87.
113. Yang Y, Jia L, Hou B, Li D, Wang J, Sun Y: **The Effect of Nitrogen on the Autoreduction of Cobalt Nanoparticles Supported on Nitrogen-Doped Ordered Mesoporous Carbon for the Fischer–Tropsch Synthesis**. *ChemCatChem* 2014, **6**(1):319-327.
114. Dlamini MW: **Spherical carbons as model supports for Fe, Co and Fe-Co Fischer-Tropsch catalysts**. 2016.
115. Xiong H, Moyo M, Motchelaho MA, Jewell LL, Coville NJ: **Fischer–Tropsch synthesis over model iron catalysts supported on carbon spheres: The effect of iron precursor, support pretreatment, catalyst preparation method and promoters**. *Applied Catalysis A: General* 2010, **388**(1):168-178.
116. Moyo M, Motchelaho MA, Xiong H, Jewell LL, Coville NJ: **Promotion of Co/carbon sphere Fischer–Tropsch catalysts by residual K and Mn from carbon oxidation by KMnO 4**. *Applied Catalysis A: General* 2012, **413**:223-229.
117. Xie W, Zhang Y, Liew K, Li J: **Effect of catalyst confinement and pore size on Fischer-Tropsch synthesis over cobalt supported on carbon nanotubes**. *Science China Chemistry* 2012, **55**(9):1811-1818.
118. Trépanier M, Tavasoli A, Dalai AK, Abatzoglou N: **Co, Ru and K loadings effects on the activity and selectivity of carbon nanotubes supported cobalt catalyst in Fischer–Tropsch synthesis**. *Applied Catalysis A: General* 2009, **353**(2):193-202.
119. Hilmen AM, Schanke D, Hanssen KF, Holmen A: **Study of the effect of water on alumina supported cobalt Fischer–Tropsch catalysts**. *Applied Catalysis A: General* 1999, **186**(1–2):169-188.
120. Jacobs G, Das TK, Patterson PM, Li J, Sanchez L, Davis BH: **Fischer–Tropsch synthesis XAFS: XAFS studies of the effect of water on a Pt-promoted Co/Al2O3 catalyst**. *Applied Catalysis A: General* 2003, **247**(2):335-343.
121. Park J-Y, Lee Y-J, Karandikar PR, Jun K-W, Bae JW, Ha K-S: **Ru promoted cobalt catalyst on γ-Al< sub> 2</sub> O< sub> 3</sub> support: Influence of pre-synthesized nanoparticles on Fischer–Tropsch reaction**. *Journal of Molecular Catalysis A: Chemical* 2011, **344**(1):153-160.
122. Rodrigues JJ, Pecchi G, Fernandes FAN, Rodrigues MGF: **Ruthenium promotion of Co/SBA-15 catalysts for Fischer-Tropsch synthesis in slurry-phase reactors**. *Journal of Natural Gas Chemistry* 2012, **21**(6):722-728.
123. Morales F, Weckhuysen BM: **Promotion effects in Co-based Fischer-Tropsch catalysis**. *Catalysis* 2006, **19**:1-40.
124. Panpranot J, Goodwin Jr JG, Sayari A: **Synthesis and characteristics of MCM-41 supported CoRu catalysts**. *Catalysis Today* 2002, **77**(3):269-284.

125. Jacobs G, Patterson PM, Zhang Y, Das T, Li J, Davis BH: **Fischer–Tropsch synthesis: deactivation of noble metal-promoted Co/Al< sub> 2</sub> O< sub> 3</sub> catalysts**. *Applied Catalysis A: General* 2002, **233**(1):215-226.
126. Kangvansura P, Poo-arporn Y, Schulz H, Worayingyong A: **The effect of promoters on reduction of Ru/ZrO2/Co/SiO2 catalyst for Fischer-Tropsch synthesis as studied by in situ XANES**. *synthesis*, **4**(5):6.
127. Rozanov VVe, Krylov OV: **Hydrogen spillover in heterogeneous catalysis**. *Russian chemical reviews* 1997, **66**(2):107-119.
128. Hong J, Marceau E, Khodakov AY, Gaberová L, Griboval-Constant A, Girardon J-S, Fontaine CL, Briois V: **Speciation of ruthenium as a reduction promoter of silica-supported Co catalysts: a time-resolved in situ XAS investigation**. *ACS Catalysis* 2015, **5**(2):1273-1282.
129. Khoobiar S: **Particle to particle migration of hydrogen atoms on platinum—alumina catalysts from particle to neighboring particles**. *The Journal of Physical Chemistry* 1964, **68**(2):411-412.
130. Conner Jr WC, Falconer JL: **Spillover in heterogeneous catalysis**. *Chemical reviews* 1995, **95**(3):759-788.
131. Nabaho D, Niemantsverdriet JH, Claeys M, van Steen E: **Hydrogen spillover in the Fischer–Tropsch synthesis: An analysis of platinum as a promoter for cobalt–alumina catalysts**. *Catalysis Today* 2016, **261**:17-27.
132. Ahmed F, Alam MK, Suzuki A, Koyama M, Tsuboi H, Hatakeyama N, Endou A, Takaba H, Del Carpio CA, Kubo M: **Dynamics of hydrogen spillover on Pt/γ-Al2O3 catalyst surface: a quantum chemical molecular dynamics study**. *The Journal of Physical Chemistry C* 2009, **113**(35):15676-15683.
133. Agmon N: **The grotthuss mechanism**. *Chemical Physics Letters* 1995, **244**(5):456-462.
134. WynáRoberts M, DavidáJackson S: **Applications of EPR to a study of the hydrogenation of ethene and benzene over a supported Pd catalyst: detection of free radicals on a catalyst surface**. *Journal of the Chemical Society, Faraday Transactions* 1994, **90**(21):3341-3346.
135. Im J, Shin H, Jang H, Kim H, Choi M: **Maximizing the catalytic function of hydrogen spillover in platinum-encapsulated aluminosilicates with controlled nanostructures**. *Nature communications* 2014, **5**.
136. Beaumont SK, Alayoglu S, Specht C, Kruse N, Somorjai GA: **A nanoscale demonstration of hydrogen atom spillover and surface diffusion across silica using the kinetics of CO2 methanation catalyzed on spatially separate Pt and Co nanoparticles**. *Nano letters* 2014, **14**(8):4792-4796.
137. Beaumont SK, Alayoglu S, Specht C, Michalak WD, Pushkarev VV, Guo J, Kruse N, Somorjai GA: **Combining in situ NEXAFS spectroscopy and CO2 methanation kinetics to study Pt and Co nanoparticle catalysts reveals key**

insights into the role of platinum in promoted cobalt catalysis. *Journal of the American Chemical Society* 2014, **136**(28):9898-9901.

138. Marcinkowski MD, Jewell AD, Stamatakis M, Boucher MB, Lewis EA, Murphy CJ, Kyriakou G, Sykes ECH: **Controlling a spillover pathway with the molecular cork effect**. *Nature materials* 2013, **12**(6):523-528.
139. Nabaho D, Niemantsverdriet JH, Claeys M, van Steen E: **Hydrogen spillover in the Fischer–Tropsch synthesis: An analysis of gold as a promoter for cobalt–alumina catalysts**. *Catalysis Today* 2016, **275**:27-34.
140. Hansma P, Elings V, Marti O, Bracker C: **Scanning tunneling microscopy and atomic force microscopy: application to biology and technology**. *Science* 1988, **242**(4876):209-216.
141. Horcas I, Fernandez R, Gomez-Rodriguez J, Colchero J, Gómez-Herrero J, Baro A: **WSXM: a software for scanning probe microscopy and a tool for nanotechnology**. *Review of Scientific Instruments* 2007, **78**(1):013705.
142. Ramuz MP, Vosgueritchian M, Wei P, Wang C, Gao Y, Wu Y, Chen Y, Bao Z: **Evaluation of solution-processable carbon-based electrodes for all-carbon solar cells**. *ACS nano* 2012, **6**(11):10384-10395.
143. Novoselov KS, Fal V, Colombo L, Gellert P, Schwab M, Kim K: **A roadmap for graphene**. *Nature* 2012, **490**(7419):192-200.
144. Thostenson ET, Ren Z, Chou T-W: **Advances in the science and technology of carbon nanotubes and their composites: a review**. *Composites science and technology* 2001, **61**(13):1899-1912.
145. Hammel E, Tang X, Trampert M, Schmitt T, Mauthner K, Eder A, Pötschke P: **Carbon nanofibers for composite applications**. *Carbon* 2004, **42**(5):1153-1158.
146. Li Y, Zhao Y, Hu W, Ahmad I, Zhu Y, Peng X, Luan Z: **Carbon nanotubes-the promising adsorbent in wastewater treatment**. In: *Journal of Physics: Conference Series: 2007*: IOP Publishing; 2007: 698.
147. Jun H, Careem M, Arof A: **Quantum dot-sensitized solar cells—perspective and recent developments: A review of Cd chalcogenide quantum dots as sensitizers**. *Renewable and Sustainable Energy Reviews* 2013, **22**:148-167.
148. Fang X, Zhao X, Fang W, Chen C, Zheng N: **Self-templating synthesis of hollow mesoporous silica and their applications in catalysis and drug delivery**. *Nanoscale* 2013, **5**(6):2205-2218.
149. Pérez-Lorenzo M, Vaz B, Salgueiriño V, Correa-Duarte MA: **Hollow-Shelled Nanoreactors Endowed with High Catalytic Activity**. *Chemistry-A European Journal* 2013, **19**(37):12196-12211.
150. Lou XWD, Archer LA, Yang Z: **Hollow Micro-/Nanostructures: Synthesis and Applications**. *Advanced Materials* 2008, **20**(21):3987-4019.
151. Kim KT, Meeuwissen SA, Nolte RJ, van Hest JC: **Smart nanocontainers and nanoreactors**. *Nanoscale* 2010, **2**(6):844-858.

152. Liu Y, Goebl J, Yin Y: **Templated synthesis of nanostructured materials**. *Chemical Society Reviews* 2013, **42**(7):2610-2653.
153. Chen Y, Chen H-R, Shi J-L: **Construction of Homogenous/Heterogeneous Hollow Mesoporous Silica Nanostructures by Silica-Etching Chemistry: Principles, Synthesis, and Applications**. *Accounts of chemical research* 2013.
154. Wu S-H, Mou C-Y, Lin H-P: **Synthesis of mesoporous silica nanoparticles**. *Chemical Society Reviews* 2013, **42**(9):3862-3875.
155. Caruso F, Caruso RA, Möhwald H: **Nanoengineering of inorganic and hybrid hollow spheres by colloidal templating**. *Science* 1998, **282**(5391):1111-1114.
156. Sanlés-Sobrido M, Pérez-Lorenzo M, Rodríguez-González B, Salgueiriño V, Correa-Duarte MA: **Highly active nanoreactors: nanomaterial encapsulation based on confined catalysis**. *Angewandte Chemie International Edition* 2012, **51**(16):3877-3882.
157. Gao T, Jelle BP, Sandberg LIC, Gustavsen A: **Monodisperse hollow silica nanospheres for nano insulation materials: Synthesis, characterization, and life cycle assessment**. *ACS applied materials & interfaces* 2013, **5**(3):761-767.
158. Chen M, Wu L, Zhou S, You B: **A method for the fabrication of monodisperse hollow silica spheres**. *Advanced Materials* 2006, **18**(6):801-806.
159. Zhu Y, Kockrick E, Ikoma T, Hanagata N, Kaskel S: **An efficient route to rattle-type Fe3O4@ SiO2 hollow mesoporous spheres using colloidal carbon spheres templates**. *Chemistry of materials* 2009, **21**(12):2547-2553.
160. Chen Z, Cui Z-M, Li P, Cao C-Y, Hong Y-L, Wu Z-y, Song W-G: **Diffusion induced reactant shape selectivity inside mesoporous pores of Pd@ meso-SiO2 nanoreactor in Suzuki coupling reactions**. *The Journal of Physical Chemistry C* 2012, **116**(28):14986-14991.
161. Chen Y, Chen H, Guo L, He Q, Chen F, Zhou J, Feng J, Shi J: **Hollow/rattle-type mesoporous nanostructures by a structural difference-based selective etching strategy**. *ACS nano* 2009, **4**(1):529-539.
162. Zhang Q, Ge J, Goebl J, Hu Y, Lu Z, Yin Y: **Rattle-type silica colloidal particles prepared by a surface-protected etching process**. *Nano Research* 2009, **2**(7):583-591.
163. Shi S, Wang M, Chen C, Lu F, Zheng X, Gao J, Xu J: **Preparation of hydrophobic hollow silica nanospheres with porous shells and their application in pollutant removal**. *RSC Advances* 2013, **3**(4):1158-1164.
164. Joo JB, Zhang Q, Lee I, Dahl M, Zaera F, Yin Y: **Mesoporous Anatase Titania Hollow Nanostructures though Silica-Protected Calcination**. *Advanced Functional Materials* 2012, **22**(1):166-174.
165. Li H, Bian Z, Zhu J, Zhang D, Li G, Huo Y, Li H, Lu Y: **Mesoporous titania spheres with tunable chamber stucture and enhanced photocatalytic activity**. *Journal of the American Chemical Society* 2007, **129**(27):8406-8407.

166. Zeng Y, Wang X, Wang H, Dong Y, Ma Y, Yao J: **Multi-shelled titania hollow spheres fabricated by a hard template strategy: enhanced photocatalytic activity**. *Chemical Communications* 2010, **46**(24):4312-4314.
167. Sakai N, Ebina Y, Takada K, Sasaki T: **Electronic band structure of titania semiconductor nanosheets revealed by electrochemical and photoelectrochemical studies**. *Journal of the American Chemical Society* 2004, **126**(18):5851-5858.
168. Song X, Gao L: **Synthesis, characterization, and optical properties of well-defined N-doped, hollow silica/titania hybrid microspheres**. *Langmuir* 2007, **23**(23):11850-11856.
169. Wang Y, Su X, Lu S: **Shape-controlled synthesis of TiO2 hollow structures and their application in lithium batteries**. *Journal of Materials Chemistry* 2012, **22**(5):1969-1976.
170. Baughman RH, Zakhidov AA, de Heer WA: **Carbon nanotubes--the route toward applications**. *Science* 2002, **297**(5582):787-792.
171. Zhou O, Shimoda H, Gao B, Oh S, Fleming L, Yue G: **Materials science of carbon nanotubes: fabrication, integration, and properties of macroscopic structures of carbon nanotubes**. *Accounts of chemical research* 2002, **35**(12):1045-1053.
172. Liang C, Li Z, Dai S: **Mesoporous carbon materials: synthesis and modification**. *Angewandte Chemie International Edition* 2008, **47**(20):3696-3717.
173. Lu AH, Hao GP, Sun Q, Zhang XQ, Li WC: **Chemical synthesis of carbon materials with intriguing nanostructure and morphology**. *Macromolecular Chemistry and Physics* 2012, **213**(10-11):1107-1131.
174. Chen X, Kierzek K, Wenelska K, Cendrowski K, Gong J, Wen X, Tang T, Chu PK, Mijowska E: **Electrochemical Characteristics of Discrete, Uniform, and Monodispersed Hollow Mesoporous Carbon Spheres in Double-Layered Supercapacitors**. *Chemistry, an Asian journal* 2013, **8**(11):2627.
175. Liu R, Mahurin SM, Li C, Unocic RR, Idrobo JC, Gao H, Pennycook SJ, Dai S: **Dopamine as a Carbon Source: The Controlled Synthesis of Hollow Carbon Spheres and Yolk-Structured Carbon Nanocomposites**. *Angewandte Chemie International Edition* 2011, **50**(30):6799-6802.
176. Su F, Zhao X, Wang Y, Wang L, Lee JY: **Hollow carbon spheres with a controllable shell structure**. *Journal of materials chemistry* 2006, **16**(45):4413-4419.
177. Yan J, Meng H, Xie F, Yuan X, Yu W, Lin W, Ouyang W, Yuan D: **Metal free nitrogen doped hollow mesoporous graphene-analogous spheres as effective electrocatalyst for oxygen reduction reaction**. *Journal of Power Sources* 2014, **245**:772-778.

178. White RJ, Tauer K, Antonietti M, Titirici M-M: **Functional hollow carbon nanospheres by latex templating**. *Journal of the American Chemical Society* 2010, **132**(49):17360-17363.
179. Feng S, Li W, Shi Q, Li Y, Chen J, Ling Y, Asiri AM, Zhao D: **Synthesis of nitrogen-doped hollow carbon nanospheres for CO2 capture**. *Chemical Communications* 2014, **50**(3):329-331.
180. Qiao Z-A, Guo B, Binder AJ, Chen J, Veith GM, Dai S: **Controlled synthesis of mesoporous carbon nanostructures via a "silica-assisted" strategy**. *Nano letters* 2012, **13**(1):207-212.
181. Sun G, Li K, Wang J, He H, Wang J, Li Y, Liu Y, Gu J: **A novel approach for fabrication of hollow carbon spheres with large size and high specific surface area**. *Microporous and Mesoporous Materials* 2011, **139**(1):207-210.
182. Liu J, Qiao SZ, Chen JS, Lou XWD, Xing X, Lu GQM: **Yolk/shell nanoparticles: new platforms for nanoreactors, drug delivery and lithium-ion batteries**. *Chemical Communications* 2011, **47**(47):12578-12591.
183. Ikeda S, Ishino S, Harada T, Okamoto N, Sakata T, Mori H, Kuwabata S, Torimoto T, Matsumura M: **Ligand-Free Platinum Nanoparticles Encapsulated in a Hollow Porous Carbon Shell as a Highly Active Heterogeneous Hydrogenation Catalyst**. *Angewandte Chemie* 2006, **118**(42):7221-7224.
184. Harada T, Ikeda S, Ng YH, Sakata T, Mori H, Torimoto T, Matsumura M: **Rhodium nanoparticle encapsulated in a porous carbon shell as an active heterogeneous catalyst for aromatic hydrogenation**. *Advanced Functional Materials* 2008, **18**(15):2190-2196.
185. Liu R, Qu F, Guo Y, Yao N, Priestley RD: **Au@ carbon yolk–shell nanostructures via one-step core–shell–shell template**. *Chemical Communications* 2014, **50**(4):478-480.
186. Galeano C, Güttel R, Paul M, Arnal P, Lu AH, Schüth F: **Yolk-Shell Gold Nanoparticles as Model Materials for Support-Effect Studies in Heterogeneous Catalysis: Au,@ C and Au,@ ZrO2 for CO Oxidation as an Example**. *Chemistry-A European Journal* 2011, **17**(30):8434-8439.
187. Wang G-H, Hilgert J, Richter FH, Wang F, Bongard H-J, Spliethoff B, Weidenthaler C, Schüth F: **Platinum–cobalt bimetallic nanoparticles in hollow carbon nanospheres for hydrogenolysis of 5-hydroxymethylfurfural**. *Nature materials* 2014, **13**(3):293-300.
188. Pérez-Lorenzo M, Vaz B, Salgueiriño V, Correa-Duarte MA: **Hollow-Shelled Nanoreactors Endowed with High Catalytic Activity**. *Chemistry–A European Journal* 2013, **19**(37):12196-12211.
189. Cotanda P, Petzetakis N, O'Reilly RK: **Catalytic polymeric nanoreactors: more than a solid supported catalyst**. *MRS Communications* 2012, **2**(04):119-126.

190. Khlobystov AN: **Carbon nanotubes: from nano test tube to nano-reactor**. *ACS nano* 2011, **5**(12):9306-9312.
191. Vázquez-Vázquez C, Vaz Bn, Giannini V, Pérez-Lorenzo Ms, Alvarez-Puebla RA, Correa-Duarte MA: **Nanoreactors for simultaneous remote thermal activation and optical monitoring of chemical reactions**. *Journal of the American Chemical Society* 2013, **135**(37):13616-13619.
192. Chen X, Kierzek K, Wenelska K, Cendrowski K, Gong J, Wen X, Tang T, Chu PK, Mijowska E: **Electrochemical Characteristics of Discrete, Uniform, and Monodispersed Hollow Mesoporous Carbon Spheres in Double-Layered Supercapacitors**. *Chemistry–An Asian Journal* 2013, **8**(11):2627-2633.
193. Galeano C, Baldizzone C, Bongard H, Spliethoff B, Weidenthaler C, Meier JC, Mayrhofer KJ, Schüth F: **Carbon-Based Yolk–Shell Materials for Fuel Cell Applications**. *Advanced Functional Materials* 2014, **24**(2):220-232.
194. He G, Evers S, Liang X, Cuisinier M, Garsuch A, Nazar LF: **Tailoring porosity in carbon nanospheres for lithium–sulfur battery cathodes**. *ACS nano* 2013, **7**(12):10920-10930.
195. Zhang K, Zhao Q, Tao Z, Chen J: **Composite of sulfur impregnated in porous hollow carbon spheres as the cathode of Li-S batteries with high performance**. *Nano Research* 2013, **6**(1):38-46.
196. Valdés-Solís T, Valle-Vigón P, Sevilla M, Fuertes A: **Encapsulation of nanosized catalysts in the hollow core of a mesoporous carbon capsule**. *Journal of Catalysis* 2007, **251**(1):239-243.
197. Gregg SJ, Sing KSW, Salzberg H: **Adsorption surface area and porosity**. *Journal of The Electrochemical Society* 1967, **114**(11):279C-279C.
198. Nongwe I, Bepete G, Shaikjee A, Ravat V, Terfassa B, Meijboom R, Coville NJ: **Synthesis of gold encapsulated in spherical carbon capsules with a mesoporous shell structure. A robust catalyst in a nanoreactor**. *Catalysis Communications* 2014, **53**:77-82.
199. Michot L, Villieras F: **.9 Surface Area and Porosity**. *Developments in Clay Science* 2006, **1**:965-978.
200. Fang X, Zang J, Wang X, Zheng M-S, Zheng N: **A multiple coating route to hollow carbon spheres with foam-like shells and their applications in supercapacitor and confined catalysis**. *Journal of Materials Chemistry A* 2014, **2**(17):6191-6197.
201. Xu F, Tang Z, Huang S, Chen L, Liang Y, Mai W, Zhong H, Fu R, Wu D: **Facile synthesis of ultrahigh-surface-area hollow carbon nanospheres for enhanced adsorption and energy storage**. *Nature communications* 2015, **6**.
202. Galeano C, Güttel R, Paul M, Arnal P, Lu AH, Schüth F: **Yolk-Shell Gold Nanoparticles as Model Materials for Support-Effect Studies in Heterogeneous**

Catalysis: Au,@ C and Au,@ ZrO2 for CO Oxidation as an Example. *Chemistry–A European Journal* 2011, **17**(30):8434-8439.

203. Han J, Xu G, Ding B, Pan J, Dou H, MacFarlane DR: **Porous nitrogen-doped hollow carbon spheres derived from polyaniline for high performance supercapacitors**. *Journal of Materials Chemistry A* 2014, **2**(15):5352-5357.
204. Petkovich ND, Stein A: **Controlling macro-and mesostructures with hierarchical porosity through combined hard and soft templating**. *Chemical Society Reviews* 2013, **42**(9):3721-3739.
205. Yang Z-C, Zhang Y, Kong J-H, Wong SY, Li X, Wang J: **Hollow carbon nanoparticles of tunable size and wall thickness by hydrothermal treatment of α-cyclodextrin templated by F127 block copolymers**. *Chemistry of Materials* 2013, **25**(5):704-710.
206. Bruno MM, Cotella NG, Miras MC, Barbero CA: **A novel way to maintain resorcinol–formaldehyde porosity during drying: Stabilization of the sol–gel nanostructure using a cationic polyelectrolyte**. *Colloids and Surfaces A: Physicochemical and Engineering Aspects* 2010, **362**(1):28-32.
207. Tang J, Liu J, Salunkhe RR, Wang T, Yamauchi Y: **Nitrogen-doped hollow carbon spheres with large mesoporous shells engineered from diblock copolymer micelles**. *Chemical Communications* 2016, **52**(3):505-508.
208. Wang Y, Zou H, Zeng S, Pan Y, Wang R, Wang X, Sun Q, Zhang Z, Qiu S: **A one-step carbonization route towards nitrogen-doped porous carbon hollow spheres with ultrahigh nitrogen content for CO 2 adsorption**. *Chemical Communications* 2015, **51**(62):12423-12426.
209. Liu T, Qu L, Qian K, Liu J, Zhang Q, Liu L, Liu S: **Raspberry-like hollow carbon nanospheres with enhanced matrix-free peptide detection profiles**. *Chemical Communications* 2016, **52**(8):1709-1712.
210. Lai Y, Yang F, Zhang Z, Jiang S, Li J: **Encapsulation of selenium in porous hollow carbon spheres for advanced lithium–selenium batteries**. *RSC Advances* 2014, **4**(74):39312-39315.
211. Han Y, Dong X, Zhang C, Liu S: **Hierarchical porous carbon hollow-spheres as a high performance electrical double-layer capacitor material**. *Journal of Power Sources* 2012, **211**:92-96.
212. Yoon SB, Sohn K, Kim JY, Shin CH, Yu JS, Hyeon T: **Fabrication of carbon capsules with hollow macroporous core/mesoporous shell structures**. *Advanced Materials* 2002, **14**(1):19-21.
213. Galeano C, Meier JC, Peinecke V, Bongard H, Katsounaros I, Topalov AA, Lu A, Mayrhofer KJ, Schüth F: **Toward highly stable electrocatalysts via nanoparticle pore confinement**. *Journal of the American Chemical Society* 2012, **134**(50):20457-20465.

214. Fu J, Xu Q, Chen J, Chen Z, Huang X, Tang X: **Controlled fabrication of uniform hollow core porous shell carbon spheres by the pyrolysis of core/shell polystyrene/cross-linked polyphosphazene composites**. *Chemical Communications* 2010, **46**(35):6563-6565.
215. Fuertes AB, Valle-Vigón P, Sevilla M: **One-step synthesis of silica@ resorcinol–formaldehyde spheres and their application for the fabrication of polymer and carbon capsules**. *Chemical Communications* 2012, **48**(49):6124-6126.
216. Yang X, Zhang Z, Fu Y, Li Q: **Porous hollow carbon spheres decorated with molybdenum diselenide nanosheets as anodes for highly reversible lithium and sodium storage**. *Nanoscale* 2015, **7**(22):10198-10203.
217. Phaahlamohlaka TN, Kumi DO, Dlamini MW, Jewell LL, Coville NJ: **Ruthenium nanoparticles encapsulated inside porous hollow carbon spheres: A novel catalyst for Fischer–Tropsch synthesis**. *Catalysis Today* 2016, **275**:76-83.
218. Zhang Z, Xiao F, Xi J, Sun T, Xiao S, Wang H, Wang S, Liu Y: **Encapsulating Pd nanoparticles in double-shelled graphene@ carbon hollow spheres for excellent chemical catalytic property**. *Scientific reports* 2014, **4**:4053.
219. Bian S-W, Liu S, Guo M-X, Xu L-L, Chang L: **Pd nanoparticles partially embedded in the inner wall of nitrogen-doped carbon hollow spheres as nanoreactors for catalytic reduction of 4-nitrophenol**. *RSC Advances* 2015, **5**(16):11913-11916.
220. Fang X, Liu S, Zang J, Xu C, Zheng M-S, Dong Q-F, Sun D, Zheng N: **Precisely controlled resorcinol–formaldehyde resin coating for fabricating core–shell, hollow, and yolk–shell carbon nanostructures**. *Nanoscale* 2013, **5**(15):6908-6916.
221. **Transmission Electron Microscopy** [https://cmrf.research.uiowa.edu/transmission-electron-microscopy]
222. **Transmission Electron Microscopy (TEM)** [https://www2.warwick.ac.uk/fac/sci/physics/current/postgraduate/regs/mpags/ex5/techniques/structural/tem/]
223. **Scanning Electron Microscopy (SEM)** [http://www2.warwick.ac.uk/fac/sci/physics/current/postgraduate/regs/mpags/ex5/techniques/structural/sem3]
224. **Electron probe micro-analyzer (EPMA)** [http://serc.carleton.edu/research_education/geochemsheets/techniques/EPMA.html]
225. **Qualitative and Quantitative Elemental Micro-Analysis** [http://www.cameca.com/instruments-for-research/epma.aspx]
226. **BET Surface Area Analysis of Nanoparticles** [http://archive.cnx.org/contents/f5c058e0-41f2-4ef6-878b-2fdc07760129@1/bet-surface-area-analysis-of-nanoparticles]

227. Fadoni M, Lucarelli L: **Temperature programmed desorption, reduction, oxidation and flow chemisorption for the characterisation of heterogeneous catalysts. Theoretical aspects, instrumentation and applications**. *Studies in Surface Science and Catalysis* 1999, **120**:177-225.
228. Niemantsverdriet JW: **Spectroscopy in catalysis**: John Wiley & Sons; 2007.
229. Nakai K, Nakamura K: **Pulse chemisorption measurement< Metal dispersion measurement>**. *BEL-CAT Application Note: CAT-APP-002* 2003:1-6.
230. **Basic operating principles of the Sorptomatic 1990** [http://saf.chem.ox.ac.uk/operating-principles-3.aspx]
231. **Raman spectroscopy** [https://www.st-andrews.ac.uk/seeinglife/science/research/Raman/Raman.html]
232. Doyle WM: **Principles and applications of Fourier transform infrared (FTIR) process analysis**. *Process control and quality* 1992, **2**:50.
233. **MCAT Organic Chemistry Review Spectroscopy** [http://schoolbag.info/chemistry/mcat/89.html]
234. Gabbott P: **Principles and applications of thermal analysis**: John Wiley & Sons; 2008.
235. Dinnebier RE: **Powder diffraction: theory and practice**: Royal Society of Chemistry; 2008.
236. **Bragg's Law Demonstration** [http://www-outreach.phy.cam.ac.uk/camphy/xraydiffraction/xraydiffraction_exp.htm]
237. Nyathi TM: **Preferential oxidation of carbon monoxide in hydrogen-rich gases over supported cobalt oxide catalysts**. University of Cape Town South Africa; 2015.
238. Xia Y, Mokaya R: **Synthesis of ordered mesoporous carbon and nitrogen-doped carbon materials with graphitic pore walls via a simple chemical vapor deposition method**. *Advanced materials* 2004, **16**(17):1553-1558.
239. Li S, Pasc A, Fierro V, Celzard A: **Hollow carbon spheres, synthesis and applications - a review**. *Journal of Materials Chemistry A* 2016, **4**(33):12686-12713.
240. Moyo M: **Cobalt and iron supported on carbon spheres catalysts for Fischer Tropsch synthesis**. Faculty of Engineering and the Built Environment, University of the Witwatersrand, Johannesburg; 2012.
241. Phaahlamohlaka TN: **Synthesis of carbon nanofibers and their subsequent use as catalyst supports for Fischer-Tropsch synthesis**. 2014.
242. Khodakov AY, Chu W, Fongarland P: **Advances in the development of novel cobalt Fischer-Tropsch catalysts for synthesis of long-chain hydrocarbons and clean fuels**. *Chemical Reviews* 2007, **107**(5):1692-1744.
243. Xiong H, Moyo M, Motchelaho MA, Tetana ZN, Dube S, Jewell LL, Coville NJ: **Fischer–Tropsch synthesis: Iron catalysts supported on N-doped carbon**

spheres prepared by chemical vapor deposition and hydrothermal approaches. *Journal of Catalysis* 2014, **311**:80-87.

244. Dagle RA, Wang Y, Xia G-G, Strohm JJ, Holladay J, Palo DR: **Selective CO methanation catalysts for fuel processing applications**. *Applied Catalysis A: General* 2007, **326**(2):213-218.
245. Van Vliet OP, Faaij AP, Turkenburg WC: **Fischer–Tropsch diesel production in a well-to-wheel perspective: a carbon, energy flow and cost analysis**. *Energy Conversion and Management* 2009, **50**(4):855-876.
246. Galletti C, Specchia S, Saracco G, Specchia V: **CO-selective methanation over Ru–γAl< sub> 2</sub> O< sub> 3</sub> catalysts in H< sub> 2</sub>-rich gas for PEM FC applications**. *Chemical Engineering Science* 2010, **65**(1):590-596.
247. Bartholomew CH, Pannell RB, Butler JL: **Support and crystallite size effects in CO hydrogenation on nickel**. *Journal of Catalysis* 1980, **65**(2):335-347.
248. Schulz H: **Selforganization in Fischer–Tropsch synthesis with iron-and cobalt catalysts**. *Catalysis Today* 2014, **228**:113-122.
249. Simonetti DA, Rass-Hansen J, Kunkes EL, Soares RR, Dumesic JA: **Coupling of glycerol processing with Fischer–Tropsch synthesis for production of liquid fuels**. *Green Chemistry* 2007, **9**(10):1073-1083.
250. Sun J, Li X, Taguchi A, Abe T, Niu W, Lu P, Yoneyama Y, Tsubaki N: **Highly-Dispersed Metallic Ru Nanoparticles Sputtered on H-Beta Zeolite for Directly Converting Syngas to Middle Isoparaffins**. *ACS Catalysis* 2013, **4**(1):1-8.
251. Cheng K, Kang J, Huang S, You Z, Zhang Q, Ding J, Hua W, Lou Y, Deng W, Wang Y: **Mesoporous beta zeolite-supported Ruthenium nanoparticles for selective conversion of synthesis gas to C5–C11 isoparaffins**. *ACS Catalysis* 2012, **2**(3):441-449.
252. Jenness GR, Schmidt JR: **Unraveling the Role of Metal–Support Interactions in Heterogeneous Catalysis: Oxygenate Selectivity in Fischer–Tropsch Synthesis**. *ACS Catalysis* 2013, **3**(12):2881-2890.
253. Xiong J, Dong X, Li L: **CO selective methanation in hydrogen-rich gas mixtures over carbon nanotube supported Ru-based catalysts**. *Journal of Natural Gas Chemistry* 2012, **21**(4):445-451.
254. Kang J, Zhang S, Zhang Q, Wang Y: **Ruthenium nanoparticles supported on carbon nanotubes as efficient catalysts for selective conversion of synthesis gas to diesel fuel**. *Angewandte Chemie* 2009, **121**(14):2603-2606.
255. Dlamini MW, Kumi DO, Phaahlamohlaka TN, Lyadov AS, Billing DG, Jewell LL, Coville NJ: **Carbon Spheres Prepared by Hydrothermal Synthesis—A Support for Bimetallic Iron Cobalt Fischer–Tropsch Catalysts**. *ChemCatChem* 2015, **7**(18):3000-3011.
256. Zhang H-X, Liu M, Bu X, Zhang J: **Zeolitic BIF Crystal Directly Producing Noble-Metal Nanoparticles in Its Pores for Catalysis**. *Sci Rep* 2014, **4**.

257. Huo C, Ouyang J, Yang H: **CuO nanoparticles encapsulated inside Al-MCM-41 mesoporous materials via direct synthetic route**. *Sci Rep* 2014, **4**.
258. Xiong K, Li J, Liew K, Zhan X: **Preparation and characterization of stable Ru nanoparticles embedded on the ordered mesoporous carbon material for applications in Fischer–Tropsch synthesis**. *Applied Catalysis A: General* 2010, **389**(1–2):173-178.
259. Yin Y, Rioux RM, Erdonmez CK, Hughes S, Somorjai GA, Alivisatos AP: **Formation of hollow nanocrystals through the nanoscale Kirkendall effect**. *Science* 2004, **304**(5671):711-714.
260. Kim S, Yin Y, Alivisatos AP, Somorjai GA, Yates JT: **IR spectroscopic observation of molecular transport through Pt@ CoO yolk-shell nanostructures**. *Journal of the American Chemical Society* 2007, **129**(30):9510-9513.
261. Chen Z, Cui Z-M, Niu F, Jiang L, Song W-G: **Pd nanoparticles in silica hollow spheres with mesoporous walls: a nanoreactor with extremely high activity**. *Chem Commun* 2010, **46**(35):6524-6526.
262. Chen W, Fan Z, Pan X, Bao X: **Effect of Confinement in Carbon Nanotubes on the Activity of Fischer−Tropsch Iron Catalyst**. *Journal of the American Chemical Society* 2008, **130**(29):9414-9419.
263. Xiao J, Pan X, Guo S, Ren P, Bao X: **Toward Fundamentals of Confined Catalysis in Carbon Nanotubes**. *Journal of the American Chemical Society* 2015, **137**(1):477-482.
264. Liu R, Qu F, Guo Y, Yao N, Priestley RD: **Au@carbon yolk-shell nanostructures via one-step core-shell-shell template**. *Chemical Communications* 2014, **50**(4):478-480.
265. Xiong H, Motchelaho MA, Moyo M, Jewell LL, Coville NJ: **Cobalt catalysts supported on a micro-coil carbon in Fischer—Tropsch synthesis: A comparison with CNTs and CNFs**. *Catalysis Today* 2013, **214**:50-60.
266. Trépanier M, Dalai AK, Abatzoglou N: **Synthesis of CNT-supported cobalt nanoparticle catalysts using a microemulsion technique: Role of nanoparticle size on reducibility, activity and selectivity in Fischer–Tropsch reactions**. *Applied Catalysis A: General* 2010, **374**(1):79-86.
267. Li S, Niu J, Zhao YC, So KP, Wang C, Wang CA, Li J: **High-rate aluminium yolk-shell nanoparticle anode for Li-ion battery with long cycle life and ultrahigh capacity**. *Nat Commun* 2015, **6**.
268. Stöber W, Fink A, Bohn E: **Controlled growth of monodisperse silica spheres in the micron size range**. *Journal of colloid and interface science* 1968, **26**(1):62-69.
269. Carballo JMG, Finocchio E, García S, Rojas S, Ojeda M, Fierro JLG: **Support effects on the structure and performance of ruthenium catalysts for the**

Fischer–Tropsch synthesis. *Catalysis Science & Technology* 2011, **1**(6):1013-1023.

270. Lee I, Zhang Q, Ge J, Yin Y, Zaera F: **Encapsulation of supported Pt nanoparticles with mesoporous silica for increased catalyst stability**. *Nano Research* 2011, **4**(1):115-123.
271. Astruc D, Lu F, Aranzaes JR: **Nanoparticles as recyclable catalysts: the frontier between homogeneous and heterogeneous catalysis**. *Angewandte Chemie International Edition* 2005, **44**(48):7852-7872.
272. Ferrari A, Robertson J: **Resonant Raman spectroscopy of disordered, amorphous, and diamondlike carbon**. *Physical Review B* 2001, **64**(7):075414.
273. Ferrari A, Robertson J: **Interpretation of Raman spectra of disordered and amorphous carbon**. *Physical Review B* 2000, **61**(20):14095.
274. Hong J, Marceau E, Khodakov AY, Gaberová L, Griboval-Constant A, Girardon J-S, Fontaine CL, Briois V: **Speciation of Ruthenium as a Reduction Promoter of Silica-Supported Co Catalysts: A Time-Resolved in Situ XAS Investigation**. *ACS Catalysis* 2015, **5**(2):1273-1282.
275. Groen JC, Peffer LA, Pérez-Ramírez J: **Pore size determination in modified micro-and mesoporous materials. Pitfalls and limitations in gas adsorption data analysis**. *Microporous and Mesoporous Materials* 2003, **60**(1):1-17.
276. Chen X, Kierzek K, Wenelska K, Cendrowski K, Gong J, Wen X, Tang T, Chu PK, Mijowska E: **Electrochemical Characteristics of Discrete, Uniform, and Monodispersed Hollow Mesoporous Carbon Spheres in Double-Layered Supercapacitors**. *Chemistry, an Asian journal* 2013, **8**(11):2627-2633.
277. Kang J, Deng W, Zhang Q, Wang Y: **Ru particle size effect in Ru/CNT-catalyzed Fischer-Tropsch synthesis**. *Journal of Energy Chemistry* 2013, **22**(2):321-328.
278. Carballo JMG, Yang J, Holmen A, García-Rodríguez S, Rojas S, Ojeda M, Fierro JLG: **Catalytic effects of ruthenium particle size on the Fischer–Tropsch Synthesis**. *Journal of Catalysis* 2011, **284**(1):102-108.
279. Bezemer GL, Bitter JH, Kuipers HP, Oosterbeek H, Holewijn JE, Xu X, Kapteijn F, van Dillen AJ, de Jong KP: **Cobalt particle size effects in the Fischer-Tropsch reaction studied with carbon nanofiber supported catalysts**. *Journal of the American Chemical Society* 2006, **128**(12):3956-3964.
280. Chen J, Liu Z-P: **Origin of selectivity switch in Fischer− Tropsch synthesis over Ru and Rh from first-principles statistical mechanics studies**. *Journal of the American Chemical Society* 2008, **130**(25):7929-7937.
281. Zeinalipour-Yazdi CD, Cooksy AL, Efstathiou AM: **CO adsorption on transition metal clusters: Trends from density functional theory**. *Surface Science* 2008, **602**(10):1858-1862.

282. Choi M, Yook S, Kim H: **Hydrogen Spillover in Encapsulated Metal Catalysts: New Opportunities for Designing Advanced Hydroprocessing Catalysts**. *ChemCatChem* 2015, **7**(7):1048-1057.
283. Nabaho D, Niemantsverdriet JW, Claeys M, Steen Ev: **Hydrogen spillover in the Fischer–Tropsch synthesis: An analysis of gold as a promoter for cobalt–alumina catalysts**. *Catalysis Today* 2016, **275**:27-34.
284. Zecevic J, Vanbutsele G, de Jong KP, Martens JA: **Nanoscale intimacy in bifunctional catalysts for selective conversion of hydrocarbons**. *Nature* 2015, **528**(7581):245-248.
285. Hilmen A, Schanke D, Holmen A: **TPR study of the mechanism of rhenium promotion of alumina-supported cobalt Fischer-Tropsch catalysts**. *Catalysis letters* 1996, **38**(3-4):143-147.
286. Lueking AD, Yang RT: **Hydrogen spillover to enhance hydrogen storage—study of the effect of carbon physicochemical properties**. *Applied Catalysis A: General* 2004, **265**(2):259-268.
287. Chung T-Y, Tsao C-S, Tseng H-P, Chen C-H, Yu M-S: **Effects of oxygen functional groups on the enhancement of the hydrogen spillover of Pd-doped activated carbon**. *Journal of colloid and interface science* 2015, **441**:98-105.
288. Lueking A, Yang RT: **Hydrogen spillover from a metal oxide catalyst onto carbon nanotubes—implications for hydrogen storage**. *Journal of catalysis* 2002, **206**(1):165-168.
289. Lee J, Kim SM, Lee IS: **Functionalization of hollow nanoparticles for nanoreactor applications**. *Nano Today* 2014, **9**(5):631-667.
290. Bruce LA, Hoang M, Hughes AE, Turney TW: **Ruthenium promotion of Fischer-Tropsch synthesis over coprecipitated cobalt/ceria catalysts**. *Applied Catalysis A: General* 1993, **100**(1):51-67.
291. Hoang M, Hughes AE, Turney TW: **An XPS study of Ru-promotion for Co/CeO 2 Fischer-Tropsch catalyst**. *Applied surface science* 1993, **72**(1):55-65.
292. Park J-Y, Lee Y-J, Karandikar PR, Jun K-W, Bae JW, Ha K-S: **Ru promoted cobalt catalyst on γ-Al 2 O 3 support: Influence of pre-synthesized nanoparticles on Fischer–Tropsch reaction**. *Journal of Molecular Catalysis A: Chemical* 2011, **344**(1):153-160.
293. Sapunov VN, Grigoryev MY, Sulman EM, Konyaeva MB, Matveeva VG: **D-Glucose Hydrogenation over Ru Nanoparticles Embedded in Mesoporous Hypercrosslinked Polystyrene**. *The Journal of Physical Chemistry A* 2013, **117**(20):4073-4083.
294. Chen X, Kierzek K, Cendrowski K, Pelech I, Zhao X, Feng J, Kalenczuk RJ, Tang T, Mijowska E: **CVD generated mesoporous hollow carbon spheres as supercapacitors**. *Colloids and Surfaces A: Physicochemical and Engineering Aspects* 2012, **396**:246-250.

295. Weidenthaler C: **Pitfalls in the characterization of nanoporous and nanosized materials**. *Nanoscale* 2011, **3**(3):792-810.
296. du Plessis HE, Forbes RP, Barnard W, Erasmus WJ, Steuwer A: **In situ reduction study of cobalt model Fischer–Tropsch synthesis catalysts**. *Physical Chemistry Chemical Physics* 2013, **15**(28):11640-11645.
297. Rayner MK, Billing DG, Coville NJ: **In-situ X-ray diffraction activation study on an Fe/TiO2 pre-catalyst**. *Acta Crystallographica Section B: Structural Science, Crystal Engineering and Materials* 2014, **70**(3):498-509.
298. Fu T, Jiang Y, Lv J, Li Z: **Effect of carbon support on Fischer–Tropsch synthesis activity and product distribution over Co-based catalysts**. *Fuel Processing Technology* 2013, **110**:141-149.
299. Bezemer GL, Radstake P, Falke U, Oosterbeek H, Kuipers H, Van Dillen A, De Jong K: **Investigation of promoter effects of manganese oxide on carbon nanofiber-supported cobalt catalysts for Fischer–Tropsch synthesis**. *Journal of catalysis* 2006, **237**(1):152-161.
300. Coronel-García M, de la Torre AR, Melo-Banda J, Martínez-Salazar A, Rodrigo RS, Zavala ND, Martínez BP, Domínguez J: **Study of Co, Ru/SBA-15 type materials for Fischer–Tropsch synthesis in fixed bed tubular reactor: I. Effect of the high Ru content on the catalytic activity**. *International Journal of Hydrogen Energy* 2015, **40**(48):17264-17271.
301. Jermwongratanachai T, Jacobs G, Shafer WD, Pendyala VRR, Ma W, Gnanamani MK, Hopps S, Thomas GA, Kitiyanan B, Khalid S: **Fischer–Tropsch synthesis: TPR and XANES analysis of the impact of simulated regeneration cycles on the reducibility of Co/alumina catalysts with different promoters (Pt, Ru, Re, Ag, Au, Rh, Ir)**. *Catalysis Today* 2014, **228**:15-21.
302. Kogelbauer A, Goodwin JJG, Oukaci R: **Ruthenium Promotion of Co/Al2O3Fischer–Tropsch Catalysts**. *Journal of catalysis* 1996, **160**(1):125-133.
303. Liu J-X, Su H-Y, Sun D-P, Zhang B-Y, Li W-X: **Crystallographic dependence of CO activation on cobalt catalysts: HCP versus FCC**. *Journal of the American Chemical Society* 2013, **135**(44):16284-16287.
304. Cook KM, Perez HD, Bartholomew CH, Hecker WC: **Effect of promoter deposition order on platinum-, ruthenium-, or rhenium-promoted cobalt Fischer–Tropsch catalysts**. *Applied Catalysis A: General* 2014, **482**:275-286.
305. Kogelbauer A, Goodwin Jr JG, Oukaci R: **Ruthenium Promotion of Co/Al2O3Fischer–Tropsch Catalysts**. *Journal of Catalysis* 1996, **160**(1):125-133.
306. Jacobs G, Ma W, Davis BH: **Influence of Reduction Promoters on Stability of Cobalt/g-Alumina Fischer-Tropsch Synthesis Catalysts**. *Catalysts* 2014, **4**(1):49-76.
307. Sermon P, Bond G: **Hydrogen spillover**. *Catalysis Reviews* 1974, **8**(1):211-239.

308. Yu Q, Li M, Zeng Q, Wu X: **Highly Porous Copper with Hollow Microsphere Structure from Polystyrene Templates via Electroless Plating**. *Journal of The Electrochemical Society* 2017, **164**(4):D135-D142.
309. Fan X, Niu L, Xia Z: **Preparation of raspberry-like silica microcapsules via sulfonated polystyrene template and aniline medium assembly method**. *Colloid and Polymer Science* 2014, **292**(12):3251-3259.
310. Chen Y, Liew KY, Li J: **Size-controlled synthesis of Ru nanoparticles by ethylene glycol reduction**. *Materials Letters* 2008, **62**(6):1018-1021.
311. Tang C-W, Wang C-B, Chien S-H: **Characterization of cobalt oxides studied by FT-IR, Raman, TPR and TG-MS**. *Thermochimica Acta* 2008, **473**(1):68-73.
312. Hadjiev V, Iliev M, Vergilov I: **The Raman spectra of Co3O4**. *Journal of Physics C: Solid State Physics* 1988, **21**(7):L199.
313. Ilie A, Hart A, Flewitt A, Robertson J, Milne W: **Effect of work function and surface microstructure on field emission of tetrahedral amorphous carbon**. *Journal of Applied Physics* 2000, **88**(10):6002-6010.
314. Ferrari AC, Robertson J: **Interpretation of Raman spectra of disordered and amorphous carbon**. *Physical review B* 2000, **61**(20):14095.
315. Iglesia E, Soled SL, Fiato RA, Via GH: **Bimetallic synergy in cobalt ruthenium Fischer-Tropsch synthesis catalysts**. *Journal of Catalysis* 1993, **143**(2):345-368.
316. Xu D, Li W, Duan H, Ge Q, Xu H: **Reaction performance and characterization of Co/Al 2 O 3 Fischer–Tropsch catalysts promoted with Pt, Pd and Ru**. *Catalysis Letters* 2005, **102**(3):229-235.
317. Hong J, Chernavskii PA, Khodakov AY, Chu W: **Effect of promotion with ruthenium on the structure and catalytic performance of mesoporous silica (smaller and larger pore) supported cobalt Fischer–Tropsch catalysts**. *Catalysis Today* 2009, **140**(3):135-141.
318. Sineva LV, Kulchakovskaya EV, Asalieva EY, Mordkovich VZ: **Effect of water on the secondary transformations of hydrocarbons in the Fischer–Tropsch synthesis on Co-zeolite catalysts**. *Mendeleev Communications* 2017, **27**(1):75-77.
319. Storsæter S, Borg Ø, Blekkan EA, Holmen A: **Study of the effect of water on Fischer–Tropsch synthesis over supported cobalt catalysts**. *Journal of Catalysis* 2005, **231**(2):405-419.
320. Fratalocchi L, Visconti CG, Lietti L, Groppi G, Tronconi E, Roccaro E, Zennaro R: **On the performance of a Co-based catalyst supported on modified γ-Al 2 O 3 during Fischer–Tropsch synthesis in the presence of co-fed water**. *Catalysis Science & Technology* 2016, **6**(16):6431-6440.
321. Bartholomew CH: **Mechanisms of catalyst deactivation**. *Applied Catalysis A: General* 2001, **212**(1):17-60.

322. Wu CH, Eren B, Bluhm H, Salmeron MB: **Ambient-Pressure X-ray Photoelectron Spectroscopy Study of Cobalt Foil Model Catalyst under CO, H2, and Their Mixtures**. *ACS Catalysis* 2017, **7**(2):1150-1157.
323. Chernavskii P, Dalmon J-A, Perov N, Khodakov A: **Magnetic characterization of fischer-tropsch catalysts**. *Oil & Gas Science and Technology-Revue de l'IFP* 2009, **64**(1):25-48.
324. Jean-Marie A, Griboval-Constant A, Khodakov AY, Diehl F: **Cobalt supported on alumina and silica-doped alumina: Catalyst structure and catalytic performance in Fischer–Tropsch synthesis**. *Comptes Rendus Chimie* 2009, **12**(6–7):660-667.
325. Hauman M, Saib A, Moodley D, Du Plessis E, Claeys M, Van Steen E: **Re-dispersion of Cobalt on a Model Fischer–Tropsch Catalyst During Reduction–Oxidation–Reduction Cycles**. *ChemCatChem* 2012, **4**(9):1411-1419.
326. Fei Tan K, Xu J, Chang J, Borgna A, Saeys M: **Carbon deposition on Co catalysts during Fischer–Tropsch synthesis: A computational and experimental study**. *Journal of Catalysis* 2010, **274**(2):121-129.
327. Saib AM, Moodley DJ, Ciobîcă IM, Hauman MM, Sigwebela BH, Weststrate CJ, Niemantsverdriet JW, van de Loosdrecht J: **Fundamental understanding of deactivation and regeneration of cobalt Fischer–Tropsch synthesis catalysts**. *Catalysis Today* 2010, **154**(3–4):271-282.
328. Lu P, Campbell CT, Xia Y: **A sinter-resistant catalytic system fabricated by maneuvering the selectivity of SiO2 deposition onto the TiO2 surface versus the Pt nanoparticle surface**. *Nano letters* 2013, **13**(10):4957-4962.
329. Wang Y, Liu J, Wang P, Werth CJ, Strathmann TJ: **Palladium nanoparticles encapsulated in core–shell silica: A structured hydrogenation catalyst with enhanced activity for reduction of oxyanion water pollutants**. *ACS Catalysis* 2014, **4**(10):3551-3559.
330. Lu J, Fu B, Kung MC, Xiao G, Elam JW, Kung HH, Stair PC: **Coking-and sintering-resistant palladium catalysts achieved through atomic layer deposition**. *Science* 2012, **335**(6073):1205-1208.
331. Chen C, Qu J, Cao C, Niu F, Song W: **CuO nanoclusters coated with mesoporous SiO 2 as highly active and stable catalysts for olefin epoxidation**. *Journal of Materials Chemistry* 2011, **21**(15):5774-5779.
332. Cheng N, Banis MN, Liu J, Riese A, Li X, Li R, Ye S, Knights S, Sun X: **Extremely Stable Platinum Nanoparticles Encapsulated in a Zirconia Nanocage by Area-Selective Atomic Layer Deposition for the Oxygen Reduction Reaction**. *Advanced Materials* 2015, **27**(2):277-281.
333. Oh J-G, Oh H-S, Lee WH, Kim H: **Preparation of carbon-supported nanosegregated Pt alloy catalysts for the oxygen reduction reaction using a**

silica encapsulation process to inhibit the sintering effect during heat treatment. *Journal of Materials Chemistry* 2012, **22**(30):15215-15220.

334. Reddy AS, Kim S, Jeong HY, Jin S, Qadir K, Jung K, Jung CH, Yun JY, Cheon JY, Yang J-M: **Ultrathin titania coating for high-temperature stable SiO 2/Pt nanocatalysts**. *Chemical Communications* 2011, **47**(29):8412-8414.
335. Yoon K, Yang Y, Lu P, Wan D, Peng HC, Stamm Masias K, Fanson PT, Campbell CT, Xia Y: **A Highly Reactive and Sinter-Resistant Catalytic System Based on Platinum Nanoparticles Embedded in the Inner Surfaces of CeO2 Hollow Fibers**. *Angewandte Chemie International Edition* 2012, **51**(38):9543-9546.
336. Geus JW, Dillen AJ: **Preparation of supported catalysts by deposition–precipitation**. *Handbook of heterogeneous catalysis* 1997.
337. Bo Z, Eaton TR, Gallagher JR, Canlas CP, Miller JT, Notestein JM: **Size-Selective Synthesis and Stabilization of Small Silver Nanoparticles on TiO2 Partially Masked by SiO2**. *Chemistry of Materials* 2015, **27**(4):1269-1277.
338. Melaet Grm, Ralston WT, Li C-S, Alayoglu S, An K, Musselwhite N, Kalkan B, Somorjai GA: **Evidence of highly active cobalt oxide catalyst for the Fischer–Tropsch synthesis and CO2 hydrogenation**. *Journal of the American Chemical Society* 2014, **136**(6):2260-2263.
339. Xie R, Wang C, Xia L, Wang H, Zhao T, Sun Y: **Controlled Preparation of Co3O4@ porous-SiO2 Nanocomposites for Fischer–Tropsch Synthesis**. *Catalysis Letters* 2014, **144**(3):516-523.
340. Nobile A, Davis M: **Importance of the anatase-rutile phase transition and titania grain enlargement in the strong metal-support interaction phenomenon in FeTiO2 catalysts**. *Journal of Catalysis* 1989, **116**(2):383-398.
341. Van de Loosdrecht J, Van der Kraan A, Van Dillen A, Geus J: **Metal-support interaction: titania-supported nickel-iron catalysts**. *Catalysis Letters* 1996, **41**(1-2):27-34.
342. Duvenhage D, Coville N: **Fe: Co/TiO 2 bimetallic catalysts for the Fischer–Tropsch reaction: Part 2. The effect of calcination and reduction temperature**. *Applied Catalysis A: General* 2002, **233**(1):63-75.
343. Shaikjee A, Coville NJ: **The role of the hydrocarbon source on the growth of carbon materials**. *Carbon* 2012, **50**(10):3376-3398.
344. Chen X, Kierzek K, Jiang Z, Chen H, Tang T, Wojtoniszak M, Kalenczuk RJ, Chu PK, Borowiak-Palen E: **Synthesis, growth mechanism, and electrochemical properties of hollow mesoporous carbon spheres with controlled diameter**. *The Journal of Physical Chemistry C* 2011, **115**(36):17717-17724.
345. Chang C-C, Chen C-C, Hung W-H, Hsu I-K, Pimenta MA, Cronin SB: **Strain-induced D band observed in carbon nanotubes**. *Nano Research* 2012, **5**(12):854-862.

346. Rietveld H: **A profile refinement method for nuclear and magnetic structures**. *Journal of Applied Crystallography* 1969, **2**(2):65-71.
347. Cheary RW, Coelho A: **A fundamental parameters approach to X-ray line-profile fitting**. *Journal of Applied Crystallography* 1992, **25**(2):109-121.
348. Cheary R: **Fundamental Parameters Line Profile Fitting in Laboratory Difiractometers**. *Journal of Research of the National Institute of Standards and Technology* 2004, **109**(1).